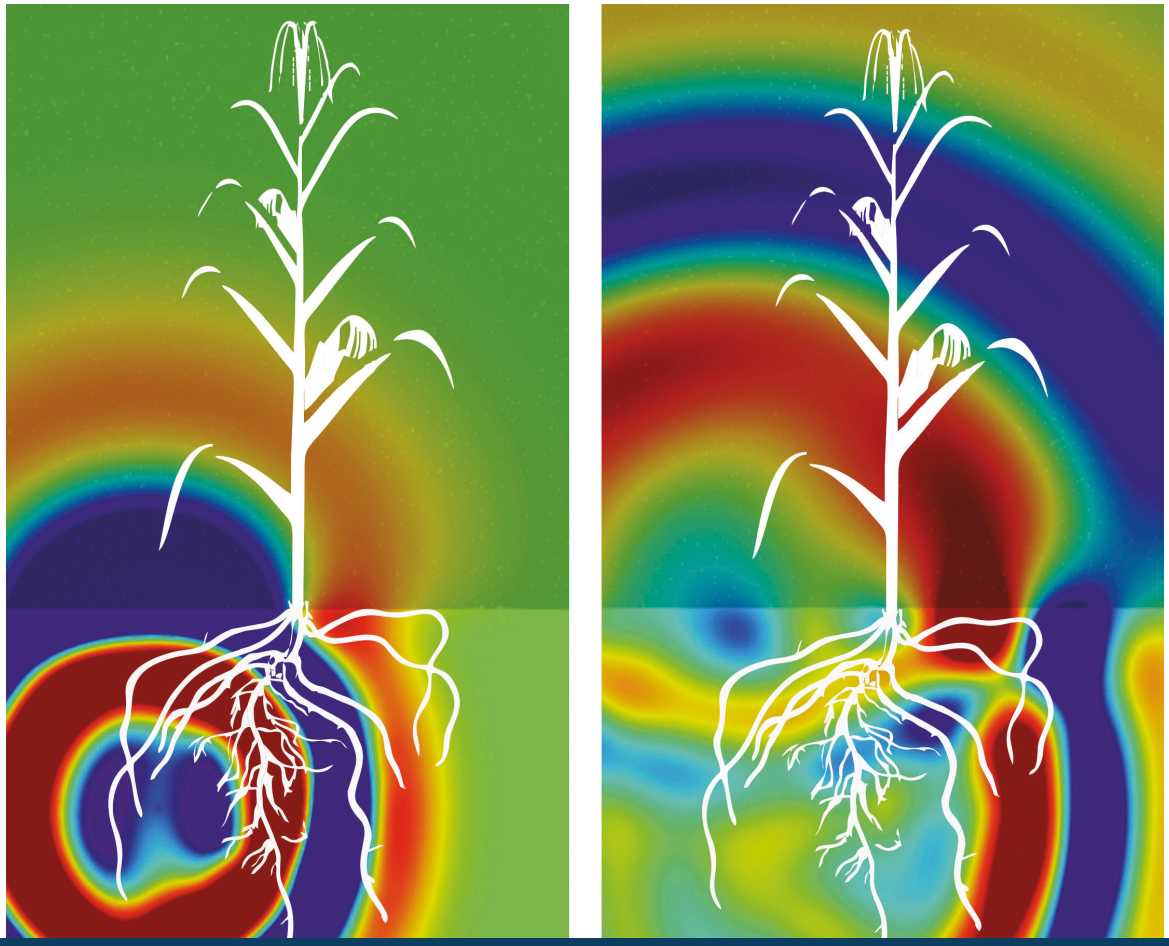

Imaging spatial and temporal soil water content variations of the soil-plant continuum using ground penetrating radar

Lena Lärm

Energie & Umwelt / Energy & Environment
Band / Volume 641
ISBN 978-3-95806-778-3

Mitglied der Helmholtz-Gemeinschaft

JÜLICH
Forschungszentrum

Schriften des Forschungszentrums Jülich
Reihe Energie & Umwelt / Energy & Environment Band / Volume 641

Forschungszentrum Jülich GmbH
Institut für Bio- und Geowissenschaften (IBG)
Agrosphäre (IBG-3)

Imaging spatial and temporal soil water content variations of the soil-plant continuum using ground penetrating radar

Lena Lärm

Schriften des Forschungszentrums Jülich
Reihe Energie & Umwelt / Energy & Environment Band / Volume 641

ISSN 1866-1793 ISBN 978-3-95806-778-3

Bibliografische Information der Deutschen Nationalbibliothek.
Die Deutsche Nationalbibliothek verzeichnet diese Publikation in der
Deutschen Nationalbibliografie; detaillierte Bibliografische Daten
sind im Internet über http://dnb.d-nb.de abrufbar.

Herausgeber und Vertrieb:	Forschungszentrum Jülich GmbH Zentralbibliothek, Verlag 52425 Jülich Tel.: +49 2461 61-5368 Fax: +49 2461 61-6103 zb-publikation@fz-juelich.de www.fz-juelich.de/zb
Umschlaggestaltung:	Grafische Medien, Forschungszentrum Jülich GmbH
Druck:	Grafische Medien, Forschungszentrum Jülich GmbH
Copyright:	Forschungszentrum Jülich 2024

Schriften des Forschungszentrums Jülich
Reihe Energie & Umwelt / Energy & Environment, Band / Volume 641

D 5 (Diss. Bonn University, 2024)

ISSN 1866-1793
ISBN 978-3-95806-778-3

Vollständig frei verfügbar über das Publikationsportal des Forschungszentrums Jülich (JuSER)
unter www.fz-juelich.de/zb/openaccess.

Referentin:
Prof. Dr. Andrea Schnepf

1. Korreferentin:
Prof. Dr. Anja Klotzsche, Universität zu Köln, Deutschland

2. Korreferent:
Prof. Dr. Andreas Kemna

Tag der mündlichen Prüfung: 08. April 2024

Angefertigt mit Genehmigung der Landwirtschaftlichen Fakultät der Universität Bonn

Abstract

The soil-plant continuum regulates a wide range of processes, which are crucial for plant performance, such as root water and nutrient uptake and the spatio-temporal distribution of soil water. Especially for agricultural crops within agro-ecosystems, detailed understanding of processes and interactions is essential, since agriculture is majorly impacted by climate change and holds the potential to meet the requirements of increasing feed and food demand. The non-invasive imaging of processes and the estimation of important parameters and state variables concerning the soil-plant continuum, in particular root system architecture, soil water content (SWC) distribution, and soil hydraulic properties, can help to optimize agricultural management practices and enhance yield productivity while minimizing the use of natural resources. Currently, most of the processes and parameters are being separately investigated, at different scales, by differing research fields, such as agrogeophysics and crop science. Since the different components influence each other, a separate consideration is not feasible, and more combined research is needed. One approach is to join agrogeophysical methods, such as ground penetrating radar (GPR), and root information to monitor and characterize the soil-plant continuum. In this study, an open-source data set including soil sensor data, root images, and GPR permittivities from five years for various crop types and agricultural treatments was established. For all of these data, new standards were created and provide a novel comprehensive data set for other researchers. Within this time-lapse data set, certain effects on the GPR signal related to soil type, surface water treatment, atmospheric conditions, and previous soil management could be identified. Therefore, the impact of row crops, such as maize, on the horizontal spatio-temporal distribution of the permittivity and hence SWC was investigated. A statistical analysis method for the visualization was developed by deriving the so-called trend-corrected spatial permittivity deviations of the vegetated field. Thereby, a link and correlation between the permittivity variability and the root volume fractions was observed. For the further quantification of the relation between the recorded GPR signals and the presence of roots and above-ground shoot, a numerical study was performed under different scenarios. Roots showed a greater impact on the synthetic GPR data than the above-ground shoot, and standard analysis tools, such as first arrival picking, could be confirmed for investigating the soil-plant continuum using crosshole GPR applications. Additionally, a new approach to derive the actual available water in the soil was presented, showing that neglect-

ing the root phase in appropriate petrophysical mixing models overestimated the SWC. For the further investigation of the plant available water, we considered the horizontal crosshole GPR-derived SWCs for a winter wheat growing season in combination with a hydrological model to derive the soil hydraulic parameters. In a first step, this sequential hydrogeophysical inversion was used for a one-dimensional averaged case and was upscaled in a second step to the plot scale, where the pseudo three-dimensional spatially distributed soil hydraulic parameters for the dual-porosity Mualem-van-Genuchten model were estimated. Considering these different aspects of soil-plant interaction of hydrological and biological processes improved the understanding of the GPR signal within the soil-plant continuum and how information can be derived and applied to non-invasively monitor and characterize cropped fields. Nevertheless, to fully facilitate GPR as a tool in sustainable agriculture, further work could focus on the use of surface GPR applications, correlation with spatially distributed root information, combining electromagnetic and root architecture models, and combining GPR with investigation methods at the pedon- to regional scale.

Zusammenfassung

Das Boden-Pflanze-Kontinuum reguliert eine Vielzahl von Prozessen, die für die Leistungsfähigkeit von Pflanzen entscheidend sind, z.B. die Aufnahme von Wasser und Nährstoffen durch die Wurzeln und die räumlich-zeitliche Verteilung des Wassers im Boden. Insbesondere für landwirtschaftliche Nutzpflanzen in Agrarökosystemen ist ein detailliertes Verständnis der Prozesse und Wechselwirkungen von entscheidender Bedeutung, da die Landwirtschaft in hohem Maße vom Klimawandel betroffen ist und das Potenzial hat, den steigenden Bedarf an Futter- und Nahrungsmitteln zu decken. Die nicht-invasive Erfassung von Prozessen und die Abschätzung wichtiger Parameter und Variablen des Boden-Pflanzen-Kontinuums, insbesondere der Architektur des Wurzelsystems, der Verteilung des Bodenwassergehalts und der hydraulischen Eigenschaften des Bodens, können dazu beitragen, die landwirtschaftlichen Methoden zu optimieren und den Ertrag zu steigern, während gleichzeitig die Nutzung natürlicher Ressourcen minimiert wird. Gegenwärtig werden die meisten Prozesse und Parameter in verschiedenen Forschungsbereichen wie der Agrargeophysik und der Pflanzenbauwissenschaft auf unterschiedlichen Skalen separat betrachtet. Da sich die verschiedenen Komponenten gegenseitig beeinflussen, ist eine getrennte Betrachtung nicht plausibel, und vereinte Forschungsmethoden sind erforderlich. Ein Ansatz besteht darin, agrogeophysikalische Methoden wie das Bodenradar (GPR) und Wurzelinformationen zu kombinieren, um das Boden-Pflanzen-Kontinuum zu beobachten und zu charakterisieren. In dieser Studie wurde ein Open-Source-Datensatz mit Bodensensordaten, Wurzelbildern und GPR-Permittivität aus fünf Jahren für verschiedene Nutzpflanzen und landwirtschaftliche Methoden erstellt. Für diese Daten wurden neue Standards geschaffen, die einen neuartigen umfassenden Datensatz für andere Forschungen darstellen. Innerhalb dieses Zeitraffer-Datensatzes konnten bestimmte Auswirkungen auf das GPR-Signal identifiziert werden, die mit der Bodenart, der pflanzenbauwissenschaftlichen Methoden, den atmosphärischen Bedingungen und der früheren Bodenbewirtschaftung zusammenhängen. Daher wurde der Einfluss von Reihenkulturen wie Mais auf die horizontale räumlich-zeitliche Verteilung der Dielektrizitätskonstante und damit auf den Bodenwassergehalt untersucht. Es wurde eine statistische Analysemethode für die Visualisierung entwickelt, indem die so genannten trendbereinigten räumlichen Permittivitätsvariabilitäten des bewachsenen Feldes abgeleitet wurden. Dabei wurde ein Zusammenhang und eine quantitative Korrelation zwischen der Permittivitätsvariabilität und den

Wurzelvolumenanteilen festgestellt. Zur weiteren Quantifizierung der Beziehung zwischen den aufgezeichneten GPR-Signalen und dem Vorhandensein von Wurzeln und oberirdischen Pflanzen wurde eine numerische Studie durchgeführt. Unter Berücksichtigung verschiedener Szenarien. Die Wurzeln zeigten einen größeren Einfluss als die oberirdischen Sprossen, und zusätzlich konnten Standardanalysewerkzeuge, wie z. B. das Erste-Ankunftszeit Picken, für die Untersuchung des Boden-Pflanzen-Kontinuums mit Hilfe von Crosshole-GPR-Anwendungen bestätigt werden. Darüber hinaus wurde ein neuer Ansatz zur Ableitung des tatsächlich verfügbaren Wassers im Boden vorgestellt, der zeigt, dass die Vernachlässigung der Wurzelphase in geeigneten petrophysikalischen Modellen den Bodenwassergehalt überschätzt. Für die weitere Untersuchung des pflanzenverfügbaren Wassers haben wir die aus horizontalen Crosshole-GPR abgeleiteten Bodenwassergehalts für eine Winterweizen-Wachstumsperiode in Kombination mit einem hydrologischen Modell zur Ableitung der bodenhydraulischen Parameter betrachtet. In einem ersten Schritt wurde diese sequenzielle hydrogeophysikalische Inversion für einen eindimensional gemittelten Fall verwendet und in einem zweiten Schritt auf die Parzellenskala hochskaliert, wo die pseudo-dreidimensionalen, räumlich verteilten bodenhydraulischen Parameter für das Mualem-van-Genuchten-Modell mit dualen Porosität geschätzt wurden. Die Berücksichtigung dieser verschiedenen Aspekte der Boden-Pflanze-Interaktion von hydrologischen und biologischen Prozessen verbesserte das Verständnis des GPR-Signals innerhalb des Boden-Pflanze-Kontinuums und der Art und Weise, wie Informationen abgeleitet und zur nicht-invasiven Überwachung und Charakterisierung von Anbauflächen verwendet werden können. Um das GPR als Werkzeug in der nachhaltigen Landwirtschaft zu etablieren, könnten sich weitere Arbeiten auf den Einsatz von Oberflächen-GPR, die Korrelation mit räumlich verteilten Wurzelinformationen, die Kombination von elektromagnetischen und Wurzelarchitekturmodellen und die Kombination von GPR mit Untersuchungsmethoden auf der pedon- bis regionalen Ebene konzentrieren.

List of publications

At the time of finalizing the dissertation to this doctoral project, parts of the doctoral thesis have been published, submitted, or are in preparation for publication by scientific journals and contributed to scientific meetings as specified below. Chapters 2 - 5 are based on the publications numbered 1 - 4, Appendices D - F are based on the publications numbered 5 - 7, respectively.

1. **Lena Lärm**[*], Felix Maximilian Bauer[*], Normen Hermes, Jan van der Kruk, Harry Vereecken, Jan Vanderborght, Thuy Huu Nguyen, Gina Lopez, Sabine Julia Seidel, Frank Ewert, Andrea Schnepf and Anja Klotzsche (2023): Multi-year belowground data of minirhizotron facilities in Selhausen. *Scientific Data* 10, 672. `https://doi.org/10.1038/s41597-023-02570-9` ([*]contributed equally to this publication)

2. **Lena Lärm**, Felix Bauer, Jan van der Kruk, Jan Vanderborght, Shehan Morandage, Harry Vereecken, Andrea Schnepf, Anja Klotzsche (2024): Linking horizontal crosshole GPR variability and root image information of maize crops. *Vadoze Zone Journal* 2024;23:e20293, `https://doi.org/10.1002/vzj2.20293`

3. **Lena Lärm**, Jan Rödder, Harry Vereecken, Anja Klotzsche: High resolution soil-root modeling for crosshole GPR data. In preparation.

4. **Lena Lärm**, Lutz Weihermüller, Jan Rödder, Jan van der Kruk, Harry Vereecken, Anja Klotzsche: Spatial variability of hydraulic parameters of a cropped soil using horizontal crosshole ground penetrating radar. In Review at Vadoze Zone Journal, Submission-ID: *VZJ-2023-12-0120-OA*.

5. Anja Klotzsche, **Lena Lärm**, Jan Vanderborght, Gaochai Cai, Shehan Morandage, Mirjam Zörner, Harry Vereecken, Jan van der Kruk (2019): Monitoring Soil Water Content Using Time-Lapse Horizontal Borehole GPR Data at the Field-Plot Scale. Vadose Zone Journal, 18(1), 190044. 2019, `https://doi.org/10.2136/vzj2019.05.0044`

6. Felix Bauer, **Lena Lärm**, Shehan Morandage, Guillaume Lobet, Jan Vanderborght, Harry Vereecken, Andrea Schnepf (2022): Development and validation of a deep learning based automated minirhizotron image analysis pipeline. Plant Phenomics, 2022, https://doi.org/10.34133/2022/9758532

7. Yi Yu, Lutz Weihermüller, Anja Klotzsche, **Lena Lärm**, Harry Vereecken, Johan Alexander Huisman (2021): Sequential and coupled inversion of horizontal borehole ground penetrating radar data to estimate soil hydraulic properties at the field scale. Journal of Hydrology 296, https://doi.org/10.1016/j.jhydrol.2021.126010

8. **Lena Lärm**, Felix Maximilian Bauer, Jan van der Kruk, Jan Vanderborght, Shehan Morandage, Harry Vereecken, Andrea Schnepf, Anja Klotzsche. Estimating the effect of maize crops on time-lapse horizontal crosshole GPR data. Presentation at EGU General Assembly 2022, EGU22, Vienna, Austria, 23 May 2022 - 27 May 2022.

9. **Lena Lärm**, Felix Maximilian Bauer, Jan van der Kruk, Jan Vanderborght, Harry Vereecken, Andrea Schnepf, Anja Klotzsche. Using horizontal borehole GPR data to estimate the effect of maize plants on the spatial and temporal distribution of dielectric permittivity. Extended Abstract for the 11th International Workshop on Advanced Ground Penetrating Radar (IWAGPR) 2021. https://doi.org/10.1109/IWAGPR50767.2021.9843173

10. **Lena Lärm**, Felix Maximilian Bauer, Jan van der Kruk, Jan Vanderborght, Harry Vereecken, Andrea Schnepf, Anja Klotzsche. Using horizontal borehole GPR data to estimate the effect of maize plants on the spatial and temporal distribution of dielectric permittivity. Presentation at the 11th International Workshop on Advanced Ground Penetrating Radar (IWAGPR) 2021.

11. **Lena Lärm**, Anja Klotzsche, Lutz Weihermüller, Jan Vanderborght, Harry Vereecken, Jan van der Kruk, Andrea Schnepf. Estimating Soil Hydraulic Properties of the Soil-Plant-Root Zone Using Time-Lapse Horizontal Borehole Ground Penetrating Radar Data in a Sequential Hydrogeophysical Inversion Approach. Poster at AGU Fall Meeting, Virtual, USA, 1 Dec 2020 - 17 Dec 2020.

Table of Contents

Chapter 1

Introduction

With the start of the Green Revolution and the development of productivity-enhancing technologies in the second half of the 20^{th} century, agriculture production has tripled and the usage of natural resources significantly increased. Still in 2023 a malnutrition and hunger is persisting in many parts of the world (Food and of the United Nations, 2022). By the year 2050, the world population will reach 9 billion and to ensure food and feed security, agricultural efficiency needs to increase by 60% (Alexandros et al., 2012). This increase needs to be achieved while the repercussions of climate change are in full swing and will only accelerate in the coming decades, which makes today's agriculture less productive but also is reducing arable land. Furthermore, political conflicts are disrupting not only agricultural production, but also affect food chains in different parts of the world. As a consequence, modern scientific research needs to address these challenges to increase and promote sustainable crop production, while trying to minimize the environmental footprint of agro-ecosystems. Thereby, research should focus on how to use less chemicals, like herbicides and fertilizer, as well as, responsible usage of crucial natural resources like soil and water.

To face these global challenges in terms of sustainable crop production, agro-ecosystems need to be fully understood. This includes detailed process understanding across different scales and interactions of the different components, under the consideration of the impacts of modern agricultural practices. The soil-plant continuum within these agro-ecosystems is a major contributor to increase the yield productivity, since it governs main processes like root water and nutrient uptake. Major influencing factors of these processes are the soil properties and crop root architecture as well as their interaction. Understanding these factors and their interaction will be beneficial to plant breeders, for optimization of the below ground traits of crops for an optimal yield potential, nutrient and water use efficiency as well as resistance to diseases (Lynch, 2007). Another important aspect would be the optimization of agricultural practices. If the spatial and temporal distribution of roots, but also the spatial and temporal distribution of soil water content (SWC) can be assessed in a non-invasive way, proxies could be provided to minimize irrigation and fertilization or to direct other soil management decisions. For example to assist precision agriculture the creation of maps indicating zones with different soil properties or soil states like, texture, water content or

salinity are beneficial (Srinivasan, 2006). Additionally, crop cultivars could be selected according to local soil conditions. These factors show the need for investigation techniques for the soil-plant continuum. These techniques need to fulfill a long list of requirements, such as being applicable across different scales, being sensitive to a number of key soil state variables and different components such as soil, water and crops. Furthermore, to consider aspects of agro-ecosystems under the application of agricultural practices and agronomic management an additional requirement is the non-invasive nature. The measurements and investigations need to be repeatable and realizable while crops are still in place, to ensure that impacts can be detected. Consequently, there is no stand-alone measurement technique which can accomplish all these requirements. Therefore, it is recommended to combine various techniques from different research fields, such as soil physics, hydrogeology, hydro- or agrogeophysics and plant science to investigate the soil-plant continuum in the field. Thereby, innovative and non-invasive tools to investigate the soil-plant continuum, so-called phenotyping methods, at field and catchment scale, where root water availability and soil heterogeneity are key aspects, are indispensable.

To study the main processes in the soil-plant continuum such as the root water and nutrient uptake, and their controlling factors, the investigation of crop root architecture and the surrounding soil volume, with the focus on SWC, is crucial, see Figure 1-1. Therefore, on one hand the knowledge of the SWC and its distribution is fundamental to understand and predict the highly dynamic water flow and transport processes in the vadose zone. Accurate understanding of field scale variability of SWC is likewise important for the management of agricultural fields in terms of maximizing yield (Vereecken et al., 2022, 2014). SWC dynamics are caused not only by precipitation and evaporation, but also by root water uptake (transpiration), whereby the root available water depends on atmospheric conditions and on root distribution (Cai et al., 2017), and the soil hydraulic parameters (SHP) (Ghanbarian-Alavijeh et al., 2010). On the other hand, acquiring information about the spatial distribution of roots, namely the root system architecture of crops, is essential since it is responsible for the plant productivity through processes like root water and nutrient uptake, and plant stability (Lynch, 2007).

To enhance process understanding, it is not feasible to consider SWC and root architecture separately, since these components mutually influence each other. Crops roots have an impact on the distribution of soil water and the soil hydraulic properties caused by their root water uptake and the therefore cause soil water depletion as well as the the accumulation of water within the root biomass (Feddes et al., 1988, Hupet and Vanclooster, 2005, Zhuang et al., 2001). Furthermore, the soil pore structure can be permanently altered by roots (Angers and Caron, 1998, Carminati et al., 2011, Gerke and Kuchenbuch, 2007, Kodešová et al., 2006, Rasse et al., 2000). On the contrary, soil properties such SHP and soil characteristics (e.g., field capacity, permanent wilting point and plant available water) influence the root growth and spatial and temporal distribution of roots. Crops may also affect the infiltration of precipitation and irrigation into the soil, where e.g., decaying roots can cause preferential flow paths (Mitchell et al., 1995) or the shoots themselves influence the amount of water, that reaches the soil, where e.g., maize crops can funnel the rainfall and create a stem flow infiltration (Bui and Box, 1992, Hupet and Vanclooster, 2005). To optimize the use of ground water and ensure sufficient ground water recharge, several research has investigated the combined impact of soil heterogeneity and vegetation type on water

balances (Schlüter et al., 2013). Since roots evidently change the physical conditions of the soil, which impacts the spatial SWC and root distribution, the combined investigation of SWC and root system architecture of the agricultural soil-plant continuum is inevitable.

To recognize the wide range of processes, it is necessary to investigate at different scales.

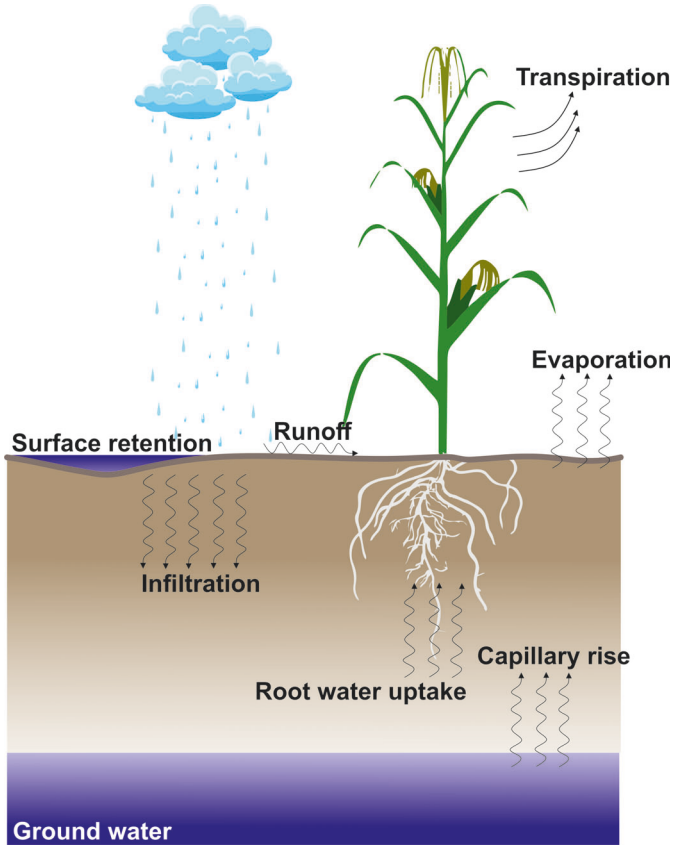

Figure 1-1: Schematic overview of the processes within the soil-plant continuum related to the soil water content distribution. Adapted from Sławiński and Sobczuk (2011).

For the understanding of these systems, which include aquifers, the vadose or critical zone, vegetation, and atmosphere, methods of all scales are necessary (Simmer et al., 2015a). The investigation scales are governed by the individual sensing volume (SV) or resolution of the respective measurement technique, see Figure 1-2. Remote sensing methods, like the regional and global satellite SWC surveys (e.g., Entekhabi et al. (2010)) or unmanned aerial vehicle (UAV)-based methods (e.g., Ge et al. (2021)) need to be linked with small-scale point measurement like the time-domain reflectometry (TDR) or direct soil sampling. While remote sensing methods can only resolve the uppermost few centimeters of the soil but investigate at a large- to regional-scale, point measurements have a high vertical resolution. However agronomic management and roots alter in deeper soil layers as well (e.g., Barej et al. (2014),

Hobley et al. (2018), Kautz et al. (2013), Maeght et al. (2013)) and field-scale information that covers a certain depth range is needed. Near-surface geophysical methods can close this gap between these large- and point-scales, and provide links at field- and catchment-scale, e.g., (Binley et al., 2015).

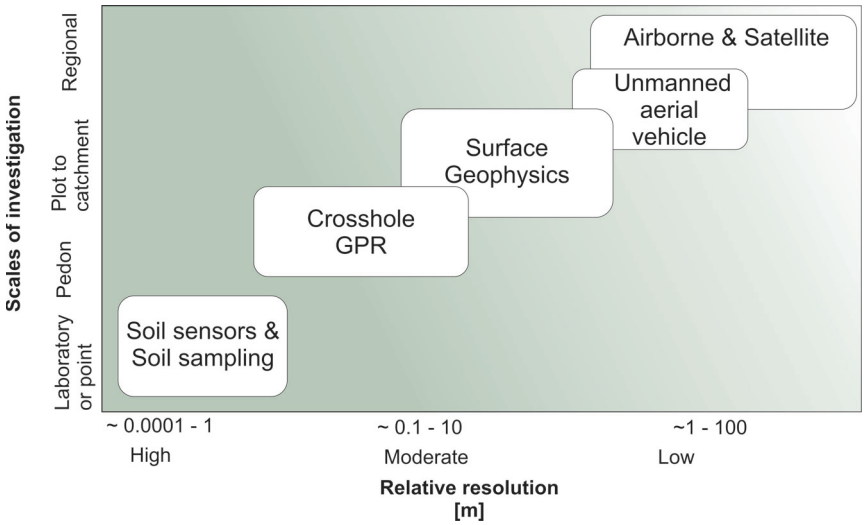

Figure 1-2: Schematic overview of the different investigation methods and the trade-off between resolution and scale of investigation. Adapted from Rubin and Hubbard (2005).

As mentioned before for detailed understanding of the soil-plant continuum one can not exclusively consider the spatio-temporal distribution of SWC or crop roots. Hence multidisciplinary research is necessary, which combines the different research ares and field investigation techniques. To investigate crop roots different investigation and root phenotyping techniques are applied. Major differences are present in the investigation scales or SV and which components are investigated. Techniques range from small scale laboratory techniques, such as magnetic resonance imaging (MRI) root observation (Bagnall et al., 2020), rhizotron images (Vamerali et al., 2011), point scale observations, using proximal soil sensor (Viscarra Rossel et al., 2010) to non-invasive tools, such as hydro- and agrogeophysics (Binley et al., 2015, Garré et al., 2021). Especially, non-invasive tools to observe crop roots and SWC in the field with a high-throughput remains a bottleneck. To derive and analyze dynamic processes of the soil-plant continuum and their link to hydrological and plant science parameters, repeated or time-lapse measurements can be important (Blanchy et al., 2020c). Therefore, methods which are easily repeated over different times and can be applied while crops are still in place to cover the full range of a vegetation period, are essential. Such time-lapse measurement techniques are additionally valuable to recognize the effects of agricultural practices or agronomic management on soil and crops and go hand in hand with non-invasive tools which are of a non-destructive nature.

1-1 Agrogeophysics - closing the gap between plant & regional scale

In recent years the concept of 'agrogeophysics' was shaped, where geophysical methods can be utilized to overcome the obstacles of modern agriculture. Agrogeophysics describes geophysical survey techniques, which are used to characterize patterns or processes within the subsoil, which are relevant for agronomic management. This research field, according to Garré et al. (2021), combines the research areas within hydrogeophysics (Binley et al., 2015) with the focus on agricultural application and proximal soil sensing or digital soil mapping, where geophysical techniques are used. Geophysical survey techniques, like electrical resistivity tomography (ERT), electromagnetic induction (EMI), induced polarization (IP), spectral induced polarization (SIP), nuclear magnetic resonance (NMR), and ground penetrating radar (GPR) can be used to link the different scales and different key soil state variables to investigate the subsurface systems in an non- or minimal-invasive manner. These commonly used techniques (ERT, EMI & GPR) provide a wide range of applications, while each of them has its advantages and disadvantages. ERT images the apparent electrical resistivity in the soil using electrodes, which require galvanic contact with the soil. Therefore, the area of investigation is often limited to the fixed locations below the electrodes. In-situ imaging of the soil-plant continuum structure, particularly SWC temporal distribution and hence SWC depletion patterns can be achieved using ERT, e.g., (Cassiani et al., 2016, Garré et al., 2012, Slater and Binley, 2021). Since EMI uses an inductive signal to map the apparent electrical conductivity of the soil, it does not require direct soil coupling. This enables a higher throughput compared to ERT and hence a mapping of large areas, and the possibility to measure while crops are still in place (Blanchy et al., 2020c, Brogi et al., 2019, Schmäck et al., 2021). One limitation of ERT and EMI is that the measured electrical conductivity is influenced by several factors next to the SWC (e.g. temperature, salinity). Therefore, often site specific relationships or additional calibration data such as TDR or soil probes are needed to derive the SWC. In contrast, GPR measures the propagation of the electromagnetic wave in the soil (Jol, 2009), which can be directly linked to the SWC (Huisman et al., 2003, Klotzsche et al., 2018) and additionally can map the structures of the subsoil.

Although each of these methods has their benefits, combining various complementary methods demonstrated a high potential to enhance the soil-plant continuum understanding. For example, recent studies identify the effects of the wide range of agricultural management practices, by applying different geophysical survey techniques and the combination of such. Shin et al. provided an overview on the use of geophysical methods for soil characterization, such as ERT, IP, EMI, GPR, NMR and seismic methods. Blanchy et al. (2020c) applied EMI and ERT to investigate the influences of cover crops, tillage, compaction, irrigation and fertilization on the SWC dynamics, with a close attention on the application of time-lapse measurements. The work of Blanchy et al. (2020a) focused on a high-throughput phenotyping platform installed in the field, to measure ERT under winter wheat considering different nitrogen treatments. Additional studies focus on fertilization and irrigation are, e.g., (Kaufmann et al., 2019, Moghadas et al., 2017). The negative effects of soil compaction on crops were, e.g., determined by Schmäck et al. (2021) using EMI and ERT, Cimpoiaşu et al. (2021) by investigating ERT combined with X-ray computed tomography and Romero-Ruiz et al. (2022) by applying Direct Current(DC)-resistivity and TDR measurements. Algeo et al.

(2018) used surface GPR for mapping changes in the shallow SWC, with the goal improve irrigation efficiency. Akinsunmade et al. (2019) investigated the agrotechnical properties of different soil types with focus on compaction using surface GPR. Another interesting study is provided in Kaufmann et al. (2020), where a novel multichannel GPR technique is presented for soil characterization. Jonard et al. (2013) applied different geophysical techniques to investigate tillage effects using GPR and EMI and validated their findings with soil sampling, capacitance probe, and soil penetrometer measurements. Hebel et al. (2021) utilized EMI and UAV based data to investigate soil information and management zones in potato fields. Next to the problems of soil compaction and agricultural management, soil salination processes and their monitoring methods require close attention since climate change increase in arid and semi-arid climate zones these factors (Besma et al., 2021). A novel soil mapping strategy was presented in Brogi et al. (2019, 2021), where a geophysics-based soil map for a area of 1 km^2 was developed using EMI and direct soil sampling as a ground-truth. They observed correlations with their EMI-based soil classifications and patterns in crop health obtained from satellite imagery, and suggested that such geophysics-based soil maps imperove commonly available soil maps in agro-ecosystem modeling.

Various studies have been performed to investigate the effects of roots on the spatio-temporal distribution of SWC within agricultural fields. Soil water depletion patterns of tree orchards have been investigated by, e.g., Cassiani et al. (2016), Vanella et al. (2022), Vargas et al. (2020) applied ERT and Robinson et al. (2012) using EMI. Additionally, crops with finer roots system have also been investigated by e.g., Shanahan et al. (2015) using EMI and Garré et al. (2013, 2011), Michot et al. (2003), Rao et al. (2020), Slater and Binley (2021) using ERT. Although all of these studies successfully demonstrate the potential of geophysical methods to investigate the soil-plant continuum, investigating explicitly roots and roots zones with their functional and structural properties remains challenging. Most of the characterization of roots is of a indirect nature, while mapping the spatio-temporal patterns caused by the roots (Garré et al., 2021). Studies have used electrical methods in the laboratory to derive root parameters and functional root properties (reviewed in Cimpoiaşu et al. (2020) and Weigand and Kemna (2017, 2018). Weigand and Kemna (2017, 2018) have applied sEIT to image crop root systems under controlled laboratory conditions, while this technique was extended to promising field applications (Weigand et al., 2022) and first results (Michels and Kemna (2022) in Revil et al. (2022)).

For these methods and for agrogeophysics in general, challenges and limitation remain (Cimpoiaşu et al., 2020, Ehosioke et al., 2020, Ge et al., 2021). For example, the resolution of ERT methods for particular events like droughts, is not equipped to map, e.g., small scale soil water depletion pattern for different genotypes (Cimpoiaşu et al., 2020). Further, the spatial resolution is often restricted by the permanently installed ERT lines. EMI enables the mapping the soil apparent electrical conductivity by using an inductive signal, since the galvanic coupling with the soil is not necessary. Hence, entire agricultural field can be mapped while crops remain intact (e.g., Blanchy et al. (2020b,c), Schmäck et al. (2021), but simultaneously spatial resolution is not quite sufficient for small scale soil heterogeneities. While these techniques are sensitive to soil characteristics such as the soil's porosity, density, clay content, pore water saturation, temperature, and salinity of the pore water, for a quantitative interpretation often site specific transfer functions have to be established. Unfortunately, most of these transfer functions are often only applicable for the respective

field site and the need for in-situ calibration remains (Garré et al., 2021, Tso et al., 2019). Blanchy et al. (2020b) investigated the relationship between SWC and electrical conductivity, to use EMI data for wheat phenotyping, with the result that plot specific relationship models should be used. Furthermore, Moghadas and Badorreck (2019) approached this problem by using a machine learning algorithm to estimate the SWC from electrical conductivity data. Additionally, Terry et al. (2023) used surface GPR, ERT and frequency domain electromagnetics (FDEM) data acquired during an infiltration experiment with an machine learning approaches to evaluate semi-automated geophysical SWC measurements in the field. In contrast to ERT or EMI, GPR has a direct link to SWC and because of the high frequency electromagnetic pulses, which the method applies, it is the method with the highest possible spatial resolution among the agrogeophysical methods (Huisman et al., 2003, Klotzsche et al., 2018).

1-2 GPR for investigating the soil-plant continuum

GPR is an electromagnetic (EM) method, which records the EM wave propagation through the subsoil, which is influenced by the dielectric properties of the soil components (Annan, 2005, Jol, 2009). The mathematical description of the EM physics are provided by Maxwell's equation and in addition the constitutive equations providing the relation to the material properties, which are the electrical conductivity σ, dielectric permittivity ε and magnetic permeability μ defined by the material properties. Typically GPR systems consist of a transmitting (Tx) and a receiving antenna (Rx). Tx is emitting short pulses of electromagnetic waves at a high frequency (between 50 MHz to 2600 MHz for commercial systems) and Rx is recording a signal over time. The recorded GPR signal can be used to derive the relative dielectric permittivity ε_r from the EM wave velocity and the electrical conductivity σ from the attenuation of the EM wave (more details and mathematical descriptions can be found in Jol (2009)). For the most common GPR cases using high frequencies, the velocity v of the subsurface material can be derived for low-loss and non-magnetic materials ($\mu \approx 1$) with

$$v = \frac{c}{\sqrt{\varepsilon_r}} \tag{1-1}$$

using

$$\varepsilon_r = \frac{\varepsilon}{\varepsilon_0}, \tag{1-2}$$

where c is the radar velocity in air (≈ 0.3 m/ns), ε is the effective permittivity of the bulk material and ε_0 ($8.85 \cdot 10^{-12}$ F m^{-1}) is the permittivity of free space. In this thesis for convenience, the relative permittivity will further be referred as the permittivity ε_r. Typically, in GPR the relationship for low loss attenuation α is used to derive the electrical conductivity σ with

$$\alpha = \frac{1}{2}\sigma\sqrt{\frac{\mu}{\varepsilon}}. \tag{1-3}$$

Both parameters ε and σ can be linked to SWC and porosity, or, clay content as well as the pore water salinity of soils, respectively. The resolution and depth of penetration/ investigation is depending on the antennae frequency, the related wavelength of the signals

and the electrical conductivity of the subsurface. The range of frequencies or band width B, where the resolutions satisfies the requirements, is a spectrum surrounding the center frequency f_c. While low frequencies have a long wavelength and can penetrate deeper into the subsurface with a loss of resolution. In contrast, high frequencies are related to shorter wavelengths and can detect small-scale features in the subsurface, but their penetration depth is smaller than for low frequencies. Note that, attenuation in natural materials consists of electrical and scattering losses. An increase in frequency leads to an increase in these losses, hence a decrease in signal strength. Additionally, high-loss materials with a high electrical conductivity result in a higher attenuation, leading to challenges in data acquisition for high electrical conductivity soils.

The non- to minimal-invasive nature of GPR, appropriate depth of investigation, large sampling volume as well as the high spatial resolution are advantages of the measurement technique. Different scales and investigation depths are measured with different surface, off-ground and crosshole GPR configurations using different frequency ranges. The most common surface GPR survey type is common offset profiling (COP), see Figure 1-3a). This method is time and cost effective. COP is measured with a constant spacing between Tx and Rx and is used to map reflection horizons (Steelman et al., 2012). In most cases, the recorded reflection data provide no information about the depth or thickness of the horizons. To convert the time axis into a depth axis, the velocity of the subsurface is crucial, where the provided travel times relates to the distance. Point measurements for GPR such as common mid point (CMP) and wide angle reflection and refraction (WARR) can provide the velocity of the subsurface, see Figure 1-3b. For CMP measurements the transmitter and receiver are moved with the same distance away from the midpoint (Figure 1-3c), while using WARR measurements the transmitter is positioned at a fixed location and the receiver is being moved with with an increasing separation. From the acquired WARR data, the velocity of the direct wave, reflections and refractions in the subsurface can be derived (more details in Huisman et al. (2003)).

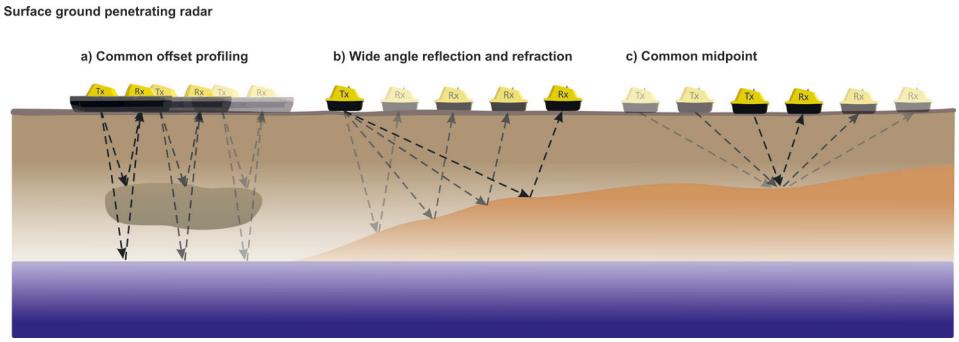

Figure 1-3: Schematic overview of surface ground penetrating radar (GPR) applications with a) Common offset profiling, b) Wide angle reflection and refraction and c) Common mid point. Transmitting and receiving antennae are labeled Tx and Rx respectively.

Borehole or crosshole GPR measurements have the advantage compared to surface GPR applications that it enables the investigation of the deeper near-subsurface between boreholes and hence can be used for, e.g., critical zone characterization (Binley et al., 2002a, Klotzsche et al., 2013) including monitoring of infiltration and recharge process (Looms et al., 2008a). Additionally crosshole GPR measurements can be directly linked with the SWC, since the distance in which the EM wave travels is know from the borehole separation. Therefore, crosshole GPR application can be used to investigate in-situ information about the soil properties. Commonly in hydrogeophysical and agrogeophycial applications, two configurations are used in the transillumination mode: zero offset profiling (ZOP) or multi-offset gathers (MOG), see Figure 1-4. Note that such transillumination measurements are affected by the borehole features like deviation, geometry and borehole filling (Annan, 2005). Acquiring ZOP data, Tx and Rx are moved simultaneously in adjacent boreholes (Figure 1-4a). This is a fast and inexpensive method, and, because of the known distance between the boreholes the EM velocity can directly be derived resulting in a one-dimensional averaged permittivity profile over depth. In contrast, MOG, is more time consuming and labor intense, because Tx is fixed at a location in one borehole and Rx is moved along the length of a neighboring borehole. This is repeated for various Tx locations, with a fixed step size for Rx (Figure 1-4b). During this process two-dimensional profiles of travel time information are recorded (Cassiani et al., 2006). The obtained MOG data can be used in inversion approaches to derive detailed 2D or 3D information between the boreholes for many number of unknowns (for detailed remarks see e.g. (Huisman et al., 2003, Klotzsche et al., 2019, 2013). In addition, borehole and surface measurements can be combined in so-called vertical radar profiling (VRP), where a single-borehole in which the Rx is places is considered and the Tx is placed at the surface. This technique is used to derive one-dimensional velocity models by inverting the arrival times the direct ground waves (Tronicke and Hamann, 2014).

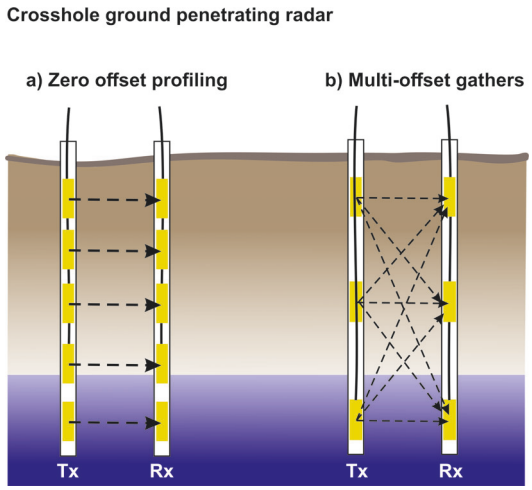

Figure 1-4: Schematic overview of crosshole ground penetrating radar (GPR) applications with a) Zero offset profiling and b) Multi-offset gathers. Transmitting and receiving antennae are labeled Tx and Rx respectively.

Linking GPR to SWC and root zones

To improve the description of the soil-plant continuum, knowledge about the SWC and the root distributions is essential. Since GPR can be directly linked to the SWC, utilizing appropriate empirical or petrophysical relationships (Huisman et al., 2003, Klotzsche et al., 2018, Steelman and Endres, 2011), research had focused in recent years to further understand the connection of the GPR signals and related SWC. Additional studies have focused on how GPR can be applied and considered for different aspects of subsoil sensing in agriculture (Liu et al., 2016).

Most of the studies consider only one aspect, either the SWC distribution and dynamics, or, the effects of root zones. In order to measure the SWC changes at a high spatial resolution within a field plot, crosshole GPR is a convenient configuration and showed a high potential to map and monitor hydrological processes and SWC (Binley et al., 2002b, Haruzi et al., 2021, Klotzsche et al., 2013, Looms et al., 2008a, Rucker and Ferré, 2004). The relation is linked to the high contrast in dielectric permittivity ε_r for the soil components, (e.g., dry sand $\varepsilon_s = 6$, air $\varepsilon_a = 1$ and water $\varepsilon_a = 84$). Investigation of infiltration processes with GPR can be beneficial to improve and optimize irrigation application to reduce water use or to map infiltration to avoid pesticide and nutrient leaching into sacred protected groundwater or surface water like lakes and rivers (Yu et al., 2020).

While several applications and case studies showed the potential to monitor SWC dynamics, specific research on roots and root phenotyping using GPR and agricultural plants is limited. In recent years, surface GPR has been used to investigate the soil-plant continuum, here we have to differentiate between coarse roots systems, such as trees, and fine roots system, such as crop roots. The root diameter of 0.002 m distinguish between coarse roots (larger than 0.002 m) and fine roots (smaller than 0.002 m), in some research small roots are additionally distinguished with diameters between 0.002 m - 0.005 m. Guo et al. (2013), Rodríguez-Robles et al. (2017) provided an comprehensive review on the detection of tree roots systems using GPR. Thereby, mostly surface GPR is used to map the distribution of tree roots systems, while investigation the reflection hyperbolas in the GPR radargrams. A wide range of studies was able to detect roots with a diameter of 0.005 m - 0.082 m and rooting depth of 0.10 - 1.10 m using frequencies between 400 - 2000 MHz (Butnor et al., 2001, Cox et al., 2005, Cui et al., 2010, Hruska et al., 1999, Raz-Yaseef et al., 2013, Rodríguez-Robles et al., 2017, Yan et al., 2013). Some studies have additionally focused on the estimation of the tree root biomass using frequencies between 1500 - 2000 MHz (Butnor et al., 2005, 2012, 2003, 2001, Cui et al., 2010, Samuelson et al., 2008, Stover et al., 2007). Additionally, a few studies investigated the potential to estimate SWC of root zones for trees by analyzing the reflection hyperbolas (Liu et al., 2020, 2019) and shrub roots (Cui et al., 2021). Detached from the distinction between fine and coarse roots are root and tuber crops, such as potatoes, sugar beets and cassavas. Delgado et al. (2017) investigated whether GPR is capable to predict root-bulking rates of cassava root by detecting the total root biomass during the vegetation period. Resulting in an over prediction for early growth stages, but with good prediction for later growth stages. Nevertheless, these studies demonstrated the possibility to utilize GPR to derive SWC and link the signal to root phenotyping in relation to SWC.

In contrast, root zones of agricultural crops, such as cereal crops, have been the focus on a few studies (Delgado et al., 2017, Klotzsche et al., 2019, Liu et al., 2016, 2017, Wijewardana and Galagedara, 2010). One of the earliest work was achieved by Wijewardana and Galagedara (2010), who estimated the spatio-temporal distributions of SWC for raised agricultural beds cropped with vegetables using surface GPR configurations similar to ZOP and MOG configurations, with focus on irrigation SWC patterns. These studies only investigated the roots zones of fine roots in a indirect manner. Liu et al. (2017) correlated 1600 MHz GPR images with root diameter and root biomass from soil cores for winter wheat and energy cane in different soil types. While Parsekian et al. (2012) were able to detect roots < 0.002 m under laboratory conditions using 1600 MHz antennae. It should be noted that such high frequency applications at the field-scale are difficult because of the high attenuation of the EM waves and hence shallow penetration depth. Using GPR to map and detect fine root systems in the field continues to be a challenge. Additionally, Guo et al. (2013) and Liu et al. (2016) state that the effect of the roots in the dielectric permittivity derived from the GPR measurements remains unsolved.

Soil hydraulic parameters obtained from geophysical data

Next to the state variables such as soil texture and SWC, the estimation of the SHP is essential to accurately describe hydrological and crop models. Geophysical data have been used in the past decades to derive these SHP using geophysical inversion approaches, such as sequential or coupled inversion. In a sequential inversion geophysical measurements are inverted to the respective state variables, independently from a the hydraulic or hydrological model. The state variables are then used as the calibration targets for the hydrologic model (Pleasants et al., 2022). Singha et al. (2014) and Pleasants et al. (2022) have noticed that the term sequential inversion Yu et al. (2021) is not consistently used in the literature. Level 1 data fusion (Yeh and Šimůnek, 2002), no specific term (Doetsch et al., 2012, Farmani et al., 2008, Kemna et al., 2002, Vanderborght et al., 2005) or uncoupled hydrogeophysical inversion (Beaujean et al., 2014, Camporese et al., 2015, Claes et al., 2020, González-Quirós and Comte, 2021, Hinnell et al., 2010, Irving and Singha, 2010) describe the same inversion approach. Different geophysical or hydrogeophysical approaches have been successfully used to estimate the SHP, e.g., using ERT time-lapse data (Huisman et al., 2010, Manoli et al., 2015, Pleasants et al., 2022) , surface GPR (Busch et al., 2013) and using crosshole GPR (Looms et al., 2008a, Rucker and Ferré, 2004, Yu et al., 2022). For the coupled inversion the hydraulic or hydrological model predicts the respective state variable, which are then transformed into geophysical variables with petrophysical relationships. These geophysical variables are then used to predict a geophysical response in geophysical forward simulations (Pleasants et al., 2022). Coupled inversion has be applied to estimate the SHP utilizing ERT (Kuhl et al., 2018, Mboh et al., 2011, Tran et al., 2016) and GPR (Jadoon et al., 2012, Yu et al., 2021). The advantage of using a coupled inversion approach is, that the no potential error can occur while the geophysical measurements are inverted to the state variables, which makes it less sensitive to errors. The drawback of coupled inversions is, the requirement a state-of-the-art hydrological and geophysical model, which associated high computational demands.

1-3 Root phenotyping in the field

For the determination of the root system architecture in the field, we first need to differentiate between destructive or invasive methods and non- or minimal-invasive methods. The most obvious root sampling method is excavation. Here the entire or parts of the root system are excavated (Böhm, 1978, Hossne et al., 2016, Weaver, 1926). Shovelomics is root crown phenotyping focusing exclusively on the uppermost part of the root system (Trachsel et al., 2010)). Further destructive root sampling method are trench profiles or trench walls which are mainly used to derive the lateral distribution of root traits. Here a trench is excavated either parallel or perpendicular to the crop row, although perpendicular to the row is most commonly used. To distinguish the roots from the surrounding soil and to count root intersections in a mesh grid, the roots are brushed or washed. The most common root sampling technique in the field is auger sampling or soil coring (do Rosário G. Oliveira et al., 2000, Wasson et al., 2020). Soil cores are being drilled into the soil surrounding the root system. A wide range of execution possibilities depending on the research question need to be considered: number and positioning of cores, core diameter and investigation depth. Soil coring requires a wide range of steps to derive quantitative root traits, after retrieving the cores from the soil, such as segmenting, removing of soil, washing roots, sorting alive and dead roots. After this the root quantification can be achieved with root counting or by scanning and consecutive image analysis. Although destructive root sampling methods are labor intensive and disturb the root growth, they have the advantage that they provide the most reliable information and they are predestined to investigate the infield variability in root system architecture at a certain point in time. Especially the excavation of monoliths can provide the spatial variability in roots traits which is especially interesting for row crops, such as maize. Soil corings and trench wall profile cannot determine the spatial variability of the entire root system, but are less labor-intensive than excavating monoliths. The major disadvantage of all three methods is the non-repeatable nature. The measurements cannot detect any time-depended developments on the same crops throughout the growing season.

A minimal- to non-invasive alternative method, are minirhizotron (MR) techniques. Here, transparent rhizotubes are directly embedded into the soil and function as observation windows (Atkinson, 2000, Buczko and Kuchenbuch, 2013, Johnson et al., 2001, Rewald and Ephrath, 2013, Vamerali et al., 2012)). MR do not only provide the opportunity to investigate root distribution, but also to investigate root development over the entire vegetation period or different crop growing seasons. Furthermore, depending on the construction and compositions of rhizotubes, they also allow the investigation of multiple roots systems, over various depths and thus enable the investigation of the horizontal variability of the root system. There are only a few MR facilities under field conditions present to this day (Cai et al., 2016, Olof Andrén, 1991, Svane et al., 2019, Vamerali et al., 2011). Their construction ranges from a inclined rhizotubes, with semi-field conditions (Svane et al., 2019) to horizontally installed rhizotubes in different soil types under natural field conditions (Cai et al., 2016). To obtain information on roots traits from MR, recordings need to be acquired from within the rhizotubes, here digital photo- or video cameras or scanners are used. Limitations of the root observation using MR are that the collected two dimensional images only show a limited section of the entire root system. Another disadvantage are the high costs of the installation and maintenance of MR facilities. Additionally, different installation techniques disturb the soil

and the rooting zone. Thereby, different interferences occur, like soil smearing, lacking contact between soil and rhizotubes, soil compaction and the rhizotubes act as obstacles for the roots, e.g., Guo et al. (2007), Johnson et al. (2001), Maeght et al. (2013), Rewald and Ephrath (2013).

The output of many in-field root sampling methods, like the here presented MR technique, are root images. Since progress in root sampling methods in field, but also in greenhouses, resulted in high-throughput data sampling of root system images, fast and accurate software-based solutions for image analysis are required. Tools to provide quantitative root information from these digital images or scans have undergone tremendous development in recent years (Atkinson et al., 2019). Since, in this work we are only considering root information from two-dimensional measurements, we are not considering available tools for three-dimensional data sets, see Atkinson et al. (2019). To acquire quantitative information from images or scans mainly two steps are required, namely root object segmentation and object quantification (Leitner et al., 2013). Especially for MR images the segmentation proves to be difficult caused by the heterogeneity between roots and soil within the images. Numerous manual or (semi-)automated software tools for root system information extraction have emerged, reviewed in Lobet et al. (2013). However, manual tools require the user to interact with each individual image and also the semi-automated and automated tools and filter algorithms (Dowdy et al., 1998, Murphy and Smucker, 1995, Zeng et al., 2010) only expedite the post processing (Vamerali et al., 2011) but still require the user's interaction. These limitation for available tools make them only applicable for certain, very homogeneous, image types, such as high-contrast root scans (Yasrab et al., 2019). Due to the heterogeneity within the most MR data sets this resulted in the manual annotation of the images. Since GPR is sensing a soil volume and image only record a planar image, an upscaling of the two-dimensional image to a three-dimensional soil volume is required. Therefore, a respective soil volume is necessary Different approaches are present in the literature, to derive this respective soil volume, e.g., from the image size and the depth of view, i.e., respective soil thickness. Most studies assume the depth of view to be 0.002 m, e.g.,(Brown et al., 2008, Merrill and Upchurch, 1994, Steele et al., 1997), which was originally suggested by Taylor et al. (1990). According to Brown et al. (2008) using a depth of view of 0.002 m would lead to an overestimation of the respective soil volume and therefore an underestimation of the root volume. Brown et al. (2008) showed, by using two different depths of view, which considered the actual root diameter, to avoid underestimation of the respective soil volume with root diameters larger than 0.002 m. A different approach was chosen by (e.g.,Cai et al. (2017), Morandage et al. (2021)), where the rhizotube radius was used to derive the respective depth of view. This accounts for the uncertainty, that the roots would grow differently, of the obstacle of the rhizotube was not present and a shorter root length were present.

1-4 Aims and Objectives

Different investigation methods for the soil-plant continuum are available and each is individually sensitive to different soil parameters and variables, ranging from physical and dielectrical properties of the soil and the roots, to parameters like root system architecture. Each investigation techniques observes the continuum at their own scale, which leads to unique advantages and challenges. What current research is missing is the link of investigation techniques across discipline, such as agropgeophysics and plant science and especially using

the information for bilateral validation. This research aims towards bringing different investigation techniques and scales closer together and to enhance the overall understanding of the soil-plant continuum.

The overarching goal of this doctoral project is to develop possibilities to promote the application of GPR as a non-invasive investigation tool for sustainable agriculture and explore its advantages and overcome its limitations. Thereby, this work focuses on the development of novel data analysis methods, data understanding, validation procedures, suggests areas of application and proposes optimized field data acquisition techniques. The following chapters are aiming towards establishing what the capabilities of GPR data are and providing a foundation of knowledge that future research can build on. To establish a data base for the indented field of attention, a comprehensive data set for two minirhizotron facilities in Selhausen was acquired, analyzed and made publicly available. This was not only to acquire information in the framework of this doctoral project, but also to provide a multidisciplinary data set available to other scientists of various research fields and to promote open science.

Furthermore, this work followed these main research objectives:

1. Collecting and providing a comprehensive data set to for a wide range of scientific fields and applications
2. Imaging the horizontal spatio-temporal variability in crosshole GPR-derived permittivities to investigate soil-plant continuum processes like soil water depletion patterns, root growth and influences of agricultural practices
3. Linking and correlating the impact of row crops on the horizontal spatio-temporal variations in crosshole GPR-derived permittivities using root information for the quantification of data acquired with non-invasive subsurface investigation tools such as GPR to derive information about and soil water content redistribution connected to root presence
4. Improving the understanding of the crosshole GPR signal related to crops and crop roots, to use this knowledge in further GPR applications such as surface GPR and to optimize investigation techniques
5. Determining the importance of considering a root phase within the soil system when calculating the soil water content in appropriate petrophysical mixing models, to derive the soil water actually present in the soil under the presence of roots
6. Identifying the potential of using crosshole GPR to derive quantitative and spatially distributed information of soil state variables for the soil-plant continuum of agricultural crops, such as soil hydraulic parameters and soil characteristics
7. Establishing GPR as a standard investigation tool to non-invasively monitor and characterize the soil-plant continuum for field practices related to sustainable agriculture

1-5 Outline of the thesis

This thesis composed of six chapters and five appendices:

Chapter 1 is the introductory chapter, which formulates the research questions and objectives that have been addressed over the course of this doctoral project. It will provide an overview of the current state of research area and related fields. First, this introductory chapter will explore the importance of investigating the soil-plant continuum and its components, and, processes under different aspects. Further, an overview of the current state of the scientific research in the field of agrogeophysics and especially the application of ground penetrating radar is provided, including the current challenges and limitations. Within the soil-plant continuum and the vadose zone static and dynamic processes are present between the different component, which are additionally dynamically influencing each other. Therefore, non-invasive parameter estimation for hydraulic and hydrogeological applications are needed, within Chapter 1, overview on the current approaches is provided. Since this work is multidisciplinary and tries to combine different field investigation methods, an overview of root phenotyping in the field is given, including the root investigation and how researchers deal with high-throughput data sets and the upscaling of two-dimensional data.

Chapter 2 provides an overview of the comprehensive sub-soil data set acquired at the two minirhizotron facilities in Selhausen, Germany. Thereby, we describe the data acquisition and processing for data collected for the years 2016 - 2021 for wheat and maize crops sown on two different soil types. The measurement techniques includes time-lapse horizontal crosshole GPR, root images, soil sensors recording soil water content, soil water potential, and, soil temperature. The research in the subsequent chapters is based on these data.

Chapter 3 is analyzing the data acquired while maize was sown on the minirhizotron facilities. Here, a novel statistical analysis for time-lapse horizontal crosshole GPR data is presented to identify horizontal variations caused by the maize crops. Hereby, the so-called trend corrected spatial permittivity deviation of vegetated field was derived. The patterns observed in the GPR data could be validated and correlated with root-image-derived root volume fraction redistribution of the soil water, and therefore an increase the soil water variability.

Chapter 4 is further exploring the influences of the different soil-plant continuum components, such as soil, water and roots, on the GPR signals. Thereby, one focus is to understand the effects of consideration of an additional root phase in the application of commonly-used petrophysical relationships to transform the GPR-derived dielectric permittivity into SWC. A numerical study is performed to derive synthetic GPR signals for different soil-plant continuum compositions including, soil, roots information based on trench wall count data, and above-ground shoots.

Chapter 5 introduces a sequential hydrogeophysical inversion approach to derive the soil hydraulic parameters for one of the rhizotron facilites using data of a growing period. In this sequential inversion the horizontal crosshole GPR derived SWC values over the growing season is combined with a hydrological model HYDRUS-1D, where root information and atmospheric conditions from the test site are included. Using this approach the SHP of

the uni- and bimodal Mualem-van-Genuchten model for an one-dimensional averaged case were investigated, while the best model setup was consider to upscale the SHP for each measurement points of the rhizotron. Using the bimodal Mualem-van-Genuchten model, the SHP along the horizontal axis are derived for the entire field-plot resulting in a pseudo 3D representation of the site.

Chapter 6 is summarizing the key findings of the doctoral project and is providing the final conclusions of this project. Recommendations for future work and research topics are provided in the outlook section.

Following these main chapters are appendices, which are divided into two parts Appendices A - C, contain the respective complementary material for the Chapters 3 to 5. Appendices D - F include additional studies, which were published in cooperation of this doctoral project:

Appendix D - Klotzsche et al. (2019) - "Monitoring soil water content using time-lapse horizontal borehole GPR data at the field-plot scale". L. Lärm performed experiments and data collection, data analysis, and performed revisions of the manuscript.

Appendix E - Bauer et al. (2022) - "Development and Validation of a Deep Learning Based Automated Minirhizotron Image Analysis Pipeline". L. Lärm performed experiments and data collection, prepared the annotated dataset, and performed revisions of the manuscript.

Appendix F - Yu et al. (2021) - "Sequential and coupled inversion of horizontal borehole ground penetrating radar data to estimate soil hydraulic properties at the field scale ". L. Lärm contributed to the methodology and software developments and performed revisions of the manuscript.

Chapter 2

Multi-year belowground data of minirhizotron facilities in Selhausen

Abstract

The production of crops secure the human food supply, but climate change is bringing new challenges. Dynamic plant growth and corresponding environmental data are required to uncover phenotypic crop responses to the changing environment. There are many datasets on above-ground organs of crops, but roots and the surrounding soil are rarely the subject of longer term studies. Here, we present what we believe to be the first comprehensive collection of root and soil data, obtained at two minirhizotron facilities located close together that have the same local climate but differ in soil type. Both facilities have 7m-long horizontal tubes at several depths that were used for crosshole ground-penetrating radar and minirhizotron camera systems. Soil sensors provide observations at a high temporal and spatial resolution. The ongoing measurements cover five years of maize and wheat trials, including drought stress treatments and crop mixtures. We make the processed data available for use in investigating the processes within the soil–plant continuum and the root images to develop and compare image analysis methods.

Adapted from: Lena Lärm*, Felix Maximilian Bauer*, Normen Hermes, Jan van der Kruk, Harry Vereecken, Jan Vanderborght, Thuy Huu Nguyen, Gina Lopez, Sabine Julia Seidel, Frank Ewert, Andrea Schnepf and Anja Klotzsche (2023): Multi-year belowground data of minirhizotron facilities in Selhausen. *Scientific Data* 10, 672. `https://doi.org/10.1038/s41597-023-02570-9` (*contributed equally to this publication)

2-1 Background & Summary

As a result of climate change, ensuring food security for the vastly growing human population is one of the major challenges of the 21st century. While climate change is exerting increasing pressure on the availability of natural resources such as water and soil nutrients, there is an increasing demand on food production. To ensure food security for the growing world population, agricultural production will have to increase by at least 60% by 2050 (Alexandros et al., 2012). The yield of agricultural crops therefore needs to be increased and yield stability under changing conditions must be preserved, if current consumption patterns are maintained. A comprehensive understanding of all processes within agro-ecosystems is crucial to identify the key parameters to maintain yield stability and increase yield. The main source of water and nutrients for plants is the rhizosphere and the surrounding soil. Key parameters for potential improvements in water and nutrient efficiency could be revealed through a comprehensive understanding of the soil–plant continuum and its processes. This includes parameters describing the root architecture, influencing processes such as root water, and nutrient uptake, which governs the yield (Lynch, 2007). Field phenotyping, especially incorporating below ground information is crucial for breeders to capitalize on developments in genetics, since information identified under controlled environment are often not accounting for "real-world" field conditions (Araus and Cairns, 2014). In-field observations also enable to investigate quantitative traits, particularly those related to root features that influence drought stress tolerance. Therefore, field phenotyping facilities including below ground information provide precious data for breeders (York, 2021). Additionally, knowledge about soil heterogeneity is crucial to understanding the distribution in soil water and nutrient content.

The data presented here include information about crop-relevant subsoil data – such as soil water content, soil water potential, soil temperature, and root development – on a high temporal-spatial resolution for multiple crop growing periods.

There are several techniques to observe roots non-destructive. The whole root system development can be observed with rhizotrons, equipped with a clear window on the side. Rhizotrons exist in various shapes for greenhouse and in-field observation (Silva and Beeson, 2011, Wasson et al., 2020). If installed above ground, these rhizoboxes allow for the sampling and imaging of root systems through easily accessible windows and apertures at the side (Rasmussen et al., 2020, Thorup-Kristensen et al., 2020). In the past, several in-field rhizotrons often took the form of covered underground cellars or walkways with transparent windows or side walls for observing root development. In order to avoid expensive construction and maintenance costs, transparent – minirhizotrons (MR) – were introduced, enabling the *in situ* observation of the root in a fixed position, but at several depths (Taylor et al., 1990). By installing transparent tubes with an inclination, they could be accessed from the surface. These rhizotubes were subsequently also used in rhizotron facilities, where they were installed horizontally from the trench walls at different depths to ensure that root distributions and root development could be observed in a larger soil volume than only at the side walls (Van de Geijn, 1994). It is important that the installation of the rhizotubes is causing as little soil disturbance as possible. Especially in fine textured soil, less soil compaction around the tube, caused by the installation process, might alter the root growth (Johnson et al., 2001).

These influences on the collected root data can be reduced to a negligible minimum when auger with the same diameter as the rhizotubes are used to drill holes for tube insertion, the soil is re-compacted according to previous bulk density measurements and a resting period is respected after tube installation (6-17 month) (Johnson et al., 2001, Joslin et al., 2006, Pritchard, 2008, Vamerali et al., 2012). The permanent installation and maintenance of MR at several depths has only been done on very rare occasions due to the high manufacturing effort involved (Svane et al., 2019, Van de Geijn, 1994). However, this kind of MR facility enables insights into processes within the soil–plant continuum at the plot scale, while offering high instrumentation for multifaceted observations at high spatial and temporal resolution.

One way to observe the root growth is imaging the roots and surrounding soil through the transparent rhizotubes with a special camera system. To analyze the resulting root images, various methods from root counting to single root analysis were performed with several manual or semi-automated software tools (Atkinson, 2000, Möller et al., 2019, Vamerali et al., 2012, Zeng et al., 2010). Depending on the targeted phenotypic traits and root image quality it is not always feasible to extract it manually from the images (Atkinson et al., 2019, Vamerali et al., 2012). In contrast to genotype analysis, which can be performed with various high-throughput methods, the phenotyping of corresponding plant architecture and anatomy is still a bottleneck (Minervini et al., 2015). Image analysis based on the convolutional neural network (CNN) is the most promising way to close this gap (Song et al., 2021). In particular, CNNs are used to automatically detect different plant organs by segmenting them from the background (Kamilaris and Prenafeta-Boldú, 2018). While this is already established for above-soil organs of plants, applying these techniques to extract information about the root system remains challenging, especially under field conditions (Ubbens and Stavness, 2017, Wang and Su, 2022). This is mainly due to the lack of availability of root image data, which are required to train a segmentation model, compared to shoot image data. Capturing shoot images is inexpensive and easy, while in-field root imaging is time- and labor-intensive (image acquisition time is 5-10 minutes on average per tube) (Atkinson et al., 2019, Yang et al., 2020).
In addition to the root information, soil sensors measure point information on soil water content, soil water potential and soil temperature. Moreover, the spatial soil water content per depth can be measured with a ground-penetrating radar (GPR) (Klotzsche et al., 2019, Yu et al., 2020) between two neighboring rhizotubes.

The two MR facilities(Cai et al., 2016) in Selhausen, Germany, enable longer term studies of the soil–plant continuum on two different soils in the same climate. To investigate the different components of the soil–plant continuum, these MR facilities offer unique conditions to record 4D subsoil information for multiple growing seasons under different field conditions and agronomic treatments. Detailed information about soil water content (SWC), soil water potential, and soil temperature was obtained at two locations within different soil types by the soil sensors mentioned above. Furthermore, morphological root information was obtained *in situ*, including relevant root system traits such as length, diameter, branching frequency, etc.. Root traits were acquired with cameras, taking images through horizontal transparent rhizotubes installed at several depths (Cai et al., 2016, Morandage et al., 2021). Since all measures to avoid altered root growth due to tube installation were taken, the root parameters are expected to have at most negligible deviations in this respect.

The data collected in this study can be used to develop, calibrate, and validate models of the soil–plant continuum across different scales (Schnepf et al., 2022b) with regard to different root zone components such as soil processes, including flow processes (Landl et al., 2021, Vereecken et al., 2016), root development (Schnepf et al., 2022a), and biopores (Landl et al., 2019) as well as different model compilations such as single-plant and (Schnepf et al., 2022b) multi-plant modeling (Morandage et al., 2019) or soil water content and root water uptake modeling (Cai et al., 2017, 2018b). The data include agronomically relevant information for breeding water-efficient cultivars and for field management under various conditions, which can be directly used by, for example, agronomists and biologists. Furthermore, the root image data provided here can be used to train and benchmark neural networks, since deep learning-based technologies are a fast and continuously developing branch of plant and agronomic data analysis. The images presented in this paper, which correspond to the root data, are – to the best of our knowledge – the largest available MR image collection, covering several years, cultivars, and agronomic treatments. In this context, the advantage of this image collection is twofold. Firstly, we provide more than 160,000 MR images in one freely available and categorized data set. Secondly, we simultaneously publish reference data that can be used for validation. On the one hand, this will help machine learning scientists to develop models, capturing more heterogeneity. On the other hand, soil and plant scientists will benefit directly from the analyzed data. The data set was acquired for the years 2016, 2017, 2018, 2020, and 2021, and will be continued in the future. The data set will thus be added to each year. Data for the years 2012–2015 are partly available, but are not included in this publication. The related above-ground data, including measurements on crop development, transpiration fluxes, and assimilation rates, will be published in a corresponding paper.

2-2 Methods

2-2-1 Minirhizotron Facilities

The data for this publication were acquired at two MR facilities, allowing us to observe root growth through the rhizotubes and to measure 4D geophysical data. A detailed description of the construction of the MR facilities is provided in Cai et al. (2016). Here, we provide a basic overview of the facilities and the data acquisition.

The MR facilities are situated within the TERENO (TERrestrial ENvironmental Observatories) Eifel/Lower Rhine observatory near Selhausen, Germany (50°52'N, 6°27'E) (see Figure 2-1a). The Selhausen test site was mentioned in various studies ranging from geophysical observations and soil physics to root and plant modeling (Bauer et al., 2011, Bogena et al., 2018, Brogi et al., 2019, Cai et al., 2017, Jadoon et al., 2012, Weihermüller et al., 2007). The weather station (`SE_BDK_002`) is located within the Selhausen test site. The recorded parameters are used to calculate the evapotranspiration with a temporal resolution of 10 min. The data are available in the TERENO Data Discovery Portal (https://ddp.tereno.net/ddp/). The soil at the two MR facilities was deposited by fluvio-glacial sediments of the river Rur catchment during the Pleistocene (Bogena et al., 2018, Cai et al., 2016, Pütz et al., 2016). Different river sediments were deposited at each MR facility. The upper terrace sediments consist of gravely, partly stony, and silty sand, and it is here where the upper terrace MR

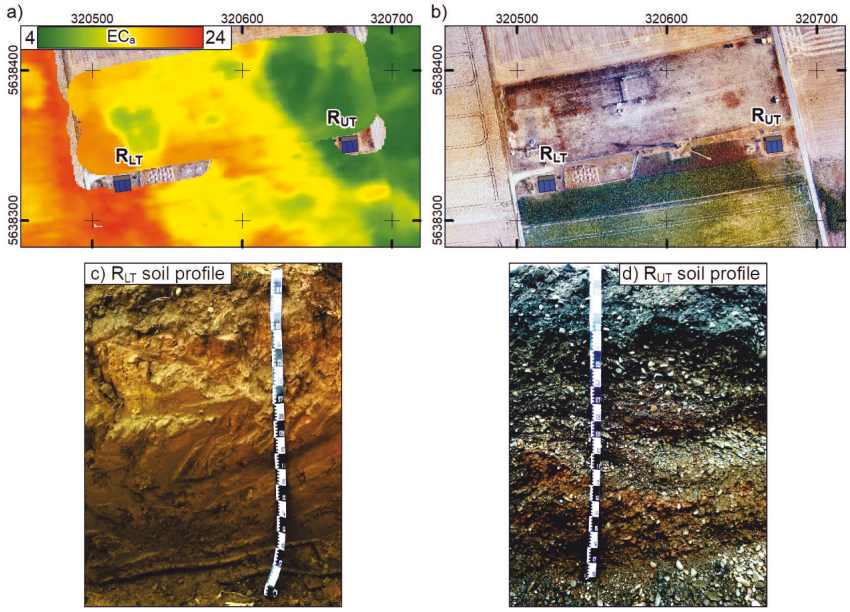

Figure 2-1: Overview of the location of the minirhizotron(MR)-facilities a) Map of the apparent electrical conductivity (ECa in [mS/m]) measured with the electromagnetic induction (EMI) (vertical diapoles, 9.7 cm depth of investigation, 135 cm coil distance) of the Selhausen test site. Provided by Brogi et al. (2019). b) Aerial photograph of the Selhausen test site and the MR-facilities. Both maps are given in WGS 1984 UTM Zone 32N [m]. For a) and b) the location of the MR-facilities is given by the blues rectangles, the upper terrace facility (R_{UT}) and the lower terrace facility (R_{LT}), the location of the access trench is indicated with a grey rectangle. c-d) Photos of the soil profiles of the loamy soil at the R_{LT} (c) and of stony soil at the R_{UT} (d).

facility (R_{UT}) is located. It is classified as Orthic Luvisol with a high stone content (>50 %) (Yu et al., 2020) according to the World Reference Base for Soil Resources (IUSS Working Group WRB, 2007). The soil at the lower terrace is classified as Cutanic Luvisol (Ruptic, Siltic) (Bauer et al., 2011), and it is here where the lower terrace MR facility (R_{LT}) is located. The soil organic content and total soil nitrogen (derived from 2020) were 1.14 % and 0.116 % (0-0.3 m), 0.66 % and 0.081 % (0.3–0.6 m), and 0.42 % and 0.059 % (0.6-1 m) in R_{LT} as well as 1.39 % and 0.128 % (0–0.3 m, with a stone weight of 45 %) in R_{UT}. The sand, silt, and clay contents are on average 16 %, 63 %, and 21 % (0–1 m, R_{UT}) and 32 %, 53 %, and 15 % (0–0.3 m, R_{UT}). The different soils cause a 4° morphology incline from R_{UT} towards R_{LT} (see Cai et al. (2016). Due to regular tilling and plowing, a 0.3-m-thick plow layer (Ap horizon) was present in the upper 0.3 m of the two MR facilities (see Figure 2-1b and 2-1c).

To compare different agronomic treatments under the same soil and atmospheric conditions, the two MR facilities were divided into three plots (Figure 2-2a). Within the individual plots, three horizontal rhizotubes were installed at each of six different depths between 0.1 m and 1.2 m, each with a length of 7 m. The rhizotubes were embedded at a distance of 0.75 m in

the horizontal axis (Figure 2-2a). For each crop growing season, a crop row orientation perpendicular to the rhizotubes was chosen. To perform the measurements within the rhizotubes an access trench was built within the ground in front of the plots, from which the rhizotubes can be reached. At R_{UT}, the soil was excavated and refilled while installing the rhizotubes, which was due to the high stone content. A plastic foil was installed down to 1.3 m depth to separate the plots. At R_{LT}, the soil is undisturbed since the installation was performed by drilling. The soil was precisely compacted layer by layer to the same bulk density as the undisturbed soil (see Cai et al. (2016). For R_{UT}, the differences in excess length is negligible, as they are less than < 0.02 m. In contrast, for R_{LT}, excess lengths are up to 0.10 m. This was taken into account during the processing of the data. Due to soil erosion and soil compaction after tillage and seedbed preparation, the depths of the rhizotubes vary between the individual measurement seasons. The individual rhizotube depths are provided in the repository "Additional_Information"
In addition to the measurements (GPR and root images) that can be performed within the rhizotubes, various soil sensors are embedded within the soil (see Soil Sensor Data section). Above ground at R_{LT}, there is a monitoring system for spectral electrical impedance tomography (sEIT) (Weigand et al., 2022).
A water reservoir is installed to provide rainwater for irrigation.

2-2-2 Study Design

The MR facilities allow an *in situ* investigation of the soil–plant continuum. To observe the impact of drought stress and planting density on different crops and the impact of crop mixtures on root development, various agronomic treatments were carried out for the different plots. This includes, depending on the growing season, surface water treatment (sheltered, natural/rainfed & irrigated), planting density, sowing date, and different crop cultivar mixtures. In this study, we present the data of multiple crop growing seasons between the years 2016 and 2021. An overview of the individual crop growing seasons and the agricultural treatments is provided in the repository "Additional_Information".

During the 2016 crop growing season, the goal was to compare different drought stress levels for winter wheat (*Triticum aestivum*, cv. Ambello). A shelter was therefore installed on Plot 1 for both MR facilities. The shelter had a cover, which was removed when no precipitation was forecasted. Plot 2 was left under natural conditions and is also referred to as the rainfed plot. For Plot 3, irrigation pipes were installed and the soil was irrigated regularly. The individual irrigation values can be found in the "Additional_Information". For crop growing seasons 2017 & 2018, *Zea mays* (cv. Zoey) was chosen and the shelter needed to be removed due to the height of the crop. This resulted in two rainfed plots (Plot 1 and Plot 2). As before, Plot 3 was irrigated. In 2018, the influence of the sowing date and the planting density was investigated on Plot 1 for R_{UT} and R_{LT}, respectively.

Since the 2020 crop growing season, the focus of research was on comparing the different crop root architectures of cultivars – purely sown and in a cultivar mixture with alternating rows. To explore the beneficial effects of mixing deep and shallow rooting cultivars, one cultivar chosen was always a deep rooting, while the other one was a shallow rooting cultivar. The surface water treatment was therefore uniform for all three plots.

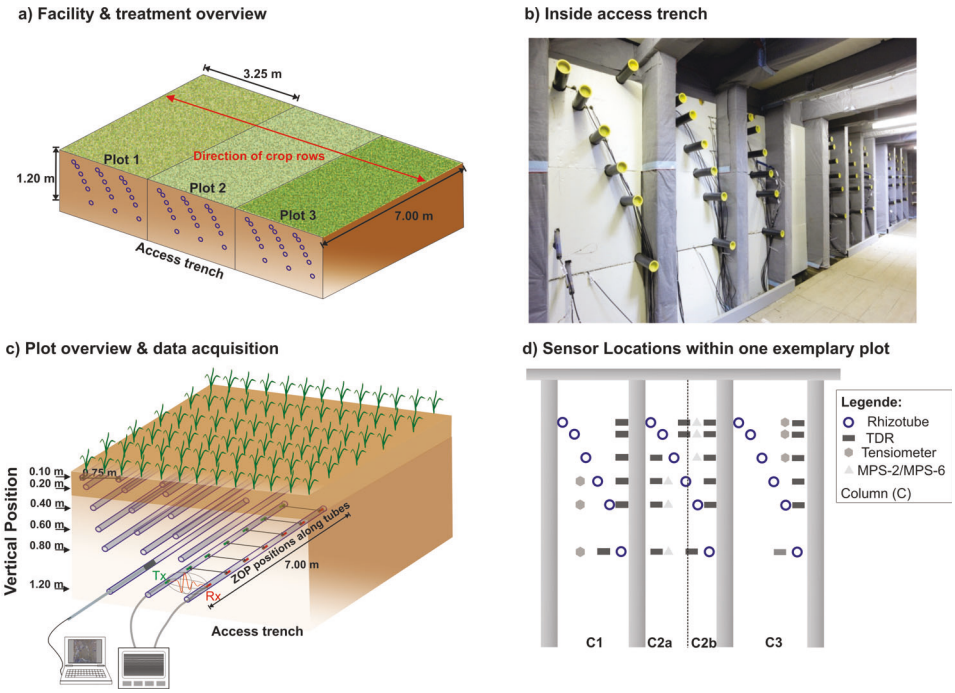

Figure 2-2: Overview of the Minirhizotron (MR)-facilities. a) Schematic setup of the MR-facilities indicating that at each of the plots a different agricultural treatment was applied for the different growing seasons. The direction of the crop rows is perpendicular to the direction of the rhizotrubes (red arrow). The measurements are carried out from the access trench. b) View within the access trench. c) Overview of one exemplary plot within the MR-facilities with the horizontal crosshole GPR ZOP measurement set up. Transmitter and receiver antennae are labeled Tx and Rx, respectively. Root image measurement are acquired using camera system attached to an index handle. d) Sensor location for one exemplary plot.

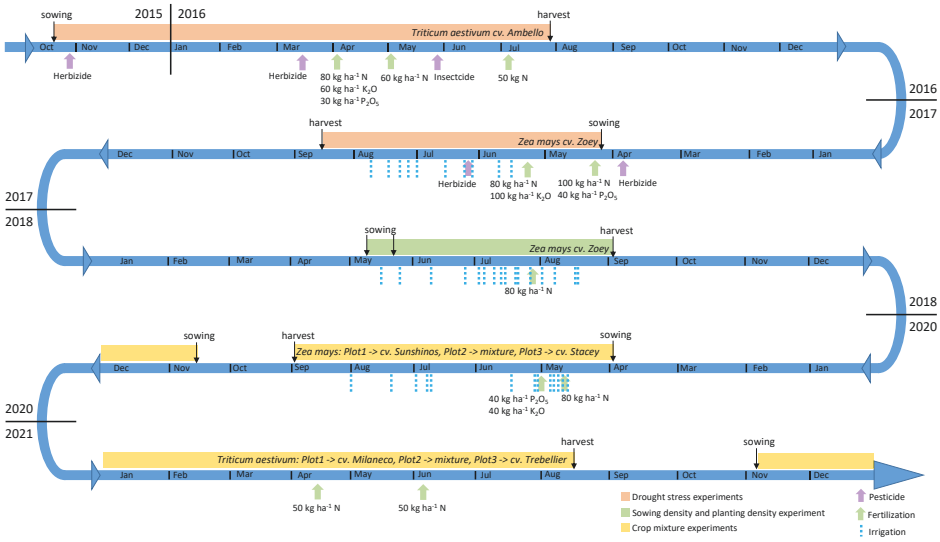

Figure 2-3: Overview of the experimental timeline including cultivars and management actions, such as sowing, harvest, pesticide applications and irrigation.

Irrigation was only applied to all crops under heavy drought conditions when the crops showed severe drought stress symptoms. For the 2020 crop growing season, two different *Zea mays* cultivars (cv. Sunshinos and cv. Stacey) were sown on Plot 1 and Plot 3, respectively. The cultivar mixture was sown on Plot 2. For the 2021 growing season, winter wheat (*Triticum aestivum*) with two different cultivars (cv. Milaneco and cv. Trebelir) was again sown on Plot 1 and Plot 3, respectively. The mixture was sown on Plot 2. In 2021, irrigation was not required since the winter wheat was sufficiently supplied by precipitation and the crops did not show any stress symptoms (Figure 2-3). In order to perform destructive measurements above and below ground in 2020 and 2021, a replication field (extra field (EF)) next to R_{LT} was sown. The EF had the same dimension and plot design as the MR facilities and was located on the west side of the facility (see Above-Ground Data section).

2-2-3 Ground-Penetrating Radar Data

Crosshole GPR Data Acquisition at the MR Facilities

The time-lapse GPR data were collected using a 200 MHz PulseEKKO borehole system manufactured by Sensors and Software (Canada). Crosshole zero-offset-profiling (ZOP) measurements were carried out, with the transmitter (Tx) and receiver antennae (Rx) located within neighboring rhizotubes. Both antennae were simultaneously pulled in parallel positions along the length of the rhizotubes, with a spacing of 0.05 m between the individual ZOP positions. An electromagnetic (EM) wave is emitted by Tx, which is sent through the soil and then recorded by Rx. Changes in soil and root properties between the rhizotubes affect

the measured GPR traces and, therefore, information about the medium parameters can be obtained (more information can be found in Klotzsche et al. (2019)). Due to the different rhizotube lengths of both MR facilities, the length over which the ZOPs are collected is 6.70 m and 6.40 m, resulting in 115 and 109 traces for R_{UT} and R_{LT}, respectively.
For a time-zero calibration, wide-angle reflection and refraction (WARR) measurements are carried out within the access trench. Here, Rx antennae are moved over a distance of 6.0 m with a step size of 0.1 m, while the Tx antennae are fixed at the zero location. At least four calibration measurements per MR facility and measurement day were performed to capture daily variations of the time-zero (see GPR Data Processing section).

In contrast to the root images, which capture the soil in contact with the rhizotubes, the ZOP measurements investigate the soil between two rhizotubes. A 1D horizontal permittivity profile is thus obtained. For the measurements seasons 2016–2018, only one horizontal permittivity plane was measured per depth. For Plot 1 and Plot 2, this were the slices between column C1 and C2, and for Plot 3 between column C2 and column C3. In 2020, two main planes were measured per depth; occasionally only one plane was measured with the same configuration as for the previous measurement seasons. Table 2-1 indicates that the number of horizontal permittivity planes was measured per measurement date.

Table 2-1: Detailed overview of the GPR data acquired during growing season 2016, 2017, 2018, 2020 and 2021.

		2016		2017		2018		2020		2021	
no	fac	date	pl	date	pl	date	pl	date	pl	date	pl
1	R_{UT}	03.02.2016	12	26.04.2017	15	25.04.2018	15	19.03.2020	12	-	-
	R_{LT}	03.02.2016	-	26.04.2017	14	25.04.2018	14	-	-	25.11.2020	29
2	R_{UT}	30.03.2016	15	03.05.2017	15	02.05.2018	15	12.05.2020	30	-	-
	R_{LT}	30.03.2016	10	03.05.2017	14	02.05.2018	14	-	-	02.12.2020	30
3	R_{UT}	08.04.2016	15	10.05.2017	14	09.05.2018	15	28.05.2020	30	-	-
	R_{LT}	08.04.2016	15	10.05.2017	14	09.05.2018	14	-	-	14.12.2020	29
4	R_{UT}	14.04.2016	15	17.05.2017	15	14.05.2018	15	03.06.2020	30	-	-
	R_{LT}	14.04.2016	15	17.05.2017	14	14.05.2018	14	-	-	14.01.2021	29
5	R_{UT}	20.04.2016	15	23.05.2017	15	24.05.2018	15	10.06.2020	30	-	-
	R_{LT}	20.04.2016	15	23.05.2017	11	24.05.2018	14	-	-	27.01.2021	29
6	R_{UT}	28.04.2016	15	31.05.2017	15	20.06.2018	15	17.06.2020	25	-	-
	R_{LT}	28.04.2016	15	31.05.2017	14	20.06.2018	14	-	-	10.02.2021	29
7	R_{UT}	04.05.2016	15	07.06.2017	15	27.06.2018	15	06.07.2020	29	04.03.2021	30
	R_{LT}	04.05.2016	15	07.06.2017	14	27.06.2018	14	-	-	-	-
8	R_{UT}	12.05.2016	15	14.06.2017	15	04.07.2018	15	15.07.2020	30	-	-
	R_{LT}	12.05.2016	15	14.06.2017	14	04.07.2018	14	-	-	09.03.2021	-
9	R_{UT}	19.05.2016	15	21.06.2017	15	09.07.2018	15	23.07.2020	5	11.03.2021	30
	R_{LT}	19.05.2016	15	21.06.2017	14	-	14	-	-	11.03.2021	-
10	R_{UT}	25.05.2016	15	05.07.2017	15	11.07.2018	15	27.07.2020	30	19.03.2021	24
	R_{LT}	25.05.2016	15	05.07.2017	14	11.07.2018	14	-	-	19.03.2021	-
11	R_{UT}	02.06.2016	15	12.07.2017	15	18.07.2018	15	05.08.2020	5	30.03.2021	15
	R_{LT}	02.06.2016	14	12.07.2017	14	18.07.2018	14	-	-	30.03.2021	29
12	R_{UT}	09.06.2016	15	19.07.2017	15	19.07.2018	15	-	-	15.04.2021	30
	R_{LT}	09.06.2016	15	19.07.2017	14	19.07.2018	14	-	-	15.04.2021	-
13	R_{UT}	13.06.2016	15	27.07.2017	15	20.07.2018	15	-	-	14.07.2021	30
	R_{LT}	13.06.2016	15	27.07.2017	14	20.07.2018	14	-	-	22.07.2021	-
14	R_{UT}	20.06.2016	15	02.08.2017	15	25.07.2018	15	-	-	28.07.2021	30
	R_{LT}	20.06.2016	14	02.08.2017	14	25.07.2018	14	-	-	28.07.2021	29
15	R_{UT}	27.06.2016	15	09.08.2017	15	01.08.2018	15	-	-	04.08.2021	30
	R_{LT}	27.06.2016	14	09.08.2017	14	01.08.2018	14	-	-	04.08.2021	28
16	R_{UT}	04.07.2016	15	14.08.2017	15	08.08.2018	15	-	-	18.08.2021	15
	R_{LT}	27.06.2016	15	09.08.2017	15	01.08.2018	15	-	-	04.08.2021	30
17	R_{UT}	20.07.2016	15	23.08.2017	15	15.08.2018	15	-	-	-	-
	R_{LT}	20.07.2016	15	23.08.2017	14	15.08.2018	14	-	-	25.08.2021	30
18	R_{UT}	27.07.2016	15	30.08.2017	15	22.08.2018	15	-	-	-	-
	R_{LT}	27.07.2016	15	30.08.2017	14	22.08.2018	14	-	-	31.08.2021	23
19	R_{UT}	01.08.2016	15	06.09.2017	15	05.09.2018	15	-	-	10.09.2021	30
	R_{LT}	01.08.2016	15	06.09.2017	14	05.09.2018	14	-	-	10.09.2021	19
20	R_{UT}	08.08.2016	15	13.09.2017	15	17.09.2018	15	-	-	29.09.2021	30
	R_{LT}	08.08.2016	15	13.09.2017	14	17.09.2018	14	-	-	-	-
21	R_{UT}	15.08.2016	15	20.09.2017	15	24.09.2018	15	-	-	03.11.2021	30
	R_{LT}	15.08.2016	15	20.09.2017	14	24.09.2018	14	-	-	03.11.2021	27
22	R_{UT}	-	-	27.09.2017	15	02.10.2018	15	-	-	-	-
	R_{LT}	-	-	27.09.2017	14	02.10.2018	14	-	-	-	-

Ground-penetrating radar data processing

From horizontal GPR crosshole ZOP measurements, we can derive the relative dielectric permittivity ε_r, which can be transformed into SWC using appropriate petrophysical relationships. All the required pre-processing steps are explained in detail by Klotzsche et al. (2019). Here, we highlight the most important aspects. Firstly, a dewow filter is applied, which reduces low-frequency noises on the GPR data. Secondly, a time-zero (T_0) correction of the ZOP data is performed and thirdly, the first breaks (FB) of the signals are estimated (Figure 2-4a).

Following this processing procedure, the EM wave travel times between the neighboring rhizotubes for each ZOP position are obtained. Since the horizontal spacing between the neighboring rhizotubes ($d_{rhizotubes}$) is known to be 0.75 m, the EM wave velocity v for each ZOP position can be calculated using the obtained travel times (t_{travel}), see Figure 2-4b. As suggested by Jol (2009), when considering low-loss and non-magnetic soils the EM velocity v can be transformed into the relative dielectric permittivity ε_r of the bulk material with

$$v = \frac{c}{\sqrt{\varepsilon_r}} \tag{2-1}$$

where c is the speed of light (~0.3 m/ns).
Because of the presence of the soil sensors and pertaining cables in the first 0.75 m away from the facility wall, GPR measurements were made between 1 and 7 m away from the facility wall. Close to the surface (depth of 0.1 m) the radar wave interferences of the critically refracted air wave and the direct wave (Klotzsche et al., 2019) occur. Therefore, these data were excluded. Additionally, at R_{LT}, an sEIT system is installed and the metal parts interfere with the GPR waves. Therefore, at a depth of 0.2 m, where the sEIT system is located, the data were also excluded.

GPR-derived permittivity can be transformed into the soil water content (SWC), which provides a parameter that is directly used in soil science. This is achieved by using different conversion formulas, which are based on empirical relationships and petrophysical, volumetric mixing models (see Huisman et al. (2003) and Steelman and Endres (2011)). In this data descriptor, we provide the permittivity values to ensure that the conversion can be chosen by the user of the data. In the past, we have used two conversions, the Topp's equation Topp et al. (1980) and the complex refractive index model (CRIM) (Steelman and Endres, 2011) (see Klotzsche et al. (2019) and the Dielectric Permittivity to Soil Water Content section).

2-2-4 Root images

Root image acquisition at the minirhizotron facilities

Images of roots and the surrounding soil were captured through the transparent rhizotubes. The amount of images obtained varied depending on the vegetation and the progress of root

development. To save resources, the depth of measurement was continuously increased at the beginning of each growing season as root depth increased. Meticulous care was taken not to omit any root depth at which roots were already present. A measurement produces always 40 images per tube. Half of the images were taken 80° clockwise and the other half were taken 80° counter-clockwise from the top point of the rhizotubes. Two different camera systems were used over time to take the images. The camera used in 2016, and for most measurements in 2017, was manufactured by Bartz (Bartz Technology Corporation). The camera used for some of the images taken in 2017 and for all images taken in 2018, 2020, and 2021 was produced by VSI (Vienna Scientific Instruments GmbH).The photographed area differs depending on the camera (Table 2-2). Table 2-3 provides a detailed overview of the images taken over the different growing seasons.

Table 2-2: Overview of the camera-systems and experiment timeline of minirhizotron images acquisition

camera system	Bartz	VSI
resolution (px)	1508 x 1020	2060 x 2060
real size (mm)	16.5 x 23.5	20 x 20
wavelength (nm)	400-780	400-780
growing season	2016 & 2017	2017 & 2018 & 2020 & 2021

Root image data processing

The post processing of the images was performed by an automated analysis pipeline including neural network segmentation and automated feature extraction following the analysis pipeline of Bauer et al. (2022). Neural network training and image segmentation were performed with the "RootPainter" (Smith et al., 2022) software. Firstly, the roots were segmented by a CNN. As part of the process, the roots are separated from the background and extracted as binary image data. A small subset of the root images is used as training data to train the CNN. The evaluation of the models was performed with the F1-score (>0.7 for each model used). More information on the models can be found in Bauer et al. (2022). The resulting neural network model was then used for the segmentation of the roots. The segmentation of the images was performed in a batch process. Secondly, the morphological features were extracted by the automated feature extraction program "RhizoVision Explorer" (Seethepalli et al., 2021). This includes multiple automated steps for thresholding obstacles and filling holes smaller than 0.2 mm as well as the skeletonization of the roots and the feature derivation from the skeletonized roots.

The root system parameters provided by the automated analysis include the total root length, branch points, branching frequency, diameter (average, maximum, median), network area, perimeter, amount of root tips, volume, and surface area (Bauer et al., 2022) (Figure 2-5).

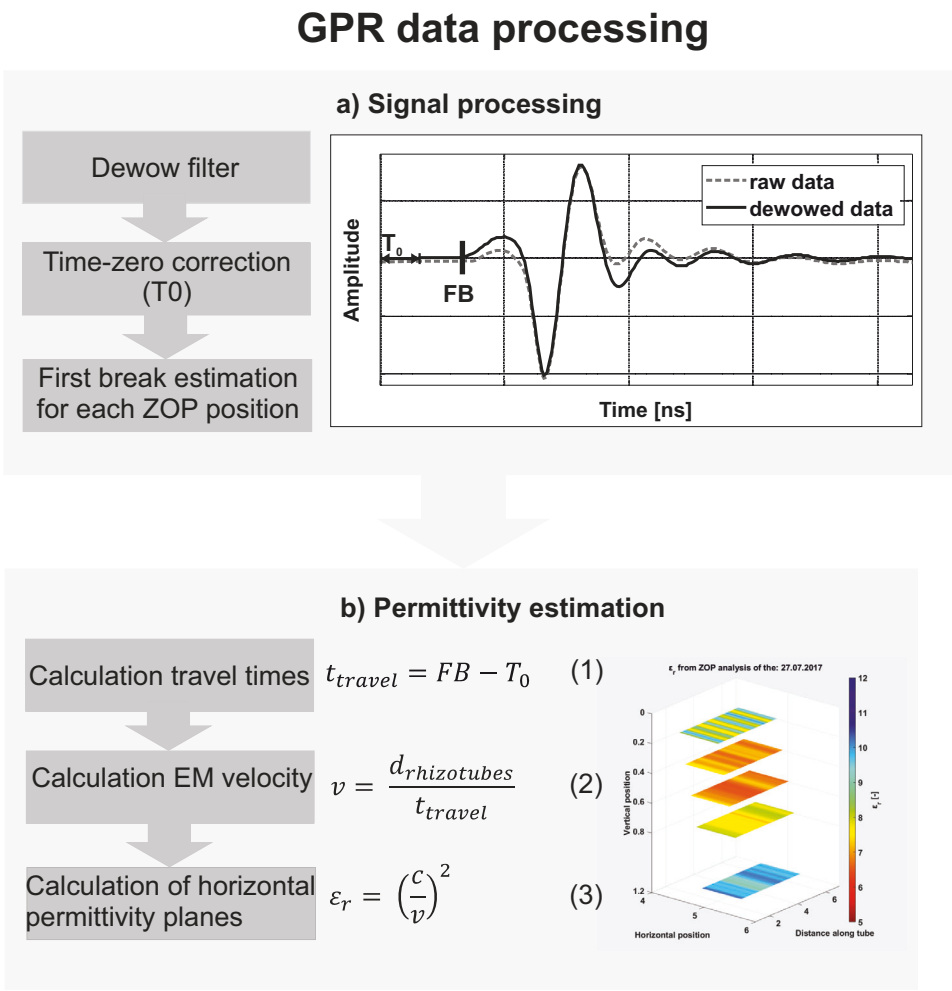

Figure 2-4: GPR processing steps

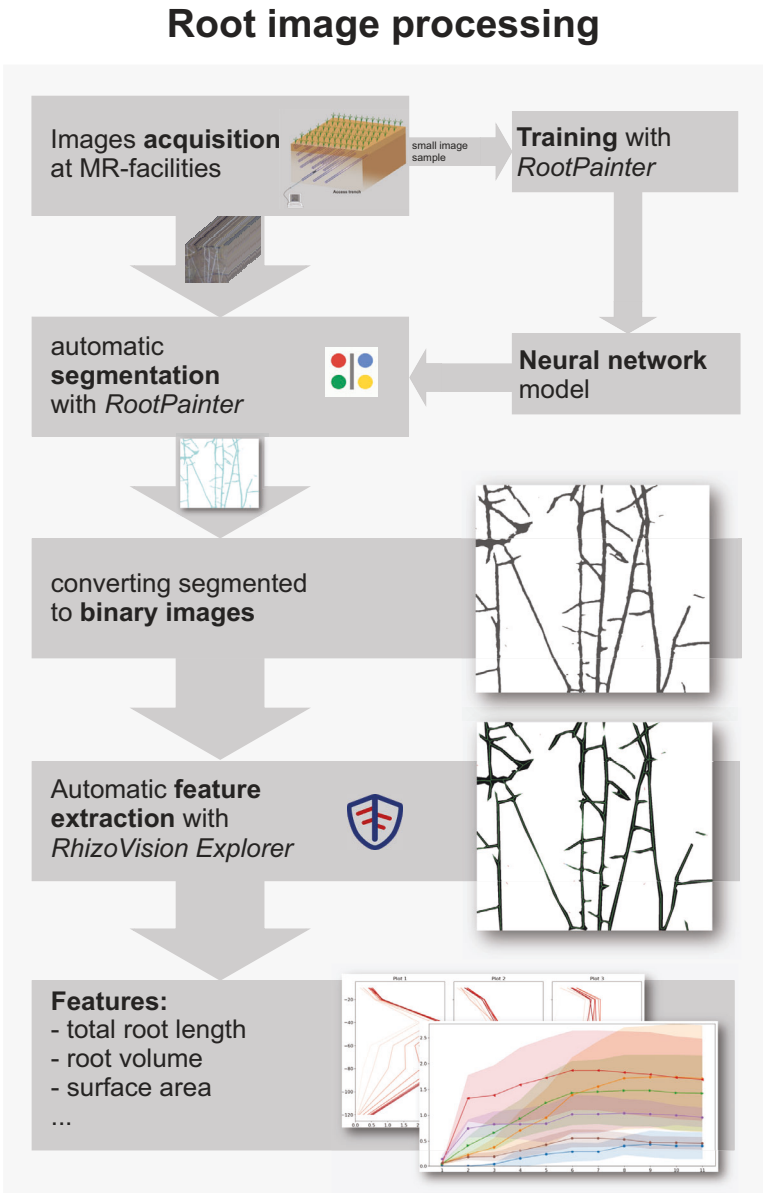

Figure 2-5: Root image processing steps

Table 2-3: Detailed overview of the images taken at the growing season 2016, 2017, 2018, 2020 and 2021.

		2015/16		2017		2018		2020		2020/21	
no	fac	date	img	date	img	date	img	date	img	date	img
1	R_{UT}	16.11.2015	719	08.06.2017	480	23.05.2018	440	02.07.2020	1,160	24.02.2021	1,480
	R_{LT}	16.11.2015	720	08.06.2017	584	23.05.2018	720	13.08.2020	1,760	14.01.2021	600
2	R_{UT}	26.11.2015	1,070	29.06.2017	1,800	30.05.2018	480	13.08.2020	1,800	03.03.2021	1,440
	R_{LT}	26.11.2015	1,073	22.06.2017	1,800	30.05.2018	720	-	-	27.01.2021	920
3	R_{UT}	17.12.2015	1,799	06.07.2017	1,800	07.06.2018	960	-	-	11.03.2021	1800
	R_{LT}	17.12.2015	1,439	29.06.2017	2,160	07.06.2018	1,075	-	-	04.02.2021	1,280
4	R_{UT}	02.02.2016	1,518	13.07.2017	1,800	18.06.2018	1,280	-	-	01.04.2021	440
	R_{LT}	21.01.2016	1,795	06.07.2017	2,160	18.06.2018	1,436	-	-	24.02.2021	1,320
5	R_{UT}	12.02.2016	1,789	20.07.2017	1,800	26.06.2018	1,400	-	-	08.04.2021	2,160
	R_{LT}	12.02.2016	1,798	13.07.2017	2,160	26.06.2018	1,800	-	-	03.03.2021	1,280
6	R_{UT}	26.02.2016	1,795	27.07.2017	1,200	05.07.2018	1,638	-	-	22.04.2021	1,560
	R_{LT}	26.02.2016	2,155	20.07.2017	2,160	18.07.2018	2,156	-	-	10.03.2021	1,640
7	R_{UT}	14.03.2016	1,792	02.08.2017	1,840	18.07.2020	1,760	-	-	21.05.2021	2,160
	R_{LT}	14.03.2016	2,158	27.07.2017	1,430	01.08.2018	2,159	-	-	07.04.2021	2,000
8	R_{UT}	26.03.2016	1,837	10.08.2017	1,959	01.08.2018	1,680	-	-	01.06.2021	520
	R_{LT}	24.03.2016	2,155	02.08.2017	2,157	23.08.2018	2,159	-	-	21.05.2021	1,960
9	R_{UT}	07.04.2016	2,157	23.08.2017	2,120	16.08.2018	1,676	-	-	07.06.2021	240
	R_{LT}	07.04.2016	2,158	10.08.2017	2,154	-	-	-	-	01.06.2021	1,960
10	R_{UT}	13.04.2016	2,160	12.09.2017	1,800	-	-	-	-	-	-
	R_{LT}	13.04.2016	2,157	24.08.2017	2,159	-	-	-	-	-	-
11	R_{UT}	29.04.2016	2,154	-	-	-	-	-	-	-	-
	R_{LT}	29.04.2016	2,157	12.09.2017	2,150	-	-	-	-	-	-
12	R_{UT}	06.05.2016	2,154	-	-	-	-	-	-	-	-
	R_{LT}	06.05.2016	2,144	-	-	-	-	-	-	-	-
13	R_{UT}	13.05.2016	2,151	-	-	-	-	-	-	-	-
	R_{LT}	13.05.2016	2,155	-	-	-	-	-	-	-	-
14	R_{UT}	20.05.2016	2,156	-	-	-	-	-	-	-	-
	R_{LT}	20.05.2016	2,155	-	-	-	-	-	-	-	-
15	R_{UT}	27.05.2016	2,152	-	-	-	-	-	-	-	-
	R_{LT}	27.05.2016	2,153	-	-	-	-	-	-	-	-
16	R_{UT}	03.06.2016	2,108	-	-	-	-	-	-	-	-
	R_{LT}	03.06.2016	2,153	-	-	-	-	-	-	-	-
17	R_{UT}	09.06.2016	2,114	-	-	-	-	-	-	-	-
	R_{LT}	09.06.2016	2,083	-	-	-	-	-	-	-	-
18	R_{UT}	16.06.2016	2,111	-	-	-	-	-	-	-	-
	R_{LT}	16.06.2016	2,142	-	-	-	-	-	-	-	-
19	R_{UT}	23.06.2016	2,087	-	-	-	-	-	-	-	-
	R_{LT}	23.06.2016	2,006	-	-	-	-	-	-	-	

2-2-5 Soil coring in the extra field

Soil coring was performed in the EF (extra field established next to R_{LT}) dedicated to destructive belowground measurements in 2020 (maize) and 2021 (winter wheat). The soil next to R_{UT} is not homogeneous, which is why a representative replica was not feasible. The maize roots were extracted once on July 14, 2020 when the crops were in BBCH 65, whereas the winter wheat roots were extracted on June 16, 2021 when the crops were in BBCH 69. The soil was cored using a root auger with an inner diameter of 0.9 m and a length of 1.0 m, and the cores were drilled directly around the plant. The soil core was then divided into 0.1 m pieces and filled into plastic bags.

For maize in 2020, four replicates were taken in Plot 1 and four replicates in Plot 3 of the EF (no core was taken in the cultivar mixture treatment – Plot 2). For winter wheat in 2021, one replicate was taken in Plot 1, one in Plot 3, and two in Plot 2 of the EF (one core for each variety in the cultivar mixture).

The soil samples were then put into refrigerators and processed step by step. The samples were later soaked in tap water, washed, and passed through several sieves with mesh sizes of 1.00 mm, 0.83 mm, and 0.5 mm until the coarsest soil and residues were cleared. The roots were subsequently stored in tap water at 3°C until they were scanned with an EPSON scanner (HP Expression 1100XL). The roots of each sample were laid (preferably without overlaps) into an acrylic glass plate filled with tap water and were subsequently scanned. The images of the scanned roots were processed using a similar procedure as for the minirhizotron images, resulting in the total length estimation of the roots and the root length density (Han et al., 2021).

2-2-6 Soil sensor data

All plots within the two MR facilities have the same layout. Each plot contains three horizontal rhizotubes per depth but the soil sensors are distributed into four columns, with the middle section divided into two columns, column C2a and C2b (see Figure 2-2 c). For each column, there are four TDR-sensors installed for each of the six depths. For the tensiometers and the soil water potential and soil temperature sensors, one sensor is installed for each depth. The distribution over the four columns is shown in Figure 2-2 c.

To measure the soil water potential for dry soil conditions and to acquire the soil temperature, MPS-2 sensors manufactured by Decagon Devices, Inc., US are used. The soil water potential is measured in a range of -9 kPa to -100,000 kPa (pF 1.96 to pF 6.01) with a resolution of 0.1 kPa. The accuracy is of ±(25% of reading +2 kPa) over the range of -9 to -100 kPa and proven to be higher for drier conditions until permanent wilting point (-1,500 kPa) under lab conditions and -4,500 kPa under field conditions by the manufacturer. The soil temperature is measured in a range of -40°C to 60°C with a resolution of 0.1°C. The soil water potential for wet soil conditions is measured using T4 pressure transducer tensiometers manufactured by UMS GmbH, Germany. The measurement range is -85 kPa to +100 kPa with an accuracy of ± 0.5 kPa. To acquire and record the soil sensor data, all sensors – with the exception of the TDR sensors – are connected to a DataTaker DT85 manufactured

by Omni Instruments Ltd, UK. The TDR sensors were manufactured by the institute's technicians and consist of three rods, with a length of 200 mm and a spacing of 26 mm. The TDR sensors are connected to institute-made multiplexers (50C81-SDM), providing a lower relative error (>1%) then commercial system (Weihermüller et al., 2013). To acquire and record the data, the multiplexers are connected to a TDR100 Time-Domain Reflectometer manufactured by Campbell Scientific, Inc., US. Because of the high stone content at R_{LT} the relationship of SWC and dielectric permittivity measured by the TDR was calibrated in the lab (Cai et al., 2016). For information on SWC calculation see Dielectric Permittivity to Soil Water Content section.

2-2-7 Soil water content using a mobile frequency domain reflectometry device

In addition to the soil sensors (see Soil Sensor Data section), the soil water content was measured using the mobile FDR device that employs the HH2 moisture sensor with the ThetaProbe ML3 (ecoTech Umwelt-Meßsysteme GmbH, Bonn, Germany). Due to the nature of the soil at R_{UT}, the soil moisture was only measured for the topsoil, while for the R_{LT} and EF, the soil water was measured at depths of 0 m, 0.30 m, 0.6 m, and 0.9 m. In total, the soil water was measured ten times in each plot of the R_{UT}, six times in each plot of the R_{LT}, and eleven times in each plot of the EF over the crop growing season. The sensor was always placed between crop rows.

2-2-8 Soil sampling

In September 2020, a new irrigation tank was installed at R_{LT} and undisturbed soil samples were taken from the trench for the new tank. The samples were taken from several depths and analyzed in the in-house soil physics lab. The soil hydraulic parameters were measured using the HYPROP (Meter, München, Germany) method (Schindler et al., 2010) and a WP4 Dewpoint Potentiometer (Decagon Devices, WA, USA). The saturated hydraulic conductivity was derived using the KSAT system (Meter, München, Germany). Soil texture was determined according to DIN ISO 11277 using the pipette method combined with wet sieving (Müller et al., 2009).
The soil hydraulic properties can be found in "Additional_Information" .

2-3 Data Records

All data were uploaded to Geonetwork in accordance with ISO 19115. The data were persistently stored and will be regularly updated (see Usage Notes). The data were subdivided according to the characteristics of the sensing method and data type. GPR data , root data root images, and soil sensor data are each available with a DOI, providing a link to a repository. Within these repositories, the data were subdivided by year of measurement. In the GPR data repository, one folder for each year contains two CSV files – one for all measurements performed on each facility in the corresponding year. The root image data repository contains a CSV file for each root trait measured in the corresponding year and facility.

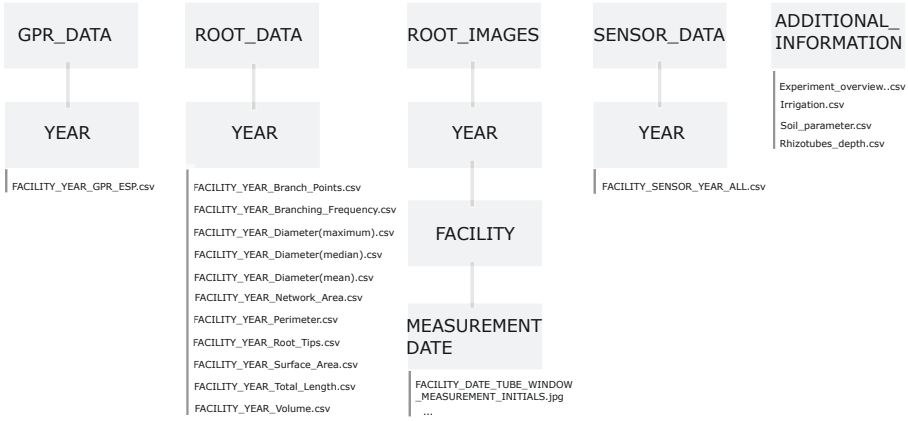

Figure 2-6: Folder structure of the repositories.

The root images were organized by year and facility. For each measurement date, one folder (labeled: YYYYMMDD) contains all images measured on that date in the corresponding facility. The sensor data repository contains one file for each sensor type and facility, corresponding to the year the data were obtained. The file names are explained in Table 2-4 and the repository structures in Figure 2-6. The data can be downloaded using the following links:

GPR data: `https://doi.org/10.34731/cg3t-nb88`,
Root data: `https://doi.org/10.34731/7x05-2r96`,
Root images: `https://doi.org/10.34731/5zwe-t974`,
Soil sensor data: `https://doi.org/10.34731/ffsk-sy65`,
Additional information: `https://doi.org/10.34731/st8e-4082`.

Table 2-4: Overview of the repository content and data labelling. The labels always contain the facility name (R_{UT}or R_{LT}) and the year the data haven been obtained. For the root images, each image is also labeled according to exact date (year (YYYY), month (MM) , day (DD)), tube and position it was taken.

repository	data label	size
GPR_Data	*FACILITY_YYYY*_GPR_EPS.csv	2.68 *MB*
Root_Data	*FACILITY_YYYY_ROOT PARAMETER*.csv	21.6 *MB*
Root_Images	*FACILITY YYYYMMDD_TUBE_WINDOW_MEASUREMENT_INITIALS*.jpg	199 *GB*
Soil sensors_Data	*FACILITY_SENSOR YYYY*_ALL.csv	103 *MB*
Additional_Information	experiment, irrigation and soil overview (CSV)	1 *MB*

Some root image data have been previously used and published. Root length data from 2016 were used by Nguyen et al. (2020). Root length data obtained from the images and the soil moisture values, measured by TDR and MPS-2 sensors on both facilities in 2016 and 2017 were used byMorandage et al. (2021). The root image data of R_{UT} from June 8, July 13,

and September 12, 2017 were used by Nguyen et al. (2022b). However, the root lengths used in these three studies were obtained by a different method and are based on a manual single root annotation (Zeng et al., 2008). The root length data of R_{UT} and R_{LT} from 2017 were published by Bauer et al. (2022) to validate the analysis pipeline used to extract all root data. The GPR data and the mean soil water content values calculated from TDR sensors from 2016 and 2017 have already been partly used by Klotzsche et al. (2019).

2-4 Technical validation

Ground-penetrating radar data

The GPR permittivities were manually checked for plausibility and unreliable data were excluded. Implausible permittivity outliers were manually detected and removed.

Root Images

The root data derived from the minirhizotron images were automatically analyzed by the pipeline following Bauer et al. (2022) using deep neural networks and automated feature extraction (Seethepalli et al., 2021, Smith et al., 2022). Using this approach, part of the total root length data has been representatively compared to a manual annotation of the images. Approximately 36,500 images were used for validation. The correlation of total root length values obtained from the same images by manual annotation and automated analysis is very high (r=0.9) (Bauer et al., 2022).

2-4-1 Soil Sensor Data

The data of the different sensor types were filtered for the different measurement ranges listed in the Methods Soil Sensor Data section. To remove outliers, we applied a Hampel filter, which involves a sliding window being moved over the data. As a window size, we used 10 data points for each size of the element, which corresponds to 5 h for the tensiometers and MPS-2 to 10 h for the TDR sensors. For the element, we calculated the median and the standard deviation. If the element deviated more than one time the standard deviation, then the element is replaced by the median (Hampel, 1974).

Additionally, the data from the different soil sensors were manually checked for plausibility and unreliable data were excluded. The TDR sensor data were filtered for errors in the TDR wave recordings and data for different dates and sensors were excluded.

2-5 Usage Notes

Figure 2-7 provides information on which periods of data are available for the different measurement seasons and the different measurement techniques. In 2019, no crops were sown on the MR facilities due to a project change. In 2020 and 2021, the data sets do not cover the

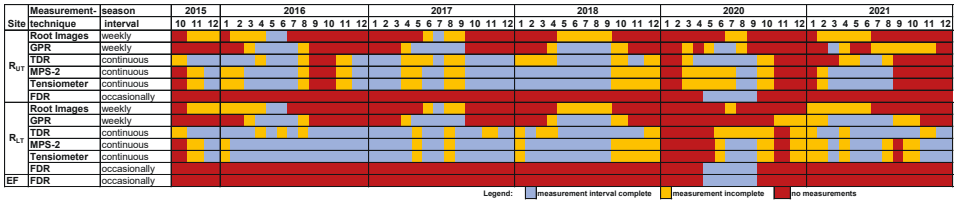

Figure 2-7: Data availability for the measurement seasons 2016 - 2021.

whole growing period due to technical issues within the access trench and the measurement systems. Different measurement intervals were used for the different measurement techniques. For the root images and the GPR measurements, weekly measurements were performed when possible during the vegetation period. The interval was adjusted to a biweekly period for the root images when the root growth stagnated.

The availability of the sensor data (TDR, Tensiometer & MPS-2) depends on the technical state of the measuring devices, and in 2020 and 2021 there were problems with the data recording system. The measurements should be recorded as continuous measurements with measuring intervals of 30 min for tensiometers and MPS-2 sensors and 1 hour for TDR sensors. All timestamps are UTC+1.

2-5-1 Soil sensor data

Due to the measurement interval and the sensitivity of the TDR permittivity time series results, we suggest applying a median filter or similar filters to the TDR data set to smooth the data as well as to remove the outliers, as mentioned above.

2-5-2 Dielectric permittivity to soil water content

Using the geophysical measurement techniques mentioned in this study, we provide the dielectric permittivity of the soil. Point information is provided by the TDR measurements and spatial information along the rhizotubes is provided by the GPR measurements. The dielectric permittivity can be converted to the soil water content. In the past, literature using TDR and GPR data measured within the MR facilities have used the empirical Topp's equation (Topp et al., 1980) and the petrophysical relationships referred to as the complex refractive index model (CRIM) (see Huisman et al. (2003)). The Topp's equation is valid for sandy loam to clay and requires the bulk permittivity of the soil (ε_r) to derive the soil water content (SWC):

$$SWC = -5.3 \times 10^{-2} + 2.92 \times 10^{-2}\varepsilon_r - 5.5 \times 10^{-4}\varepsilon_r^2 + 4.3 \times 10^{-6}\varepsilon_r^3. \tag{2-2}$$

For the petrophysical relationship CRIM, which considers the different dielectric components of the soil (air, soil matrix, and soil water), we obtain

$$SWC = \frac{\sqrt{\varepsilon_r} - (1-\phi)\sqrt{\varepsilon_s} - \phi}{\sqrt{\varepsilon_w} - 1}. \tag{2-3}$$

For the CRIM approach, additional parameters such as the porosity ϕ and the permittivity of the soil matrix ε_s, air ($\varepsilon_a = 1$) and water ($\varepsilon_w = 84$, at 10°C) are necessary. The permittivity of the soil matrix is 4.7 and 4.0 for R_{UT} and R_{LT}, respectively (Robinson et al., 2005). The porosity in the plow layer is considered to be 0.33 and 0.4 for R_{UT} and R_{LT}, respectively. For underlying subsoil, the porosity is considered to be 0.25 and 0.35, respectively (Weihermüller et al., 2007). In particular, for R_{UT}, we recommend using the CRIM relationship instead of the Topp's equation due to the high stone content.

2-5-3 Soil hydraulic parameters

To provide information on, for example, rhizosphere modeling, we provide an overview of the soil hydraulic parameters, which were derived for the MR facilities using different methods. InCai et al. (2017), soil hydraulic parameters (SHP) for both MR facilities can be estimated. These were derived by inverse modeling using soil water content, potential measurements, and root observations of winter wheat. Yu et al. (2020) and Jadoon et al. (2012) estimated the SHP using hydrogeophysical inversion for R_{UT} and R_{LT}, respectively. The SHP for R_{LT} was derived by an inverse parameter estimation using a 1-dimensional CO_2 transport and carbon turnover model, with direct soil sampling and laboratory analysis by Bauer et al. (2011).

2-5-4 Updates

The data corresponding to this paper will be updated regularly on a yearly basis once the analysis is finalized. The updated data can be downloaded from these DOIs:

GPR data: `https://doi.org/10.34731/renq-an61`,
Root data: `https://doi.org/10.34731/jnhr-ke36`,
Root images: `https://doi.org/10.34731/jgd1-tq27`,
Soil sensor data: `https://doi.org/10.34731/rb0q-a208`,
Additional Information: `https://doi.org/10.34731/ke7b-a021`.

2-5-5 Above-ground data

The related above-ground data are managed by the Crop Science group of the Institute of Crop Science and Resource Conservation (INRES), University of Bonn, and will be available upon demand in a future data paper. These data have been partially published in Nguyen et al. (2020),Nguyen et al. (2022a), (2022b) (Nguyen et al., 2022b). The data measured within the EF were carried out by the project partner at INRES.

2-5-6 Code availability

Custom code was used to process the data. For the GPR Data we used MATLAB version: 9.13. 0 (R2022b) to run the codes. The root image processing and soil sensor data is run with Python 3.10.10. Processing codes for the roots images can be found in the Supporting

Material for Bauer et al. (2022) at `https://doi.org/10.34731/pbn7-8g89`. The soil water content data measured with the FDR device was processed using R version 4.0.2.
The custom codes can not be made publicly accessible due to copyright issues, but are available upon request, by contacting the corresponding or senior author.

Chapter 3

Linking horizontal crosshole GPR variability with root image information for maize crops

Abstract

Non-invasive imaging of processes within the soil-plant continuum, particularly root and soil water distributions, can help optimize agricultural practices such as irrigation and fertilization. In this study, in-situ time-lapse horizontal crosshole ground penetrating radar measurements and root images were collected over three maize crop growing seasons at two minirhizotron facilities (Selhausen, Germany). Root development and GPR permittivity were monitored at six depths (0.1 m – 1.2 m) for different treatments within two soil types. We processed these data in a new way that gave us the information of the "trend-corrected spatial permittivity deviation of vegetated field", allowing us to investigate whether the presence of roots increases the variability of GPR permittivity in the soil. This removed the main non-root-related influencing factors: static influences such as soil heterogeneities and rhizotube deviations, and dynamic effects, such as seasonal moisture changes. This trend corrected spatial permittivity deviation showed a clear increase during the growing season, which could be linked with a similar increase in root volume fraction. Additionally, the corresponding probability density functions of the permittivity variability were derived and cross-correlated with the root volume fraction, resulting in a coefficient of determination (R^2) above 0.5 for 23 out of 46 correlation pairs. Although both facilities had different soil types and compaction levels, they had similar numbers of good correlations. A possible explanation for the observed correlation is that the presence of roots causes a redistribution of soil water, and therefore an increase in soil water variability.

Adapted from: Lena Lärm, Felix Bauer, Jan van der Kruk, Jan Vanderborght, Shehan Morandage, Harry Vereecken, Andrea Schnepf, Anja Klotzsche: Linking horizontal crosshole GPR variability with root image information for maize crops. Vadoze Zone Journal e20293, `https://doi.org/10.1002/vzj2.20293`.

3-1 Introduction

The soil-plant continuum is influenced by multiple factors, including soil properties, soil nutrients, root system architecture, precipitation, irrigation, evapotranspiration, fertilization, and agricultural practices. Understanding how these factors interact in crops is beneficial to plant breeders for optimizing the below-ground traits, achieving an optimal yield, efficiently using nutrients and water, as well as resistance to diseases. Both experimental and theoretical studies describe how plant roots can influence soil water variability and how they interact with soil heterogeneity. Spatial variability in crop roots (e.g., row crops) can also lead to soil water variability (Hupet und Vanclooster, 2002; Baroni et al., 2013). However, the presence of crop roots may decrease soil water variability since plants take up water from regions where water is present (Garré et al. 2011; Schlüter et al. 2013). Finally, crop roots and above-ground shoot may also increase variability in water infiltration and in this way impact soil water variability. Crops may funnel the rainfall that is intercepted by the canopy, thus creating local infiltration near the stem and roots. This can alter the soil structure and generate preferential infiltration paths so that more water is found in the presence of roots than without (Bui & Box, 1992; Hupet & Vanclooster, 2005).

Commonly used techniques to investigate the spatial and temporal distribution of roots and the soil water content (SWC) at the field scale mainly focus on investigating either root system architecture or soil properties. In-situ exploration of the root system architecture can be achieved using labor intensive and destructive methods like excavation (Weaver & Bruner, 1926; Böhm, 1978), shovelomics root crown phenotyping (Trachsel et al., 2010), auger sampling, and trench wall methods (e.g., Wasson et al., 2016; do Rosário et al., 2000; van Noordwijk et al., 2001). The main disadvantage of these destructive methods is the lack of repeatability. Non-invasive assessment could be used to optimize irrigation and fertilization, and guide cultivar selection according to local soil conditions (Atkinson et al., 2019). A minimal-invasive alternative is provided by minirhizotron (MR)-techniques, whereby transparent rhizotubes are permanently or temporarily installed within the soil, providing observation windows (e.g., Vamerali et al., 2011; Atkinson et al., 2019; Rewald, 2013; Johnson et al., 2001). These methods are less destructive, providing an option for the long-term monitoring of roots at the plot-scale (e.g., Andrén et al., 1991; Vamerali et al., 2011; Cai et al., 2016; Svane et al., 2019). MR techniques enable the observation of both root distribution and root development during the vegetation period, so that different crop growing seasons can be compared. However, MR facilities are expensive to install and maintain, and root observations are limited to two-dimensional images that provide only a restricted display of the root system. Additionally, different installation techniques can disturb the soil and the rooting zone. This can cause soil smearing, loss of contact between soil and rhizotubes, soil compaction, and the rhizotubes can act as obstacles for root growth (e.g., Rewald, 2013; Guo et al., 2007; Johnson et al., 2001; Maeght et al., 2013).

In the past decades, the field of non-invasive 'agrogeophysics' has been established for in-situ investigation of root systems and the soil below agricultural crops (Garré et al., 2021). In agrogeophysics, methods such as Electrical Resistivity Tomography (ERT), Electromagnetic Induction (EMI) and Ground Penetrating Radar (GPR) are often applied. ERT uses electrodes in the soil to image the electrical resistivity and has been shown to be well suited

for in-situ monitoring of the soil-plant continuum and its structure, in particular soil water content and accordingly, soil water depletion patterns (Cassiani et al., 2016; Garré et al., 2012). Weigand & Kemna (2017; 2018) have sucessfully used spectral electrical impedance tomography (sEIT) to image crop root systems under controlled labratory conditions, but it remains challenging to utilize these methods for in-field root phenotyping. Shanahan et al. (2015) identified a correlation in EMI derived conductivity and SWC in root zones of wheat during soil water depletion dependent on the soil lithology. Additionally, Whalley et al. (2017) considered EMI, ERT and penetrometer measurements to quantify differences in genotypic root activity from soil drying profiles of wheat. Under certain field conditions, such as drought, the resolution of the ERT method is not sufficient to monitor small scale differences in soil water depletion for different crop genotypes (Cimpoiaşu et al., 2020). Further, the usage of fixed, permanently installed ERT lines can limit the monitoring area. EMI can map the apparent electrical conductivity of the soil by using an inductive signal; its lack of dependence upon a galvanic coupling with the soil results in a higher throughput compared to ERT. Both EMI and ERT can be used while crops are still growing (e.g., Shanahan et al., 2015; Whalley et al., 2017; Blanchy et al., 2020a; Blanchy et al., 2020b; Schmäck et al., 2021). For a detailed review on EMI and ERT, refer to Ehosioke et al. (2020) and Cimpoiaşu et al. (2020). When investigating the soli-plant continuum, each of these methods has benefits but also limitations. The EMI and ERT signals are influenced by the electrical conductivity of the soil, which is controlled by the porosity, density, clay content, pore water saturation, temperature, and salinity of the pore water. Hence, deriving the SWC from these methods may be challenging. Furthermore, while EMI is a high-throughput method, allowing large areas to be mapped in a short amount of time, it lacks spatial resolution. Several studies indicate the potential of monitoring root water uptake or soil water distribution. However, the signal is influenced by multiple factors and the spatial resolution is limited.

GPR is a geophysical method that can provide both high levels of spatial resolution and a direct link to SWC (e.g., Klotzsche et al., 2018), making it an ideal tool to monitor SWC as affected by root water uptake. GPR uses electromagnetic wave (EM) propagation in the soil (Jol, 2009) from which one can derive the relative dielectric permittivity (ε_r), and the attenuation of the EM wave can be linked to the electrical conductivity σ when using full-waveform inversion approaches (Klotzsche et al., 2019b). GPR typically uses high frequencies (50 MHz – 3.6 GHz). The depth of penetration depends on the frequency of the antennae, as well as the attenuation of the EM wave, which is related to the electrical conductivity of the soil. This creates a trade-off between spatial resolution and the depth of penetration. The GPR-derived permittivity can be linked directly to SWC by using appropriate empirical or petrophysical relationships (e.g., Steelman & Endres, 2011; Huisman et al., 2003). The contrast in ε_r for different soil components (e.g., dry sand $\varepsilon_s = 6$, air $\varepsilon_a = 1$ and water ε_w 80 (20 °C)) enables the establishment of a link between the ε_r and SWC. Note that depending on the frequency of the antennae and the applied petrophysical relationships, uncertainties can be present in the GPR-derived SWCs. GPR techniques can be divided in two major groups: surface and crosshole GPR. For surface GPR, the EM wave velocity, and therefore the ε_r can be derived from the direct ground EM wave or reflected EM waves (Jol, 2009). When using the reflected EM waves, the derivation of the SWC is dependent on what is known about the soil horizon thickness. In contrast, using crosshole GPR allows a direct link from the EM wave velocity to ε_r (for more details see Klotzsche et al., 2018). In recent years, surface GPR has been used to investigate the soil plant continuum with large

root systems such as tree roots (reviewed in Guo et al., 2013 and Rodríguez-Robles et al., 2013) and shrub roots (e.g., Liu et al., 2020; Liu et al., 2019; Parsekian et al., 2012; Cui et al., 2021). Although some studies investigated the possibility of estimating agricultural root systems (Delgado et al., 2017; Klotzsche et al., 2019a/ Appendix D; Wijewardana & Galagedara, 2010; Liu et al., 2017), the detection and mapping of finer root systems found in crops is still challenging using surface GPR. Individual fine roots of < 0.002 m can only be detected using a higher frequency GPR (1600 MHz antennae) as shown by Parsekian et al. (2012) under laboratory conditions. However, high-frequency applications at the field-scale are difficult because of the high attenuation of the EM waves and the accompanying reduced penetration depth. Note that for most research questions it is more interesting, although also more challenging, to investigate the entire root system and its root system architecture rather than to just consider individual fine roots. This becomes even more challenging to quantify the entire root system and the surrounding soil.

Klotzsche et al. (2019a)/ Appendix D used time-lapse horizontal borehole GPR data to investigate the link between SWC, atmospheric conditions, soil, and crop types over several crop growing seasons. The authors showed that wheat and maize crops have different effects on the GPR signal and hence the SWC distribution. Individual maize crop rows were shown to have a clear impact on the SWC distribution, with a higher SWC below the maize rows in dry soil conditions. Regardless of the findings linking the atmospheric conditions and soil types to SWC distribution over time in the subsurface, open questions remained such as the effect of the roots and crops themselves on the obtained SWC along the horizontal rhizotubes. However, the influence of the wheat root system on the GPR signal could not be identified and hence the root systems of the individual crops and their direct effects on SWC were not estimated.

In this study, we provide multi crop growing season information about spatial variation in both soil water content and root observations. It shows the potential of GPR to non-invasively monitor and characterize the soil-plant continuum of maize crops by linking time-lapse horizontal crosshole GPR measurements and time-lapse root volume fractions derived from root images over the course of three crop growing seasons and within two soil types. Maize was used because of the larger crop row spacing, which provides a higher contrast between the root system and the soil as compared to crops with narrow crop row spacing, such as wheat. Fine root systems are challenging, since GPR acquires information about a volume of soil which includes, e.g., soil, water, roots, nutrients, fertilizer, microbes, and additionally applied agricultural management practices. The linking of time lapse GPR measurements and root images obtained for three crop growing seasons allowed the investigation of whether the presence of roots influences the GPR permittivity. Calculation of the spatial permittivity deviation was done by subtracting the mean of the horizontal permittivity profile for each measurement date from the permittivity distribution. This was done to eliminate the effects due to the 'dynamic' factors caused by different atmospheric conditions during the crop growing season. Blanchy et al. (2020b) used time-lapse EMI and ERT measurements to detect changes in electrical conductivity caused by cover crops, compaction, irrigation, and tillage. They subtracted a reference survey from the time-lapse surveys to remove influences from the static effects, such as soil texture, and then analyzed the dynamic part of the electrical conductivity over time. Similar to this study, the 'static' spatial permittivity deviations that were assumed to be caused by heterogeneities, e.g.,

variability of soil properties, or artifacts, e.g., unknown exact distances between emitting and receiver antennas, were subtracted from the spatial permittivity deviations of vegetated fields to obtain trend-corrected spatial permittivity deviations. The static spatial permittivity deviations were derived from spatial permittivity deviations measured in bare-field soil. These trend-corrected spatial permittivity deviations of the vegetated fields are a measure of the soil water or permittivity variability that is generated by the presence of roots. In this study, the key hypothesis is that spatial variation in root volume fraction can be linked with spatial variability in GPR permittivity. To test this hypothesis, we used repeated crosshole GPR measurements and root observations within minirhizotrons. First, the experimental setup is described, which is followed by a description of the root image measurement and data analysis. Next, the GPR measurements and processing steps are discussed. The time-lapse root data are then shown, followed by the time-lapse GPR data. Finally, a link between the RVF and GPR permittivity data variability is investigated.

3-2 Experimental setup

3-2-1 Minirhizotron facilities

Two MR facilities were present at the test site within the TERENO (TERrestrial ENvironmental Observatories) Eifel-Lower Rhine observatory close to Selhausen (North Rhine-Westphalia, Germany) with the geographic coordinates 50°52'N, 6°27'E. They were geologically situated within fluvio-glacial sediments of the Rur river catchment (Bogena et al., 2018). Various studies have investigated the Selhausen test site using geophysical measurement techniques (e.g., Weihermüller et al., 2007; Bauer et al., 2011; Jadoon et al., 2012; Brogi et al., 2019).

At the Selhausen test site, different river deposits were present. The deposits could be observed due to a morphological slope of 4° from the upper terrace down to the lower terrace. Sediments at the upper terrace consisted of gravely, partly stony, and silty sand, whereas the lower terrace consisted of a silty, sandy, and slightly gravely loam with significant clay content, which gave the sediments of the lower terrace a firm consistency. The fluvio-glacial sediments were covered by a plow layer with a thickness of 20 - 30 cm, for both terraces.

The MR facilities were situated in both the upper and lower terrace such that each MR facility was located in a river deposit where different soil properties were present, (see Cai et al., 2016). The upper (R_{UT}) and lower (R_{LT}) MR facilities each consisted of three plots (Figure 3-1a), which allowed the comparison of different agricultural treatments and different soil properties under the same atmospheric conditions. In each plot, three rhizotubes of 7 m length were installed at six different depths, between 0.1 m and 1.2 m, below the surface. Rhizotubes were laid parallel to one another other with a horizontal distance of 0.75 m. It is important to note that the depths of the rhizotubes varied between the individual crop growing seasons due to soil erosion and soil compaction after tillage and seedbed preparation (depths were measured every season). One end of each rhizotube was present in an access trench from which the measurements were performed. In the lower facility, R_{LT}, tubes were installed in horizontally drilled boreholes and deviations could be up to 0.10 m. Because of the high stone content at R_{UT}, drilling horizontal boreholes was not possible (Cai et al., 2016). Instead, the soil was excavated in layers and refilled

during the installation of the rhizotubes. The deviations in horizontal distance between R_{UT} rhizotubes were less than 0.02 m. Additionally, in order to make the measurements within the rhizotubes, various sensors were installed within the soil to measure the soil water potential (tensiometers & MPS-2 sensors manufactured by UMA GmbH, Germany, Decagon Devices, Inc., US, respectively), soil water content (time domain reflectometer (TDR) in-house production), and soil temperature (MPS-2 sensors). Above-ground at R_{LT} there was a monitoring system for sEIT installed 3.5 m away from the trench (Weigand et al., 2022).

The MR facilities provided ideal circumstances to study the different components of the soil-plant continuum under field conditions and included data from different above- and below-ground measurement techniques, e.g., semi 4D geophysical data and information from root images. The below-ground data acquired within the MR facilities between 2016 and 2021 can be found in Lärm et al., 2023/ Chapter 2. The below-ground geophysical measurements were analyzed by Cai et al. (2016), Klotzsche et al. (2019a)/ Appendix D, Yu et al. (2020/ Appendix F; 2021), and Weigand et al. (2022). Other soil and root measurements were analyzedd by Cai et al. (2017), Cai et al. (2018), and Morandage et al. (2021). Above-ground crop measurements are described by Nguyen et al. (2022).

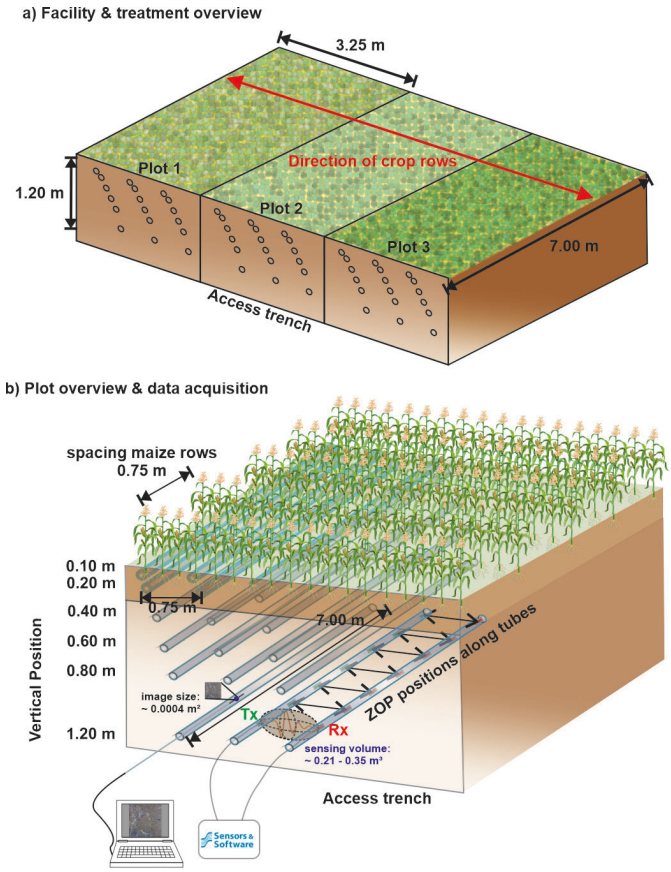

Figure 3-1: a) Overview of the minirhizotron (MR) facilities. At each of the plots, different agricultural treatments were applied for the different crop growing seasons. The direction of the crop rows was perpendicular to the direction of the rhizotrubes (red arrow). The measurements were carried out within an access trench. b) Overview of one representative plot within the MR facilities with the horizontal crosshole ground-penetrating radar (GPR) zero-offset-profiles (ZOP) measurement setup. Transmitter and receiver antennae are labeled Tx and Rx, respectively. Root images were acquired using a camera system attached to an index handle.

3-2-2 Experiment design and agricultural practices

In the time since the MR facility was installed, different wheat and maize cultivars have been sown for various crop growing seasons (e.g., Morandage et al., 2021 and Klotzsche et al., 2019a/ Appendix D). Agricultural treatments, such as sowing density, sowing date, crop cultivars, and surface water treatment (sheltered, natural & irrigated) vary for the different crop growing seasons. This study considered three seasons (2017, 2018 & 2020) in which maize (Zea mays) was sown. Different agricultural practices, which included irrigation, sowing density, and varying cultivars were simultaneously carried out for both MR facilities (overview in Table 1). For the crops growing seasons 2017 and 2018, the cultivar cv. zoey was sown on all three plots. A different sowing date (R_{UT}) and sowing density (R_{LT}) were chosen for Plot 1 in 2018. For the 2020 crop growing season, two different cultivars, cv. stacey and cv. sunshinos, were planted on the outer plots (Plot 1 & Plot 3), respectively. For Plot 2, a mixture of the two cultivars with alternating rows was sown. The spacing between the individual maize crop rows was 0.75 m. When a higher sowing density was applied, crop row spacing was kept constant and the interrow distance was decreased. During the 2017 and 2018 growing seasons, an irrigation treatment was applied. While Plot 1 and Plot 2 were rain-fed, Plot 3 was irrigated on a regular basis throughout the growing seasons. During the 2018 crop growing season, crops on Plots 1 and 2 showed severe stress symptoms and emergency irrigation was necessary on a few occasions to ensure the continuation of the experiment. For the 2020 growing season, additional irrigation due to stress conditions was carried out equally on all three plots. The individual irrigation volumes can be found in the Supplemental Material, Appendix A-3 Table A-3.1 and A-3.2. Additionally, Table 3-1 provides information about the sowing, harvest dates, the dates for the different maize vegetation stages, and measurement times. Prior to the maize crop growing seasons, winter wheat had been sown on the MR facilities. The last winter wheat crops were harvested on 26.07.2016 (Klotzsche et al. 2019a/ Appendix D), with the soil laying fallow for 9.5 months without crop cover. Due to changes in project funding, in 2019 a flower meadow was planted but not further investigated.

Table 3-1: Overview of the crop growing seasons used in this study, including the different agricultural practices, the maize growing stages, and number of measurement days.

Property	Year	2017		2018		2020
	MR-Facility	R_{UT}	R_{LT}	R_{UT}	R_{LT}	R_{UT}
Treatment	Plot 1	Rain-fed	Rain-fed	Rain-fed	Rain-fed	Irrigated
	Plot 2	Rain-fed	Rain-fed	Rain-fed	Rainfed	Irrigated
	Plot 3	Irrigated	Irrigated	Irrigated	Irrigated	Irrigated
Cultivar	Plot 1					Zea mays L. 'Sunshinos'
	Plot 2	Zea mays L. cv. 'Zoey'		Zea mays L. cv. 'Zoey'		Mixture
	Plot 3					Zea mays L. 'Stacey'
Sowing Density [Plants m^{-2}]	Plot 1				16	
	Plot 2	10.66		10.66	10.66	10
	Plot 3					
Sowing	Plot 1			22.05.2018		
	Plot 2	04.05.2017		08.05.2018	08.05.2018	29.04.2020
	Plot 3					
Emergence	Plot 1			26.05.2018		
	Plot 2	09.05.2017		14.05.2018	13.05.2018	12.05.2020
	Plot 3					
Tasseling	Plot 1			21.07.2018		
	Plot 2	09.07.2017		10.07.2018	09.07.2018	12.07.2020
	Plot 3					
Silking	Plot 1			23.07.2018		
	Plot 2	14.07.2017		12.07.2018	11.07.2018	15.07.2020
	Plot 3					
Harvest	Plot 1			02.09.2018		
	Plot 2	12.09.2017		22.08.2018	22.08.2018	23.09.2020
	Plot 3					
Number of GPR meas.		22	21	22	19	9
Number of Root Images meas.		9	9	7	6	2

3-3 Root image measurements and processing

The root images were obtained within the rhizotubes using a digital camera on an aluminum index handle, see Figure 3-2b. Two different camera systems were used. For the 2017 data set the Bartz system (Bartz Technology Corporation) was used and for the 2018 and 2020 data sets the VSI system (Vienna Scientific Instruments GmbH). Due to time constraints, images were taken only at certain locations along the rhizotubes. The images taken from one rhizotube were composed of four groups of five images. The between-group spacing was 0.93 m (Figure 3-2a) and the within-group spacing varied between 0.08 m - 0.12 m. For the time-lapse data set, 40 images were captured from each rhizotube. This consisted of twenty images at an angle of 80° from the left side and twenty at an angle of 80° from the right side (Figure 3-2b). For comparison, the GPR-ZOP spatial measurement range is indicated in Figure 3-2a. In addition to the time-lapse root images, which were obtained over the three growing seasons 2017, 2018 and 2020, a continuous root image data set was collected during the 2020 growing season. This data set consisted of continuous sequences of root images over a length of 4 m in the rhizotubes (see 3-2a). These measurements required approximately 7-fold more time than the regular root image measurements.

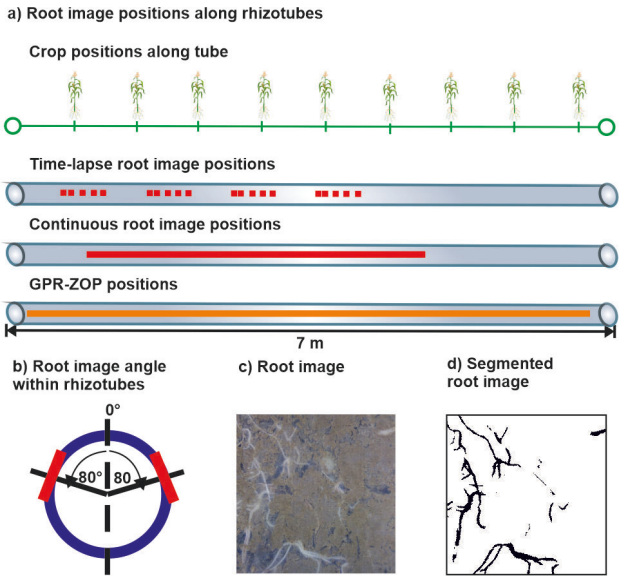

Figure 3-2: a) Root image locations within rhizotubes, with the location of the aboveground crop rows in comparison to the image locations. The upper rhizotube illustrates the positions of the time-lapse root images, the middle rhizotube illustrates the positions of the high spatially resolute root image measurement in 2020, the lower rhizotube illustrates the section where the ground-penetrating radar (GPR) zero-offset-profiles (ZOP) measurements were acquired. b) Root image angles within the rhizotubes, c) representative root image, d) corresponding segmented root image after an automatic image analysis pipeline, developed by Bauer et al. (2022)/ Appendix E.

The root image data set acquired over the 2017 crop growing season was briefly discussed in Morandage et al. (2021). For this study, the automatic image analysis pipeline developed by Bauer et al. (2022)/ Appendix E was used to derive information from the root images (Figure 3-2c). The pipeline consists of the following processing steps. i) Pre-processing of the images, which includes renaming, distortion correction, cropping, and resizing. While resizing, the dimensions of the images were changed to 0.0165 m by 0.0235 m and 0.02 m by 0.02 m for the Bartz and VSI camera system, respectively, resulting in a root image size of 0.0004 m^2 and adds up to an area of 0.016 m^2 per rhizotube. For the continuous root image over 4m, the image sizes of 0.02 m by 0.02 m were made every 0.02 m, covering an image area of 0.16 m^2. ii) Applying an automated image segmentation using RootPainter (Smith et al., 2020), performed by a pre-trained neural network model; and iii) converting the segmented images to binary images (Figure 3-2c), from which the root traits were extracted by RhizoVision Explorer (Seethepalli et al., 2021) for each individual root image.

The root volume per image was calculated by RhizoVision Explorer using the root length and the root diameter. To compare the root traits with the GPR measurements, the root volume fraction [%] (RVF) was used. This was defined as the volume percentage of

space occupied by the roots in a respective soil volume, see Equation 3-1. The respective soil volume was derived by assuming that the roots visible in the image were displaced by the rhizotube and would have otherwise grown within a volume that was equal to the image area times the outer rhizotube radius (0.032 m), see Equation 3-2 (e.g., Cai et al., 2017; Morandage et al., 2021). This resulted in a sensing volume (SV) of 1.24·10-5 m^3 and 1.28·10-5 m^3 per image, for the Bartz and VSI camera systems respectively. Accordingly, the RVF was calculated by using the RV and the respective soil volume V_{soil}

$$RVF = \frac{RV}{V_{soil}}, \tag{3-1}$$

while using

$$V_{soil} = L \cdot W \cdot r_{rhizotubes}, \tag{3-2}$$

newline where L is the length of the image, and W is width of the image. To compare the RVF data with the GPR measurements and taking into consideration the different V_{soil} of the methods, the mean RVF of four root image windows per position along the rhizotubes was used. This refers to images on either side of the two neighboring rhizotubes, from where the transmitting antenna (Tx) and receiver antenna (Rx) are inserted. Using four root images increases the image area to 0.001551 m^2 for each position along the rhizotube for the Bartz and to 0.0016 m^2 for the VSI camera system. Note that images in both directions were used and not only in the GPR measurement direction to account for the scale difference between the size of the root images and the SV of the GPR measurements. The root length density (RLD) was also calculated for 2017, as it is a common parameter in rhizosphere science, and an overview in comparison with the RVF can be found in Table 3-2. The values for the years 2018 and 2020 can be found in the Supplementary Appendix Tables A-3.1 and A-3.2.

Table 3-2: Comparison of the root volume fraction (RVF) and the root length density (RLD) as minimum, maximum and mean for R_{UT} and R_{LT} in 2017, respectively.

	$\mathbf{R_{UT}}$		$\mathbf{R_{LT}}$	
	RVF	RLD	RVF	RLD
	[%]	[cm cm^{-3}]	[%]	[cm cm^{-3}]
Minimum	0.0000005	0.0006	0.000001	0.001
Maximum	0.36	1.84	0.75	2.1
Mean	0.01	0.103	0.042	0.25

In 2017, photographs were taken at different crop growth stages until the crops reached the reproductive stage to illustrate crop development at both facilities. A description of the individual growth stages is included in Figure 3-3. From this the growth stages of the crops both above- and below-ground can be recognized. For Plot 3 in R_{UT}, an increased height of about 20 cm can be observed in Figure 3-3a for 29.06.2017, shown behind the line indicated by the two red arrows. Overall, the crops at R_{LT} performed visibly better than at R_{UT}. A similar trend can be seen in the root images for the 27th of July 2017 (Figure 3-3c). While a greater number of thicker roots are visible for deeper positions in R_{UT}, the roots in R_{UT} are thinner and less distributed in the deeper soil. Ritchie et al. (1966) describes that the

optimal development of maize is only dependent on nutrient uptake after the dough stage (reproductive stage 4), meaning that at this point maize crops are expected to require less water. Previous to this stage, the development of the yield (number, size, and weight of the maize ears) is highly dependent on both the soil water and nutrient availability.

b) Vegetative stages of maize

	Vegetative (V) Stages						Reproductive (R) Stages		
	VE	V1	V3	V6	V9	VT	R1	R2 - R5	R6
Growing Stage	Emergence	First Leaf	Third Leaf	Sixth Leaf	Ninth Leaf	Tasseling	Silking	R2 - Blister R3 - Milk R4 - Dough R5 - Dent	Maturity
Days after Emergence (after Hanway, et al., (1966))		7	12	21	30	56	66	R2 - 78 R3 - 92 R4 - 102 R5 - 114	130
Date in 2017	09.05	16.05		31.05	07.06	09.07	14.07	27.07 (R2)	16.09
Date in 2018	26.05* 14.05	02.06* 21.05	07.06* 26.05	16.06* 04.06	25.06* 13.06	21.07* 09.07	31.07* 19.07	12.08* (R2) 31.07 (R2)	03.10* 21.09
Date in 2020	12.05	19.05	24.05	02.06	11.06	07.07	17.07	29.07 (R2)	19.09

c) Root images of the 27.07.2017

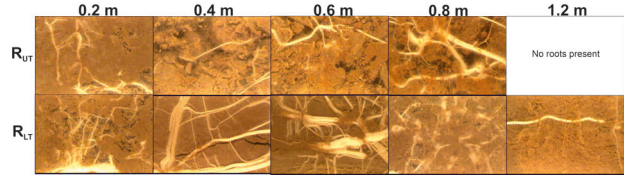

Figure 3-3: a) Images of both minirhizotron (MR) facilities during the 2017 crop growing season. (b) Overview of the maize vegetation stages and the corresponding dates for the crop growing seasons. (c) Root images of July 27, 2017 for different depths for both MR facilities. *For Plot 1 at R_{UT} , a later sowing date is applied. Hence, the respective dates for the different crop growing stages vary.

3-4 GPR measurements and processing

During the three growing seasons under study, weekly time-lapse GPR measurements and discontinuous time-lapse root images were acquired. The time-lapse GPR data were acquired using the crosshole Zero-Offset-Profiling (ZOP) measurement technique, employing a 200 MHz PulseEKKO borehole system manufactured by Sensors & Software. For ZOP measurements, Tx and Rx were located within adjacent rhizotubes, see Figure 3-1b. Tx emitted an EM wave through the soil and the signal was recorded by Rx. Tx and Rx were moved in simultaneously in 0.05 m increments over the length of the rhizotubes. For time-zero calibration of the crosshole GPR data, wide-angle reflection and refraction (WARR) measurements in air were performed within the access trench. In this procedure, Tx was fixed, and Rx moved in 0.1 m increments over the 6 m distance. In total, over all three growing seasons, 53 datasets were obtained for R_{UT} and 40 for R_{LT}. For each measurement day, the permittivity values of the GPR measurements were estimated every 0.05 m along 5 m of the horizontal borehole length, resulting in 100 GPR traces per measurement depth. Only data between 2.5 m and 6 m were considered because GPR data from close to the access trench where the soil sensors were located were not reliable and were therefore excluded. The 1.2 m depth in Plot 3 of R_{LT} was not measured due to a broken rhizotube, and a data gap is present between 2.8 m and 3.3 m along the rhizotubes at 0.2 m depth due to the installed sEIT line (Weigand et al., 2022), which affected the GPR measurements.

To estimate the relative dielectric permittivity (ε_r) from horizontal GPR crosshole ZOP measurements, several processing steps are required: i) apply a dewow filter, ii) correct for time-zero, and iii) estimate the first signal breaks (for more details see Klotzsche et al., 2019a/ Appendix D). After finalizing these steps, picked travel times of the EM wave between the adjacent rhizotubes were obtained for each ZOP position. Because of the known horizontal distance (0.75 m) between the rhizotubes, using the picked travel times allowed calculation of the EM velocity for each ZOP position. Considering low-loss and non-magnetic soils (Jol, 2009), the EM velocity could be transformed into the relative dielectric permittivity ε_r of the bulk material with,

$$v = \frac{c}{\sqrt{\varepsilon_r}} \tag{3-3}$$

where

$$\varepsilon_r = \frac{\varepsilon}{\varepsilon_0}, \tag{3-4}$$

c is the speed of light (0.3 m/ns), is the effective permittivity of the bulk material, and ε_0 is the permittivity of free space with 8.85·10-12 F/m. Note that from this point forward when permittivity is mentioned in the text, it refers to relative dielectric permittivity ε_r.

To obtain SWC from the relative permittivity, a petrophysical or empirical relationship is needed. One of the most common petrophysical volumetric mixing models is the Complex Refractive Index Model (CRIM) (Huisman et al., 2003). In this, it is assumed that the soil system consists of different phases, with different dielectric properties and volume fractions. The general formula for a system with n dielectric components is expressed by

$$\varepsilon^a = \Sigma_{i=1}^{n} \chi_i (\varepsilon_i)^\alpha \tag{3-5}$$

where ε^a is the bulk permittivity of the mixed system and α is a fitting exponent, which accounts for the geometry of the system. χ_i and ε_i indicate the volume fraction and permittivity of the i-th component of the system, respectively. Commonly, three-phase soil systems are used, which include soil, water, and air. Using $\alpha = 0.5$ for the geometry factor and $\varepsilon_a = 1$ for the permittivity of air, Equation 3-5 can be reformulated for a three-phase system to

$$\varepsilon_r = ((1-\phi)\cdot\sqrt{\varepsilon_s} + \theta\cdot\sqrt{\varepsilon_w} + (\phi-\theta))^2, \tag{3-6}$$

where ϕ is the soil porosity. ε_s and ε_w represent the permittivities of the soil (solid phase) and water components of the system, respectively. θ represents the volumetric SWC. Rearranging Equation 3-6, the SWC for the three-phase system could be calculated using:

$$\theta = \frac{\sqrt{\varepsilon_r} - (1-\phi)\sqrt{\varepsilon_s} - \phi}{\sqrt{\varepsilon_w} - 1}. \tag{3-7}$$

Like Klotzsche et al. (2019a)/ Appendix D, an ε_w= 84 at 10°C was used, which represents the mean soil temperature obtained from the soil temperature sensors. ε_a was 4.7 and 4.0 for the R_{UT} and R_{LT}, respectively. The SV of the GPR data, described by the Fresnel volume, is an elongated rotational ellipsoid where the foci are at the locations of Tx and Rx, see Figure 3-1. The size of the volume depends on the spacing between the antennae, center frequency, and the bulk permittivity of the soil. The SV for intermediate soil water content conditions for R_{UT} was approximately 0.35 m^3 (see Klotzsche et al. 2019a/ Appendix D). Note that the SV for the GPR data was significantly larger than the investigated soil volume to obtain the RVF values, such that a direct comparison was not possible. In addition, the GPR-derived permittivity values are influenced by the soil, the water content of the soil, and the water content of the roots. The separate contribution of each factor cannot be disentangled with this type of measurement setup. Since the RVF was very small (see Table 3-2) and the dielectric permittivity of the soil particles was small compared to that of water, the main contribution to the bulk soil permittivity came from the soil water (e.g., Cassidy, 2009). Additionally, uncertainties of the solid phase are higher for dry conditions with a low saturation of the soil. Therefore, in the following, the obtained relative permittivity from the measured GPR signals and its spatial and temporal variability is discussed.

3-5 Spatial and temporal variability of the soil-plant continuum

Root images and crosshole GPR data were acquired, when possible, on a weekly or biweekly basis over three crop growing seasons. The total number of measurements per crop growing season is shown in Table 3-1. For the GPR dataset, the information from the 0.1 m deep rhizotubes was excluded, mainly due to the interference of the critically refracted air wave with the direct wave. The GPR traces at a depth of 0.2 m also shows an impact of this interference, particularly for dry conditions. However, the uncertainties remain in an acceptable range and the data can still be used for further analysis (Klotzsche et al., 2019a/ Appendix D, Yu et al. 2021/ Appendix F & F). Since the GPR has a larger SV than the root images, the data acquired from the root images at a depth 0.1 m is included.

3-5-1 Time- lapse root data

From the results of the automatic image analysis pipeline (Bauer et al., 2022/ Appendix E), the RVF information was derived for each rhizotube for both MR facilities. For each plot, the mean RVF was calculated at each depth, taking into consideration both rhizotubes, which were also used for the GPR measurements. In some cases where unrealistic RVF values occurred due to changes in image settings and acquisition errors, data needed to be excluded.

The curves for the root development over time with the root arrival for 2017 are shown in Figure 3-4, where the RVF is plotted for all three plots for R_{UT} and R_{LT} as function of time. Depths of 1.2 m were only measured late in the crop growing season, due to the absence of roots in the earlier vegetation stages. For most of the root arrival curves an increase in RVF over time was observed, where a strong increase in RVF was mostly present around the date of tasseling and silking. During tasseling, the male flowers start to shed their pollen. This takes place when the plant has reached its full height. Silking is the emergence of silks from the ear shoot of the female maize flower. At the end of the crop growing season, up to the harvest date, there was a significant decrease in RVF. In general, R_{LT} showed higher RVF than R_{UT}. For R_{UT} the maximum RVF was below 0.08% and for R_{LT} the maximum RVF was 0.15%, see Figure 3-4. In addition, there were considerable differences in root development at the different depths, both between the MR facilities and between individual plots. The highest RVF for both R_{LT} and R_{UT} were found in Plot 1, at 0.8 m and 0.1 m, respectively. The next highest RVF obtained in R_{UT} was at Plot 3, followed by Plot 2 and for R_{LT} Plot 2 followed by Plot 3. The maximum rooting depths for both MR facilities in the 2017 crop growing season and the results obtained using an additional excavation measurement showed similar results (see Klotzsche et al., 2019a/ Appendix D) and Morandage et al., 2021). In these studies, a maximum rooting depth of 1 m for R_{UT} and of 1.40 m for R_{LT} was detected, which exceeded the maximum observation depth for R_{LT}. Figure 3-5 shows the same RVF data as Figure 3-4 but plotted as function of depth, such that the depth distribution is both more clearly visible and not median-filtered over time. A comparison of the three individual plots of R_{UT} and R_{LT} reveals significant differences. The natural/rain-fed Plot 1 and Plot 2 at R_{UT} had maximum values at a depth of 0.1 m and 0.6 m, although for Plot 1 the maximum value at depth 0.1 m was significantly larger than at depth 0.6 m. Note that the axis for the 0.1 m depth was significantly larger than the other depths. At R_{LT}, the natural/rain-fed Plot 1 showed two maxima in RVF at depths of 0.8 m and 0.4 m, whereas for Plot 2 a maximum was present only at a depth of 0.8 m. Note that the axis range for Plot 1 was again significantly larger than for Plot 2 and 3. The irrigated Plot 3 showed a local maximum in RVF at a depth of 0.4 m for R_{UT} and at depths of 0.1 m and 0.4 m for R_{LT}. The same analysis was carried out for 2018 and 2020, and the results can be found in the Supplemental Material, Appendix A-3 Figures A-3.1 to A-3.3, respectively. The depth distribution of 2018 was similar to that of 2017, and what few differences were observed were possibly related to differences in measurement dates. A large difference was visible for R_{UT} Plot 3, where the highest values in RVF were present at depths of 0.4 m and 0.6 m. During the 2020 growing season, only two measurements at R_{UT} were possible, and therefore no comparison was made.

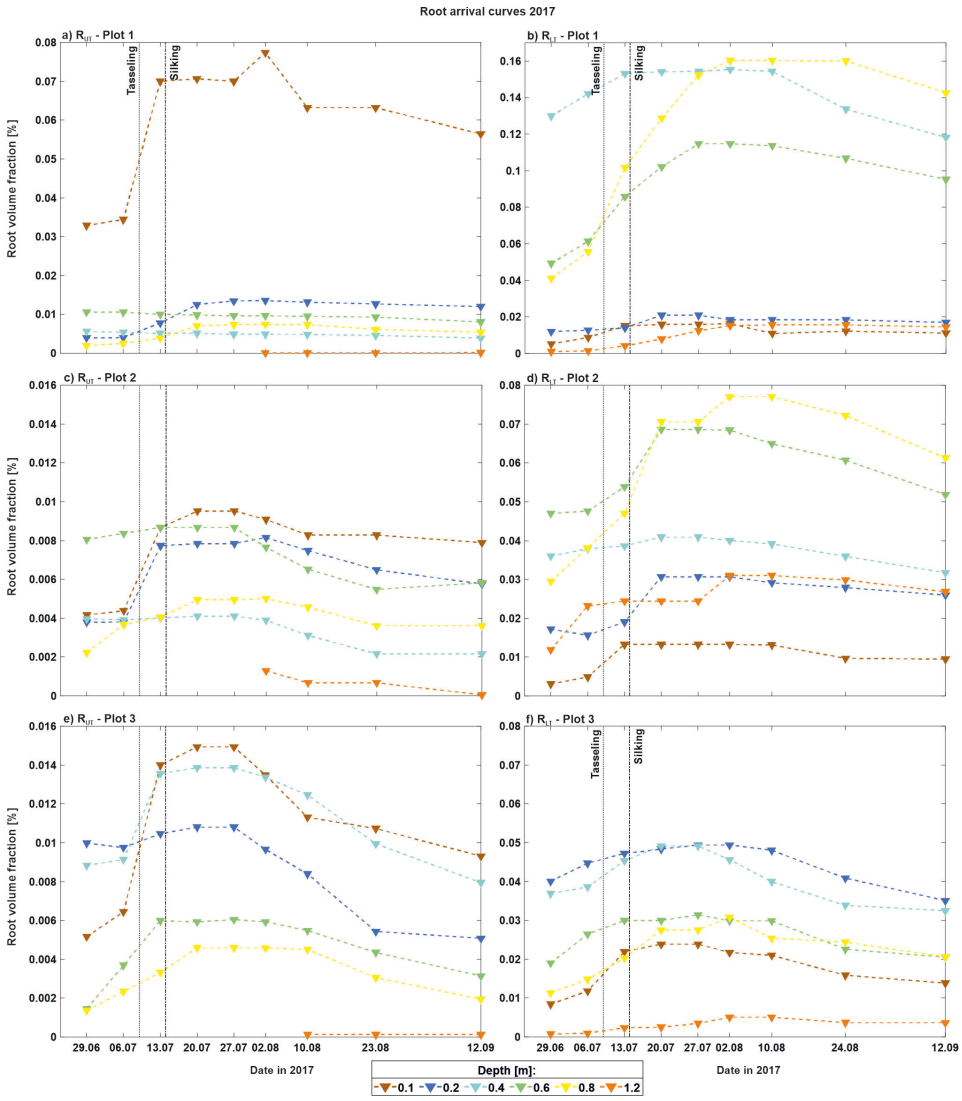

Figure 3-4: Root arrival curves in root volume fraction (RVF) for 2017 for the three plots for R_{UT} and R_{LT}, left and right, respectively. The root images were measured within the same rhizotubes where the ground-penetrating radar (GPR) antennae was placed. The colored triangles represent the RVF over time, which were median-filtered over 3 measurement days. The colors indicate the different depths. Tasseling and silking are indicated by the vertical lines. Note the different y-axes scales for Plot 1 in comparison to Plots 2 and 3.

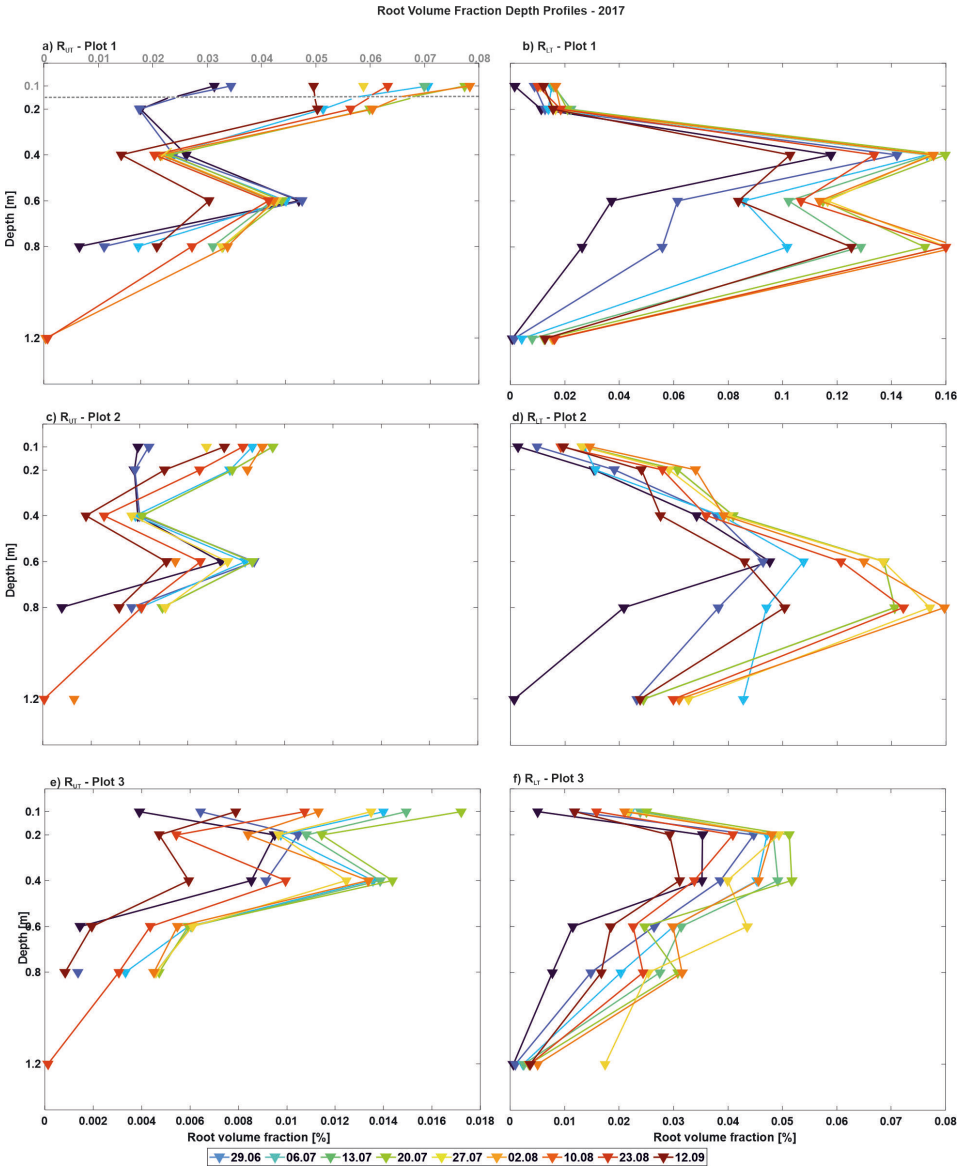

Figure 3-5: Root volume fraction (RVF) depth profiles of 2017 for R_{UT} a), c), and e) and R_{LT} b), d), and f). The colored triangles represent the RVF values for the different depths, where the different colors represent the measurement date over the crop growing season. Note the different x-axis for R_{UT} and R_{LT} below all plots and a separate axis for Plot 1 of R_{LT} and a depth 0.1 m of Plot 1 of RUT shown on top of the figure.

3-5-2 Time-lapse GPR data

For each measurement day, the permittivity values of the GPR measurements were estimated for each position (every 0.05 m) along the horizontal rhizotubes for five depths and three plots/treatments. The obtained permittivity values were then plotted as horizontal permittivity profiles between the rhizotubes. Figure 3-6 shows semi-three-dimensional images for a 1.2-m-depth by 9-m-width by 3.5-m-length soil volume, obtained for 26.04.2017 and 27.07.2017, which show the horizontal permittivity profiles before and during the maize growing season.

Overall, the permittivity of R_{LT} indicated higher values than R_{UT}, which was related to the porosity ϕ and soil type differences of both MR facilities. While the topsoil of R_{UT} had an approximate porosity of $\phi = 0.33$ and the subsoil of $\phi = 0.25$, the topsoil and subsoil of R_{LT} had a porosity $\phi = 0.4$ and $\phi = 0.35$, respectively. Additionally, at R_{LT} a shallower water table depth was present (seasonal fluctuations between $3 - 5$ m below the surface, see Jadoon et al. (2012)). Generally, the permittivity increased with increasing depth for R_{UT} and R_{LT}. Comparing the two measurement days, the permittivities before the growing season were generally slightly higher than during the season for both MR facilities, which was related to the weather conditions. To better understand the seasonal changes, the mean permittivity per depth over time was compared with the weather data (Figure 3-7 and Figure 3-8 for R_{UT} and R_{LT}, respectively).

Similar to the findings from the root arrival curves and RVF depth distribution (Figure 3-4 & Figure 3-5), there was a difference in permittivity between the individual plots. For R_{UT} a permittivity gradient between the three plots was present (Figure 3-6a and b), with Plot 1 having the lowest permittivity values, followed by Plot 2 and Plot 3. This was particularly evident before the growing season (see gray frames in Figure 3-7). The difference was particularly distinct at depth 0.2 m (plow layer), while the irrigated Plot 3 showed the highest permittivity values. Although Plot 1 and Plot 2 received the same surface water treatment, Plot 1 showed lower permittivity values at all depths.

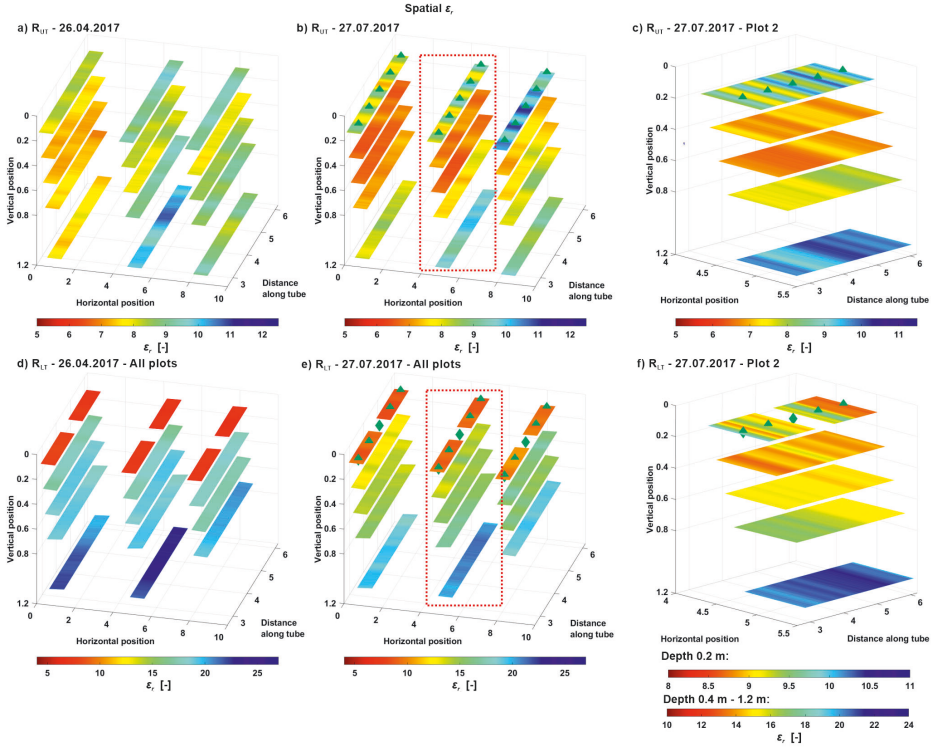

Figure 3-6: Semi-3D plots of horizontal permittivity profiles for 2 days during the crop growing season 2017. Permittivity results for R_{UT} and R_{LT} for the dates April 26, 2017, and July 27,2017, for a) and b) and d) and e), respectively. The different colors represent the permittivity values along the rhizotubes, the green diamonds indicate the aboveground location of the maize crop rows, and the red dashed rectangles indicate two zooms for Plots 2 shown in c) and f) with an adjusted color bar. Note that for April 26, 2017, no crops were sown, while for July 27,2017, maize crops were present.

Additionally, it can be assumed that because of the larger SV of the GPR measurements, information acquired below a depth of 1.2 m included naturally deposited soil. Similar to R_{UT}, R_{LT} had a visible permittivity gradient between the individual plots, with Plot 1 showing the lowest permittivity values, and Plot 3 the highest (Figure 3-6 and Figure 3-8b & d). Additionally, this gradient from lower to higher permittivity values was equally noticeable over all depths. In contrast to R_{UT}, the 0.2 m depth had the lowest permittivity values, compared greater depths, and the permittivity increased with increasing depth. The horizontal permittivity variations were smaller compared to the vertical variation for both MR facilities (Figure 3-6c and f). The areas along the rhizotubes with higher permittivity values in depths of 0.2 m coincided with the spatial above-ground location of the maize crop rows, indicated by green diamonds (see also Klotzsche et al., 2019a/ Appendix D). These patterns were more distinct for R_{UT} than for R_{LT}, caused by the higher permittivity changes for R_{UT}. Greater depths did not show these clear permittivity patterns, although there were variations along the rhizotube with smaller differences. The semi three dimensional plots of winter wheat in Klotzsche et al. (2019a/ Appendix D), did not show the same patterns within the horizontal permittivity profiles.

To investigate a possible link between permittivity variations and atmospheric changes, comparisons between the mean permittivity values per day and depth, and the daily precipitation and temperature for both MR facilities were made (Figure 3-7 and Figure 3-8). Similar to the findings observed in Figure 3-6, it was found that along the rhizotubes that the mean permittivity: i) was higher for R_{LT} than for R_{UT}, ii) mostly increased with increasing depth, except for at a depth of 0.2m for R_{UT}, where the highest mean permittivity was observed during periods with high precipitation and irrigation events, and iii) showed dependence on the weather conditions, where high permittivity values were observed during periods with high precipitation/irrigation and lower temperatures. Presumably the responses to changes in the weather conditions were different due to the different soils of the MR facilities. While for R_{UT} there was a faster response of the mean permittivity at all depths, R_{LT} exhibited a delayed response with increasing depth. As previously mentioned, this was likely caused by the higher porosity of the fine grained soil, and for R_{LT}, perhaps additionally due to the closer distance of the ground water table and the associated capillary rise (see Klotzsche et al., 2019a/ Appendix D). Interestingly, for R_{LT} a trend was observed that did not seem to correlate with the weather conditions. After the silking and tasseling, a steady decrease in mean permittivity at all depths was apparent, even in correlation with precipitation events when temperatures did not change. The lack of effects of precipitation events was likely because the increase in SWC was counteracted by an increased root water uptake. This effect was less recognizable for R_{UT}. The same analysis was carried out for 2018 and 2020, and results confirming these findings can be found in the Supplemental Material, Appendix A-3 Figures A-3.4 and A-3.6, respectively.

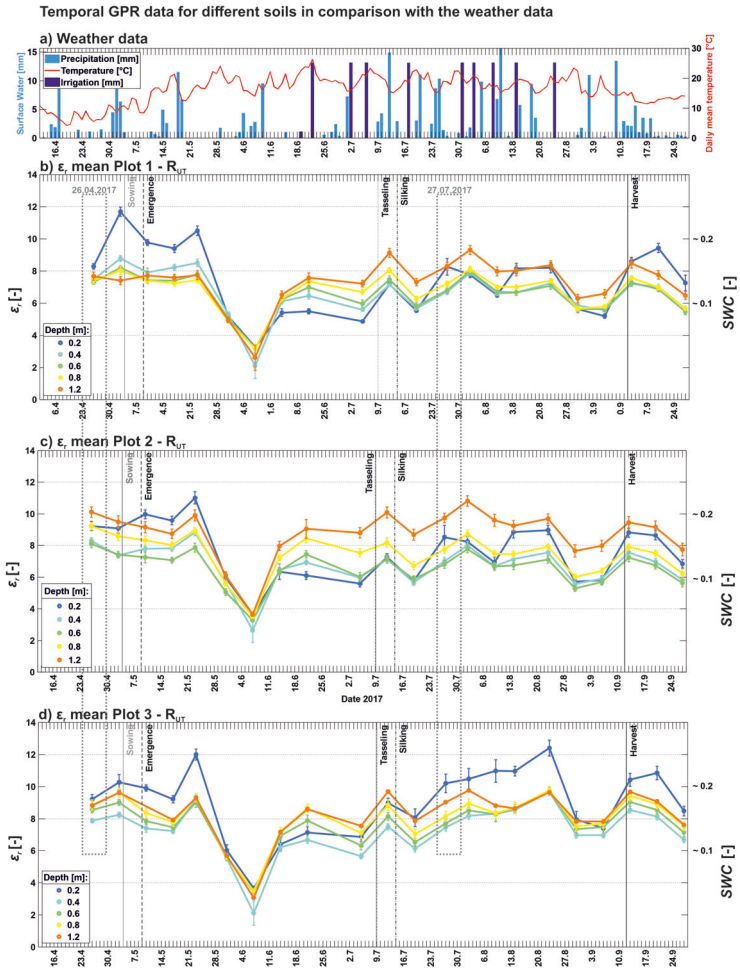

Figure 3-7: Comparison of the weather data and permittivity for R_{UT} during the 2017 crop growing season. a) Weather data: the solid red line represents the daily temperature values, and the light blue bars represent the daily precipitation values. The dark blue irrigation values are only valid for Plot 3. Mean permittivity per depth for Plots 1–3 are shown in b) and d). The colored circles with the error bars indicate the permittivity mean along the rhizotube with its standard deviation as error bars. The colored solid lines connect the individual measurement days. The horizontal lines represent the dates for the vegetation stages and sowing and harvest dates. For convenience, the approximate soil water content (SWC) values were added on the right-hand axis for b) and d) using the three-phase complex refractive index model (CRIM).

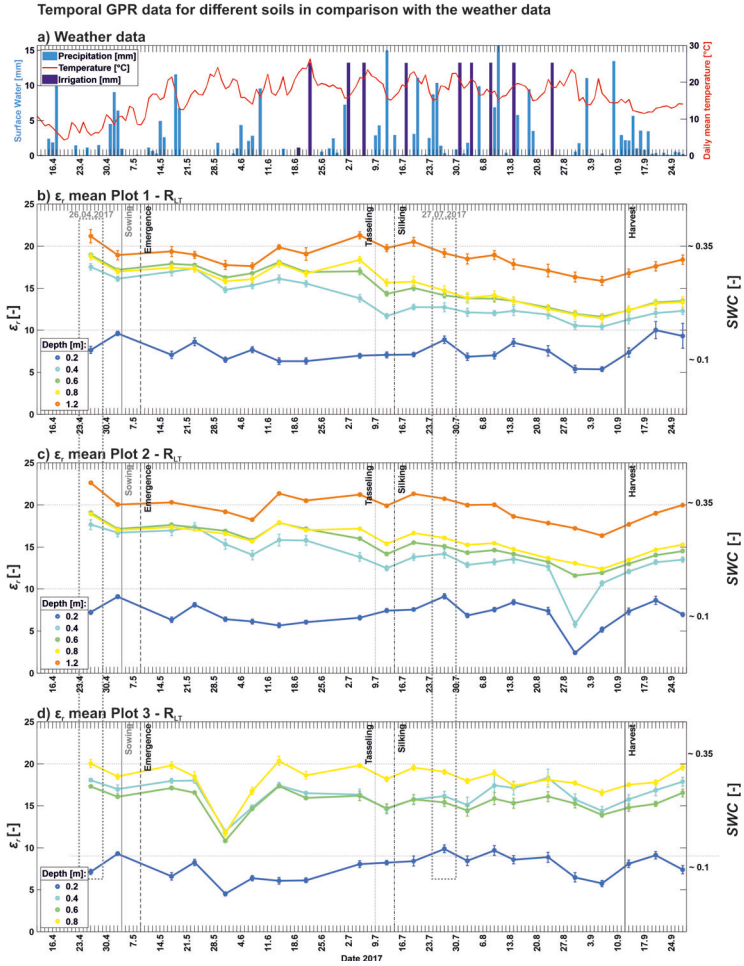

Figure 3-8: Comparison of the weather data and permittivity for R_{LT} during the 2017 crop growing season. a) Weather data: the solid red line represents the daily temperature values, and the light blue bars represent the daily precipitation values. The dark blue irrigation values are only valid for Plot 3. Mean permittivity per depth for Plots 1–3 are shown in b) and d). The colored circles with the error bars indicate the permittivity mean along the rhizotube with its standard deviation as error bars. The colored solid lines connect the individual measurement days. The horizontal lines represent the dates for the vegetation stages and sowing and harvest dates. For convenience, the approximate soil water content (SWC) values were added on the right-hand axis for b) and d) using the three-phase complex refractive index model (CRIM).

3-6 Linking depth-dependent RVF with depth-depentent GPR permittivity variablity

This section investigates the connection between the RVF and GPR permittivities. Although Plots 1 and 2 at R_{UT} and R_{LT} had the same surface water treatment in 2017 and 2018, the observed RVF depth profiles shown in Figures 3-4 and 3-5 and permittivities in Figures 3-6, 3-7 and 3-8 obtained in 2017 showed distinct differences. The measured RVF and permittivity data from 2018 show significantly smaller differences, as shown in see Appendix A-3, Figures A-3.1 - A-3.3, . A possible explanation for the larger differences between Plots 1 and 2 in R_{UT} and R_{LT} in 2017 than in 2018 is the application of different surface water treatments for Plots 1 and 2 from previous years. While Plot 2 was always under rain-fed conditions, Plot 1 was sheltered between 2012 - 2016 for R_{UT} and between 2014 - 2016 for R_{LT}. The rain-out shelter for Plot 1 resulted in drier soil and, consequently, both a different root distribution within the soil profile and lower crop growth compared to the other plots. This generated a so-called "memory effect". Consequently, the soil conditions at the beginning of the experiment were not the same for both years, resulting in different patterns in SWC and root growth.

The influence of the maize crops on the horizontal permittivity profiles is clearly shown in Figure 3-6c and f. Five crop rows were present along the rhizotubes, overlapping with the GPR measurements as shown in Figure 3-2, and five peaks could be identified in the permittivity values at the shallowest depth of 0.2 m. This indicated that increased SWC values were present between the two rhizotubes, probably due to the presence of shallow crown roots.

Since root images were collected only at selected locations, as indicated in Figure 3-2, no direct comparison could be made between the observed RVF and permittivity along the rhizotubes. Only once on 5.8.2020, a labor-intensive continuous image of the roots made along the complete rhizotubes was acquired. Figure 3-9 shows the results, and includes the measured permittivity values. Additionally, five peaks in the permittivity can be observed at the 0.2 m depth, which correspond to the five maize rows, though they show a considerable shift. The permittivity peaks at 1.5 m and 2.25 m along the rhizotubes also correlated with the corresponding root information (RVF). However, while multiple small peaks in RVF were present between 2.5 m and 5 m, there was no clear direct correlation between the RVF and permittivity data. Although the SV of the RVF was limited to the area directly around the rhizotube and the GPR SV represented the larger soil volume in between two rhizotubes, these results indicate that the presence of roots increase the variability in permittivity. In contrast, permittivity in a bare-field (BF), where no roots are present, showed very small variation in permittivity (Figure 3-6). In the following section it is assumed that the roots observed along the rhizotubes represented the root growth at that specific depth and an investigation of whether a correlation exists between the average RVF along the rhizotubes and the variability in permittivity follows.

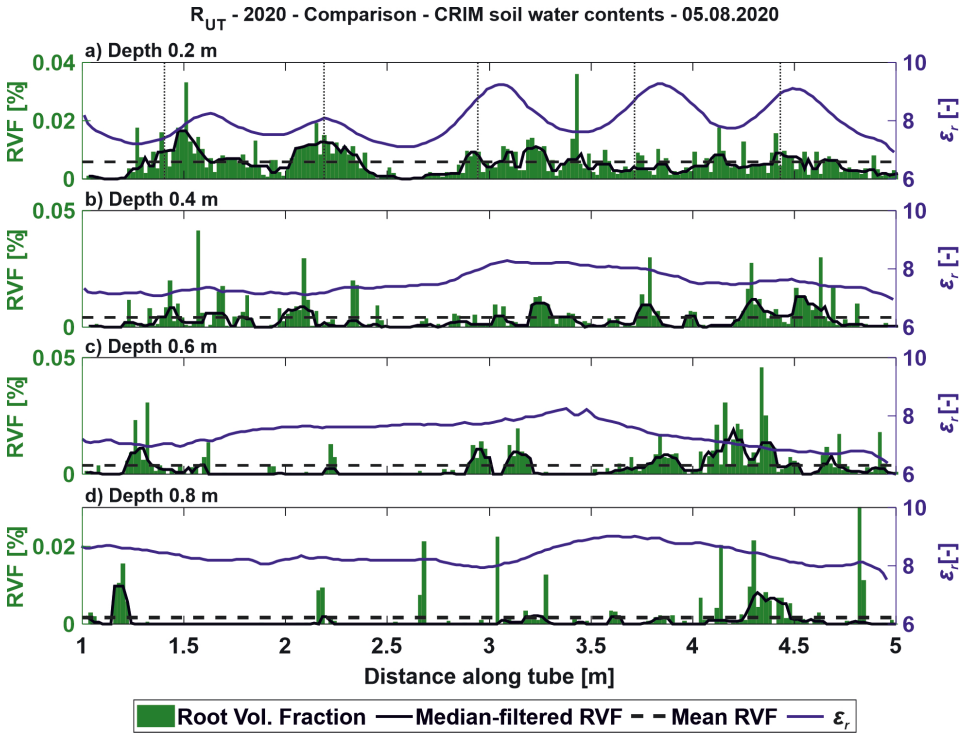

Figure 3-9: Comparison of the permittivity high-resolution root image dataset measured on August 5, 2020, and the respective root volume fraction (RVF). The different plots represent the different depths of 0.2–0.8 m, a)–d), respectively, for Plot 2 at R_{UT}. The solid blue line indicates the permittivity. The green bars indicate the RVF along the rhizotubes. The black solid line indicates the smoothed RVF along the rhizotube over five positions. The dashed black line represents the mean RVF along the rhizotubes.

3-6-1 Calculation of time-lapse variability analysis of GPR data

The investigation into the effects of the soil-plant continuum on the GPR-derived permittivity, distinguished between static and dynamic influences. Static influences were soil heterogeneity and variations in the distances between rhizotubes, and exerted a time-constant effect on the permittivity at the MR facilities. The dynamic influences were dominated by the temporal changes in permittivity caused by the seasonal variations in weather conditions (e.g., precipitation, evapotranspiration) as well as the soil water depletion caused by the root water uptake. To come up with a proxy for the permittivity changes related to the presence of roots, it was necessary to optimally reduce static effects and minimize the dynamic influences caused by atmospheric conditions for each measurement day.

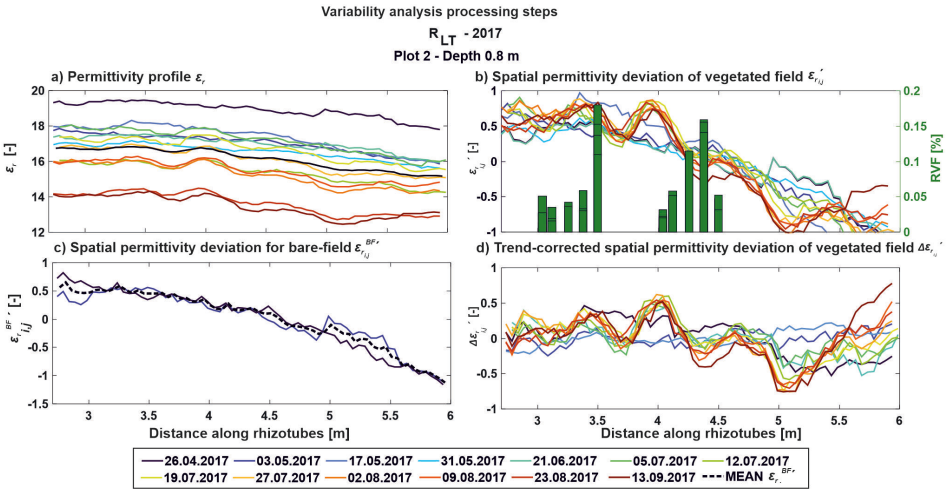

Figure 3-10: Processing steps to derive the trend-corrected spatial permittivity deviation of the vegetated field for R_{LT} Plot 2, depth 0.8 m. The different colors represent the measurement dates. a) Daily permittivity profile ε_r along the rhizotubes for all dates during the measurement season 2017. b) Daily spatial permittivity deviation of the vegetated field ${\varepsilon_{ri,j}}'$. The green bars indicate the root volume fraction (RVF) derived from root images for the different measurement positions. c) Daily spatial permittivity deviation for the bare-field ${\varepsilon_r^{BF}}_{i,j}'$. The dashed black line represents the mean of the 2017. d) Trend-corrected spatial permittivity deviation of the vegetated field $\Delta{\varepsilon_{ri,j}}'$.

When investigating the horizontal permittivity profiles over the course of the measurement season, it was observed that the vertical permittivity variations with depth for the different dates were caused by changes in the weather conditions (Figure 3-10a), as shown in the exemplary case for depth 0.8 m within Plot 2 of R_{LT}. To minimize the dynamic factors caused by different atmospheric conditions during the crop growing season, each day needed to be considered separately. As a first step, we reduced the dynamic influences for each horizontal permittivity profile:

$$ {\varepsilon_{ri,j}}' = \varepsilon_{ri,j} - \overline{\varepsilon_{ri,\cdot}} \tag{3-8} $$

by calculating the mean $\overline{\varepsilon_{ri,\cdot}}$ along the rhizotubes for each horizontal permittivity profile and then this value was subtracted from the $\varepsilon_{ri,j}$ of the individual ZOP positions along the rhizotubes. Here $i$and j indicate the date and the position along the rhizotube, respectively. These so-called spatial permittivity deviations ${\varepsilon_{ri,j}}'$ represent the deviations of the individual permittivities at the individual ZOP positions j from the mean $\overline{\varepsilon_{ri,\cdot}}$ along the horizontal permittivity profiles and are independent from the seasonal changes in SWC conditions. Data from the growing season and the BF measurements, which were collected before the sowing of the maize crops, were considered separately. Comparing the derived spatial permittivity deviations ${\varepsilon_{ri,j}}'$ for all measurement dates in Figure 3-10b and c, a trend of reoccurring patterns is observed. The obtained spatial permittivity deviations for the BF

measurements shown in Figure 3-10c have a much smoother and more regular trend than the measurements from the growing season. The mean BF spatial permittivity deviations $\overline{\varepsilon_r^{BF}{}_{\cdot,j}{}'}$ were calculated for each season separately and for all positions along the rhizotube j, since small changes were present between the individual ($\overline{\varepsilon_r^{BF}{}_{\cdot,j}{}'}$) values for each year. All daily spatial permittivity deviations for the BF $\overline{\varepsilon_r^{BF}{}_{it,j}{}'}$ can be found in Appendix A-3 Figure A-1.1 for 2017 and 2018. Additionally, the $\varepsilon_r^{BF}{}_{i,j}{}'$ values for R_{UT} can be found in the Supplemental Material, Appendix A-3 Figure A-3.7. As a final step, the trend-corrected spatial permittivity deviations $\Delta\varepsilon_{ri,j}{}'$, were derived for each GS measurement along the horizontal permittivity profiles. Static effects were removed by subtracting ($\overline{\varepsilon_r^{BF}{}_{\cdot,j}{}'}$) from the daily variability during the crop growing season, represented by $\varepsilon_r^{GS}{}_{i,j}{}'$:

$$\Delta\varepsilon_{ri,j}{}' = \varepsilon_r^{GS}{}_{i,j}{}' - \overline{\varepsilon_r^{BF}{}_{\cdot,j}{}'} . \quad (3\text{-}9)$$

From the sample dataset in Figure 3-10d, the static trend along the rhizotube disappears, and the fluctuating of minima and maxima around zero remained. This approach filters out both the dynamics of the spatially averaged permittivities that are caused by dynamic boundary conditions, as well as the temporally averaged spatial variation of permittivities outside of the growing season that resulted from spatial variations in soil properties and unknown variations in inter-rhizotube distances. In this way, the obtained deviations reflect the dynamic variability in the relative permittivity during the growing season.

3-6-2 Results and discussion of time-lapse variability of the GPR data

The approach introduced above to derive the trend-corrected spatial permittivity deviations for the vegetated field $\Delta\varepsilon_{ri,j}{}'$ was applied to Plots 1-3 of R_{UT} and R_{LT} in 2017, and the results are shown in Figure 3-11. Only days when root information and GPR data were both available were considered. Several different patterns emerge as a function of time, including several consistently increasing maxima and minima during the growing season. These patterns were present at the same horizontal location along the rhizotube at different depths and were identified in the $\Delta\varepsilon_{ri,j}{}'$ data, shown in Figure 3-11 d for Plot 2 in the blue and red frames, respectively. A possible explanation is that the soil water depletion processes had an influence beyond a certain depth range/volume of soil. For R_{UT}, patterns were not as distinct as those for R_{LT}, which had clear maxima and minima along the rhizotube. This could have been caused by fewer roots present in the soil at R_{UT}, see Figure 3-5a, c & e. For Plot 3, where irrigation was applied, distinctive peaks are apparent along the rhizotubes on certain days, e.g., 09.08.2017 and 23.08.2017 between depths 0.4 m to 0.8 m and at a horizontal distance of 2.3 m to 3 m. In both cases, measurements were taken a few days after irrigation was applied (see Appendix A-3 Table A-3.1 and A-3.2) and the peaks were probably due to the drip irrigation system which caused spatially variable infiltration.

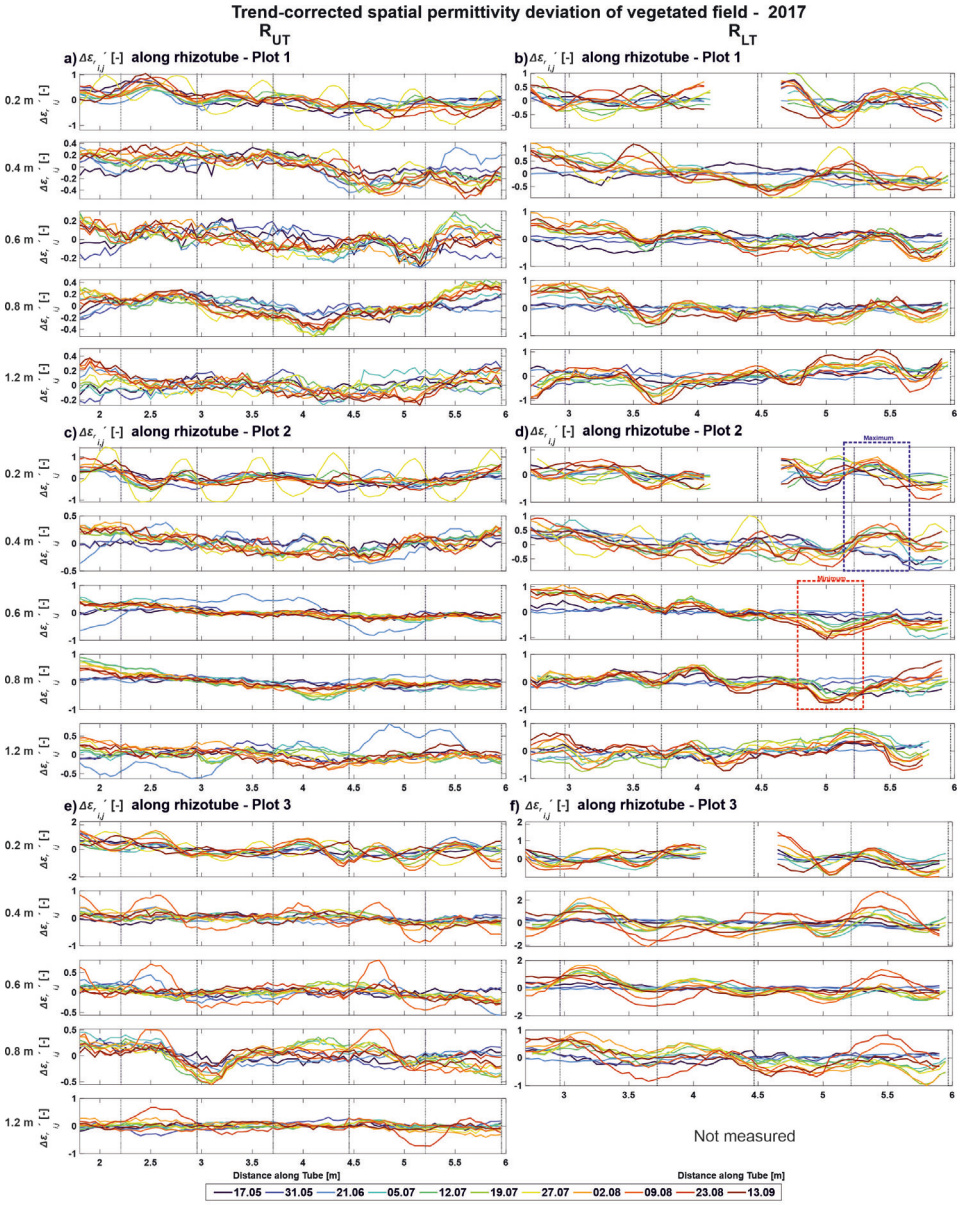

Figure 3-11: Trend-corrected spatial permittivity deviation $\Delta\varepsilon_{ri,j}{}'$ of the vegetated field, along the rhizotubes over the different plots & depths, for R_{UT} and R_{LT} in 2017. The colored solid lines represent different dates during the crop growing season. The data gap of R_{LT} at 0.2 m depth is caused by the presence of the sEIT line.

The same analysis was performed for 2018 and 2020, which can be found in the Supplemental Material, see Appendix A-3 Figures A-3.7 A-3.8 and A-3.9. Evaluating the patterns of $\Delta\varepsilon_{ri,j}{}'$ for the different crop growing seasons, recurring patterns were observed at some locations (e.g., R_{UT}, Plot 1, depth 0.4 m between 4.5 m and 5.5 m; R_{LT}, Plot 2, depth 0.4 m and 0.6 m, see Figure 3-11, Supplemental Material, see Appendix A-3 Figure A-3.8). These reoccurring patterns indicate that spatial variations in permittivity likely correspond with static soil properties that may have influenced water flow and root growth.

3-6-3 Probability density function of the trend-corrected permittivity deviation

To quantify the values of $\Delta\varepsilon_{ri,j}{}'$ in more detail, a normal distribution model was fitted to the data and a range of one standard deviation from the mean (SD) was obtained for the vegetated and bare-fields. The SD of bare-field plots was considerably smaller than that of the vegetated field plots (an example of which is shown in Figure 3-12 for depths 0.2 m and 0.6 m, in Plot 2 at R_{UT} and R_{LT}). The presence of the crops clearly increased the permittivity $\Delta\varepsilon_{ri,j}{}'$ variability. When comparing both MR facilities, SD values were generally lower at R_{UT} than at R_{LT}.

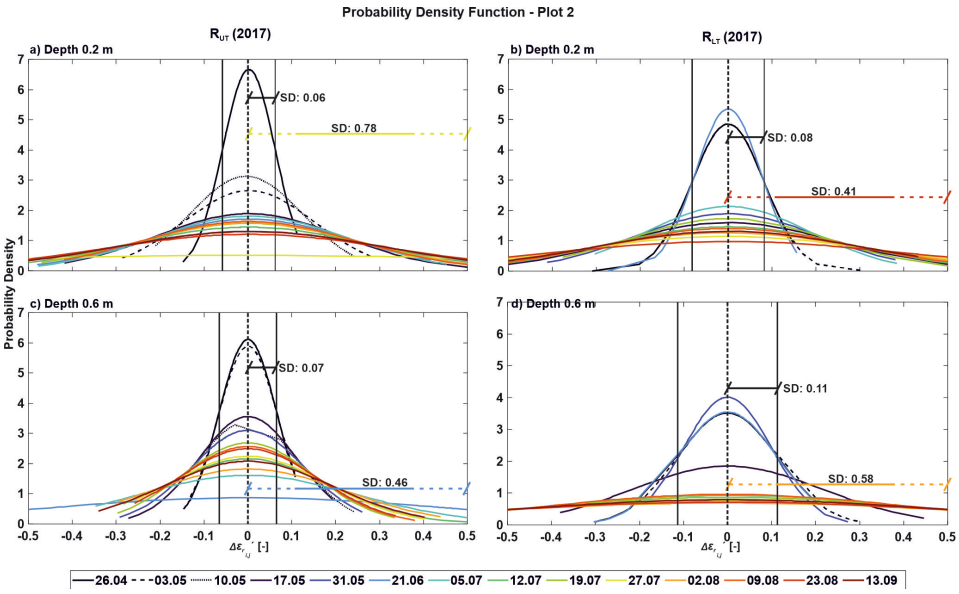

Figure 3-12: Probability density function (PDF) of of trend-corrected spatial permittivity deviation $\Delta\varepsilon_{ri,j}{}'$ for depths 0.2 m and 0.6 m for Plot 2, for both MR-facilities of 2017, respectively. The black solid, dashed and dotted lines represent the dates for the bare-field measurements and the colored lines represent the PDF of trend-corrected spatial permittivity deviation $\Delta\varepsilon_{ri,j}{}'$ for the crop growing season measurements. For PDFs with the most narrow and widest peaks we added the respective values of the standard deviation (SD).

By plotting all SD values from 2017 for R_{UT} and R_{LT} for the different depths in Figure 3-13, low values were observed under bare field conditions (non-colored lines), whereas the values for later times initially increased and then decreased. These results indicate that the variability in $\Delta\varepsilon_{ri,j}{}'$, and therefore SWC, was increasing during the growing season.

A comparison of the different plots for R_{UT} revealed that Plot 1 generally had a higher SD than Plot 2, except for 27.07.2017, and that the SD in Plot 1 was at its maximum at a depth of 0.2 m. Plot 3 showed higher SD values than both Plots 1 and 2. For R_{LT} Plot 3 had the highest SD values, but the difference between Plots 1 and 2 was small.

3-6-4 Cross-correlation of depth dependent RVF and depth dependent GPR variability

The RVF values in Figure 3-5, as well as the permittivity variability showed an increase during the growing season. Here, the RVF and SD were cross-correlated individually for every depth as shown in Figure 3-14. To account for the SD variability in the bare-soil conditions present at the MR facilities, the first bare-field measurement was added to the cross-correlation with an RVF value of 0. Almost all the results from 2017 and 2018 returned a positive correlation, with one exception where the coefficient of determination (R^2) was 0. The remaining cross-correlations resulted in R2 ranging between 0.02 and 0.9 (Table 3-3). Out of the 46 cross correlations, 23 had an $R^2 > 0.5$ ($0.51 < R^2 < 0.9$) and 23 values had an $R^2 < 0.5$ ($0.02 < R^2 < 0.49$). At 0.4 m depth, the correlations are the lowest, whether this has to do with the interface between the top- and subsoil interface needs to be investigated. These results indicate that at most depths the SD, and therefore the permittivity variability, is increasing with increasing RVF. When considered alongside the bare field measurements, the presence of roots leads to increased variability in permittivity.

Table 3-3: Coefficient of determination between the root volume fraction and the SD for R_{UT} and R_{LT} for both years 2017 and 2018.

	R_{UT}						R_{LT}					
	2017			2018			2017			2018		
Depth [m]	Plot 1	Plot 2	Plot 3	Plot 1	Plot 2	Plot 3	Plot 1	Plot 2	Plot 3	Plot 1	Plot 2	Plot 3
0.2	0.6	0.3	0.37	0.84	0.08	0.56	0.62	0.55	0.37	0.49	0.78	0.72
0.4	0.53	0.45	0.14	0.9	0.07	0.2	0.33	0.06	0.26	0.0	0.13	0.19
0.6	0.65	0.19	0.02	0.07	0.51	0.66	0.64	0.49	0.73	0.48	0.67	0.47
0.8	0.69	0.53	0.57	0.45	0.11	0.86	0.87	0.65	0.58	- a	0.34	0.76
1.2	- [a]	- [a]	- [a]	- [a]	- [a]	- [a]	- [a]	- [a]	[b]	- [a]	- [a]	- [b]

[a] Three or less data pairs – No cross-correlation was performed.

[b] No GPR measurements carried out.

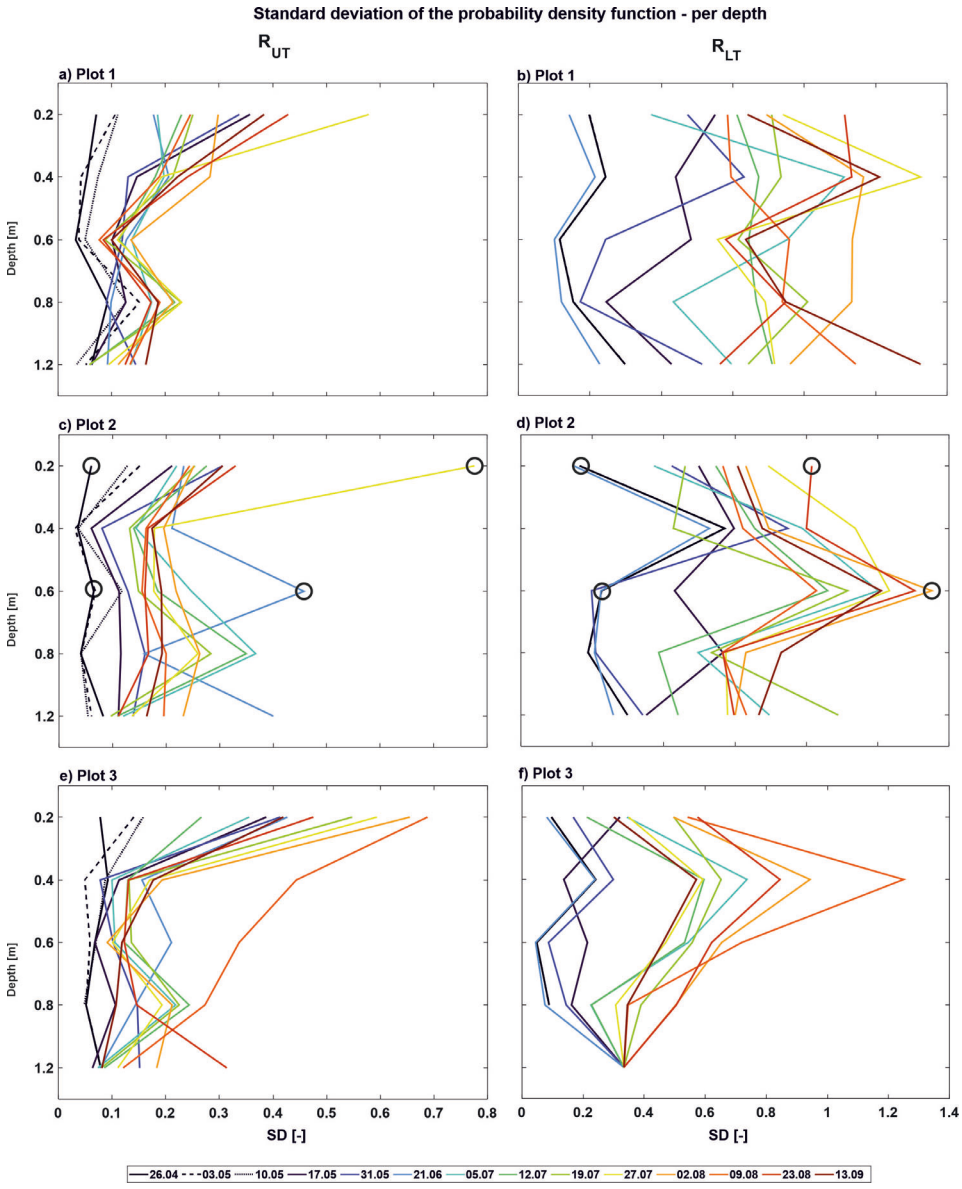

Figure 3-13: Standard deviation (SD) values for different depths in 2017 for R_{UT} and R_{LT}, respectively. The black circles indicate the minimum and maximum of the SD, indicated in Figure 3-12.

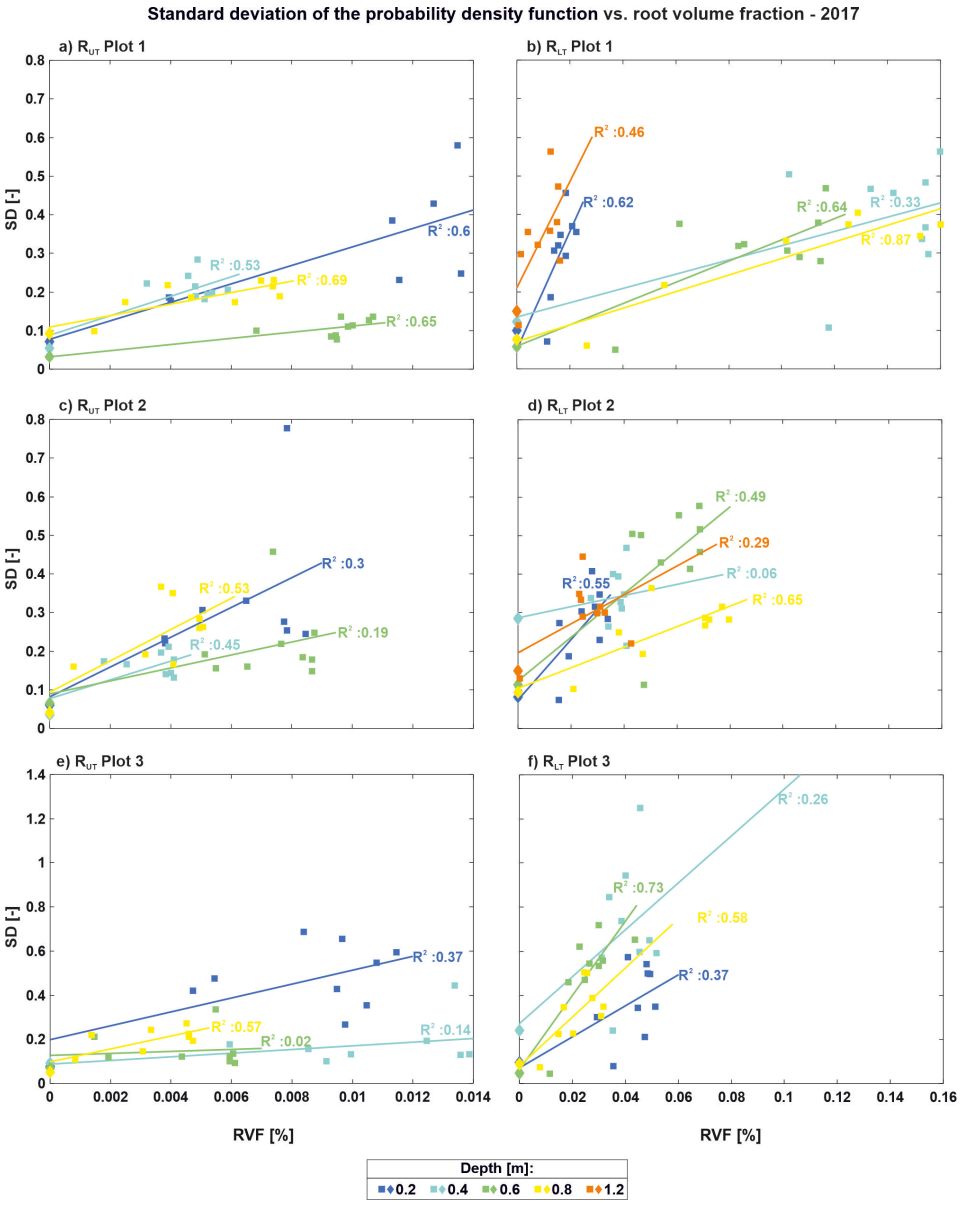

Figure 3-14: Correlation between the root volume fraction (RVF) and the standard deviation (SD) for the individual plots for R_{UT} and R_{LT} in 2017, respectively. The colored squares represent the values for the RVF and the SD for the vegetated field and the colored diamonds represent the values during the bare-field, where the RVF was set to 0, the different colors represent the different depths. The colored lines represent the linear regression per plot and depth, the R^2 values are indicated next to the regression lines.

3-7 Conclusions and outlook

In this study, root images and time-lapse horizontal crosshole GPR measurements were made to non invasively monitor the root zone of maize crops at different depths for different treatments and different soils. Repeated root images and GPR measurements were carried out before and during three separate maize growing seasons. Overall, the analysis of the root images acquired in the upper (R_{UT}) and lower terrace (R_{LT}) MR facilities showed that the RVF of the maize crop increased during the crop growing seasons and decreased towards the harvest date. The RVF varied between soil types: in the stoney upper terrace the roots were not able to reach greater depths due to the stones, whereas the roots were able to grow deeper than the lowest rhizotube in the lower terrace. In addition to soil type, the surface water treatment and previous soil management seemed to influence the RVF. It was observed, for instance, that in a plot that was sheltered in previous growing seasons, the maize crops developed more roots than in a plot that was not previously sheltered.

Using the crosshole GPR-derived permittivity values, both the temporal and spatial (vertical & horizontal) permittivity distributions were able to be monitored and variations for different soil types, weather conditions, and surface water treatments were observed. A direct comparison between the root images and the GPR-derived permittivity values was not possible because of the significant difference in sensing volumes of the two methods (0.21 m^3 – 0.35 cm^3 for each GPR-ZOP position and 1.28x10-5 cm^3 for each set of root images). A time-lapse variability analysis was introduced, where the trend-corrected spatial permittivity deviations were derived for the vegetated field where static influences (soil heterogeneity or variations in the distance between rhizotubes), as well as dynamic influences (atmospheric conditions) were removed. Next, a probability density function (PDF) model was fit, describing the trend-corrected spatial permittivity deviations for both the vegetated and bare-fields to obtain a proxy for the permittivity variability. A low standard deviation, and therefore low permittivity variability, was obtained before and early in the crop growing season, with larger values obtained later in the crop growing season. To investigate the relationship between the trend-corrected spatial permittivity deviations with the RVF in more detail, the PDF standard deviation of the trend-corrected spatial permittivity deviations during each season was cross-correlated with the RVF values for each depth, plot, and soil type. Almost all results for 2017 and 2018 were positively correlated, with coefficients of determination ranging between $0.02 < R^2 < 0.9$ (Table 3-3). Out of the 46 cross correlations, 23 values had an $R^2 > 0.5$, ($0.51 < R^2 < 0.9$) and 23 values had a $R^2 < 0.5$ ($0.02 < R^2 < 0.49$). These relatively large coefficients of determination show a clear link between RVF and the permittivity variability at multiple soil depths. Additionally, both soil types reacted similarly and provided a comparable number of good correlation pairs, even when within different facilities.

More investigations are necessary to understand why the correlation at some depths is weak. A possible explanation is the difference between the SV of the GPR measurements and the root image data. The root images represent a significantly smaller two-dimensional space on the rhizotube surface, while the root volume present in the soil volume between the rhizotubes, which is measured by the GPR, remains unknown. Acquiring denser and higher resolution of higher frequency GPR data (between 500 - 1000 MHz) would enhance

the imaging of the subsurface between the boreholes. Extending the GPR-ZOP data, with multi-offset GPR data, combined with a ray-based travel time inversion (e.g., Binley et al., 2001, Musil et al., 2006), would also enhance the resolution between the rhizotubes towards 2D and 3D images instead of 1D profiles. These higher resolution images could possibly improve the understanding of processes within the soil-plant continuum and might also allow a more localized correlation. In addition, a possible improvement to the RVF could involve obtaining continuous root images along the entirety of the rhizotubes (as shown in Figure 3-9). With recent technological developments, measurements along an entire rhizotube can be performed simultaneously, and these RVF data would be expected to better represent the actual RVF changes at different depths and times.

The presented results are based on measurements made during several growing seasons in different soils for different treatments. Taking multiple high resolution GPR measurements made during the day and night cycle for very hot days and very wet days, and analyzing the results with improved imaging approaches would provide additional information. To optimize the monitoring parameters, the construction of a detailed soil-plant-root model that could record time-lapse soil water content changes (depending on the root activity) under changing atmospheric influences would be ideal. In this way, synthetic GPR data could be generated and processed, and the acquisition parameters could be optimized to include as much information as possible to describe the rhizosphere processes that take place under field conditions.

Although the rhizotron facilities provide a great opportunity to deepen the understanding of below ground soil-plant interactions, such facilities are destructive, limited to the plot-scale, and are both expensive and time-consuming. Therefore, future challenges will involve finding ways to up-scale the link between the permittivity variability and the root image data to surface data. In a next step, combined rhizotube and surface investigations could be analyzed to investigate if a similar link can be observed for above-ground data between root information and GPR data. Furthermore, providing root and plant models with GPR-derived permittivity and hence SWC distribution could help to establish possible surface measurements and to understand the measured signals.

To conclude, this study has established a link between the root volume of maize crops and the spatial variability of horizontal crosshole GPR-derived permittivity values, which is an important step in investigating processes within the soil-plant continuum in more detail. The current approach and the above-described improvements open new possibilities for the combination of non-invasive geophysical measurements with root information measurements to enhance crop models and agricultural management decisions.

Chapter 4

High resolution soil-root modeling for crosshole GPR data

Abstract

Using non-invasive geophysical tools, such as ground penetrating radar, to investigate the soil-plant continuum of agricultural crops, has become increasingly popular in the past decades. One major challenge which these tools face is the high complexity of this continuum, where the different components dynamically influence each other, and the processes are not yet fully understood. A first step towards understanding the impact the different soil-plant continuum component, such as soil, water and roots, have on the GPR signal is provided in this study. We investigated the influence of the roots on the soil water content calculation in a synthetic feasibility study before we performed synthetic forward modeling using an open-source electromagnetic simulation software gprMax. Here, we analyzed the GPR traces considering scenarios with different soil-plant continuum compositions containing, soil, roots and above-ground shoots. Thereby, we included the two realistic root contribution, related to contrasting soil types based on trench wall counts of the minirhizotron facilities, in the models. We observed that the roots have a higher impact than considering an above-ground shoot in the modeling. Additionally, if roots are not considered in the soil water content calculation using appropriate mixing models.

Adapted from: Lena Lärm, Jan Rödder, Harry Vereecken, Anja Klotzsche: High resolution soil-root modeling for crosshole GPR data. In preparation.

4-1 Introduction

Investigating the soil-plant continuum of agricultural crops in a non-invasive matter using geophysical measurements techniques such as ground penetrating radar (GPR) has shown to be challenging in terms of small-scale soil heterogeneities, which effect processes like infiltration, soil water depletions and root growth. The processes within the soil-plant continuum are highly dynamic and impacting factors range from atmospheric weather conditions, soil physical and chemical properties, nutrients, micro-organisms to root architecture and agricultural management. As shown in Chapter 3 it is challenging to identify and quantify these influences directly in the GPR signals. Thereby, we have observed and investigated that for crops with a high inter crop row distance such as maize an influence on the distribution in dielectric permittivity along a horizontal axis is present. Especially at very dry conditions below the plants an increased permittivity and hence soil water content (SWC) was observed compared to the surrounding soil. This could not clearly be related to the actual water present in the soil, the roots or if it was affected by the above ground shoot and its related stem flow infiltration. Regardless these effects, in a first step, we were able to qualify the influence of maize roots on the GPR signal throughout the growing season using statistical methods like spatial and temporal permittivity variability analysis for the GPR measurements acquired at the rhizotron facilities (Chapter 3). Nevertheless, fine root systems, as present in cereal crops (e.g., maize), remain challenging, since with the GPR we acquire information about a volume of the rhizosphere system, which includes soil, water, roots, and nutrients.

To provide a possible proxy for a sustainable crop production, it is essential to derive the available water content in the soil without the effect of water-filled roots from the GPR data. Conventionally, to calculate the SWC a petrophysical relationship is utilized which accounts for the different component of the soil. Therefore, we investigate here the possibilities if and how a distinction between water in the soil and roots is possible using horizontal borehole GPR data by performing synthetic forward modeling with an open-source electromagnetic simulation software gprMax (Warren et al., 2016). Additionally, questions about above-ground effects are addressed by incorporating in the realistic model the part of the plants. As a first step, we added a root contribution to this petrophysical relationship and investigated the influence of this root component on the GPR-derived SWC. To realistic model the root distributions in the soil related to maize crops, we considered the root volume fraction (RVF) information derived from trench wall root count acquired for maize crops (see Appendix D, Morandage et al. (2021)). In the next step, we define a synthetic forward model of the minirhizotron (MR) facilities using the soil information and the root trench counts. The upper (R_{UT}) and lower (R_{LT}) MR-facilities each is situated in different soil type, see Chapter 2. Similar to previous studies, we used the standard first arrival time picking of the GPR electromagnetic waves to derive the dielectric permittivity of the soil and hence the SWC of the soil-plant continuum, see Chapter 2 and 3.

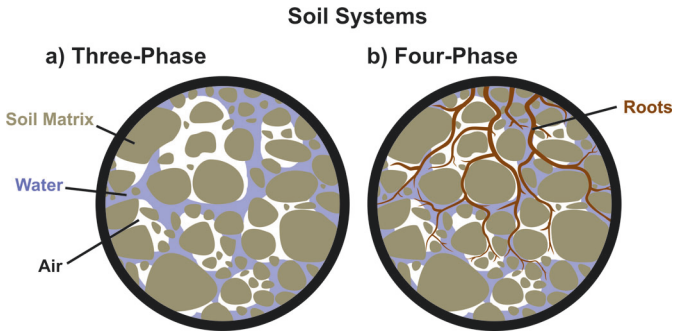

Figure 4-1: Illustration of the soil system for the soil-plant continuum: a) three-phase and b) four-phase system including roots.

4-2 Materials and Methods

4-2-1 GPR-derived soil water content considering crop roots

As shown in Chapter 3 the GPR data and its first arrival time can be used to derive the dielectric permittivity of the soil system (Equation 4-1), which can be related to SWC. To derive the SWC petrophysical or empirical relationship are required (Huisman et al., 2003, Klotzsche et al., 2018). A widely used petrophysical volumetric mixing model is the complex refractive index model (CRIM). In contrast to Topps equations (see Chapter 5 Equation 5-1), mixing models can also consider additional components next to soil, water and air, such as a root fractions. The general form of the mixing model assumes that the soil consists of different phases with different dielectric properties and volume fractions. For a system with n dielectric components the general formula is

$$\varepsilon_r^a = \Sigma_{i=1}^{n} \chi_i (\varepsilon_i)^\alpha \tag{4-1}$$

where ε_r^a is the relative dielectric bulk permittivity of the mixed system, χ_i and ε_i are the volume fraction and the permittivity of the i-th component of the system and α is a fitting exponent, which describes the geometry of the system. Conventionally, soil systems are considered to be three-phase, containing soil, water, and air (see Figure 4-1a). The often used CRIM is derived by using a geometry factor of $\alpha = 0.5$ and considering the permittivity of air to be $\varepsilon_a = 1$. Using these values, we can transform Equation 4-1 to calculate the bulk permittivity ε_r of a three-phase soil system

$$\varepsilon_r = ((1-\phi) \cdot \sqrt{\varepsilon_s} + \theta \cdot \sqrt{\varepsilon_w} + (\phi - \theta))^2, \tag{4-2}$$

where ϕ is the porosity of the soil. ε_s, ε_w are the permittivities of the soil (solid phase) and water components of the system, respectively, and θ is the volumetric water content in the soil. This equation (Equation 4-2) can then be rearranged to calculate the SWC of the three-phase soil system to

$$\theta = \frac{\sqrt{\varepsilon_r} - (1-\phi)\sqrt{\varepsilon_s} - \phi}{\sqrt{\varepsilon_w} - 1}. \tag{4-3}$$

It should be noted that when we apply the three-phase system to derive the SWC, this SWC cannot distinguish between water in the soil or water in the roots. Especially for row crops with spatially varying roots distribution in the field, like maize, the uncertainty on the SWC without including roots information can be high. Therefore, to improve the SWC estimation, which is available to the crops, we need to extend the three-phase soil system by a fourth phase, which considers the root volume inside the pore space (Figure 4-1b). Thereby, we assume that the porosity equals the summations of RVF, water in the pores and air. The RVF is considered to be the percentage of roots in a soil volume. Extending Equation 4-2 with the RVF and the corresponding permittivity of the roots ε_R, we derive:

$$\varepsilon_r = ((1-\phi)\cdot\sqrt{\varepsilon_s} + \theta\cdot\sqrt{\varepsilon_w} + (\phi - RVF - \theta) + RVF\cdot\sqrt{\varepsilon_R})^2, \tag{4-4}$$

under the assumption that the roots grow within the pore space. Similar to Equation 4-3, we can reformulate Equation 4-4 to derive the SWC for a four-phase soil system

$$\theta = \frac{\sqrt{\varepsilon_r} - (1-\phi)\cdot\sqrt{\varepsilon_s} - (\phi - RVF) - RVF\cdot\sqrt{\varepsilon_R}}{\sqrt{\varepsilon_w} - 1}. \tag{4-5}$$

4-2-2 Deriving root volume fraction from trench wall counts

To use realistic field data as root information, we used the root count density values acquired on trench walls at the MR facilities in Selhausen. In 2017 for the MR facilities trenches were excavated and the roots were counted on the trench walls and the root count density (RCD) was derived (Huisman et al., 2003, Klotzsche et al., 2018). Here a trench was dug, next to a maize plant and on the wall a grid was installed (Figure 4-2a and b). Within each 3.75 cm by 3.75 cm grid cell the RCD was obtained (Figure 4-2c). In a few steps we calculated the RVF from the RCD for each grid cell. First, we derived the root length (RL) per grid cell dimensions and the RCD

$$RL = (RCD\cdot A_{grid})\cdot L_{grid}, \tag{4-6}$$

where A_{grid} is the size of the grid cell and L_{grid} is the length of the grid cell. In the next step, we calculated the root volume using

$$RV = RL\cdot\pi\cdot\frac{d_{max}^2}{4}, \tag{4-7}$$

with d_{max} is the maximum root diameter recorded for the data in 2017 (Appendix E, Chapter 3), with a value of 0.05 cm. We considered the respective soil volume V_{soil} to be the area of the grid A_{grid} cell times the maximum root diameter d_{max} as

$$V_{soil} = A_{grid}\cdot d_{max} \tag{4-8}$$

and

$$RVF = \frac{RV}{V_{soil}} \tag{4-9}$$

to derive the RVF per grid cell.

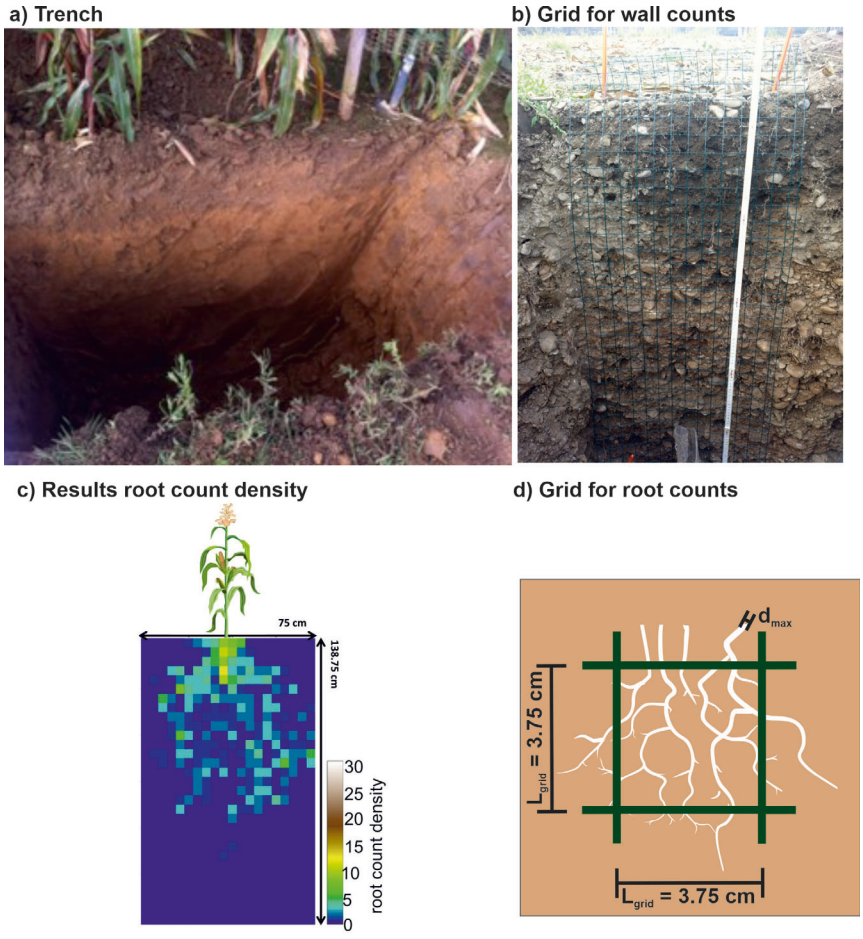

Figure 4-2: Overview of the trench wall counts to derive the root count density. a) Finalized trench perpendicular to the maize crop rows. b) Grid on the trench wall, in which the roots were counted. c) Results for the root count density for R_{UT}, adapted by Appendix D and d) schematic illustration of the trench wall root counts for one grid cell with a size of 3.75cm.

As Figure 4-3 indicates the distribution of the *RVF* varies for the different soil types of the MR facilities. For R_{UT} the highest number of roots is present close to the surface and decreases with increasing depth (Figure 4-3a). Additionally, the *RVF* distribution in the horizontal axis is less distributed as for R_{LT}. For R_{LT} the *RVF* indicated higher amounts of roots in general, but also indicated a more complex distribution in both directions of the recorded profile. For the later comparison of the different SWC calculations (Equation 4-2 & Equation 4-4), we derived the *RVF* mean per depth (Figure 4-3b). The depth distribution of *RVF* shows a similar distribution of root length density as shown in Morandage et al. (2021). For R_{UT} a mean value of 3% and maximum value of 13% for the shallow depths , which decreased with increasing depth was observed. For R_{LT} the mean is higher with up to 10% at a depth of 0.6 m, and reaching an overall maximum of 20% between 0.6 m and 0.8 m depth.

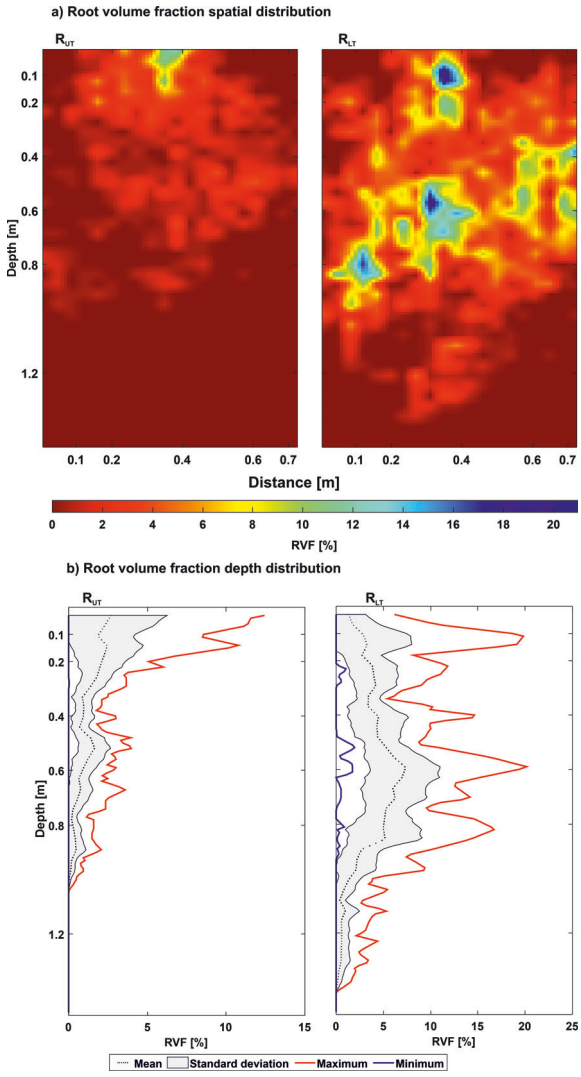

Figure 4-3: Root volume fraction (*RVF*) for both MR facilities with a) *RVF* values calculated for every grid cell and then interpolated to a cell size of 1 cm. b) *RVF* depths profiles for R_{UT} and R_{LT} with corresponding mean, standard deviation, maximum & minimum distribution.

4-3 Feasibility study - petrophysical relationships considering roots

To investigate the necessity to account for the root fraction at the MR facilities or if the effect is minor and can be neglected, we performed a feasibility study by calculating the three- and four phase SWC for a range of relative bulk permittivity values, porosities (see Appendix C-1) and root volumes, which are common for agricultural systems in Selhausen (e.g., Appendix D; Chapter 3). As Figure 4-3b shows the *RVF* maximum values of about 20% for R_{LT}, whereas mean values up to 10% were recorded (for R_{LT}). Therefore, we are using a maximum *RVF* of 20% for this feasibility study. For the calculation of the SWC using Equation 4-2 and Equation 4-4, we used $\varepsilon_w = 84$ for a temperature of 10°C in the soil, and $\varepsilon_s = 4$ (Appendix D). For ε_R we applied a value of 70, which anticipates that roots almost entirely consist of water. For the porosity of the soil system, we used $\phi = 0.35$ and $\phi = 0.25$, which is the porosity of the subsoil for R_{LT} (Figure 4-4) and R_{UT} (Appendix C-1). By comparing the results for a range of *RVF* values for the three-phase and four-phase CRIM, we can observe that for increasing amounts of roots, the differences become more significant (Figure 4-4). Note that the three-phase SWC is equal to the four-phase SWC with a *RVF* of 0% (Figure 4-4a). For lower bulk permittivity values the four-phase SWC reaches values below zero, in that case in Figure 4-4b the values were replaced with a SWC of 0 for illustration purposes.

Analyzing the four-phase SWCs depending on the *RVF*, we notice a decrease in SWC with an increase in *RVF* (Figure 4-4b). Hence, using a three-phase SWC CRIM is overestimating the SWC if the root phase is not considered in the calculation. For dry soils/ soil with low permittivity, already a low presence of roots will lead to an absence of water on the soil phase, e.g., with a permittivity of $\varepsilon_r = 4$, a *RVF* values above 3.8% will lead to a four-phase SWC of 0, while the three-phase SWC is 0.04. For a soil with $\varepsilon_r = 8$, the threshold for the *RVF*, where there no water left in the soil is *RVF* = 12.06%. This effect is even more pronounced with a lower porosity in the soil, see Appendix C-1. Considering these observations using a three-phase SWC calculation is feasible either if no or very few roots are present or if the root distribution is evenly distributed (and known). Therefore, for analyzing the variations of SWC related to maize roots, which have in our study a row separation of 0.75 m, a four-phase SWC calculation is recommended, when the *RVF* exceeds a threshold of 5%. For crops with narrow crop row separation, e.g., winter wheat, a more homogeneous root distribution can be assumed, therefore using a three-phase SWC leads to an evenly distributed error.

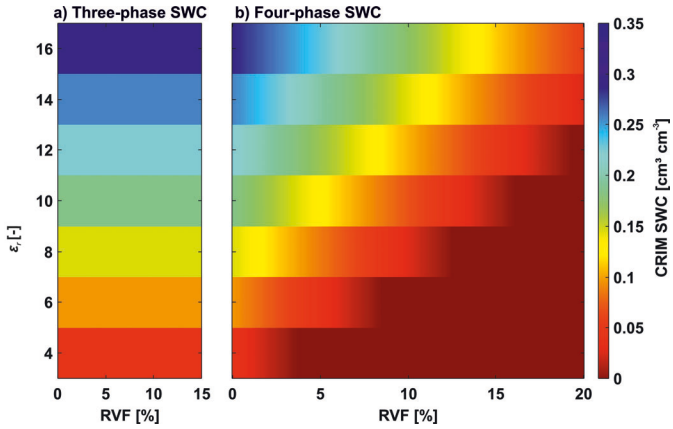

Figure 4-4: Results of the feasibility study for a) three-phase and b) four-phase CRIM equation for varying bulk permittivity and *RVF* of the soil-plant continuum. Porosity was defined as $\phi = 0.35$.

4-4 gprMax forward modeling

As we have seen from the feasibility study, we should consider the root fraction for maize crops when a certain number of roots are present (e.g., after silking). To further improve our understanding of the effects of the roots on the GPR signal, we performed several synthetic tests ranging from various soil parameters, root systems, above-ground shoot, changing electrical conductivity values of the roots, up to the possibilities to consider higher frequencies. Therefore, to realistically model the influences of the different components of the soil-plant continuum on the GPR signal, we performed our synthetic study using an open-source electromagnetic simulation software gprMax (Warren et al., 2016). gprMax is a finite difference time domain solver, which can used to model 2D or 3D electromagnetic waves. In this study, we are not investigating the spatial variabilities in the GPR signal along the horizontal axis as we would with the horizontal rhizotubes, rather we are focusing on the comparison of the GPR signal between different set ups of the soil-plant continuum. Therefore, we modeled four scenarios where the model consists of: I) soil, II) soil and roots, III) soil and above ground shoot, and IV) soil, roots, and above ground shoot (Figure 4-5). As a template for our model domain, we are considering the setup of the MR facilities cropped with maize, see Chapters 2 & 3. We defined a two-layered model, which includes an above ground air layer with a $\varepsilon_a = 1$ and a soil layer with varying bulk permittivity depending on the soil-plant continuum scenario based on realistic values for the rhizotrons for dry and wet condition (Figure 4-5, Table 4-1). The models have a cell size of 0.01 m, and the model domain was defined with 1.75 m in x-direction, 2 m in the z-direction including 10 cells of perfect matched layers. Similar to, the MR facilities, we calculated ZOP GPR traces at six different depths with a horizontal spacing of 0.75 m and with Tx and Rx in adjacent rhizotubes, see Chapter 2.

To calculate the bulk permittivity, we assumed the below-ground half space to be a three-phase soil-air-water system (Equation 4-2), when the soil does not include roots

(Scenario I and III) and to be a four-phase system (Equation 4-4), while the soil includes roots (Scenario II & IV). The *RVF* (Equation 4-6 - 4-9) was calculated from trench wall counts (Figure 4-3).

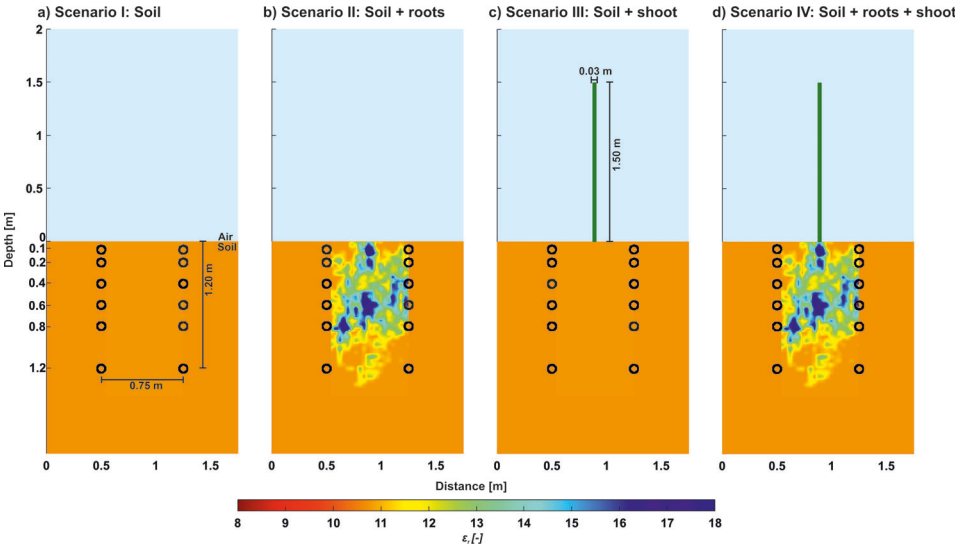

Figure 4-5: Schematic overview of the different scenarios for R_{LT} with a soil water content (SWC) of 0.2 [cm^3 cm^{-3}]. a) Scenario I with only of soil, b) Scenario II with soil and roots, c) Scenario III with soil and shoot and d) Scenario IV with all the different components soil, roots and above-ground shoot. Note that the permittivity was derived using Equation 4-2 for Scenario I & III and Equation 4-4 for Scenario II & IV.

To model the above-ground shoot (Scenario II & IV), we used a cylindrical shape with a diameter of 0.03 m and a height of 1.5 m, which should represent the shoot during the time of the trench wall counts. We explicitly considered the scenario with the above-ground shoot since we observed for dry soil conditions interferences of the shallow GPR data, which were not clear if they were related to shoot itself (see Chapter 3). Note that, we modeled the scenarios with the shoot in a 3D domain with a y-direction of 1.5 m to realistically model the EM propagation related to the shoot, while Scenarios I and II were modeled in 2D to keep the computations costs low. For the 3D models, we extended the roots in 3D by keeping them constant in the y-direction.

For simplification we are using a constant electrical conductivity of σ_s= 0.015 [S m^{-1}] for a loamy soil (Brovelli and Cassiani, 2011) for all model components in the first part of the study. Additional calculations were performed, where the electrical conductivity of the roots was assumed to be σ_R = 0.05 [S m^{-1}] for the roots (Rao et al., 2020). Since the σ_R is usually not constant for the entire root system, it may vary with root age, root order and root diameter, see Rao et al. (2020). Furthermore, they investigated in their simulation study, that the electrical conductivity of the roots may change with the root growth away from the root collar and found conductivities between σ_R = 0.0154 – 0.03 [S m^{-1}] for roots

up to three weeks old. Since the root system used in this study was mature, nevertheless to account for different conductivities we used an additional root electrical conductivity of σ_R = 0.03 [S m^{-1}]. For most of the tests a Ricker wavelet was considered as source pulse with a center frequency of 200 MHz as used in the field measurements. Additional simulations were performed using a center frequency of 500 MHz to investigate whether the various effects can be better discriminated using higher frequency and hence shorter wavelengths.

Since the two MR facilities were built in two different soil types, which result in different soil permittivities, but also in a different root distribution. We calculated GPR traces for a range of realistic expected permittivity values for dry and wet conditions for both facilities (Table 4-1) Similar to Chapters 2 & 3, we derived the bulk permittivity using the first arrival times of the GPR traces and the known distance between the Tx and Rx.

Table 4-1: Overview of the different model input parameters to calculate the SWC related to the three-phase and four-phase CRIM. Note that a homogeneous soil was assumed and no differentiation between top and subsoil was included.

		$\mathbf{R_{UT}}$				$\mathbf{R_{LT}}$	
ϕ	[-]	0.25[a]				0.35[a]	
ε_w	[-]	84					
ε_s	[-]	4.7				4	
SWC in HHS	[cm^3 cm^{-3}]	0.05	0.15	0.25	0.10	0.20	0.35
σ_s	[S m^{-1}]	0.015					
σ_R	[S m^{-1}]	0.03/0.05					
GPR frequency	[MHz]	200/500					

[a] Similar to the porosity of the subsoil of the facilities, see Chapters 2 & 3 and Appendix D

4-5 Effects of roots on the GPR signal

To get a first impression on how the root distribution in the soil would influence the GPR signal in the different depths for the MR facilities, we investigate the GPR traces related to model Scenario I and II (5a and b). Therefore, we modeled GPR ZOP traces for a set of SWC values, which are common for both tests sites (dry, intermediate, and wet conditions). The modeled traces are standard analyzed such as the experimental data by first arrival time picking and calculate the permittivity of the soil system (Table 4-2, see Chapters 2 & 3.).

First, we investigate the wave types and effect of the SWC on the GPR traces related to soil changes itself (Scenario I). For the shallow depth of 0.1 m, the direct wave and the critical refracted air wave are interfering in both cases and no differentiation between these events is possible (Figure 4-6). Therefore, using current analysis tools like first arrival time picking, such data needs to be rejected from the interpretations since the air wave interference causes an under estimation of the permittivity and hence the SWC (Table 4-2 & Table 4-3).

Table 4-2: Permittivity results for the two-dimensional study for Scenario I & II for R_{UT} & R_{LT}, for different SWC conditions. The misfit between the picked travel time permittivity and the permittivity of the HHS is provided in brackets below the values. Note the ε_r of the HHS is considered as the true value.

Depth	**R_{UT}**		**R_{UT}**	
[m]	**Scenario I**	**Scenario II**	**Scenario I**	**Scenario II**
SWC in the HHS	**0.05**		**6.08**	
ε_r in the HHS	**5.22**		**6.08**	
0.1	3.06 (-41.3%)	3.10 (40.67%)	3.36 (-44.71%)	3.39 (-44.26%)
0.2	4.83 (-7.49%)	5.15 (1.36%)	5.55 (-8.81%)	5.98 (-1.68%)
0.4	5.21 (0.13%)	5.54 (6.23%)	6.09 (0.08%)	7.55 (24.08%)
0.6	5.21 (0.13%)	5.50 (5.39%)	6.09 (0.08%)	8.29 (36.19%)
0.8	5.21 (0.13%)	5.33 (2.18%)	6.09 (0.08%)	7.79 (28.02%)
1.2	5.21 (0.13%)	5.22 (-0.06%)	6.09 (0.08%)	6.33 (4.01%)
SWC in the HHS	**0.15**		**0.20**	
ε_r in the HHS	**9.62**		**10.78**	
0.1	4.39 (-54.34%)	4.40 (-54.22%)	4.69 (-56.51%)	4.70 (-56.40%)
0.2	8.15 (-15.28%)	8.30 (-13.71%)	8.89 (-17.48%)	9.10 (-15.54%)
0.4	9.62 (0.02%)	10.05 (4.57%)	10.77 (-0.06%)	12.70 (17.85%)
0.6	9.62 (0.02%)	10.02 (4.19%)	10.77 (-0.06%)	13.75 (27.58%)
0.8	9.62 (0.02%)	9.78 (1.66%)	10.77 (-0.06%)	13.07 (21.30%)
1.2	9.62 (0.02%)	9.61 (-0.04%)	10.77 (-0.06%)	11.10 (2.95%)
SWC in the HHS	**0.25**		**0.35**	
ε_r in the HHS	**15.35**		**20.32**	
0.1	5.77 (-62.39%)	5.78 (-62.33%)	6.82 (-66.43%)	6.83 (-66.41%)
0.2	11.62 (-24.25%)	11.69 (-23.83%)	14.31 (-29.58%)	14.43 (-28.99%)
0.4	15.35 (0.01%)	15.90 (3.60%)	20.32 (0.00%)	22.96 (12.98%)
0.6	15.35 (0.01%)	15.87 (3.41%)	20.32 (0.00%)	24.50 (20.57%)
0.8	15.35 (0.01%)	15.55 (1.36%)	20.32 (0.00%)	23.51 (15.71%)
1.2	15.35 (0.01%)	15.35 (0.01%)	20.32 (0.00%)	20.78 (2.26%)

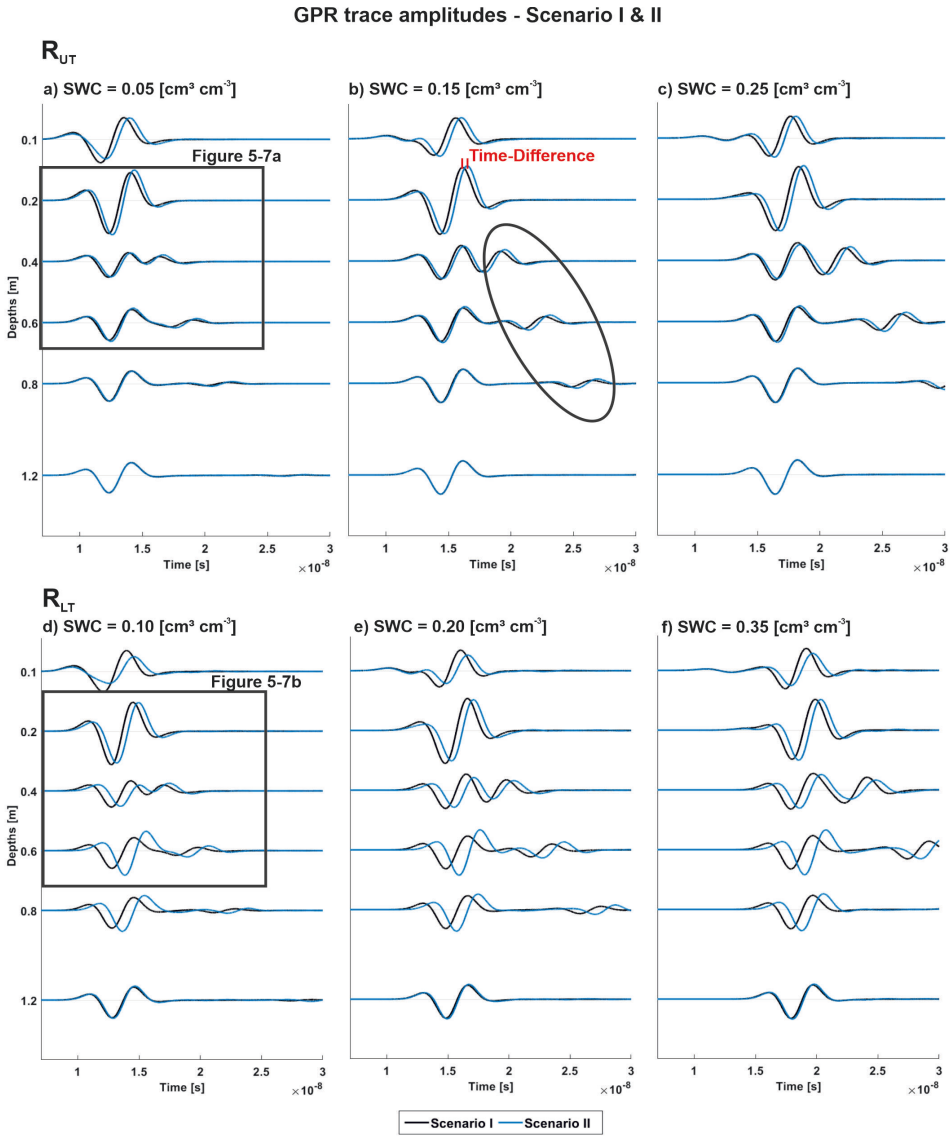

Figure 4-6: GPR traces modelled in 2D for 200 MHz, where the black and blue solid line indicates Scenario I and II for the different depths of the MR facilities. The corresponding traces are shown for the different MR facilities and different soil water content (SWC) conditions a)-c) for R_{UT} and d)-f) for R_{LT}. The black box in a) indicates the zoom area shown in Figure 4-7.

Klotzsche et al. (2016) observed similar features and concluded that only full-waveform approach can analysis such events. By comparing the 'true' permittivity values with the first arrival time picking derived permittivity, we clearly can see that with increasing depth and permittivity the misfit decreases and have the smallest errors (Table 4-2). For the depth 0.1 m the misfit shows values between 41.3% and 66.43% for R_{UT} (SWC = 0.05 cm^3 cm^{-3}) and R_{LT} (SWC = 0.35 cm^3 cm^{-3}), respectively. For depth 0.2 m this misfit is already significantly lower, between 7.49% and 29.58%, for the remaining depths the misfits is smaller than 1%. For all the different SWC conditions and for both MR facilities the 'measured' permittivity underestimates the permittivity present in the homogeneous half space (HHS), see Table 4-2. We will further exclude this depth from the detailed analysis. This wave interferences are also partly present at depth 0.2 m, especially for very dry soil conditions with a low permittivities. Nevertheless, for depth 0.4 m the first arrival time picking becomes more robust to reconstruct the actual soil permittivity (Scenario I), although the interferences still effect the amplitude of the trace, and it is not possible to clearly distinguish between the different wave types. Starting from depth 0.4 m, the different wave types begin to be separated and the direct wave is less affected by the reflection from the subsurface, which arrives later in time (Figure 4-6, black circle). For increasing permittivity these reflections become clearer and more distinct. Note that, both MR facilities are affected by these wave interferences, although R_{LT} is less impaired since the overall permittivity is higher as for R_{UT}.

In the next step, we increased the complexity of the model by incorporating the root information (Scenario II). By comparing the EM waves for the different scenarios (I & II), we first notice a difference in the travel times, where the first arrival of the EM wave is delayed for Scenario II (Figure 4-6 and Figure 4-7). This effect differs for the different SWC conditions and the MR facilities, whereas with increasing SWC the travel time difference between Scenario I and II increases and the travel time differences for R_{LT} are larger than for R_{UT}. The time shift is caused by the increased permittivity associated with the *RVF* and therefore an overall decreased wave velocity and hence resulting in later arrival times.

For Scenario II at R_{UT} we notice, that only for the depth 1.2 m for all SWC conditions, the misfit between the permittivity of the HHS and the 'measured' permittivity $<$ 1% (Table 4-2) indicating that the roots have a significant effect on the permittivity values and in most cases lead to an increased permittivity. Interestingly to notice is the effect of the roots for the shallow depth of 0.2m depth. The misfits between the 'measured' permittivity and the permittivity of the homogenous half space (HHS) for Scenario I & II, is smaller for Scenario II (Table 4-2). Especially for dry conditions for the soil permittivity between $5<\varepsilon_r<6$, the misfit is reduced by 5%. The additional root phase in soil system reduces the interferences on the first arrival time, which is related to the higher overall permittivity in the soil system, where the interferences have less influences. While for Scenario I, the true permittivity values are identified by the first arrival picking for most cases below 0.4 m depth, for Scenario II the misfit depends on the amount of roots present in this depth range (Table 4-2. For example, for R_{LT} the highest misfits are observed for the depths 0.6 m and 0.8 m, where also the highest *RVF* are present (Figure 4-3).

Considering the entire phase of the traces, we notice differences in for the first cycle amplitude and in the maximum amplitude, e.g., R_{UT} depth 0.2 m and R_{LT} depth 0.2 m – 0.6 m (Figure 4-7). Furthermore, for some depths a phase shift in late arrivals is especially

recognizable for R_{LT} at depths 0.6 m and 0.8 m, again associated with the highest *RVF* area. To quantify these phase shifts, we estimated the travel times differences of the maximum amplitude (Table 4-3). For R_{UT} it is the largest time difference can be observed for 0.2 m depth and for R_{LT} for the 0.6 m depth, which correlated with high *RVF* values. Additionally, we notice an increasing difference with increasing SWC.

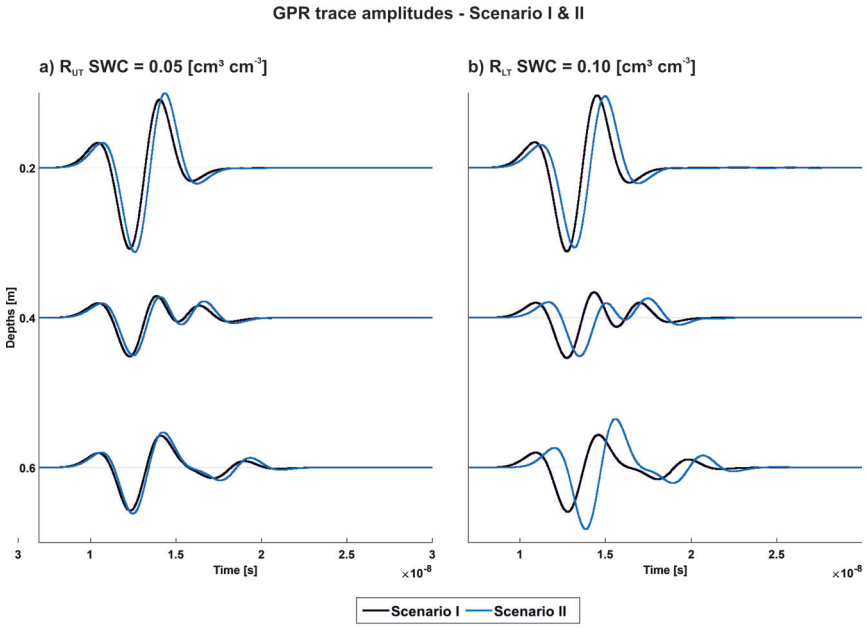

Figure 4-7: Detailed view of Figure 4-6 for the traces of the depth of 0.2, 0.4, and 0.6 m for a) R_{UT} and b) R_{LT}, where the black and blue solid line represents Scenario I and II, respectively.

Table 4-3: Differences between the travel times of the maximum amplitude between Scenario I and II, for R_{UT} and R_{LT}.

		Travel time differences					
		R_{UT}			R_{LT}		
SWC in the HHS	[cm³ cm⁻³]	**0.05**	**0.15**	**0.25**	**0.10**	**0.20**	**0.35**
	Depth	[ns]					
0.2		0.31	0.37	0.40	0.46	0.50	0.46
0.4		0.20	0.24	0.22	0.71	0.64	0.66
0.6	[m]	0.13	0.16	0.17	1.0	1.02	1.06
0.8		0.08	0.06	0.07	0.87	0.85	0.88
1.2		0.01	0.01	0.00	0.09	0.10	0.11

An influence of the roots on the amplitude of the traces is especially recognizable for R_{LT} (Figure 4-6 and Figure 4-7). Using the estimated permittivity of each scenario, we calculated the three-phase and four-phase SWC either ignoring the root part in the calculation or using

the *RVF* information. As expected from the feasibility study, if the root parts are not incorporated, the SWC is overestimated, depending on the *RVF* (compare to Figure 4-3). The overall errors are smaller in contrast to the true values for higher SWC values and decrease with depth. Note that if the *RVF* are not incorporated in the calculations, errors between -3% to 55% can occur (not considering depth 0.1 m).

Table 4-4: Three-phase soil water content (SWC) for Scenario I and three-phase and four-phase SWC results for Scenario II for R_{UT} & R_{LT} and different SWC conditions between 0.05 – 0.35. The [%] misfit between the three- & four-phase SWC is provided in brackets.

Depth [m]	$\mathbf{R_{UT}}$ Scenario I	$\mathbf{R_{UT}}$ **Scenario II**		$\mathbf{R_{LT}}$ **Scenario I**	$\mathbf{R_{LT}}$ **Scenario II**	
	three-phase SWC	**three-phase SWC**	**four-phase SWC**	**three-phase SWC**	**three-phase SWC**	**four-phase SWC**
SWC in HHS		**0.05**			**0.10**	
0.1	-0.02	-0.01	-0.04 (157.14%)	0.02	0.02	-0.01 (-134.78%)
0.2	0.04	0.05	0.02 (-50.00%)	0.09	0.10	0.06 (-39.18%)
0.4	0.05	0.06	0.05 (-18.64%)	0.10	0.13	0.09 (-36.57%)
0.6	0.05	0.06	0.05 (-17.54%)	0.10	0.15	0.07 (-55.33%)
0.8	0.05	0.05	0.05 (0.00%)	0.10	0.14	0.12 (-11.43%)
1.2	0.05	0.05	0.05 (0.00%)	0.10	0.11	0.10 (-6.60%)
SWC in HHS		**0.15**			**0.20**	
0.1	0.03	0.03	0.01 (-81.48%)	0.06	0.06	0.03 (-49.21%)
0.2	0.12	0.12	0.10 (-19.51%)	0.16	0.17	0.13 (-22.75%)
0.4	0.15	0.16	0.15 (-6.92%)	0.20	0.23	0.19 (-20.94%)
0.6	0.15	0.16	0.15 (-6.33%)	0.20	0.25	0.17 (-32.94%)
0.8	0.15	0.15	0.15 (0.00%)	0.20	0.24	0.23 (6.64%)
1.2	0.15	0.15	0.15 (0.00%)	0..20	0.21	0.20 (-3.40%)
SWC in HHS		**0.25**			**0.35**	
0.1	0.06	0.09	0.07 (-23.91%)	0.12	0..12	0.09 (-27.12%)
0.2	0.19	0.22	0.19(-11.52%)	0.26	0..26	0.23 (-14.45%)
0.4	0.25	0.28	0.28 (-3.50%)	0..35	0.39	0.34 (-12.99%)
0.6	0.25	0.28	0.28 (-3.50%)	0.35	0.40	0.32 (-20.54%)
0.8	0.25	0.28	0.28 (-0.36%)	0.35	0.39	0.38 (-4.08%)
1.2	0.25	0.28	0.28 (0.00%)	0.35	0.36	0.35 (-1.97%)

To characterize in more detail the observed wave interferences, we calculated the corresponding frequency spectra of the GPR traces for the Scenario I and II for the intermediate soil conditions with a SWC of 0.15 cm^3 cm^{-3} and 0.2 cm^3 cm^{-3}, for R_{UT} and R_{LT}, respectively (Figure 4-8). For the frequency spectra for depth 0.2 m and 0.6 m depth, we notice that the center frequency of the data is at around 200 MHz. The constructive interference at 0.2 m cause a higher amplitude of the frequency spectrum almost twice as high as for depth 1.2 m. For depth 0.6 m we can observe the interferences of the direct air wave and the refracted wave also in the frequency spectra causing two peaks in the frequency spectrum, for both MR facilities, which indicates the partly overlap of the EM waves (Figure 4-6). Comparing the different scenarios, we notice that for Scenario II the center frequency is slightly reduced.

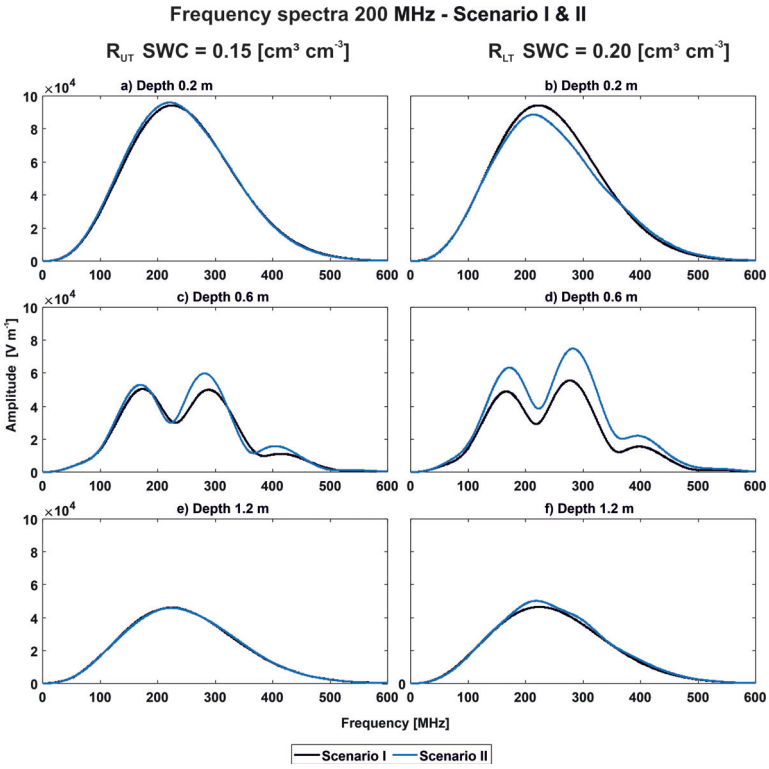

Figure 4-8: Frequency spectra for a SWC of 0.15 cm^3 cm^{-3} and 0.2 cm^3 cm^{-3} for R_{UT} and R_{LT}, respectively, for exemplary depths of 0.2, 0.6 and 1.2 m. Frequency spectra for R_{UT} are shown in a), c) and e), and for R_{LT} in b), d) and f). The black and blue solid line indicates Scenario I and II, respectively.

For a better understanding, how the EM waves propagates in the two-dimensional space with and without the presences of the roots, we analyzed the image plots for various time steps of the EM wave propagations. We chose to estimate these time steps the R_{LT} setup with the SWC of 0.10 [cm^3 cm^{-3}] at depth 0.2 m (Figure 4-9). Thereby, we notice for Scenario I, that the EM wave propagated relatively circular and uniform through the soil, whereas for Scenario II, the EM wave show more scatterings and amplitude changes over the half space. At 3 ns and 5 ns (Figure 4-9b and c, f and g), clearly the development of the different wave types at the soil-air interface is visible, where the wave in air travels faster as the wave in the soil. At later times of 7 ns (Figure 9d, h), clearly an event can be observed with increased amplitude (Figure 4-9d, black circle). Below, these positive interferences, a time shift and a diminished amplitude is present (Figure 4-9d, black arrow), Both events can be related to the phase and amplitude of the corresponding measured traces as shown in Figure 4-6d. The electrical field distribution when the Tx ad Rx are located at depth 0.6 m for the same model case, show overall less wave interferences, although the wave interaction close to the surface can be observed (see Appendix C-2 Figure C-2.1).

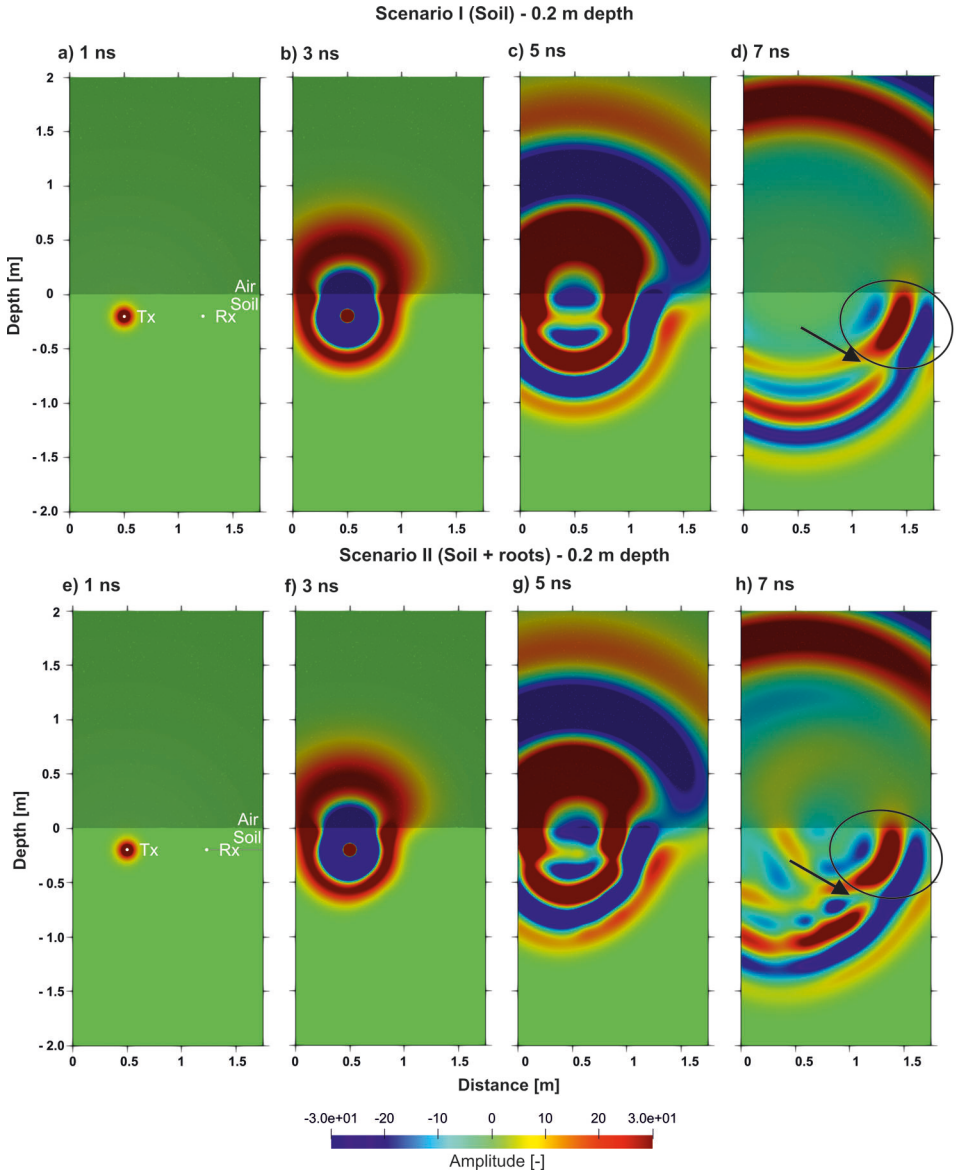

Figure 4-9: Image plots a)-d) for Scenario I and e)-h) for Scenario II of the forward modeled electrical field distributions through the model domain for four time steps when the Tx and Rx are located at 0.2 m depth in the R_{LT} with a SWC of 0.1 [$cm^3\ cm^{-3}$].

4-6 Effects of electrical conductivity of the roots on the GPR signal

To investigate the influence of the root electrical conductivity, we tested different conductivities for the root component in the soil system, while keeping the electrical conductivity of the soil at $\sigma_s = 0.015$ [S m^{-1}] constant. Since the root electrical conductivity varies with age, root system architecture and diameter, we tested two different conductivities based on literature values. For the fraction of the roots we considered the corresponding root electrical conductivity of either $\sigma_R = [0.05$ S m$^{-1}]$ or $\sigma_R = 0.03$ [S m^{-1}], and for the fraction of the soil we considered the electrical conductivity of the soil with $\sigma_s = 0.015$ [S m^{-1}]. We performed these tests for exemplary models of Scenario I and II with the SWC of 0.15 cm^3 cm-1 and 0.2 cm^3 cm-1 for R_{UT} and R_{LT}, respectively (Figure 4-11). As expected by the increased electrical conductivity and hence higher wave attenuation, for the cases with the larger electrical conductivities of the roots the amplitudes are smallest. But, overall, only minor differences in the first cycle amplitudes between the traces of the three cases are visible indicating that the electrical root conductivity does not have a large effect on the GPR traces. This finding suggests that in further research with more complex soil or/and root models, the different electrical root conductivities are not a major contributor on the GPR signals rather than the soil electrical conductivity.

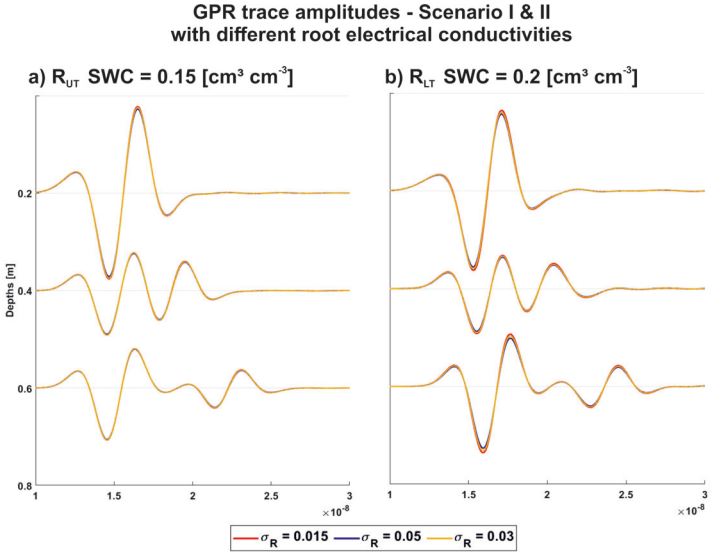

Figure 4-10: GPR traces modeled in 2D for 200 MHz while using different electrical root conductivities σ_R for Scenario II for a) R_{UT} with a SWC of the HHS of 0.15 [cm^3 cm^{-3}] and b)) R_{LT} with a SWC of the HHS of 0.2 [cm^3 cm^{-3}], where the red solid line indicates $\sigma_R = 0.015$ [S m^{-1}], the blue solid line indicates $\sigma_R = 0.05$ [S m^{-1}], and the yellow solid line indicates $\sigma_R = 0.03$ [S m^{-1}]. Note that only traces related to the highest *RVF* region are plotted.

4-7 Effects of the measurement frequency on the GPR signal

When talking about resolution and reconstruction of medium properties it is also necessary to consider the actual sensing volume (SV) of the GPR measurements. The SV of GPR measurements is characterized by the Fresnel volume, which has the shape of an elongated rotational ellipsoid. The foci of this ellipsoid are the locations of Tx and Rx. The dimensions (size of volume) depend on the distance between Tx and Rx, GPR center frequency, and bulk soil permittivity (Appendix D). As the recent research related to the MR facilities focused on 200 MHz data because of the commercial availability, the previous tests were focusing on this frequency. Since roots and the related rhizosphere are in the millimeter to centimeter scale, higher frequency GPR data such as 500 MHz would be more suitable to better disentangle the different contributions of the medium. Note that, antennae in the GHz range should not be considered since the distance of the rhizotubes and the wave attenuation would prevent the detection of the signal.

Since the bulk soil permittivity depends on the actual SWCs and soil structural properties, we calculated like in Appendix D the SV as a function of SWCs for the MR-facilities for 200 MHz and 500 MHz to estimate the possibilities to detect roots or the rhizosphere in the soil better (Table 4-5). Using 500 MHz antennae instead of a 200 MHz antennae, the SV could be reduced by a factor between 3 to 4, and especially for wet conditions with a high permittivity/SWC. Therefore, we perform forward modeling using a source wavelet with a center frequency of 500 MHz to investigate if the interfering waves and effects caused by the presence of the roots can better be distinguished and analyzed. For an exemplary

Table 4-5: Sensing volume (SV) for the different SWC and different frequencies for R_{UT} and R_{LT}.

	R_{UT}		R_{LT}		
Frequency [MHz]	**200**	**500**		**200**	**500**
SWC in HHS			SWC in HHS		
[cm^3 cm^{-3}]	[m^3]		[cm^3 cm^{-3}]	[m^3]	
0.05	0.43	0.11	**0.10**	0.39	0.10
0.15	0.28	0.08	**0.20**	0.25	0.07
0.25	0.20	0.06	**0.35**	0.16	0.05

model scenario, we considered a for R_{UT} and R_{LT} a SWC of 0.15 cm^3 cm^{-3} and 0.2 cm^3 cm^{-3}, respectively (Figure 4-11). When using 500 MHz as the frequency for the source wavelet, we can recognize similar findings as for the 200 MHz simulations. First, we can notice the interference of the direct air wave and refracted air wave, where for the 0.1 m depth we observe small amplitude prior to the actual first arrival of the EM wave. For the 0.2 m depth the interfering wave arrive at the Rx location almost at the same time as the direct ground wave and are very difficult to distinguish the first arrivals. For traces at a depth of 0.4 m and 1.2 m we notice, clear amplitudes after the arrival of the direct ground wave, where with increasing depth the interfering wave arrival times increases and we can clearly distinguish the events (Figure 4-11, black circles). For the comparison between Scenario I and II, the differences while using a frequency of 500 MHz seem more significant than using 200 MHz. Overall, we notice a later first arrival time when including the roots into the model. While for R_{UT} and the uppermost depths for R_{LT} the arrivals times are not significantly different,

for the traces below depth 0.8 m for R_{LT} larger offset can be observed. Additionally, the interfering waves are also affected by this delay in travel time. Interestingly to notice is phase and the amplitude behavior of the traces at depth 0.2 m to 0.6 m for Scenario II for R_{LT}. These traces show an increase amplitude for the first direct waves in contrast to Scenario I. The corresponding frequency spectra are minorly affected by the roots and the wave interfered as the 200 MHZ data (Appendix C-3, Figure C-3.1). While for the for data at depth 1.2 m the center frequency is at about 500 MHz, for depth 0.2 m depth the center frequency is reduced to approximately 400 MHz to 420 MHz.

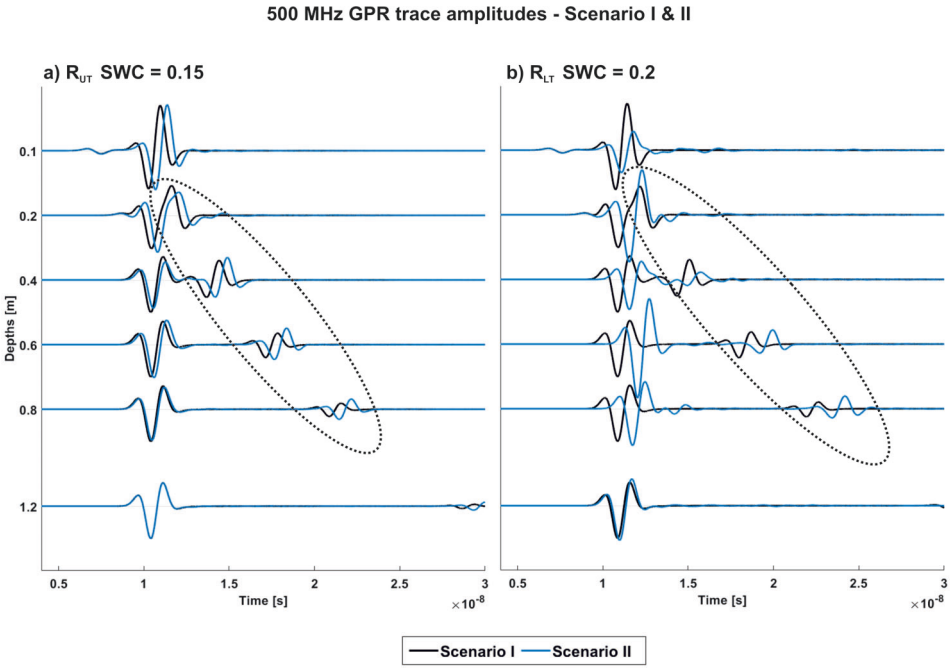

Figure 4-11: GPR traces modeled in 2D for 500 MHz, where the black solid line indicates Scenario I and the blue solid line represents Scenario II for the different depths of the MR facilities. The traces are shown for a) R_{UT} with a SWC of 0.15 [cm^3 cm^{-3}] for the HHS and b) R_{LT} with a SWC of 0.2 [cm^3 cm_{-3}] for the HHS.

4-8 Effects of the above-ground shoot on the GPR signal

To further investigate the influence of the above-ground shoot on the GPR traces, we need to expand the model domain into 3D (Scenario II and IV) to realistically model the EM propagation related to cylindrical object on top of the soil. Note that, cylindrical objects cannot be modeled properly in the 2D space. We assumed the above-ground shoot to be a cylinder with a diameter of 0.03 m and a height of 1.5 m. First, we considered only one maize plant on the soil, and second, we extend the model to multiple maize plants. For the second part, we

extended the model domain in the z-direction and added shoots with the same dimension as before, with a separation of 0.12 m. The root distribution was just extended in the z-direction.

When considering the EM wave results of the three-dimensional study for Scenario III and IV, we first notice the same influences of the direct air wave and refracted wave shallow depths (Figure 4-12). The difference in the two scenarios is the presence of roots. Under the consideration of the presence of the above-ground shoot for both scenarios, we notice the same influence of roots, where the first arrival is delayed, and the amplitudes are smaller. But in the uppermost depths 0.1 m to 0.4 m, we can see later wave arrivals, which were not present in the two-dimensional simulation without the above-ground shoot. When considering not one but multiple above-ground shoots, we can identify multiple reflections in the uppermost depths (Figure 4-12c & d). When we compare the permittivity of the

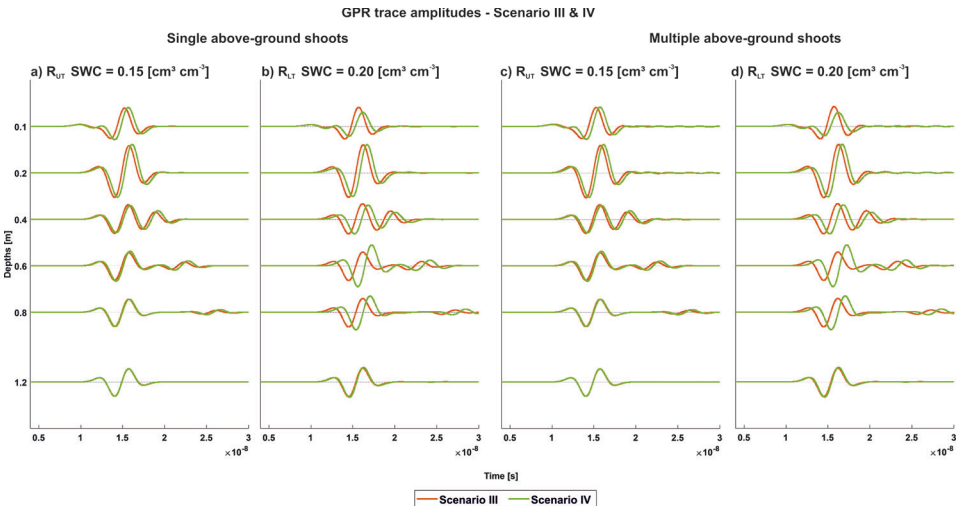

Figure 4-12: Three-dimensional synthetic EM waves for 200 MHz, where the orange solid line indicates Scenario III and the green solid line represents Scenario IV for the different depths of the MR facilities. The EM waves are shown for a) R_{UT} with a SWC of 0.15 [cm^3 cm^{-3}] for the HHS and b) R_{LT} with a SWC of 0.2 [cm^3 cm^{-3}] for the HHS.

HHS with the 'measured' permittivity, we again have the highest misfits present in the uppermost depths (Table 4-6). Furthermore, we can compare the misfits of Scenario I and III, to estimate the influence of the above-ground shoot on the signal. Whereas the misfit decreases between the 'true' and 'measured' permittivity, e.g., for depth 0.2 m at R_{UT} (SWC = 0.15 cm^3 cm^{-3}) the misfit for Scenario I is 15.28% and for Scenario III (single plant) it is 12.03% (Table 4-2 & Table 4-6). This effect is even more enhanced under consideration of multiple above-ground shoots, here for Scenario III a misfit of -9.92% is present. Since we only consider the first arrival of the traces to derive the 'measured' permittivity the misfits for the scenarios without the above-ground shoot and the one with shoot are not significant. Note that, the shoots seem to only affect later arriving reflections in the signal and therefore the first arrival time picking is only minorly affected.

When analyzing the three- and four-phase SWC under consideration of the above-ground shoot (single & multiple), the effects are dominated by the impacts we had already noticed, so that only depth and 0.1 m and 0.2 m indicate different SWC values between single and multiple shoots (Appendix C-4, Table 4-4). Concluding, we can additionally note, that the *RVF* has the same influence on the misfit and the difference between the three- & four-phased SWC, as noticed for Scenario I & II, where the misfit increases with the increased presence of roots and the difference between (Table 4-4 & Appendix C Table C-4.1). Note that, changed infiltration patterns, caused funneled precipitation by stem flow, into the soil could not considered in this study.

In the frequency spectra (Appendix C-4, Figure C-4.1), we can see an influence of the above-ground shoot, but only for the depth of 0.6 m, where the maximum around 300 MHz is significantly larger than for the scenarios without the above-ground shoot. Furthermore, we notice the same effects on the spectra as for Scenario I & II, where in the depth 0.2 m indicates an amplitude twice the amplitude as for depth 1.2 m, caused by the interferences with the reflected and refracted wave. But no significant difference is noticeable between a single and multiple above-ground shoots.

Table 4-6: Permittivity results for the two-dimensional study for Scenario III & IV for R_{UT} & R_{LT}, for different SWC conditions. The misfit between the picked travel time permittivity and the permittivity of the HHS is provided in brackets below the values. Note the r of the HHS is considered as the true value.

Depth [m] **SWC in HHS**	**R_{UT}** **0.15**		**R_{LT}** **0.2**	
ε_r in the HHS	**9.62**		**10.78**	
	Single above-ground shoot			
0.1	4.69 (-51.22%)	4.71 (-51.06%)	5.00 (-53.66%)	5.01 (-53.50%)
0.2	8.46 (-12.03%)	8.68 (-9.68%)	9.24 (-14.30%)	9.52 (-11.68%)
0.4	9.62 (0.0%)	10.03 (4.26%)	10.74 (0.32%)	12.64 (17.25%)
0.6	9.62 (0.0%)	10.00 (4.00%)	10.74 (0.32%)	13.67 (26.83%)
0.8	9.62 (0.0%)	9.76 (1.49%)	10.74 (0.32%)	12.97 (20.32%)
1.2	9.62 (0.0%)	9.59 (-0.25%)	10.74 (0.32%)	11.00 (2.04%)
	Multiple above-ground shoots			
0.1	5.05 (-47.52%)	5.06 (-47.33%)	5.38 (50.08%)	5.38 (-50.08%)
0.2	8.66 (-9.92%)	8.94 (-7.07%)	9.50 (11.89%)	9.83 (-8.79%)
0.4	9.62 (0.0%)	10.03 (4.26%)	10.74 (0.32%)	12.64 (17.25%)
0.6	9.62 (0.0%)	10.00 (4.0%)	10.74 (0.32%)	13.67 (26.83%)
0.8	9.62 (0.0%)	9.76 (1.49%)	10.74 (0.32%)	12.97 (20.32%)
1.2	9.62 (0.0%)	9.59 (0.25%)	10.74 (0.32%)	11.00 (2.04%)

4-9 Conclusion and Outlook

Since the effects of roots and the rhizosphere on the GPR signals are not fully understood we investigated various effects in a numerical study using realistic model scenarios. A feasibility study demonstrated the need that *RVF* should be considered in the SWC calculations if a threshold of 5% is reached and especially under the consideration of row crops. In trench wall root count data values above this threshold were observed and therefore we considered this root information as input for our synthetic models. To disentangle the different influences of the soil, water, roots, and above-ground shoots, we considered different scenarios with varying compositions and calculated the corresponding GPR traces. Because we have seen influences by the presence of roots and above-ground shoots on field measurements, we used two MR facilities as a template for the setup of the model, with varying soil types and root distributions.

We observed two major impacts on the GPR signal. First, the air-subsoil interface causes critical refracted air waves and reflections, which are nearly impossible to distinguish from the direct ground wave for shallow investigation depths of 0.1 m. Here, we noticed that an increase in permittivity and therefore SWC or root fraction (associated with higher permittivity), results in a better distinction between the different wave types. Additionally, such effects can be minimized, when using a higher measurement frequency with shorter wavelength where such events can be better recognized. Note that, also the SV with higher frequencies is reduced and therefore, small-scale variability can better be detected.

Second, the presence of roots, which resulted in a permittivity increase for the grid cell, lead to an effect on the first arrival time and amplitudes of the GPR trace. This time shift causes an overestimation in SWC, if a conventional three-phase soil system calculation for the SWC is used. To calculate the SWC for the soil-plant continuum as a soil system with four phases (soil, air, water, and roots), we used the mean *RVF* between the transmitting and receiving antenna. This approach bares the uncertainty of the SV of the GPR measurements, since depending on frequency and bulk permittivity of the soil, different SV are present in the shape of an elongated rotational ellipsoid with the foci at the locations of transmitting and receiving antennae. When calculating the four-phase SWC all roots present in the ellipsoid should be considered, but the estimation of the number of roots is nearly impossible with the investigation techniques currently available. Here modeling approaches, which could provide factors to use either root information derived from root images or trench wall counts, to derive the *RVF* for a certain soil volume, would be beneficial. Additionally, the estimation of the *RVF* from the root count density contains uncertainties. We considered the roots to grow straight through the grid and the root diameter to equal over the entire root system. Especially maize roots have a distinct root system architecture with the crown root on top of the soil and close to the shoot. Few studies have investigated the distribution of the root diameter distribution in the field, especially considering row crops, such as maize (Buczko et al., 2008). Anderson (1987) found larger maize root diameters within the crop row and Qin et al. (2005) detected larger root diameters in the topsoil. When considering the root as an individual phase within the soil system, we considered the root permittivity to be similar to the permittivity of water, but research in the permittivity of roots is rarely available. Al Hagrey (2007) only provided a permittivity for wood cellulose, depending on the water content between $4.5 < \varepsilon_R < 22$, because of the non-wooden nature of crop roots,

realistic values are unknown. Further research could include the investigation of the root permittivity in general, but also considering the root growth and decay under this aspect. Incorporating the distribution of the root permittivities into a root architecture model and combining this with a soil modeling tool for the precise generation of the model domain for the electromagnetic simulation would be more than beneficial to study the influence of the soil components on the GPR signal in more detail. With the here described approach, we adjusted the grid cell bulk permittivity under the presence of roots. Since coarse roots, as are present for maize crown roots have diameters > 2 mm and are of a wooden texture, they could cause reflection effects in the EM wave.

As one open question from the experimental data is related on how much crops above the surface effect GPR signals close to the surface. Therefore, we investigated the effects of a single and multiple above-ground shoots. While only late arrival phases and amplitudes are affected by the shoots, the first arrival times should not be affected. Note that infiltration processes related to stem flow, could not be investigated with the current model set up.

This simulation study is only the first step towards fully disentangling the GPR signal since here the soil profile had constant properties, which is not feasible, when investigating row crops. Additional simulations considering more soil layers could be performed. Furthermore, with this approach the time component in the soil-plant continuum has not been considered. While infiltration of precipitation and irrigation as well as soil water depletion are taking place, the bulk permittivity distribution varies. In this study the SWC conditions and therefore the permittivity of the HHS was considered to be equal. The use of a more realistic permittivity profile in all dimensions, would be essential here common soil modeling tools like HYDRUS-1D could be used to derive permittivity profiles, see Chapter 5. Further, the influence of soil nutrient/ fertilization (Kaufmann et al., 2019), management practices (Blanchy et al., 2020c) could be investigated.

Further advantages could be provided by using more sophisticated analysis approaches, such as full-waveform inversion (FWI) (Klotzsche et al., 2019, 2016, Yu et al., 2022). As observed in this study, effects caused by the root presence, conductivity changes and above-ground shoots are related to later EM wave phases and amplitudes, the FWI approaches, have the potential to analyze these effects. Considering FWI approaches have an increased computational demand and hence additions to data acquisitions should be considered.

Chapter 5

Spatial variability of hydraulic parameters of a cropped soil using horizontal crosshole ground penetrating radar

Abstract

Soil hydraulic parameters play a crucial role in crop growth, as they control the spatio-temporal distribution of water in the soil-plant continuum and thus affect water availability for crops. To provide reliable information on the soil hydraulic parameters at different scales, measurement techniques with a good spatial resolution and low labor costs are required. In this study, we used crosshole ground penetrating radar (GPR) derived soil water contents measured along horizontal rhizotubes under a controlled experimental test site cropped with winter wheat to estimate the parameters of the unimodal and dual-porosity Mualem-van-Genuchten model in a non-invasive manner. We applied a sequential hydrogeophysical inversion approach for a one-dimensional averaged case, by combining the GPR-derived soil water content with a hydrological model (HYDRUS-1D). To optimize the chosen approach, we considered different model configurations and performed additional synthetic studies. In addition, this approach was upscaled by deriving the 3D spatial distribution of soil hydraulic parameters for the entire field plot. We observed correlations between the individual soil hydraulic parameters. $\alpha 2$ and $n2$ in the dual-porosity Mualem-van-Genuchten model showed a negative correlation for both soil layers, while λ and K_s in the Mualem-van-Genuchten model showed only for the plow layer a correlation. Finally, we derive parameters for crop growth studies including the soil water content at field capacity, permanent wilting point and plant available water and their spatial variability.

Adapted from: Lena Lärm, Lutz Weihermüller, Jan Rödder, Jan van der Kruk, Harry Vereecken,

Anja Klotzsche: Spatial variability of hydraulic parameters of a cropped soil using horizontal crosshole ground penetrating radar. In Review at Vadoze Zone Journal, Submission-ID: *VZJ-2023-12-0120-OA*

5-1 Introduction

Understanding the hydraulic processes within the vadose zone is important for various applications including environmental studies, ecosystem science, agriculture, soil science, meteorology, and hydrology. To investigate the wide range of processes that influence the hydrological response between the subsurface and the atmosphere, it is necessary to access the hydrological systems at different scales (Vereecken et al., 2008; Vereecken et al., 2022). For example, small-scale modeling of rhizosphere processes and root-soil interactions requires information on the processes and parameters at the point- to rhizosphere(pedon)-scale (Schnepf et al., 2022), whereas land-surface or Earth system models used for ecosystem quantification and prediction require information at the field to regional scale (Looy et al., 2017; Vereecken et al., 2016; Simmer et al., 2015). Methods are therefore needed to provide soil parameters at different scales. When hydrological dynamics are in focus of interest, the soil water retention (SWR) and hydraulic conductivity characteristics (HCC) must be known, whereby the soil hydraulic parameters (SHP) usually derived either directly or indirectly. Direct methods are based on experiments, often conduced in the laboratory (rarely in the field), which are costly and labor intensive (Durner & Lipsius, 2005). Laboratory measurements of hydrological dynamics (SWR & HCC) are based on a variety of techniques using small-scale soil columns of a few cm3 (typically 100 - 300 cm3) in volume. In the field, the small representative volume for the estimation of the SHP by in situ soil water and matric potential sensors also limits this approach to relatively small units – mostly to the pedon scale. It is common practice to repeat the small-scale point measurements (usually by taking undisturbed samples for laboratory measurements) at the field scale for several sites, and to upscale the laboratory hydraulic parameters to the entire field site. Although, a detailed vertical representation of the heterogeneous soil can be mapped at the point locations, spatial distributions between the points and small-scale heterogeneities cannot be captured (Kool et al., 1987).

Over the last two decades, geophysical methods have been widely used to estimate indirect SWC. . Most popular techniques are Electrical Resistivity Tomography (ERT) (Michot et al., 2003; Brunet et al., 2010; Samouëlian et al., 2005), Electromagnetic Induction (EMI) (Brosten et al., 2011; Moghadas et al., 2017; Altdorff et al., 2017; Corwin & Lesch, 2005; Doolittle & Brevik, 2014; Sheets & Hendrickx, 1995), and Ground Penetrating Radar (GPR) (Huisman, Hubbard, Redman, & Annan, 2003; Klotzsche et al., 2018). While ERT and EMI provide the electrical conductivity as physical parameter, GPR is able to provide both the dielectric permittivity and electrical conductivity. Using petrophysical relationships such as Archies law for electrical conductivity or Topp's equation for permittivity (Topp et al., 1980), both parameters can be related to soil water content, which can be used as inputs to estimate hydraulic properties (SWR & HCC). A promising approach is the combination of non-invasive geophysical measurements and laboratory-based point information to upscale hydrological parameters to the catchment-scale. For example, large-scale 1 km2 EMI measurements were performed to obtain high resolution electrical conductivity maps for different sensing depths. Based on these maps and the obtained clusters, representative locations were selected for soil sampling that could be used for extrapolation in the obtained clusters (Brogi et al., 2019, 2021).

Another option to derive the SHP is to use time-lapse geophysical data sets and combine them with sequential or coupled inversion approaches. For the sequential inversion, the geophysical quantity such as electrical conductivity or GPR travel time (related to relative dielectric permittivity) is first converted to soil water content. In a second step, these derived soil water content estimates are used in an inversion to estimate the SHP using appropriate hydrological models. This approach has been successfully applied, for example, by Huisman et al. (2010) or Manoli et al. (2015) to obtain the SHP from ERT. Other successful studies have been performend with surface (Busch et al., 2013) and crosshole GPR (Looms et al., 2008; Rucker & Ferré, 2004; Yu et al., 2021/ Appendix F).

A more complex inversion scheme is the coupled hydrogeophysical inversion, where the geophysical information is not converted to soil water content prior to the inversion but used directly as information in the inversion process (Hinnell et al., 2010). In general, the coupled inversion will overcome potential errors introduced by the conversion of the measured geophysical quantity to the soil water content used in the sequential inversion, and therefore, this inversion scheme should be more reliable. On the contrary, the coupled inversion requires a state-of-the-art hydrological and geophysical model, both of which are often computationally demanding, and therefore, the computational requirements are increased in contrast to the sequential inversion approach (Yu, et al., 2021). Coupled inversions have been performed by e.g. Mboh et al. (2011), Kuhl et al. (2018), Tran et al. (2016) for ERT and by e.g., Yu et al. (2021)/ Appendix F for GPR. Yu et al. (2021) compared the performance and the reliability of both inversion approaches for GPR data acquired during an infiltration experiment. It was observed that in the presence of fast dynamics caused by infiltration or heavy rainfall, a coupled inversion should be considered, while for long term investigations covering entire seasons a sequential inversion can be equally efficient.

Even though most geophysical techniques can determine the water content in either two dimensions (Cassiani et al., 2012; Klotzsche et al., 2019/ Appendix D, Lärm et al., 2023b/Chapter 3) or even three dimensions (Beff et al., 2012; Koestel et al., 2008), the SHP was primarily estimated in one dimension (e.g., Jadoon et al., 2012; Busch et al., 2013). To our knowledge, a two- or three-dimensional estimation of the SHP based on geophysical data has yet to be performed. Especially, for small-scale field trials such as those used in breeding and fertilization experiments, the small-scale heterogeneity of the underlying soil might be significant for both analysis and the modelling processes involved in crop growth. Hereby, it is established that water and nutrient uptake by the plants through their root system is heavily reliant on the current water and nutrient availability in the small-scale volume surrounding the roots (rhizosphere). Even small changes can significantly affect the crop performance (Schnepf et al., 2022; Landl et al., 2019). In addition, biochemical processes like greenhouse gas formation often depend on the conditions of designated hotspots (e.g., Kravchenko et al., 2017). Therefore, the knowledge of the two- or three-dimensional states of the soil (e.g., water content, matric potential) is important, and as this information can generally be predicted by spatially resolved models, spatially resolved soil hydraulic parameters are also required.

In this study, we demonstrate that horizontal crosshole 200-MHz time-lapse GPR data can be used to derive the one-dimensional vertical SHP. Additionally, we explore the potential to map pseudo-3D representations of the SHP across a controlled experimental test site cropped with winter wheat. Therefore, time-lapse soil water content information was

extracted from crosshole GPR data along 7 m long rhizotubes. This data was then inverted to estimate the soil hydraulic parameters at a resolution of 0.05 meters. After demonstrating the feasibility of our sequential inversion for a one-dimensional averaged scenario, we utilize the approach to upscale the SHP to the entire field-plot providing detailed information about a soil volume with the dimension 3.0 m by 1.2 m by 0.75 m.

5-2 Materials and Methods

5-2-1 Data acquired at the minirhizotron facility Selhausen

To parameterize the hydrological model for this study, a comprehensive and detailed dataset is required. Therefore, we used the minirhizotron facility (MR facility) R_{LT} (Lärm et al., 2023a)/ Chapter 2) located within the TERENO (TERrestrial ENvironmental Observatories) Eifel-Lower Rhine observatory in North Rhine-Westphalia, Germany (Pütz et al., 2016, Bogena et al., 2018). The facility was situated within the lower terrace of the Rur-river system (Weihermüller et al., 2007; Brogi et al., 2019). The loess soil of the R_{LT} was formed by eolian deposits during the Pleistocene and is characterized as a Cutanic Luvisol (Ruptic, Siltic) (Bauer et al., 2012) based on the World Reference Base for Soil Resources (IUSS Working Group WRB, 2007). The soil contained 17% clay, 70% silt, and 13% sand as reported by Weihermüller et al. (2007). The soil is comprised of two distinct layers, namely the topsoil or plow layer that spans from 0 - 30 cm and the subsoil located below. For further details regarding the construction and setup of the MR-facilities, we refer to the works by Cai et al. (2016) and Lärm et al.(2023a)/ Chapter 2. Our investigation aimed to observe the effects of natural conditions, we focused on the middle Plot 2 of R_{LT}, where no additional surface water treatment such as rainout sheltering, or irrigation were applied (Figure 5-1). Within this plot, three sets horizontal rhizotubes with six depths ranging between 0.1 m and 1.2 m and a horizontal separation of 0.75 m between the rhizotubes. GPR and root image measurements were conducted utilizing these rhizotubes, as shown in Figure 5-1. A thorough dataset of all required parameters, including boundary conditions, soil states, precipitation, evapotranspiration, soil water content, soil water potential, and crop growth observations, is available for this site.

The field dataset was acquired during the crop growing season 2016 while winter wheat (cultivar Ambello) was grown (Table 1), the dielectric permittivity data is published in Lärm et al., (2023a)/ Chapter 2. Crop management practices, including pest control and fertilization, were executed in compliance with regional standards. The wheat was sown with a seeding density of 300 – 320 grains per m2 at a crop row separation of 12 cm perpendicular to the direction of the rhizotubes. The climatic variables used were obtained from the TERENO weather station (`SE_BDK_002`) located approximately 15 m away. Technical terms are defined upon first usage. Daily reference evapotranspiration (ET_0) was calculated according to FAO Irrigation and drainage paper 56 (Allen et al., 1998). Details of the calculation and gap filling is describecd by Graf et al. (2020) and Rahmati et al. (2020).

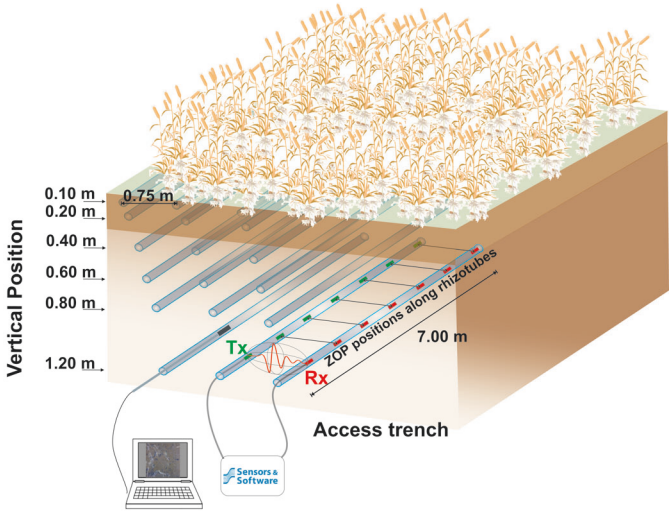

Figure 5-1: Schematic illustration of a plot within the minirhizotron facility and the zero-offset profiling GPR measurement and root imaging setup.

Table 5-1: Overview crop management and measurements for the crop growing season 2016.

Crop Cultivar	Winter Wheat (cv. Ambello)
Sowing Date	26.10.2015
Flowering Date	03.06.2016
Harvest Date	26.07.2016
GPR Measurements	20 (from 30.03.2016 to 08.08.2016)
Root Measurements	22 (from 16.11.2015 to 22.07.2016)
***LAI* Measurements**	20 (from 17.12.2016 to 22.07.2016)

The maximum rooting depth for various measurement dates was determined from available total root length values obtained from root image data sets captured using a minirhizotron camera (Bartz Technology Corporation, Carpinteria, CA, USA) inserted inside rhizotubes. The images were analyzed using an automatic image analysis pipeline developed by Bauer et al. (2022)/ Appendix E. Additionally, the leaf area index (LAI) was regularly measured during the vegetation period using a plant canopy analyzer (LIA-220, LI-COR Inc., USA).

5-2-2 GPR-derived soil water contents

GPR data were obtained through crosshole Zero Offset Profiling (ZOP), wherein the transmitting antenna (Tx) and the receiving antenna (Rx) were placed in adjacent rhizotubes at the same depth. The measurements were taken using a 200 MHz PulseEKKO System from Sensors & Software (Canada). The antennae are moved in parallel along the length of neighboring rhizotube with a 0.05 m measurement spacing. The standardized processing of crosshole GPR-ZOP data involves three steps: i) de-wow filtering, ii) time-zero correction, and iii) detection

of the first break point to estimate the travel time for each measurement point (for further details, refer to Klotzsche et al., 2019/ Appendix D). The velocity of the electromagnetic wave is determined by utilizing the known distance of 0.75 m between the rhizotubes along with the estimated travel time from each ZOP measurement location.The calculated v is converted into relative dielectric permittivity ε_r [-] using

$$\varepsilon_r = (\frac{c}{v})^2, \tag{5-1}$$

where c indicates the speed of light [m s^{-1}]. Considering appropriate petrophysical relationships or empirical equations, the volumetric SWC θ [cm^3 cm^{-3}] can be derived from the relative dielectric permittivity ε_r. For R_{LT} we use the Topp's equation (Topp et al., 1980)

$$\theta = -5.3 \times 10^{-2} + 2.92 \times 10^{-2}\varepsilon_r - 5.5 \times 10^{-4}\varepsilon_r^2 + 4.3 \times 10^{-6}\varepsilon_r^3. \tag{5-2}$$

The GPR-derived soil water content (SWC) values at a depth of 0.1 m in the uppermost rhizotube produced unrealistically low results due to interference from critically refracted air and direct waves (Klotzsche et al., 2016, 2019/ Appendix D). Thus, these values were omitted from the study. Moreover, the data at both ends of the 7 m rhizotubes were also excluded because they were affected by the access trench, soil sensors on one end, and the excavation trench on the other end. Only data within the range of 3 to 6 meters from the access trench was included. This resulted in 61 GPR SWC values for each depth, which were combined to create a semi-3D horizontal SWC depth plane. Another option is to use the mean SWC along the rhizotube, which is suitable for winter wheat because of its low crop row separation (refer to Klotzsche et al., 2019/ Appendix D). Due to the 2016 installation of a spectral electrical impedance tomography (sEIT) monitoring system between 5.5-6 meters along the rhizotubes (Weigand et al., 2022), data measured at a depth of 0.2 meters had to be disregarded.

5-2-3 Soil hydraulic modeling

The soil hydraulic parameters were estimated from GPR-derived SWC using the HYDRUS 1D software (Simunek, Van Genuchten, & Sejna, 2013), which solves the one-dimensional Richards equation (Richards, 1931) for a partially saturated, porous, and ridged medium:

$$\frac{\partial\theta(h)}{\partial t} = \frac{\partial}{\partial z}[K(h)(\frac{\partial h}{\partial z}) + 1] - S, \tag{5-3}$$

where t is time [d], z is the positive upward vertical coordinate [cm], and $K(h)$ is the hydraulic conductivity [cm d-1] as a function of the pressure head h [cm]. The sink term S determines the quantity of water extracted from the soil through root water uptake. To characterize root water uptake, we utilized the Feddes model (Feddes, Bresler, & Neuman, 1974) and adapted the Feddes root water uptake parameters from Wesseling (1991) for wheat vegetation. $P0$ was set to 0 cm, $P0_{opt}$ to -1 cm, $P2H$ to -5000 cm, $P2L$ to -9000 cm, and $P3$ to 16000 cm. The simulation domain reached a depth of 200 cm and includes an uppermost layer, which is the plow layer that is 30 cm thick and rests above the subsoil (Bt horizon). To apply the

sequential hydrogeophysical inversion approach to the field data, we extended the model to three layers, introducing a new layer between 100 and 200 cm depth. The model was discretized using 303 nodes, with the node spacing increasing with depth.

As the upper boundary condition, daily atmospheric conditions with surface runoff were used. Daily precipitation was distributed throughout the day using the sine function embedded in HYDRUS-1D. To differentiate potential transpiration T_0 from ET_0 during crop growth, we utilized Beers-Law:

$$T_0^{K_c} = ET_0(1 - e^{-k \cdot LAI}), \tag{5-4}$$

where k is the radiation extinction factor which typically ranges between 0.5 to 0.75 (here set to 0.625). Since FAO 56 calculated ET_0 is only valid for a grass reference the T0 was adjusted during crop growth using Kc vales as a function of LAI with

$$T_0^{K_c} = T_0 \cdot K_c. \tag{5-5}$$

Thus, the crop coefficient (K_c) was set to 1 during the initial growth stages and increased to a maximum of 2 at maximum leaf area index (LAI) during the flowering stage. Kc then decreased to 1.2 at harvest during the senescence period. The Kc values for intermediate periods were linearly interpolated and illustrated in Figure 5-2. The allowable minimum

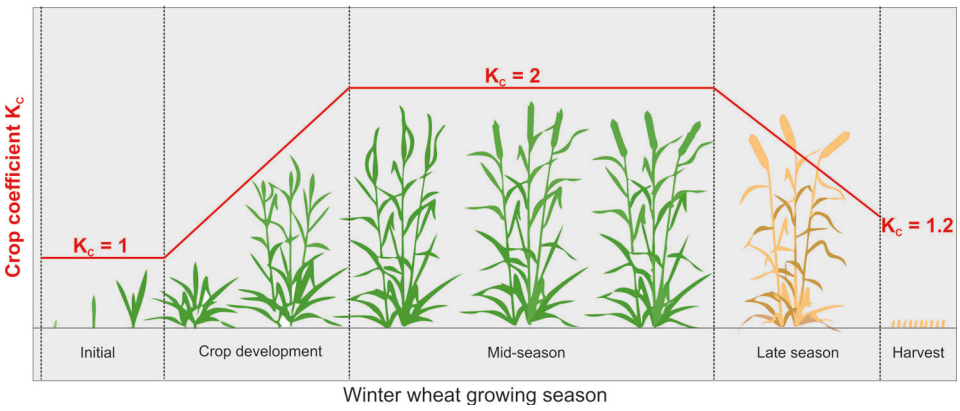

Figure 5-2: Crop coefficient K_c over the crop growing season of winter wheat. Adjusted after Pokorny (2019).

pressure head at the soil surface (hCritA) was set at -15,000 cm, which results in a transition of the upper boundary from flux to a fixed pressure head. The water table is situated between 3 to 5 meters below ground, contingent upon seasonal changes (Jadoon et al., 2012).

Therefore, the lower boundary was set to a specified pressure head [cm], as calculated from soil water potential (SWP) measurements at a depth of 140 cm recorded close to the

MR facility. To calculate the SWP at a depth of 200 cm (total simulation depth) a constant offset of 60 cm was added to the values recorded at 140 cm depth.

Two functions were considered for describing the soil water retention and hydraulic conductivity curve. The first is the unimodal or single porosity Mualem-van-Genuchten model (Van Genuchten, 1980; Mualem, 1976), referred to hereafter as the unimodal model. The second is the bimodal or dual-porosity model by Durner (1994), referred to hereafter as the dual porosity model. In the case of a dual porosity model, the soil water retention curve is described by:

$$\theta(h) = \theta_r + (\theta_s - \theta_r) \sum_{i=1}^{k} \omega_i Se_i \tag{5-6}$$

and

$$Se_i = [1 + |\alpha_i h|^{n_i}]^{m_i}, \tag{5-7}$$

where θ_r and θ_s are the residual and the saturated water contents [cm^3 cm^{-3}], respectively, k is the order of porosity in the soil system (here $k = 1$ for the unimodal and $k = 2$ for dual-porosity model), Se is the effective saturation [-], ω_i is the weighting factor ($\sum \omega_i = 1$). α_i [cm^{-1}], n_i [-], and m_i [-] are empirical parameters, whereby α_i can be related to the inverse of the air entry values and ni to the width of the pore size distribution, whereas mi is classically related to n_i by m_i = 1-1/n_i.

The relative soil hydraulic conductivity function *K(h)* is given by Priesack & Durner (2006):

$$K(h) = K_s \sum_{i=1}^{k} \omega_i Se_i^{\lambda} \left[\frac{\sum_{i=1}^{k} (1 - (1 - Se_i^{1/m_i})^{m_i})}{\sum_{i=1}^{k} \omega_i \alpha_i} \right]^r \tag{5-8}$$

where K_s [cm d^{-1}]is the saturated hydraulic conductivity, λ [-] is the tortuosity factor, r is a shaping factor for the relative hydraulic conductivity function and set to $r = 2$ according to (Mualem, 1976). This dual-porosity model's parametrization assumes two components in the soil: the soil matrix and macropores; unlike the SP model, which has only the matrix. As in numerous crop growth investigations, details regarding field capacity (FC), permanent wilting point (PWP) and plant available water (PAW) are necessary to compute soil characteristics obtained from the soil water retention and hydraulic conductivity curves. Therefore, FC was calculated by determining the SWC at a pressure head of pF 1.8 (equivalent to a height of 330 cm), while PAW was calculated as the difference in SWC between FC and PWP, defined at a pressure head of pF 4.2 (equivalent to a height of 15,000 cm) (Novák, 2018).

5-2-4 Sequential inversion

To estimate the SHP in the MvG models (unimodal and dual-porosity model), the Shuffled-Complex-Evolution algorithm (SCE-UA) as described by Duan et al. (1993 and 1994) was used. The SCE-UA is a global search routine that has been effectively utilized in hydrogeophysical inversion research conducted by Kuhl et al. (2018), Mboh et al. (2011), Busch et

al. (2013) and Yu et al. (2021)/ Appendix F. Normalized individual error terms were calculated for the plow and subsoil layers due to the presence of one rhizotube and four rhizotubes respectively. The squared sum of the differences between modeled SWC θ_{modj} and observed SWC θ_{obsj} were divided by the mean of the modeled SWC $\overline{\theta_{modj}}$per layer. Based on this, the cost function to be minimized can be written as:

$$CF = \sum_{i=1}^{n_{Layer}} \frac{\sum_{j=1}^{n_depths} (\theta_{modj} - \theta_{obsj})^2}{\overline{\theta_{obsj}}} \tag{5-9}$$

where CF is the normalized squared mean error, θ_{obs} and θ_{mod} are the observed GPR-derived and HYDRUS-1D modeled SWC, respectively. The inversion was terminated, when the objective function did not improve more than 0.01% within the last 10 inversion loops. Except for λ, expert knowledge was utilized to choose the feasible space for the parameter optimization for all parameters. According to the study conducted by Peters et al. (2011), a physical threshold of HCC = -2 for λ always yields robust results.

Various model setups were examined in this study, including two versus three layers and unimodal versus dual-porosity soil hydraulic characteristics. To determine the most suitable model for the data, we utilized the Akaike Information Criteria (AIC) (Akaike, 1974):

$$AIC = \ln(\frac{SSR}{N}) + 2_{n_{SHP}} + \frac{2n_{SHP}(2n_{SHP}+1)}{N - n_{SHP} - 1}, \tag{5-10}$$

where N is the number of GPR-derived SWCs, n_{SHP} is the number of optimized SHP and SSR is the sum of squared residuals between measurements and model results. The model with the lowest AIC values is deemed the best. Equation 5-10 demonstrates that the AIC's right-hand side penalizes the number of model parameters used. The AIC is advantageous over other statistical measures as it can be used even for a small number of observations N.

5-3 Results and Discussion

5-3-1 Field data set for hydraulic modeling

The TERENO weather station (`SE_BDK_002`) gathers data on on daily reference evapotranspiration (ET_0) and the precipitation (Figure 5-3a). The precipitation data shows sporadic rain events, with fewer occurrences during October 2015 and mid-May 2016, and higher rainfall events in June. Evapotranspiration is at its lowest during winter, increasing in spring and reaching its maximum during summer.

Based on the data from the root images, it is evident that the depth of root growth progressively increased until it reached a plateau during the flowering period, as demonstrated in Figure 5-3b. Due to constraints of the MR facility, root observation was feasible only until a depth of 1.2 m. Given that wheat is a crop known for its deep-rooting nature (Thorup-Kristensen et al., 2009), we extrapolated the rooting depth to a depth of 140 cm. The Leaf Area Index (LAI) exhibits low values during the initial growing stages but shows a significant increase from mid-March to early May (refer Figure 5-3b). The LAI fluctuates around a maximum between mid-May and early July, followed by a decrease towards the end

of the growing season. Both the LAI and the rooting depth are considered to be zero after the harvest date, assuming no root activity after removal of the shoots. As described earlier, using Equations 5-4 and 5-5, we adjusted the crop transpiration using a crop coefficient. This crop coefficient was linearly interpolated, according to Figure 5-2. The respective dates for changing the crop coefficient were determined by the observed LAI pattern (see Figure 5-3c).

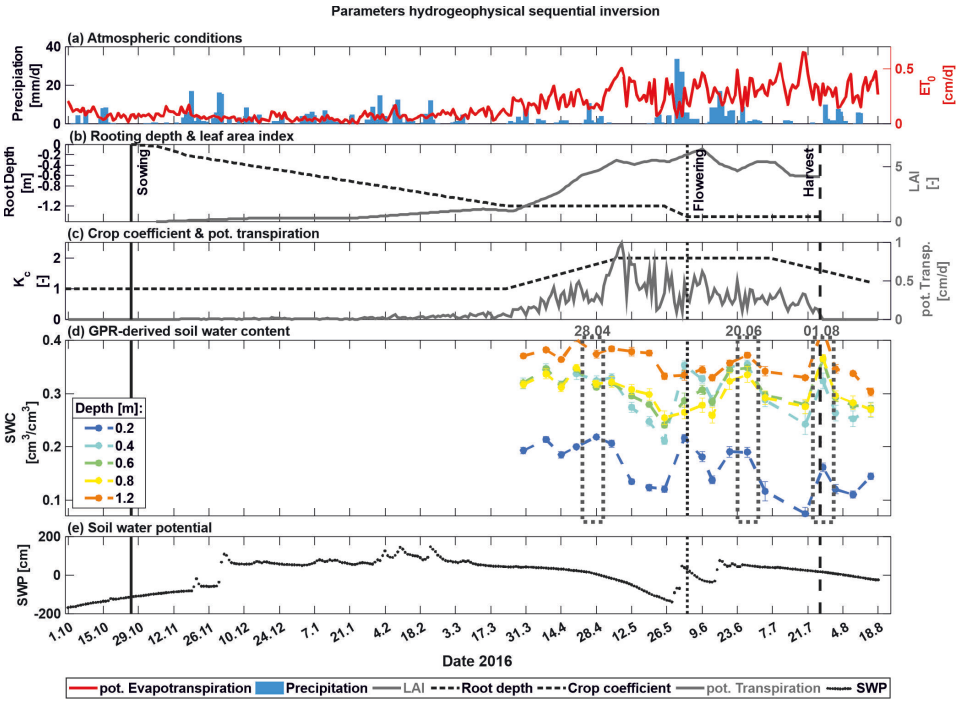

Figure 5-3: Parameters for the hydrogeophysical sequential inversion with (a) daily precipitation (blue bars) and reference grass evapotranspiration (red line). (b) leaf area index (LAI) (grey solid line) and the rooting depth (black dashed line) (c) crop coefficient (black dashed line) and rescaled potential transpiration (grey solid line). d) mean GPR-derived soil water content (SWC) (colored dashed lines) (e) soil water potential (SWP) at 140 cm depth (black dots). The vertical solid black line indicates Sowing date, the vertical dotted black indicates Flowering date and vertical dashed black line indicates Harvest date. The grey dashed frames indicate the GPR-derived SWC, which are shown in more detail in Figure 5-5.

To explore the temporal and vertical variations in GPR-derived SWC across both time and depth, we initially utilize the analysis the arithmetic mean of the SWC values along the rhizotubes (Figure 5-3a). Generally, lowest mean SWCs were detected in the plowed topsoil layer (0.2 m), with increasingly elevated amounts in deeper zones of the soil profile. Moreover, the temporal variability decreases with increasing depth as the dynamics stem primarily from the surface atmospheric conditions imposed, including evapotranspiration and precipitation. Fur-

thermore, heavy rainfall in June around flowering caused relatively high degree of saturation at 0.4 m depth. When comparing the mean GPR-derived SWC values (Figure 5-3d) with the precipitation and the evapotranspiration data (Figure 5-3a), a distinct correlation between SWC and the rainfall and drought events becomes evident. It should be noted that the differences in SWC between drier and wetter periods are not significant since the fine grained soil at the MR which allows it to hold water for extended periods, even during prolonged dry spells in the summer. The soil profile's lower boundary can be studied by analyzing SWP values taken at a depth of 140 cm near the MR facility (see Figure 5-3d). Generally, seasonal fluctuations occur with noticeable SWP increases during the winter months (October - February) and detectable increases towards the summer months (March - August), which reflect groundwater depletion and recharge throughout the year.

5-3-2 One-dimensional inversion results

As a first step, the mean GPR-derived SWC along the rhizotubes at each measurement depth were used in an inversion. In order to find a hydrological model that best represents the water flux dynamics at the MR facility, four different model setups were tested. Namely, a two-layer and a three-layered model with either single- or dual porosity soil characteristics. The convergence of the cost function for the individual parameters, we refer to Appendix B-1, Figure B-1.1 . Figure 5-4 compares the modeled SWCs of the four optimized models mentioned, whereby the largest differences in predicted SWC between the individual models can be found in the plow layer and the lowest depth of 1.2 m. As the best model cannot be distinguished visually, the AIC was computed, and the models were ranked accordingly. The two-layer single porosity model had the lowest AIC value of 1918 (Table 5-2), indicating that it is the best model in terms of representing the measured SWC and fitted parameters. The second-best model was the two-layer dual porosity model, closely followed by the three-layer single porosity model with AIC values of 3115 and 3129, respectively. Here, the AICs were relatively similar for both model setups because the total number of optimized parameters was the same and the SWCs were equally well matched. The largest AIC was calculated for the three-layer dual-porosity model (AIC = 4910), which was primarily due to the model's requirement to fit a larger number of parameters.

When additionally considering the root mean square error (RMSE) we were able to evaluate if the two- or the three-layered model would be detailed enough to represent the measured data. We noticed that the RMSE generally indicated that the additional layer did not result in a significantly better fit between the modeled and the GPR derived SWC (see Table 5-2). Therefore, we identified the two-layered model to be best suited to represent our system. Comparing the RMSE between the single- and dual-porosity model, we noticed for the two-layered models the same RMSE for both the single- and dual porosity model (RMSE = 0.033). For the three-layered model the RMSE is slightly smaller for the dual-porosity model (RMSE = 0.032). As mentioned, the two-layered unimodal model yielded lowest AIC and was therefore the best model to describe the GPR-derived SWC followed by the two-layer dual-porosity model. Looking at the weighting factor $\omega 2$ of the dual porosity model fitted to the data, one can see that for the plow layer $\omega 2$ is 0.85, indicating a certain degree of bimodality, whereas for the subsoil layer the weighting factor yielded 1 indicating no bimodality.

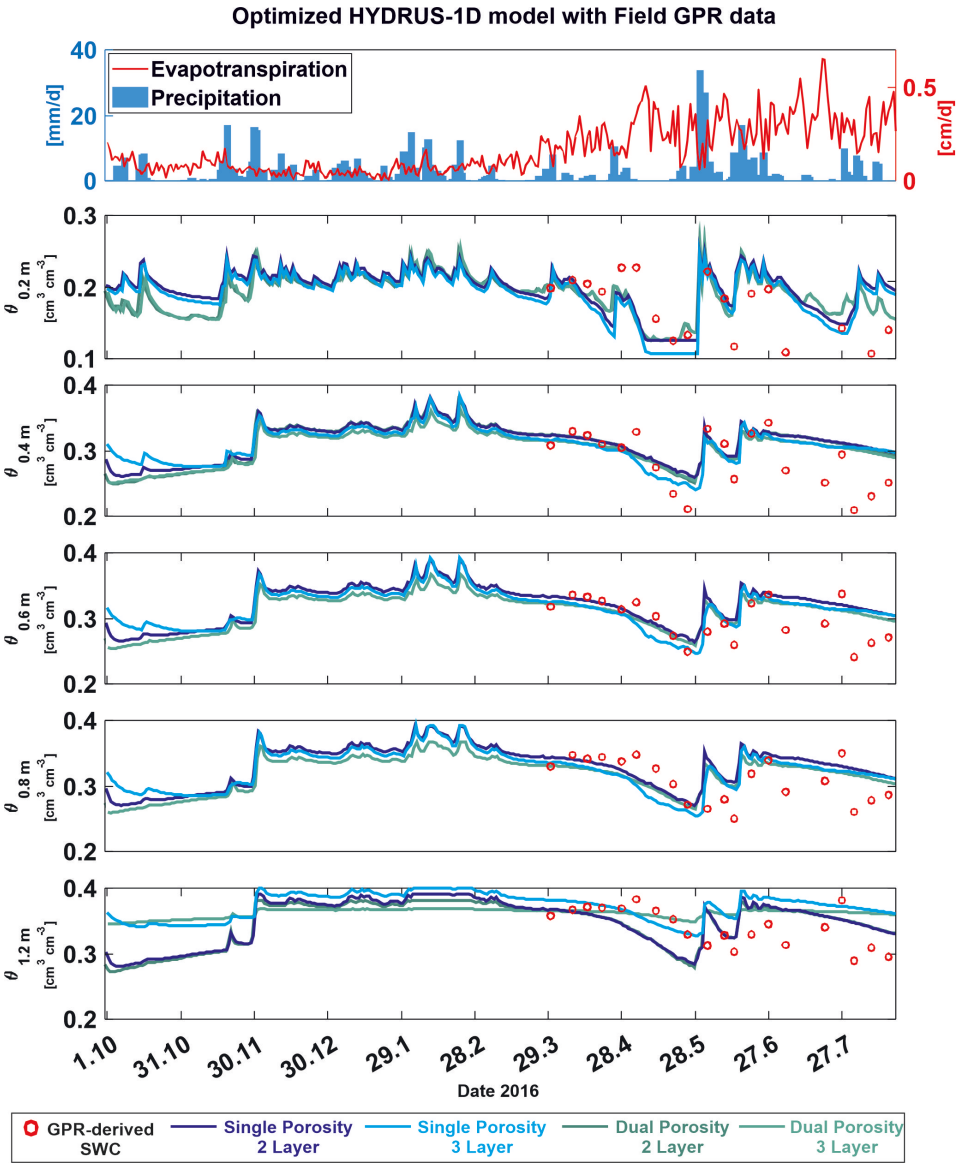

Figure 5-4: Results for the inversion of the horizontally averaged GPR-derived SWCs. The uppermost plots show the atmospheric conditions followed by the different SWC measurement depths. The solid lines indicate the modeled SWC for the different model setups. The red circles indicate the GPR-derived mean SWCs

Table 5-2: Results for the inversion of the horizontally averaged GPR-derived SWCs, with boundaries set in the SCE-UA optimization and the optimized SHP values for the different models. For the selection of the best model, the R^2 and AIC were calculated for each soil layer individually and over all depths.

					SHP			
			Lower boundary	Upper boundary	Two-layered model		Three-layered model	
					unimodal	dual-porosity	unimodal	dual-porosity
Plow layer	θ_s	[cm^3 cm^{-3}]	0	0.01	0.002	0.009	0.004	0.01
	θ_r	[cm^3 cm^{-3}]	0.25	0.45	0.25	0.275	0.25	0.276
	α	[1 cm^{-1}]	0.009	0.1	0.0795	0.0998	0.0546	0.099
	n	[-]	1.1	3.0	1.118	2.789	1.129	1.998
	K_s	[cm d^{-1}]	10	200	199.75	10.31	139.8	12.38
	λ	[-]	-2	10	4.59	-1.28	6.39	-.1.15
	$\omega 2$	[-]	0.85	1	-	0.864	-	0.851
	$\alpha a2$	[1 cm^{-1}]	0.001	0.01	-	0.0088	-	0.0091
	$n2$	[-]	1.1	1.6	-	1.445	-	1.382
		RMSE			**0.0034**	**0.0268**	**0.04**	**0.0268**
		AIC			**142**	**253**	**0.3927**	**253**
Subsoil layer1	θ_s	[cm^3 cm^{-3}]	0	0.01	0.009	0.006	0.013	0.005
	θ_r	[cm^3 cm^{-3}]	0.3	0.45	0.387	0.379	1.261	0.366
	α	[1 cm^{-1}]	0.008	0.1	0.0086	0.0299	107.88	0.0423
	n	[-]	1.1	3.0	1.358	2.091	0.1723	2.048
	K_s	[cm d^{-1}]	0.8	200	159.52	192.51		133.04
	λ	[-]	-2	10	-0.6	-0.06		-1.88
	$\omega 2$	[-]	0.85	1	-	1	-	0.957
	$\alpha a2$	[1 cm^{-1}]	0.001	0.01	-	0.0061	-	0.0047
	$n2$	[-]	1.1	1.6	-	1.501	-	1.495
		RMSE			0.019	0.019	0.019	0.014
		AIC			722	722	243	457
Subsoil layer2	θ_s	[cm^3 cm^{-3}]	0	0.01	-	-	0.005	0.004
	θ_r	[cm^3 cm^{-3}]	0.3	0.45	-	-	0.4	0.367
	α	[1 cm^{-1}]	0.08	0.1	-	-	0.01	0.0552
	n	[-]	1.1	3.0	-	-	1.166	1.964
	K_s	[cm d^{-1}]	0.8	200	-	-	86.1778	156.67
	λ	[-]	-2a	10	-	-	1.74	0.61
	$\omega 2$	[-]	0.85	1	-	-	-	0.999
	$\alpha a2$	[1 cm^{-1}]	0.001	0.01	-	-	-	0.0015
	$n2$	[-]	1.1	1.6	-	-	-	1.372
		RMSE			-	-	**0.023**	**0.017**
		AIC			-	-	**127**	**236**
		Number of optimized parameters			**12**	**18**	**18**	**27**
		RMSE			**0.033**	**0.033**	**0.035**	**0.032**
		Overall AIC			**1918**	**3115**	**3129**	**4910**

Overall, Figure 5-4 shows that none of the utilized models perfectly represent the GPR-derived SWC. A pattern of SWC underestimation during spring (March to April) and overestimation at later times is evident. Furthermore, all models exhibit less temporal SWC variability compared to the GPR-derived SWC, although they effectively capture high rainfall events at all measurement depths.

Sharp gradients in SWCs can result in incorrect estimations of GPR-derived SWC when the first arrival time (first break) is used (Yu et al., 2021/Appendix F). To determine if this occurs under natural field climatic conditions, a synthetic modeling study was conducted using the three-dimensional finite difference time domain software gprMax (Warren et al., 2016) (refer to Appendix B-1 for detailed results). For the simulation, we utilized the projected soil water content profiles for the two-layered unimodal model (refer to Table 5-2 and Figure 5-2). From these profiles, we computed the distribution of relative dielectric permittivity throughout the entire depth of the soil profile for the 20 days in which GPR data were collected in the field. We subsequently used these relative dielectric permittivity profiles as input in gprMax. Finally, synthetic radargrams were simulated and analyzed following

the same procedure (first arrival) as the real measurements (refer to Appendix B-2, Figure B-2.1a). This exercise demonstrates that the first arrival time analysis accurately estimated the simulated soil water contents (SWCs). Additionally, infiltration water after rainfall events did not create significant gradients in soil water content that could impact SWC estimation from the radargrams (refer to B-2, Figure B-2.1).

The second issue to be discussed is the adequacy of the number of GPR-derived SWC measurements needed to accurately estimate the SHP. As indicated earlier, our field experiments yielded only 20 measurements over a period of 6 months. As such, it is uncertain whether this insufficient number of data points contains sufficient information to constrain the inversion. To investigate further, we utilized a synthetic model that was configured in the manner specified in the previous section and grounded on the approximated parameters for the dual-layer unimodal model discussed prior (refer to Appendix B-3). We created three sets of synthetic GPR-derived SWC measurements, i) for the 20 available field experiment measurement days, both with and without ii) white noise, and iii) daily measurements over a period of 6 months without noise. Based on all three scenarios, successful retrieval of the SHP was achieved. Therefore, it can be concluded that the 20 available measurements provide sufficient information to constrain the hydrogeophysical sequential inversion. For more details, please refer to Appendix B-3, Table B-3.1.

5-3-3 Upscaling to a pseudo-3D sequential inversion

To investigate the horizontal variability of the SHP along the rhizotubes, the GPR-derived SWCs for each measurement day can be visualized and examined over time for all 61 measurement points. Figure 5-5 displays the horizontal depth planes of three different measurement dates (April 28th, June 20th, and August 1st). Typically, the lowest SWCs were detected in the plow layer (0.2 m), while the deeper soil profile showed systematically higher values. Temporal variability decreases with increasing depth due to atmospheric conditions at the surface. Patches of GPR-derived SWC variability demonstrate that soil conditions are heterogeneous, affecting variability in the SHP. To explore the spatially distributed SHP, 61 individual inversions were performed at each location along the rhizotubes at each measurement depth. Based on the previous inversion of mean GPR-derived SWC, a two-layer setup, consisting of a plow (topsoil) and a subsoil layer, provides sufficient detail for parameter estimation. Since bimodality may exist within the soil hydraulic characteristics, excluding it a priori during inversion is not advised. Additionally, the dual-porosity function allows for flexibility in yielding an unimodal characteristic if the weighting factor is close to or equals 1 (refer to Equation. 5-10). Therefore, the dual-porosity soil hydraulic model was chosen for the inversion. After inverting the SHPs to all GPR-derived SWCs for all individual locations within the rhizotubes located in the plow and subsoil layers, the soil water retention and hydraulic conductivity curves were plotted in Figure 5-6. As depicted in the figure, we observed a noticeable dual-porosity pattern in the wet range for the plow layer in Figure 5-6a and c, while the soil characteristics for the subsoil layer displayed a more unimodal pattern (Figure 5-6b and d). The dual-porous nature of the plow layer and the unimodal nature of the subsurface layer were also observed in the 1D inversion.

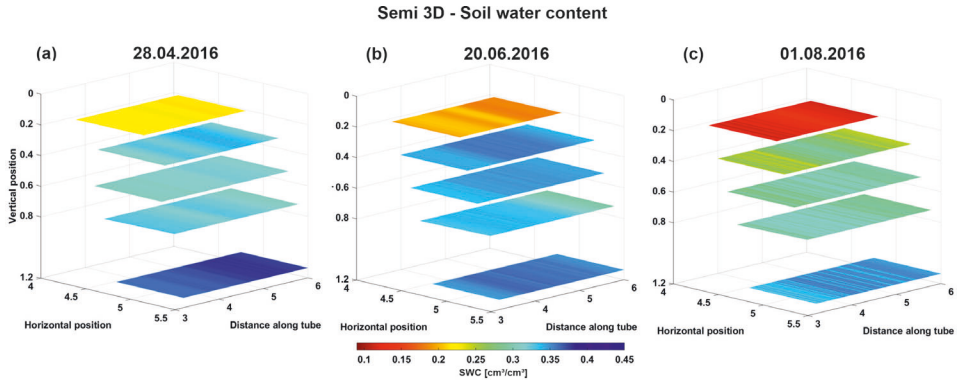

Figure 5-5: GPR-derived soil water contents (SWC) for three selected dates during the crop growing season: (a) 28th of April, (b) 20th of June, and (c) 1st of August 2016.GPR-derived soil water contents (SWC) for three selected dates during the crop growing season: (a) 28th of April, (b) 20th of June, and (c) 1st of August 2016.

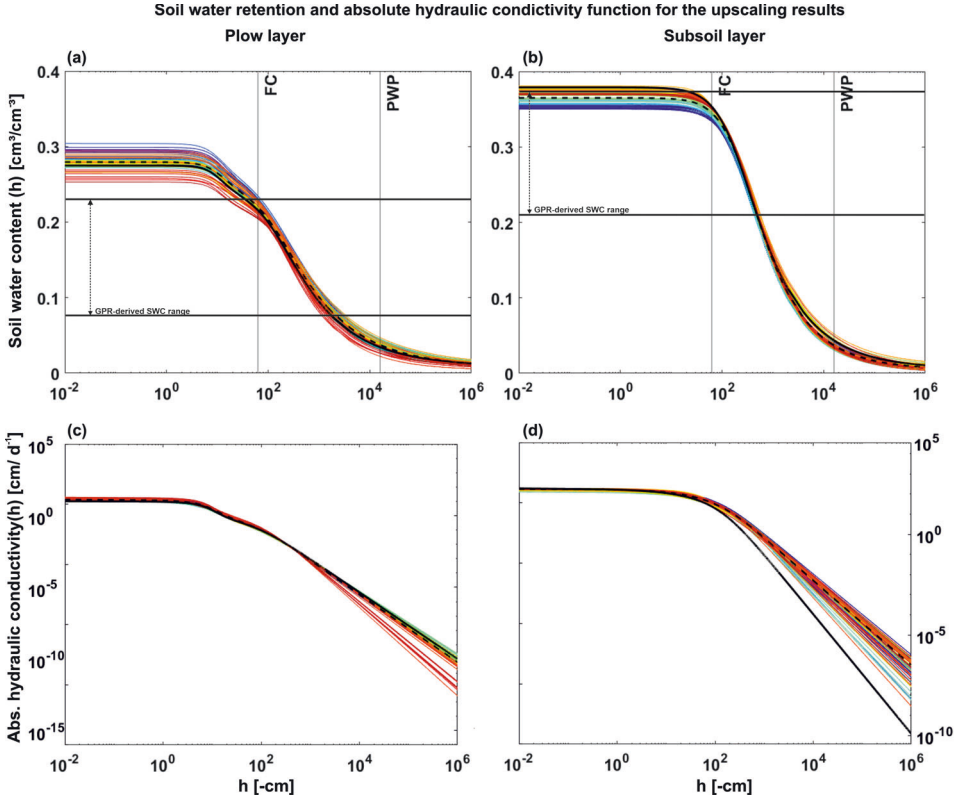

Figure 5-6: Soil water retention (a &b) and relative hydraulic conductivity function (c & d) for the plow and subsoil layer respectively. The different colors represent the results along the rhizotubes. The black dashed line and the black solid line indicate the results of the 1D field study and the mean of the upscaling results, respectively. The vertical lines in the soil water retention functions represent the pressure head and the corresponding soil water content values at field capacity (FC) and permanent wilting point (PWP).

To examine the dual-porosity behavior of both layers in more detail, a histogram of the weighting factor $\omega 2$ is plotted in Figure 5-7. For the plow layer, there is almost no spread in the weighting factor $\omega 2$, with 59 of the models having a $\omega 2$ between 0.85 and 0.86, and only two between 0.86 and 0.87. Hence, the plow layer shows a bimodality of 15%. In contrast, for the subsoil layer, $\omega 2$ is much more variable, ranging from 0.88 to 1, and is highly skewed toward 1, indicating low bimodality to near unimodality. The estimated SHP for the 61 locations along the rhizotubes are shown in Figure 5-8, where the plots include not only the estimated parameter for each individual GPR location, but also the mean parameter calculated from the individually optimized parameters along the rhizotubes (here denoted as Mean upscaling results, see Figure 5-8), as well as the results of the inversion based on the mean SWCs along the rhizotubes.

For the plow layer, there is a deterministic trend is present for the soil matrix parameters $\alpha 2$ and *n2* (see Figure 5-8a). For $\alpha 2$ between 3 and 4.0 m, the values are generally below the mean of the inversion results based on the mean SWC. In contrast, between 4 and 6 m the values are above this mean. This trend is reversed for *n2*, suggesting a negative correlation between matrix α and n as already found by Zhang et al. (2022) for laboratory derived data. A similar trend can be seen for the subsurface layer in Figure 5-8b.

To investigate this further, Figure 5-9 shows the negative correlation between $\alpha 2$ and *n2* for both soil layers. The R^2 gives values of 0.4 and 0.53 for the plow and subsoil layer, respectively. When analyzing K_s and λ within the plow layer, we can notice similar patterns along the locations of the rhizotubes, where high values for both parameters above the mean of the upscaling results, between 3.0 and 3.7 m are present, which then decrease below the mean towards 5.1 m. Between 5.1 and 6.0 m a slight increase is present towards values around the mean. This similar trend of K_s and λ suggests a correlation between those parameters (see Appendix B-4, Figure B-4.1). For all other parameters estimated in for the plow layer (θ_s, θ_r, $\alpha 1$, and $n1$) no clear trend is visible.

In contrast to the plow layer a clear trend along the rhizotube location for the estimated θ_s can be found in the subsoil layer (Figure 5-9b), where the values between 3 and 4.4 m (roughly at the center of the rhizotube) are higher than 0.37 cm^3 cm^{-3} and decrease steadily towards the end of the rhizotube. The remaining parameters (θ_r, K_s, λ, $\alpha 1$, and $n1$) do not follow a clear trend, and only for $\omega 2$, α, and $n2$ high variability in the first half of the rhizotube is noticeable, which is smaller for the second half along the tube. Finally, there is no correlation between K_s and λ compared what was present in the plow layer.

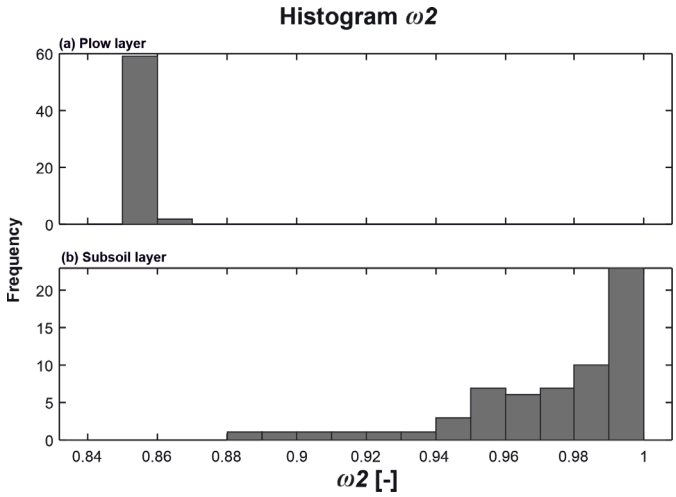

Figure 5-7: Histogram of the weighting factor $\omega 2$ for (a) the plow layer and (b) the subsoil layer for all 61 GPR locations.

In a final step, we compared the effective (mean) SHPs for the MR facility. On the one hand, a set of SHPs was estimated based on the mean SWC derived from the spatially resolved GPR measurements and on the other hand, the SHPs were estimated from resembled mean retention and conductivity pairs of the individual curves and depicted in Figure 5-3a and b. For K_s and λ the parameters were averaged directly over the length of the rhizotubes. The offset and the direction of the offset between the different mean values is quite variable. In some cases the values are very similar, e.g., θ_s, $n2$ within the plow layer. Whereas within the subsoil layer, the values between the different mean SHP are quite large Additionally, no clear trend is present, where the upscaling mean or results from the one-dimensional study is consistently larger than the other.

Information on FC, PWP, and PAW is often required in crop growth studies (Kersebaum et al., 2015). The variability of these parameters can significantly affect plant performance under conditions such as water stress or nutrient deficiency and, consequently, crop productivity, including yield (Van Keulen et al., 1987; Aggarwal, 1995 The SWC at FC, PWP, and PAW was individually calculated for each GPR-derived SWC location along the rhizotubes, as shown in Figure 5-10. Furthermore, we incorporated the SWC at FC, PWP, and PAW obtained through the inversion of the average SWC and upscaled approach mean. The SWC levels at PWP (Figure 5-10b) and PAW (Figure 5-10c) indicate a symmetrical distribution in the topsoil layer, while FC (Figure 5-10a) also shows a symmetrical distribution in the subsoil layer. However, the remaining parameters are skewed towards the lower SWC range. Furthermore, the soil characteristics of individual layers can be compared. The SWC at FC is lower for the plow layer and exhibits slightly more variability in the subsoil layer. Conversely, the SWC at PWP is higher and more variable for the plow layer. Three outliers are observed for the subsoil layer, which are very different from the other values, while there is only one outlier at the lower end of the range for the plow layer. The SWC at PAW

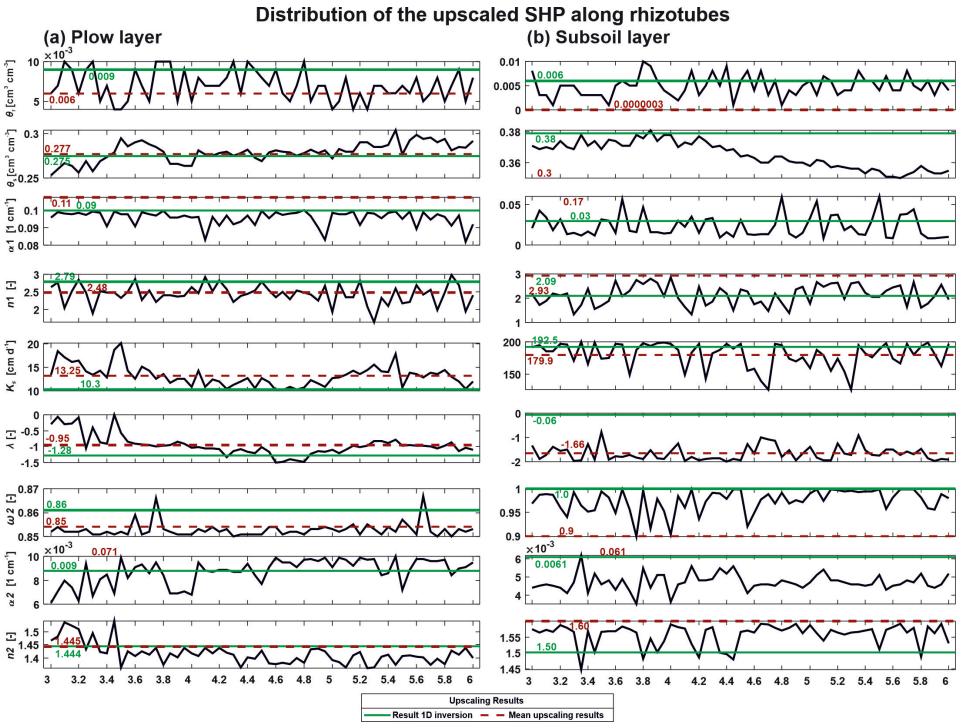

Figure 5-8: a) and b) show the upscaling results for the plow layer and the subsoil layer, respectively. The individual subplots indicate the results along the rhizotube for the soil hydraulic parameters. The black solid lines show the individual optimization results, the red dashed line indicates the mean of the upscaling results, and the green solid line indicates the results of the inversion based on mean SWCs along the rhizotubes. Note, for some SHP the mean values were out of range to show values along the rhizotubes, hence only the corresponding values is indicated.

in the plow layer is lower compared to that of the subsoil layer. Furthermore, there is a higher variability in the subsoil layer, as indicated by a wider range between the 25% an 75% percentiles. When comparing the boxplot median to the results of the inversion method using mean SWC, it is evident that the inversion of the mean SWC produces a result outside the quartiles for the SWC at FC and PWP of the subsoil layer. For the SWC at PWP, the value is near the upper whisker, indicating considerable variability beyond the upper quartile. Meanwhile, for SWC at FC and PWP in the plow layer, the results of the one-dimensional inversion are positioned close to the lower quartile.

For the SWC at PAW, the results based on the inversion of the mean SWC are close to the median of the upscaling results for the plow and subsoil layers, respectively. Moreover, we can evaluate the convergence of the results obtained by inverting the mean SWC values and the soil characteristics data from upscaling (refer to Figure 5-6a and b). The results for the SWC at FC show the mean SWC and the upscaling results are similar, but they differ for the

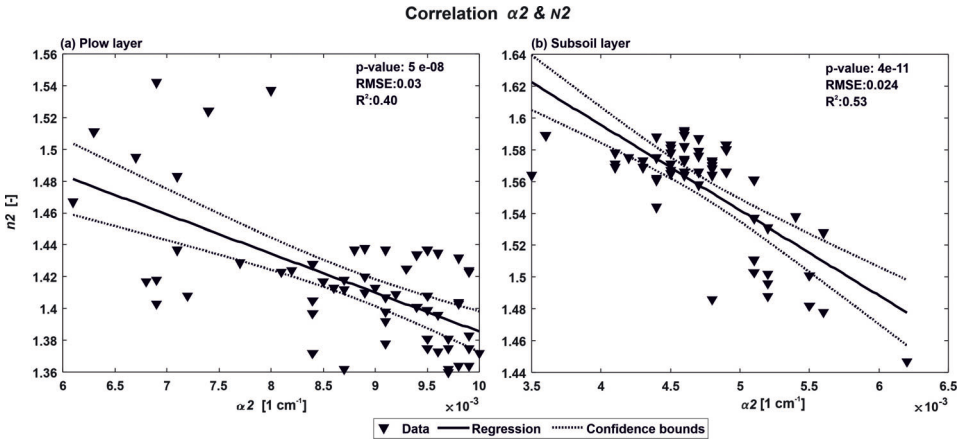

Figure 5-9: Correlation between α and $n2$, for a) plow layer and b) the subsoil layer based on the inversion along the 61 locations within each rhizotube.

plow and subsoil layers. Additionally, there is a considerable difference in the mean results exists for SWC at PWP, with the same direction as for SWC at FC. Mean results for SWC at PAW are once again similar. With the approach to derive the SHP from crosshole GPR-ZOP data over a soil volume of approximately 4 m^3 demonstrates our ability to provide a single SHP parameter set for the entire soil volume. We can also produce a semi-3D distribution of the SHP that can be used for soil modeling at different scales, at a single plant scale such as soil-plant interaction models, or at large scales such as effective crop models.

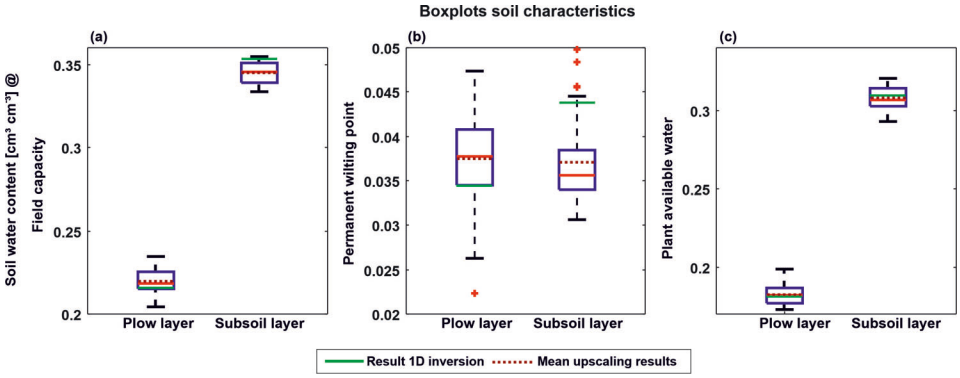

Figure 5-10: Boxplot for the upscaling results for the soil water content at field capacity (a), permanent wilting point (b) and plant available water (c). The green solid line indicates the values based on the inversion of the mean SWC along the rhizotubes and the dark red dashed line indicates the mean upscaling result. The red solid line shows the median from the upscaling results, the blue box the 25% and 75% percentile, the black whiskers the most extreme data points not considered as outliers, and stars the outliers.

5-4 Summary and Conclusions

In this presented study, the soil hydraulic parameters (SHP) were calculated using the uni- and bimodal Mualem-van-Genuchten model (MvG). The method relied on time-lapse 200-MHz horizontal zero-offset-profiling (ZOP) crosshole GPR derived data, which determined the soil water content (SWC) over the course of a winter wheat crop growing season.

We have shown that our sequential hydrogeophysical inversion approach can accurately determine the soil hydraulic parameters for a one-dimensional averaged scenario, where we used the averaged GPR-derived SWC along the rhizotubes. The findings indicate that these measurements provide sufficient details to calculate the SHP for the plow (topsoil) and subsoil layer, with the added capability of also estimating the parameters of bimodal MvG. Regardless of the good fit of the GPR-derived SWCs by the optimized model, some discrepancies were identifiable, where the modeled SWCs showed less variability than the measured ones. To ensure that this discrepancy is not caused by the method how SWCs were derived from GPR data (i.e., first arrival time), we performed synthetic modeling. Therefore, the calibrated model was utilized in conjunction with gprMax, a three-dimensional finite difference time domain software (Warren et al., 2016). Simulated EM waves were analyzed in the same manner as those measured in the field. The findings indicate that the method of picking the first arrival times is appropriated under natural atmospheric conditions, as sharp SWC gradients did not affect the analysis, as suggested earlier by Yu et al. (2021)/Appendix F.

In the next step, a pseudo-3D sequential inversion of the SHP was performed, using the individual GPR derived SWCs from the different locations along the rhizotubes (N = 61 per rhizotube). The results show that the calculated SHP vary across the locations of the rhizotubes. The pseudo 3D SHP differ from the SHPs estimated using the mean GPR-derived SWC along the rhizotubes, as well as from the calculated mean of the upscaled SHPs. The latter was obtained by fitting the soil hydraulic properties to the average soil water retention function. Moreover, some SHPs showed correlation, for instance, a negative correlation was observed between matrix $\alpha 2$ and $n2$ as previously demonstrated for lab data by Zhang et al. (2022), and between K_s and λ but here only for the plow layer. From the soil water retention functions for the different methods used to estimate the SHP (inversion of the mean GPR-derived SWCs, inversion of SWC along individual locations along the rhizotubes or averaging of the latter) further soil water characteristics were estimated, including field capacity, permanent wilting point, and the plant available water. The results showed that the different techniques for calculating the SHPs also yield different SWCs at field capacity, permanent wilting point, and plant available water.

Based on this research, it can be concluded that the two upscaling methods (inversion on mean GPR-derived SWC and mean dual-porosity SHPs from individual soil hydraulic characteristics along the rhizotubes) produces different SHPs. A next step would be to analyze how these variations in SHP would affect crop growth, for example, by using a dynamic crop growth model. Another consideration would be how these small-scale heterogeneities would impact biogeochemical processes like greenhouse gas (GHG) emissions using an appropriate biogeochemical model.

Chapter 6

Conclusions and Outlook

Conclusions

In this doctoral project approaches to promote the application of GPR as a non-invasive tool to investigate the processes within the soil-plant continuum to advance sustainable agriculture were explored. By using a multi crop growing season data set, novel statistical data analysis methods were developed, using time-lapse crosshole GPR measurement and utilizing root images to provide a link, correlation and validation between root presence and permittivity distribution.Consequently, missing links between the dielectrical properties of roots and the GPR signal were identified and further explored using a numerical modeling. To provide input at plot to catchment scale for modeling across different scales, horizontally distributed soil hydraulic parameters and soil characteristics for a cropped field were estimated by combining GPR-derived SWCs and hydraulic modeling, with the application of a hydrogeophysical inversion approach.

The first part (Chapter 2) described the acquisition and analysis of a comprehensive data set acquired at two minirhizotron facilities, including time-lapse crosshole GPR data, root images, soil sensors data (soil water potential, SWC and soil temperature), and additional root corings. These data were collected over five crop growing seasons for winter wheat and maize and served as a data basis for the remaining chapters. Especially the deep learning based automated minirhizotron image analysis pipeline developed by Bauer et al. (2022) (see Appendix E) made the analysis of the enormous minirhizotron image set feasible. In two parts the pipeline is combining state-of-the-art software tools, where first a segmentation by a pre-trained model is taken place using "RootPainter" (Smith et al., 2022), which is followed by an automated feature extraction using "RhizoVision Explorer" (Seethepalli et al., 2021). The publicly availability and standardized description of this data set will enhance the use across scientific fields and applications. It provides possibilities for the development, parameterization, calibration, and validation of models across scales, train and benchmark neural networks and provide ground truthing data for other field inventions.

The second part (Chapter 3) was complementing findings in Klotzsche et al. (2019) (see Appendix D), where time-lapse horizontal crosshole GPR data collected over multiple crop growing seasons was used to investigate the link between SWC, atmospheric conditions, soil and crop types. Individual maize crop rows showed an effect on the SWC distribution, with increased SWC below the rows in dry soil conditions. This effect could not be recorded for winter wheat. The roots were not considered for the calculation of the SWC, and no validation of the signals was performed. In Chapter 3 time-lapse in-situ crosshole GPR permittivity and root volume fraction derived from root images were collected before and during three maize crop growing seasons for the two minirhizotron facilities with varying soil types. Identifying soil type, agronomic management and the progress during crop growing season as influencing factors for the vertical distribution of roots, and the vertical and horizontal permittivity variability. To further explore the horizontal permittivity variability the so-called trend-corrected spatial permittivity deviation of vegetated field were derived, with the goal to remove impacting factors (soil heterogeneities, rhizotube deviations and seasonal SWC changes). A clear trend, which increased over time could be identified and be linked to the vertical root volume fractions over time. To validate this link a cross-correlation between the standard deviation of the trend-corrected spatial permittivity deviation of vegetated field and the vertical root volume fraction distribution was performed. Resulting in positive correlation, with coefficients of determination ranging between $0.02 < R^2 < 0.9$. Even though the link could be validated, questions about the patterns in the horizontal permittivity variability remain. A horizontal validation is still missing, therefore infiltration or soil water depletion processes caused by roots can not be conclusively identified or be separated from the presence of roots. Additionally, using the image-derived root volume fraction bares uncertainty caused by the difference in sensing volume and the use of depth of investigation, which remains un-validated. Especially, missing is spatially distributed root information and knowledge on how the roots influence the bulk dielectric permittivity and therefore the GPR signal. Nevertheless, this chapter showed the ability to image horizontal spatio-temporal variability in crosshole GPR-derived permittivities using a novel statistical analysis. Which is the first step towards fully visualizing processes in the soil-plant continuum, like soil water depletion patterns, root growth and influences of agricultural practices. The link and correlation between the permittivity variations and the vertical root volume fractions enables a first basic quantification of the impact of row crops on the horizontal spatio-temporal permittivity variations, hence the SWC.

The following Chapter 4 explored the influences of different soil components on the GPR signal. Therefore, we investigated synthetic EM waves using the open-source electromagnetic simulation software gprMax. The minirhizotron facilities, described in Chapter 2 served as a template for the model domain, trench wall root counts for maize crops were transformed to a permittivity distribution, using a petrophysical-mixing model for a four-phase soil system (soil, water, air and roots). Using a conventional three-phase soil system petrophysical relationship, the actual SWC for a cropped soil is overestimated. Using different scenarios with varying compositions of soil, roots and above-ground shoots, showed an impact of the air-subsoil interface causes critical refracted air waves and reflections on the uppermost depths, which aggravates the estimation of the permittivity. Further, higher permittivity related to the presence of the root phase, is impacting the first arrival and amplitude of the EM wave. To exclude the above-ground shoots as an impacting factors for the patterns, below crop rows, scenarios including a single and multiple above-ground shoots, were considered.

Consequently, shoots are not worth considering in modeling approaches and that infiltration and soil water depletion processes cause patterns below crop rows. Further studies should consider a spatial-temporal distribution of the permittivity caused by infiltration processes and incorporate root-soil interaction models to investigate the impact of root water uptake processes on the GPR signal. This numerical study improved the understanding of crosshole GPR signals in relation to crops and crop roots. Which was the first step towards fully understanding the impacting factors on the EM wave and using this knowledge to interpret data in other GPR applications. Additionally, it was determined that the consideration of a root phase in the calculation of the soil water content in appropriate petrophysical mixing models is crucial to derive the soil water actually present in the soil under the presence of roots.

The spatio-temporal distribution in SWC is mainly controlled by the soil hydraulic parameters. Therefore, crosshole GPR can be used to derive the soil hydraulic parameters non-invasively by applying sequential hydrogeophysical inversion approaches. This was performed in Chapter 5, for one minirhizotron facility cropped with winter wheat by combining GPR-derived SWC data with a hydrological model (HYDRUS-1D). First, a one-dimensional averaged case was investigated while considering different configurations. Further, the best model configuration was used for the upscaled estimation of the pseudo 3D-spatial distribution of soil hydraulic parameters of the dual-porosity Mualem-van-Genuchten model. For parameter distribution correlations were found between $\alpha 2$ and $n2$ in both soil layers and for λ and K_s for the plow layer. Furthermore, the soil hydraulic parameters were used to calculate the soil characteristics, such as field capacity, permanent wilting point and plant available water, which could benefit to investigate the impact of small scale heterogeneities on dynamic crop growth models. This chapter highlighted the potential of using crosshole GPR for the quantitative and spatially distributed estimation of information on soil state variables for the soil-plant continuum of agricultural crops, such as soil hydraulic parameters and soil characteristics. This showed the potential to use surface GPR applications to estimate maps soil hydraulic properties, which is a major advantage to point-scale soil sensor estimation or direct sampling.

The compilation of the different parts of this doctoral project, has shown how a comprehensive insight into horizontal crosshole GPR data and how it can be used, analyzed and validated to investigate the spatio-temporal distribution of the GPR-derived information such as permittivity, SWC, soil hydraulic parameters and soil characteristics for agricultural fields at plot scale. Some challenges still remain, however, novel approaches were demonstrated to establish GPR as a standard investigation tool to non-invasively monitor and characterize the soil-plant continuum for field practices related to sustainable agriculture.

Outlook

Building on the mentioned observations, conclusions and explored limitations, the following section should provide suggestions for further research. Based on this, suggestions can be made to promote GPR as an adequate tool for sustainable agriculture with close attention to field applications.

Advancing GPR field applications

For shallow soil depths interference caused by the air-subsurface interface occurred, in the experimental field (Chapter 2) and synthetic data (Chapter 4), which caused the standard first arrival time picking to be erroneous. One approach to solve this issue, as suggested in Appendix D, is to apply more sophisticated analysis approaches such as full-waveform inversion Klotzsche et al. (2016, 019b). On the other hand, there are field measurement configuration, which provide a solution. Yu et al. (2020) have used surface and borehole GPR in combination during an infiltration experiment at one MR facility, where the SWC derived for the depths 0.1 m and 0.2 m returned more reliable information. Another advantage of this combined application was possibility to use higher frequencies (500 MHz), than the ones available for crosshole applications, where only 200 MHz antennae were commercially available at the time. Higher frequencies are able to detect small scale heterogeneities, further applying this approach to a cropped field would be beneficial. This would enable to investigate the shallow processes within the soil-plant continuum, which were left undetected in this project. Patterns below the crop rows, as observed in dry soil conditions below maize crops (Chapter 3 and Appendix D), infiltration (caused by stem flow and preferential flow paths) or soil water depletion processes could be imaged. The application of higher frequencies is not only valid for the use in crosshole-to-surface applications. As shown in Chapter 4 this would also benefit crosshole and surface applications, since contributions to the GPR signal could be disentangled at millimeter to centimeter scale. These contributions range from small scale soil heterogeneities to single roots, with certain diameters, such as maize crown roots.

The described data acquisition and analysis relies on the installment of a minirhizotron facility or at least rhizotubes in the subsurface, which is very cost- and labor-intensive. Here, the application of surface GPR techniques as described in Chapter 1 would be beneficial, which are more time-, cost and labor efficient and do not require any pre-installments. Further, data acquisition is particularly suitable to map large fields in a short amount of time. Especially if mounted on, or pulled by agricultural equipment, e.g., tractors. First approaches to overcome obstacles which remained so far for most surface GPR applications as a tool for sustainable agriculture, is the absence of velocity information (crucial for the permittivity estimation). Here novel simultaneous multi-offset multichannel GPR system (Kaufmann et al., 2020) are promising to be used for the fast mapping of field scale permittivity distribution and the parameters. With the development of artificial intelligence and deep learning algorithms the obstacles of the data analysis for surface GPR to directly derive the SWC could be resolved in the future.

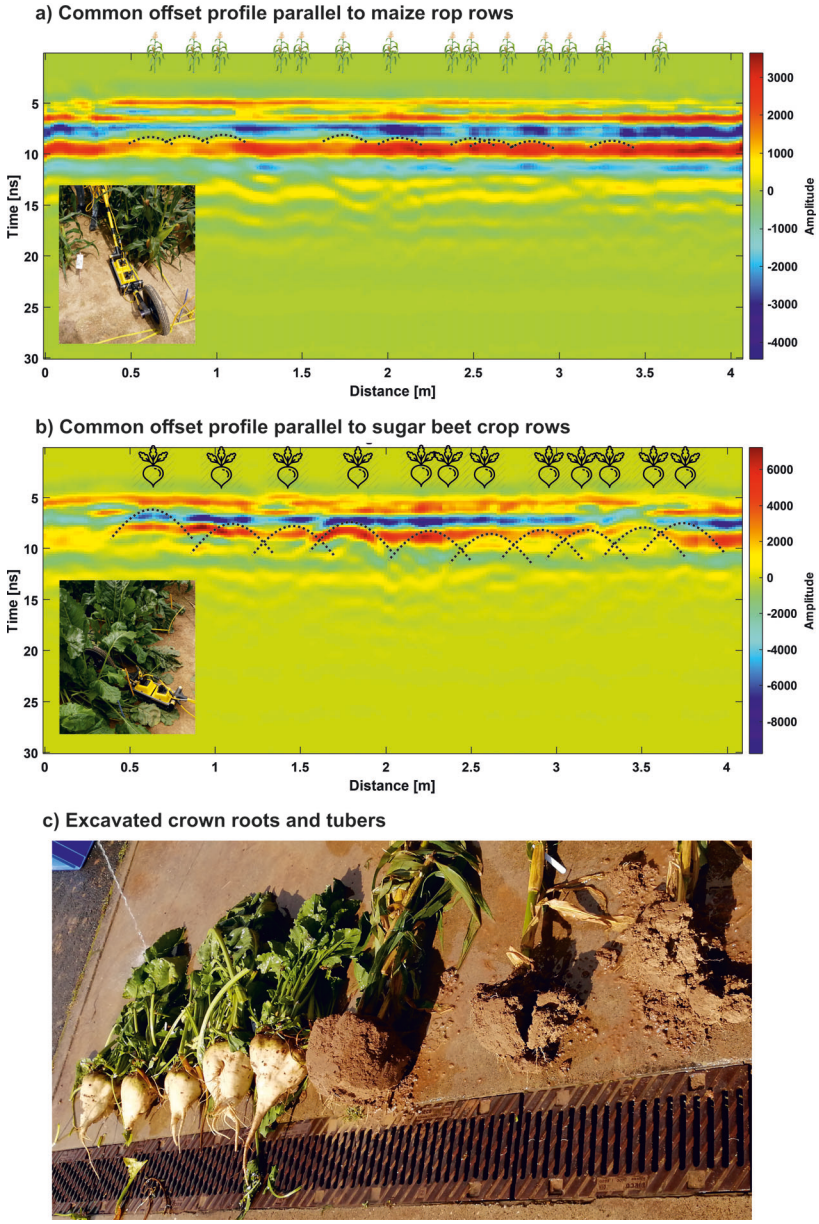

Figure 6-1: First field trials using surface GPR at Campus Klein-Altendorf. Common offset profile parallel to crop rows for a) maize and b) sugar beets. Schematic illustration of a plot within the minirhizotron facility and the zero-offset profiling GPR measurement and root imaging setup. c) Excavated maize crown root systems and sugar beet tubers.

As mentioned by Binley et al. (2015), Garré et al. (2021) the different hydrogeophysical and agrogeophysical techniques are sensitive to different key soil state variables and the direct link to soil-plant continuum processes remains a challenge and additionally requires the application of site specific transfer functions for a quantitative interpretation. Therefore, GPR could be coupled with other measurement techniques or additional geophysical tools, such as EMI, and ERT. Very promising are the results of imaging the root activity in the laboratory (Weigand and Kemna, 2017, 2018) and field (Michels and Kemna, 2022, Weigand et al., 2022), which could be coupled with time-lapse GPR applications. But also measurements from different scales of investigation such as drones and point-scale soil sensors could be beneficial. However, novel inversion approaches, such as joint inversion (Doetsch et al., 2010, Kowalsky et al., 2005, Moghadas et al., 2010) or machine learning approaches (Moghadas and Badorreck, 2019) will be necessary.

First field trials have been performed using surface GPR applications in combination with EMI and sEIT measurements for a field cropped sugar beets and maize (Figure 6-1a and b). For the surface GPR different antennae frequencies (200, 500 and 1000 MHz) and antennae configuration (COP parallel, adapted surface ZOP with crop row between transmitting and receiving antenna , multichannel measurements and adapted surface MOG) were used. Subsequent to the measurements, the maize crown root systems and sugar beet tubers were excavated and analyzed for validation, see Figure 6-1c. In future, time-lapse surface GPR measurements could be carried out and the data analysis methods, suggested validation procedures and parameter estimation approaches as described in Chapter 3 to 5 could be applied. Note that, for cropped field measurements the size of the antennae arrays and the crop type need to be considered. While for crops like maize and sugar beet, with a larger crop row spacing, 500 and 1000 MHz antennae could be used, for wheat field such an application can not be considered.

GPR are measurements in the field, especially crosshole measurements, with the commercially available systems, are quite labor-intensive. Here the automatization using, e.g., robots would benefit the data acquisition. Surface antennae or special designed antennae systems could be mounted onto robots arms and be inserted into the ground, like cone penetration tests, without needing a prior installment of rhizotubes or boreholes. Further surface GPR antennae could be mounted onto robots be pulled by them. One major obstacle in this application could be that robots contain quite a large amount of metal, which because of the ferromagnetic properties interferes with the EM wave. Which also needs to be considered if GPR equipment is mounted onto or pulled by other agricultural equipment.

For a better understanding of the soil heterogeneities, which could be used to improve the trend-corrected spatial permittivity deviation of vegetated fields, a comprehensive investigation of the bare-field soil conditions could be recorded prior to measurements for cropped fields. Here repeated bare-field measurements as described in Chapter 3 could be performed over a longer period without crops present on the field, where different soil conditions are recorded. Especially, very dry conditions are of interest to estimate the structure without SWC distribution patterns, hence the recorded permittivity would only impacted by the soil structure. When different soil water conditions are recorded, information on preferential flow paths, infiltration and drying patterns and how variable the soil conditions are, could be acquired. This could simplify the interpretation of the patterns recorded, while crops

where in place and link these patterns to processes like soil water depletion caused by root presence. This approach is universal for the different GPR applications and can be performed for crosshole, crosshole to surface and surface configurations or even be performed by the mentioned robot applications. Additionally, when using non-to minimal-invasive techniques such as GPR and root images acquired within minirhizotron and in the field, appropriate validation approaches remains a challenge.

Advancing validation approaches

A three-dimensional validation for the root images and GPR could be carried out using, e.g., lysimeters with installed rhizotubes, as mentioned by Garré et al. (2011). Here crops such as maize could be sown and investigated throughout the crop growing season. Prior bare-field measurements to better understand the patterns caused by soil heterogeneity should be performed. Additional infiltration experiments and measurements under dry conditions and at field capacity to identify flow paths and drying patterns would be beneficial. This could help to differentiate patterns caused by the soil heterogeneity and by irrigation and soil water depletion patterns caused by roots. Additionally, within the lysimeter installed rhizotubes could be used to investigate the root growth throughout the entire crop growing season. Within these rhizotubes crosshole GPR measurements could be performed. Additional surface and crosshole-to-surface applications are possible. As recent developments have shown, GPR system could also be directly be mounted onto the lysimeter (Steinbeck et al., 2022). After the crop growing season, the entire root system could be excavated and analyzed and a correlation between the actual root presence in the soil and the root images could be derived. Additional research questions could be investigated using this controlled experiment, when additionally measuring above-ground parameter such as leaf gas exchange, leaf water potential and crop growth parameter (e.g., Nguyen et al. (2022a)) to estimate the behavior of the plant and root waters under stressed conditions Lobet et al. (2014) are performed. The downside of using a lysimeters is the scale, the amount of planting space is limited and the investigation of the plant behavior within the crop row is not feasible.

For a better validation of the variability in the permittivity information spatially root image data sets with a high spatial resolution are necessary, while the vertical root information was feasible to provide a first estimate on how the variability correlated with the presence of roots, the information is not yet sufficient enough to explain all recorded permittivity patterns. Therefore, especially in the horizontal direction but also in the vertical direction a higher resolution images are necessary, such that small scale variabilities can be detected. The use of the root images for validation is still facing a major obstacle: the sensing volume. The root information is derived from a two-dimensional image and upscaled using a respective soil volume, which is derived from the diameter of the rhizotubes, until this day there is no standardized way on how this upscaling should be performed as well no appropriate validation is available. When comparing the GPR information, which is acquired for a three-dimensional space between the rhizotubes and the root images, which capture the soil in contact with the rhizotube, the validation inherits a bias. To explore the impact of this bias and scale difference modeling approaches could be of help, where root system architecture models are used to simulate field sampling (Morandage et al., 2019). Therefore, modeling approaches could be used to solve different kinds of challenges.

Advancing analysis and field sampling through modeling

With Chapter 4 some questions which resulted from investigating the permittivity variability in chapter 3 have been approached, but still challenges remain, where the combination of electromagnetic modeling, and root system architecture and root-soil-interaction models could be beneficial. Since the sensing volume is dependent on the GPR antennae frequency and the bulk permittivity of the soil (see Chapter 3), combined models could derive the sensing volume for the permittivity present in the soil and calculate from the incorporated root system architecture model the roots present in the soil volume sensed by the GPR. When this is performed for different SWC conditions and root distributions and compared to virtual field sampling (Morandage et al., 2019), factors for the validation using root images and GPR data acquired in the field could be developed, which are valid for different crop and soil types. Using this information, the root field sampling techniques could be optimized and manual labor as well as data analysis efforts be kept to a minimum. Furthermore, the combination of these models could be beneficial to model small scale heterogeneities in SWC and root distribution and additionally investigate the influence in the GPR signal. Since we have seen in Chapter 4, that the root phase, soil-air interface and above-ground shoot mainly influences later events in the EM wave, novel analysis approaches such as full-waveform inversion (Klotzsche et al., 2019) are required. These combined models could be used to synthetically estimate which GPR measurements configurations best to detected the soil-plant continuum components. Hereby, a digital twin of e.g., minirhizotron facilities, lysimeters or an agricultural field (including robot applications) could be developed. With the mirrored model domain, field measurement campaign including the above mentioned GPR configurations, such as crosshole, surface-to-crosshole and different surface techniques using different antennae configurations (ZOP, MOG, COP and multichannel) and antennae frequencies. Further, GPR has the possibility to investigate as plot to catchment scale, hence the derive information could be used as input for agro-ecosystem modeling to connect models at different scales.

Advancing knowledge about agro-ecosystems through modeling

To incorporate the spatial distribution of soil parameters into models as mentioned above the spatially derived soil hydraulic parameters, see Chapter 5 could be used. The parameter set was derived along one pair of rhizotubes for two soil layers cropped with winter wheat. Additional parameter sets could be derived using the sequential hydrogeophysical inversion approach as described in Chapter 5, for more than one rhizotube pair (vertically and horizontally neighboring), which would results in an actual three-dimensional distribution of the soil hydraulic parameters. Further, it would be interesting to quantify, how crops influence the soil hydraulic parameters. Thereby, the SHP of a bare-field and for different crops could be estimated. Especially row crops, such as maize, are interesting to investigate since the spatial distribution of the SHP, will be more heterogeneous. Here using a one-dimensional modeling tool such as HYDRUS-1D might not be sufficient enough and a two- to three-dimensional modeling tool could bring advantages, but with higher computational costs. Further, when considering the root growth in the three-dimensional model, the spatio-temporal distribution of the roots needs to be considered. Here root images with a high spatial resolution are required, to fully comprehend for the difference in root distribution for the different directions parallel and perpendicular to the crop row. For extended process understanding

a distribution in soil hydraulic parameters in multiple direction could be compared to the variability in permittivity, as derived from the trend-corrected spatial permittivity deviation of the vegetated field.

The estimation of pseudo- or actual three-dimensional distribution of the soil hydraulic parameters, soil characteristics or additionally the spatio-temporal distribution of the SWC, could be used as input for agro-ecosystem models at different scales. Here GPR-derived information could close the gap between point- to rhizosphere(pedon)-scale (Schnepf et al., 2022b) and regional land-surface or earth system models (Vereecken et al., 2022, 2016), where it can either be used as an input or ground truth. Additionally, the output from said models could be used for electromagnetic modeling approaches with different field applications, such as antennae development, optimization of field measurement campaigns.

Chapter A

Appendix A: Linking horizontal crosshole GPR variability and root image information of maize crops

A-1 Daily spatial permittivity deviation for the bare-field

The results of the spatial permittivity deviation of the bare-field ${\varepsilon_r^{BF}}_{i,j}{}'$ for 2017 and 2018, indicate that the two years show similar values along the rhizotubes for the different plots and depths with similar patterns for both sites. Since no crops were present for these measurements, these daily variabilities along the rhizotubes are linked to the soil heterogeneity and the rhizotube deviation. Comparing for R_{UT}, all depths for all three plots we identify minima and maxima in ${\varepsilon_{ri,j}}'$ along the rhizotubes. These are more distinct and the variation between the individual measurement seasons is less significant, compared to R_{LT}. In contrast, R_{LT} does not show these clear minima and maxima in ${\varepsilon_r^{BF}}_{i,j}{}'$, only in depths 0.2 m and 0.4 m changes on the extend of ${\varepsilon_r^{BF}}_{i,j}{}'$ along the rhizotubes are recognizable. For the depths below we can see trends along the rhizotubes where ${\varepsilon_r^{BF}}_{i,j}{}'$ is either steadily increasing (e.g., Plot 3 depth 0.8 m) or steadily decreasing (e.g., Plot 2 depth 0.8 m) along the rhizotubes. Additionally, the variation between the individual measurement seasons is larger for R_{LT} compared to R_{UT}.

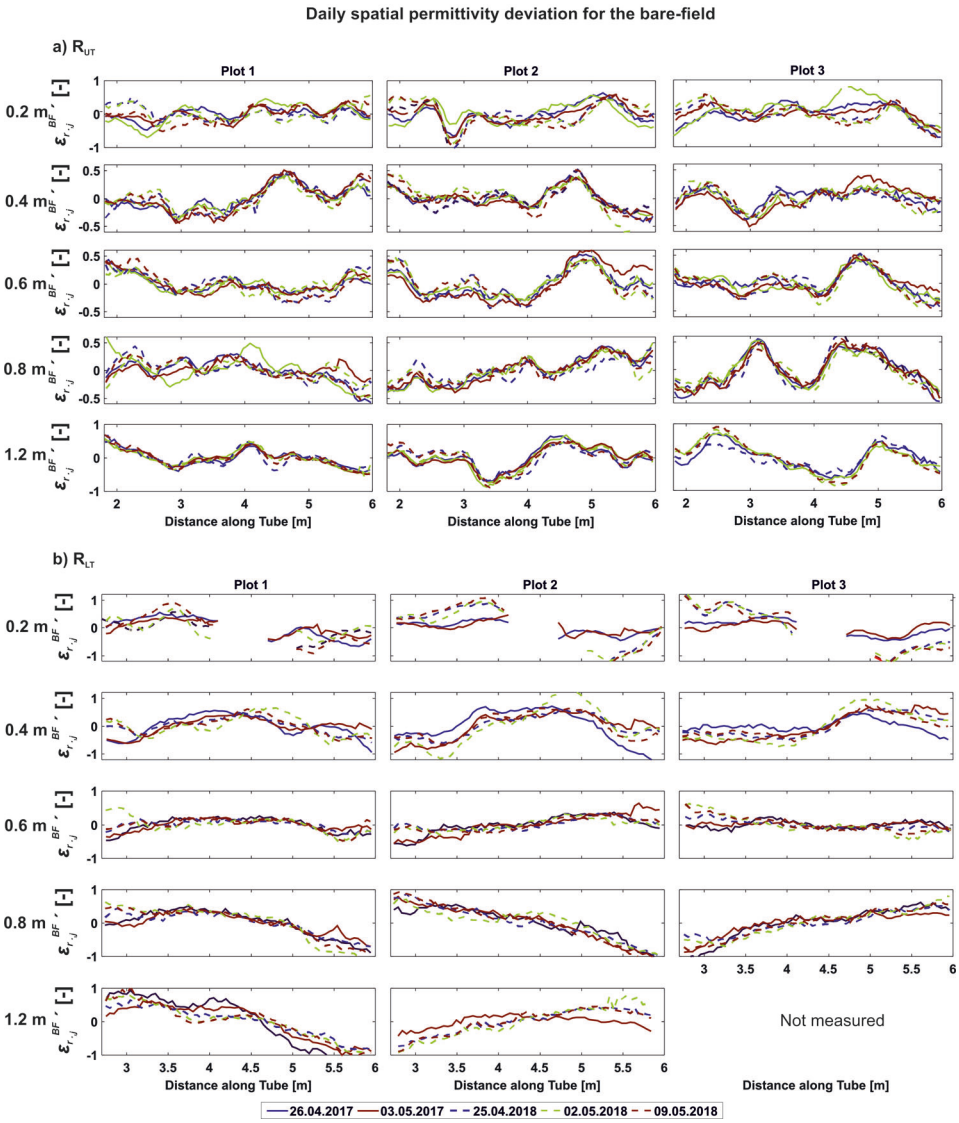

Figure A-1.1: Daily spatial permittivity deviation for the bare-field $\varepsilon_r^{BF}{}_{i,j}{}'$ along the rhizotubes under bare-field conditions for a) R_{UT} and b) R_{LT} for the crop growing seasons 2017 and 2018. The colored solid lines indicate the daily spatial permittivity deviation for the bare-field $\varepsilon_{ri,j}{}'$ values of 2017 and the colored dashed lines the daily spatial permittivity deviation for the bare-field $\varepsilon_{ri,j}{}'$ of 2018.

A-2 Probability density function of the trend-corrected permittivity deviation 2018

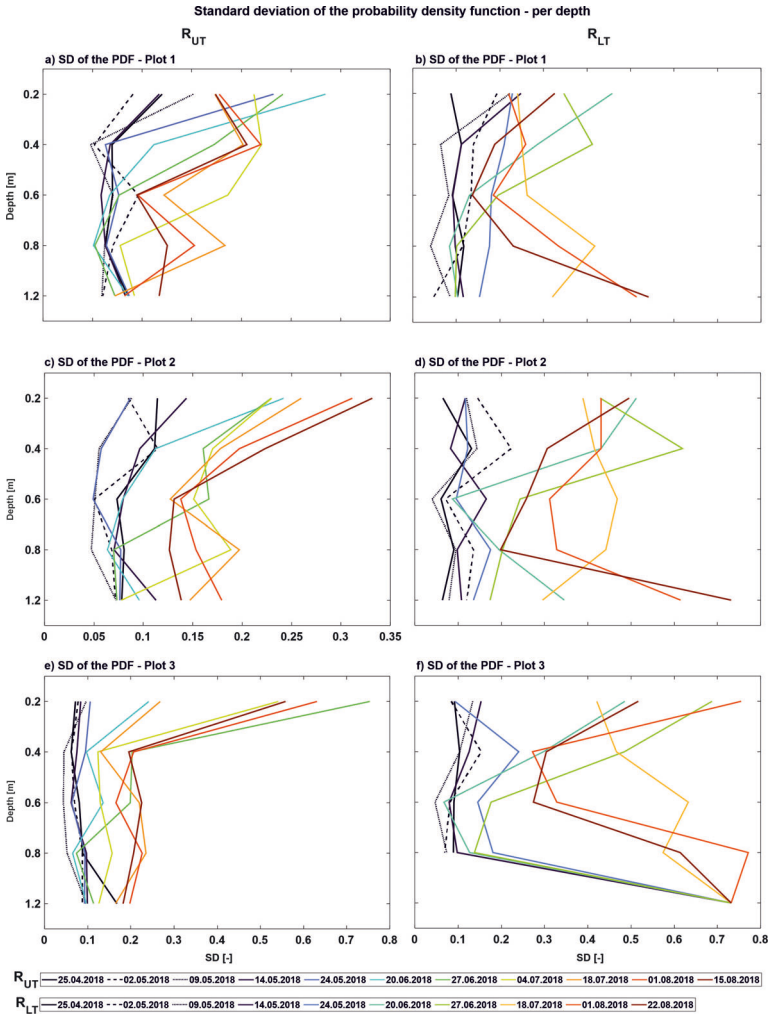

Figure A-2.1: Standard deviation (SD) values for different depths in 2018 for R_{UT} and R_{LT}, respectively. Note that the axes limits differ between the different depths to show the SD variations between the individual depths.

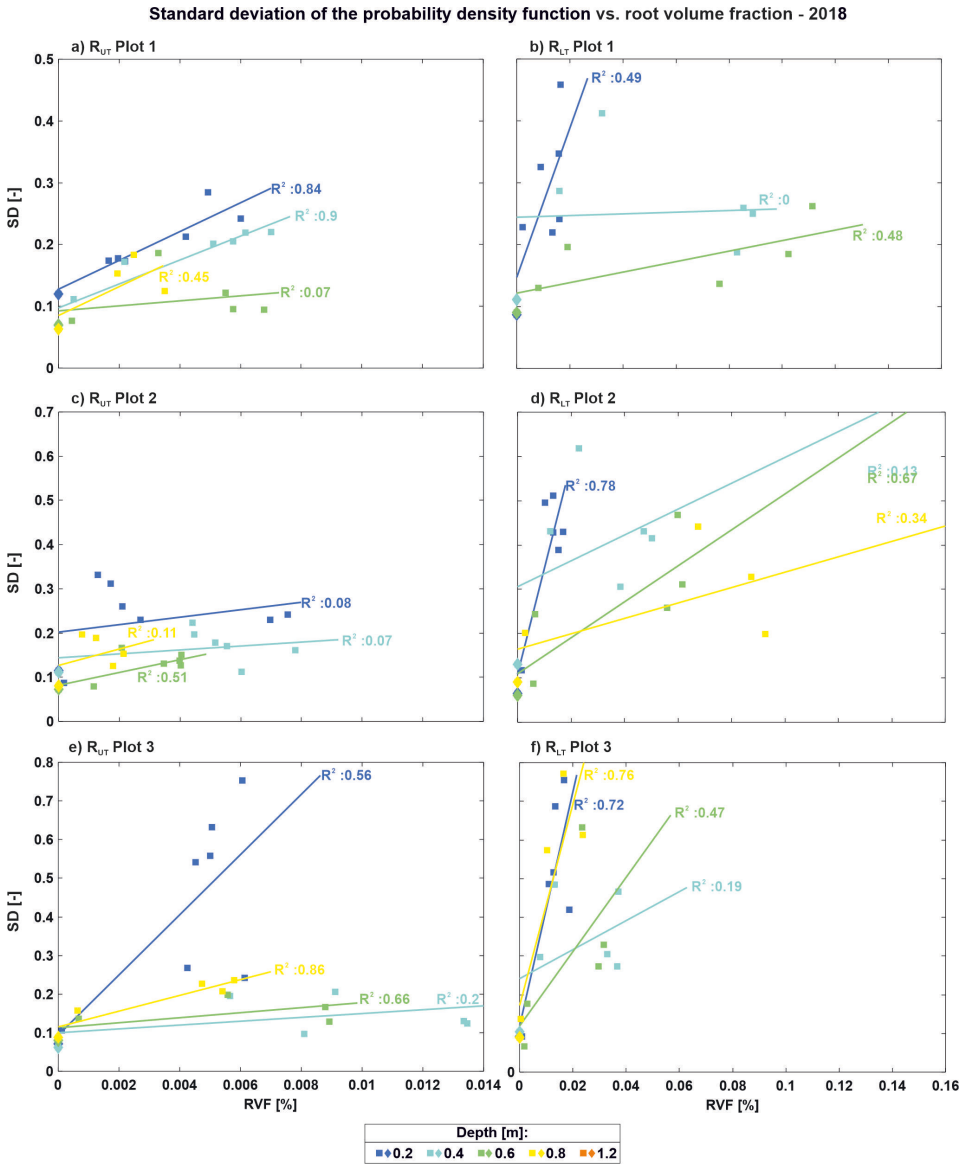

Figure A-2.2: Correlation between the root volume fraction (*RVF*) and the SD for the individual plots for R_{UT} and R_{LT} in 2018, respectively. The colored squares represent the values for the *RVF* and the SD for the vegetated field and the colored diamonds represent the values during the bare-field, where the *RVF* was set to 0, the different colors represent the different depths. The colored lines represent the linear regression per plot and depth, the R^2 values are indicated next to the regression lines.

A-3 Supplementary Material - Linking horizontal crosshole GPR variability and root image information of maize crops.

Table A-3.1: Irrigation amounts applied on R_{UT} in 2017, 2018 & 2020.

Date	Plot 1	Plot 2	Plot 3
		mm	
19.06.2017	-	-	1.10
22.06.2017	-	-	13.19
02.07.2017	-	-	13.19
06.07.2017	-	-	13.19
17.07.2017	-	-	13.19
31.07.2017	-	-	13.19
03.08.2017	-	-	13.19
08.08.2017	-	-	13.19
14.08.2017	-	-	13.19
24.08.2017	-	-	13.19
SUM 2017	0	0	119.81
16.05.2018	-	-	6.59
25.05.2018	-	-	6.59
07.06.2018	-	-	8.79
26.06.2018	-	-	26.37
03.07.2018	-	-	18.46
05.07.2018	13.19	13.19	13.19
09.07.2018	-	-	26.37
13.07.2018	-	-	21.98
17.07.2018	21.98	21.98	21.98
26.07.2018	-	-	23.74
01.08.2018	13.19	13.19	26.37
05.08.2018	17.58	17.58	26.37
15.08.2018	-	-	30.77
SUM 2018	65.94	65.94	257.57
20.05.2020	2.39	2.33	2.32
22.05.2020	2.24	2.29	2.32
25.05.2020	2.10	2.12	2.13
27.05.2020	8.42	8.02	8.79
02.06.2020	5.00	5.00	5.00
03.06.2020	5.08	5.08	5.08
12.06.2020	5.00	5.00	5.00
23.07.2020	-	-	-
24.07.2020	15.00	15.00	15.00
29.07.2020	5.00	5.00	5.00
10.08.2020	7.01	7.01	7.01
26.08.2020	5.27	5.27	5.27
31.08.2020	7.01	7.01	7.01
SUM 2020	69.52	69.13	69.93

Table A-3.2: Irrigation amounts applied on R_{LT} in 2017, 2018.

Date	Plot 1	Plot 2	Plot 3
		mm	
19.06.2017	-	-	1.10
22.06.2017	-	-	13.19
02.07.2017	-	-	13.19
06.07.2017	-	-	13.19
17.07.2017	-	-	13.19
31.07.2017	-	-	13.19
03.08.2017	-	-	13.19
08.08.2017	-	-	13.19
14.08.2017	-	-	13.19
24.08.2017	-	-	13.19
16.05.2017	-	-	6.59
SUM 2017	0	0	126.4
25.05.2018	-	-	6.59
07.06.2018	-	-	8.79
26.06.2018	-	-	26.37
03.07.2018	-	-	18.46
05.07.2018	-	-	13.19
09.07.2018	-	-	26.37
11.07.2018	-	-	6.59
13.07.2018	-	-	21.98
17.07.2018	-	-	0.00
18.07.2018	-	-	21.98
26.07.2018	-	-	23.74
01.08.2018	-	-	26.37
05.08.2018	-	-	26.37
15.08.2018	-	-	0.00
16.08.2018	-	-	15.38
SUM 2018	0	0	242.18

Table A-3.3: Comparison of the root volume fraction (*RVF*) and the root length density (RLD) as minimum, maximum and mean for R_{UT} and R_{LT} in 2018, respectively. The RLD was calculated using the total (root) length and the median diameter, per root image. The total (root) length is an additional output of RhizoVision, which not further used on this study.

	R_{UT}		R_{LT}	
	RVF	**RLD**	**RVF**	**RLD**
	[%]	[cm^3 cm^{-3}]	[%]	[cm^3 cm^{-3}]
Minimum	0.00000006	0.00027	0.00000012	0.00042
Maximum	0.15	0.95	0.70	2.29
Mean	0.006	0.07	0.008	0.30

Table A-3.4: Comparison of the root volume fraction (*RVF*) and the root length density (RLD) as minimum, maximum and mean for R_{UT} in 2020, respectively. The RLD was calculated using the total (root) length and the median diameter, per root image. The total (root) length is an additional output of RhizoVision, which not further used on this study.

	$\mathbf{R_{UT}}$	
	RVF	**RLD**
	[%]	[cm^3 cm^{-3}]
Minimum	0.00000006	0.0028
Maximum	0.186	0.53
Mean	0.0056	0.05

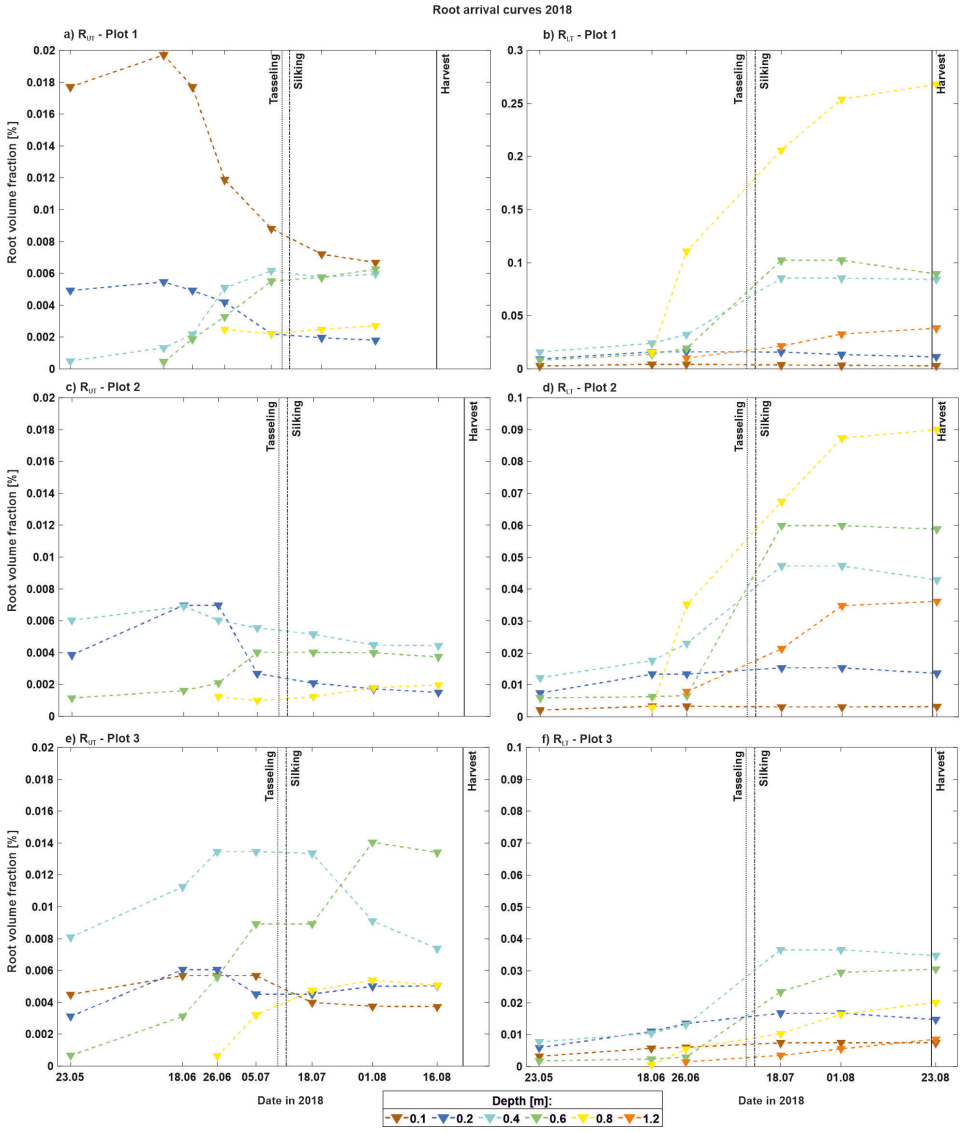

Figure A-3.1: Root arrival curves in root volume fraction (*RVF*) for 2018 for the three plots for R_{UT} and R_{LT}, left and right, respectively. The root images were measured within the same rhizotubes where the ground penetrating radar (GPR) antennae are placed. The colored triangles represent the *RVF* over time, which are median-filtered over 3 measurement days. The colors indicate the different depths. Tasseling and Silking are indicated by the vertical lines. Note the different y-axes scales for Plot 1 in comparison to Plot 2 and Plot 3.

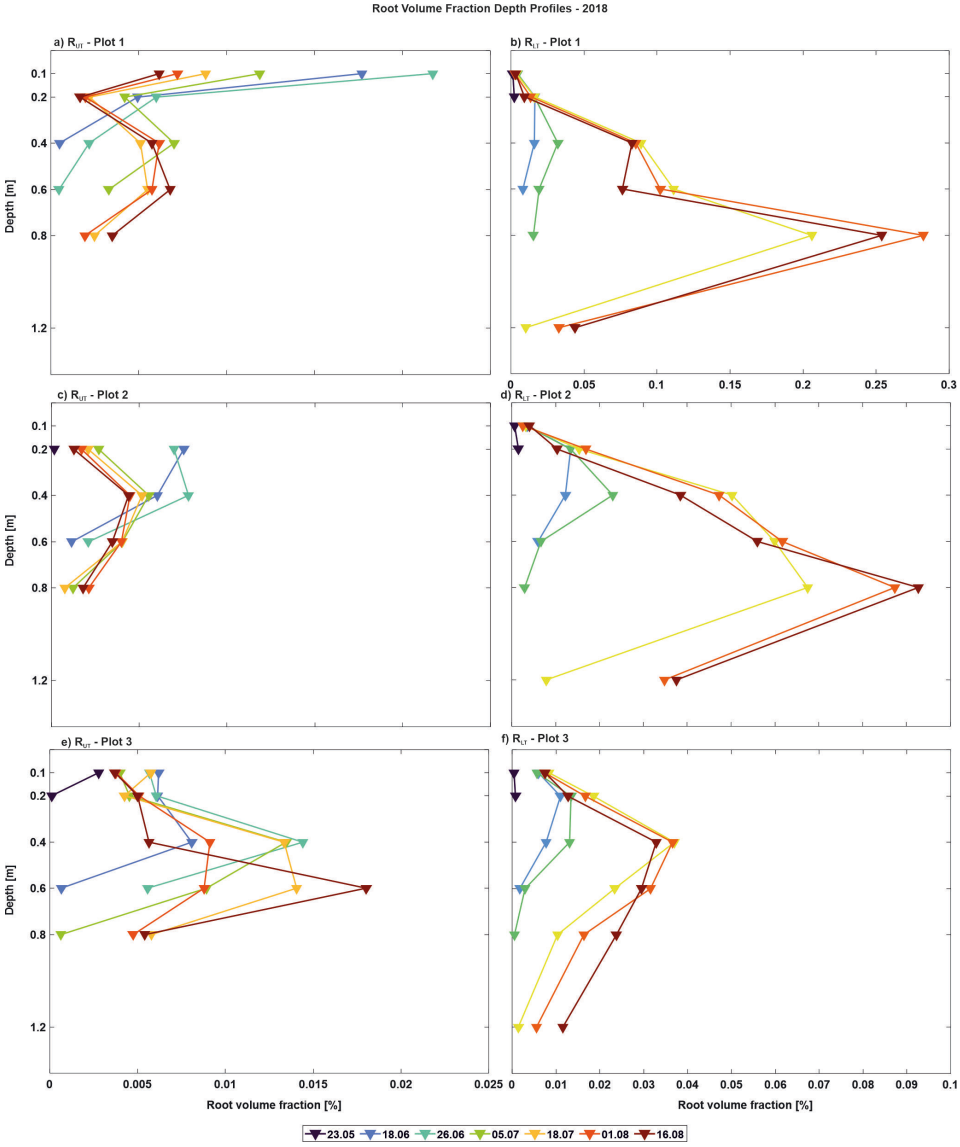

Figure A-3.2: Root volume fraction (*RVF*) depth profiles of 2018 for R_{UT} a), c) & e) and R_{LT} b), d) & f). The colored triangles represent the *RVF* values for the different depths, where the different colors represent the measurement date over the crop growing season.

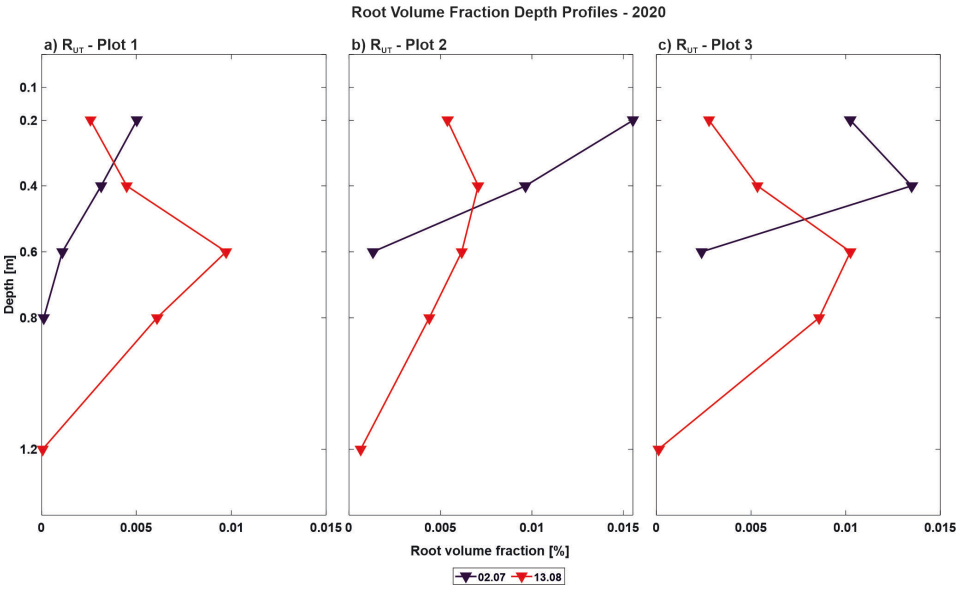

Figure A-3.3: Root volume fraction (*RVF*) depth profiles of 2020 for R_{UT}. The colored triangles represent the *RVF* values for the different depths, where the different colors represent the measurement date over the crop growing season.

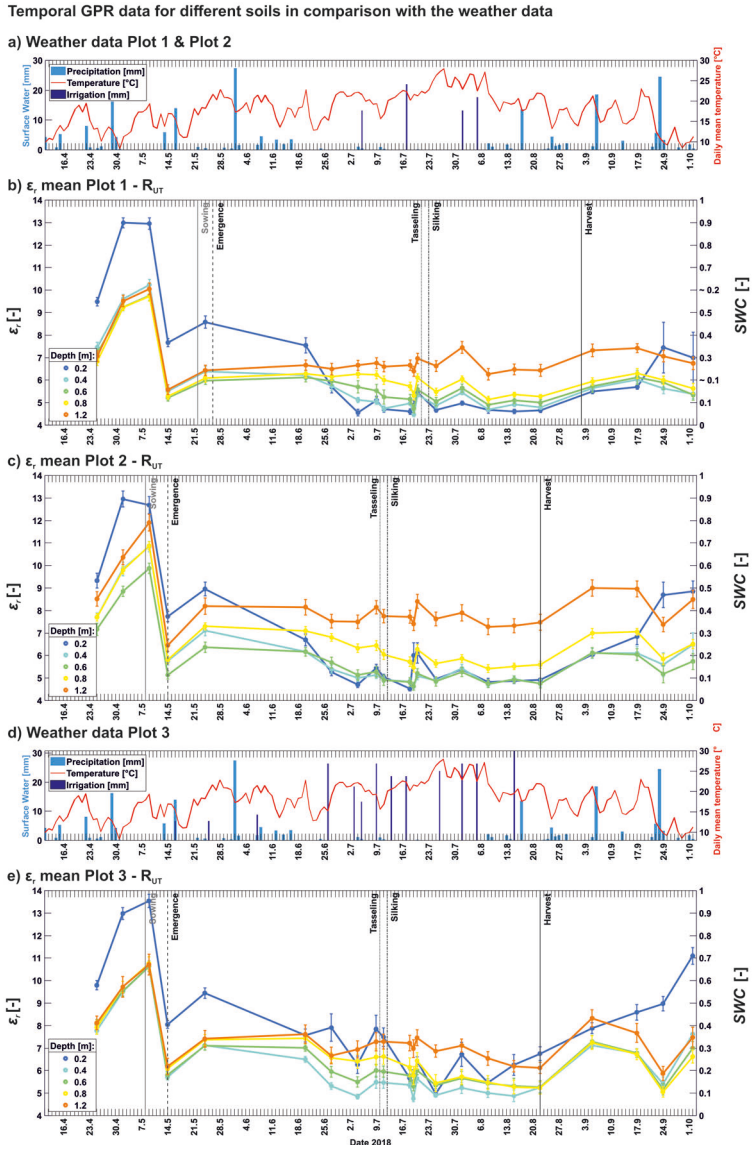

Figure A-3.4: Comparison of the weather data and permittivity for R_{UT} during the 2018 crop growing season. a) weather data: the solid red line represents the daily temperature values and the light blue bars represent the daily precipitation values. The dark blue irrigation values are only valid for Plot 3. b)-d) show mean permittivity per depth for Plot 1 2 & 3. The colored circles with the error bars indicate the permittivity mean along the rhizotube with its standard deviation as error bars. The colored solid lines connect the individual measurement days. The horizontal lines represent the dates for the vegetation stages and sowing and harvest dates. For convenience the approx. SWC values were added on the right-hand axis for b)-d) using the three-phase complex refracted index model (CRIM).

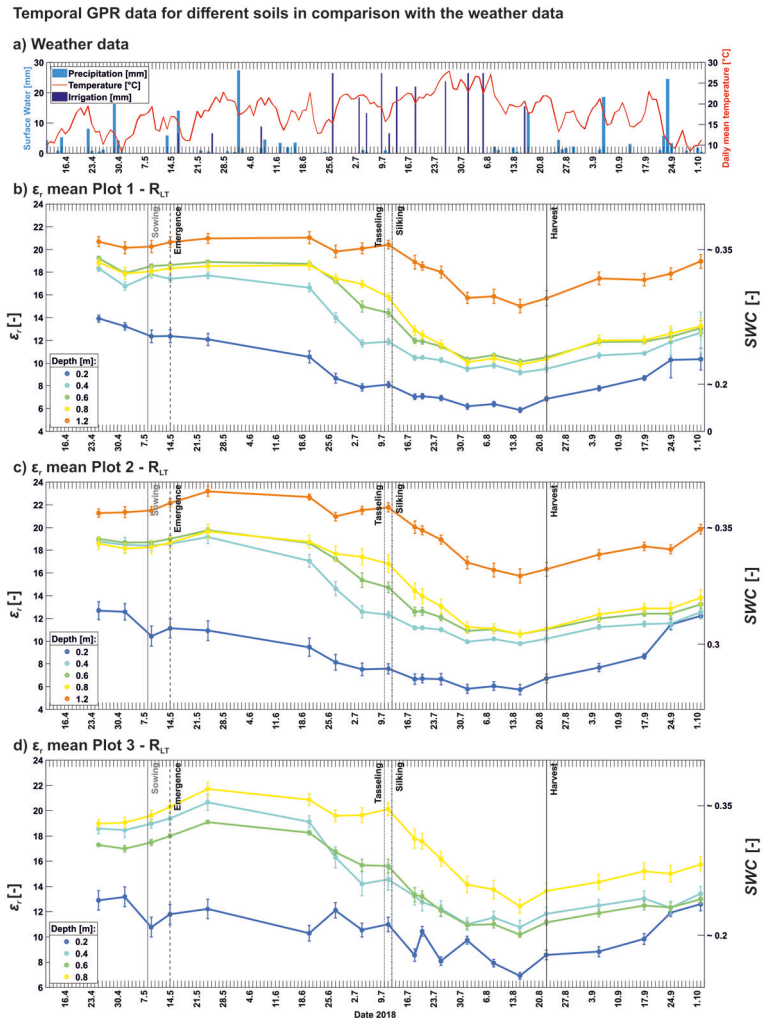

Figure A-3.5: Comparison of the weather data and permittivity for R_{LT} during the 2018 crop growing season. a) weather data: the solid red line represents the daily temperature values and the light blue bars represent the daily precipitation values. The dark blue irrigation values are only valid for Plot 3. b)-d) show mean permittivity per depth for Plot 1 2 & 3. The colored circles with the error bars indicate the permittivity mean along the rhizotube with its standard deviation as error bars. The colored solid lines connect the individual measurement days. The horizontal lines represent the dates for the vegetation stages and sowing and harvest dates. For convenience the approx. SWC values were added on the right-hand axis for b)-d) using the three-phase complex refractive index model (CRIM).

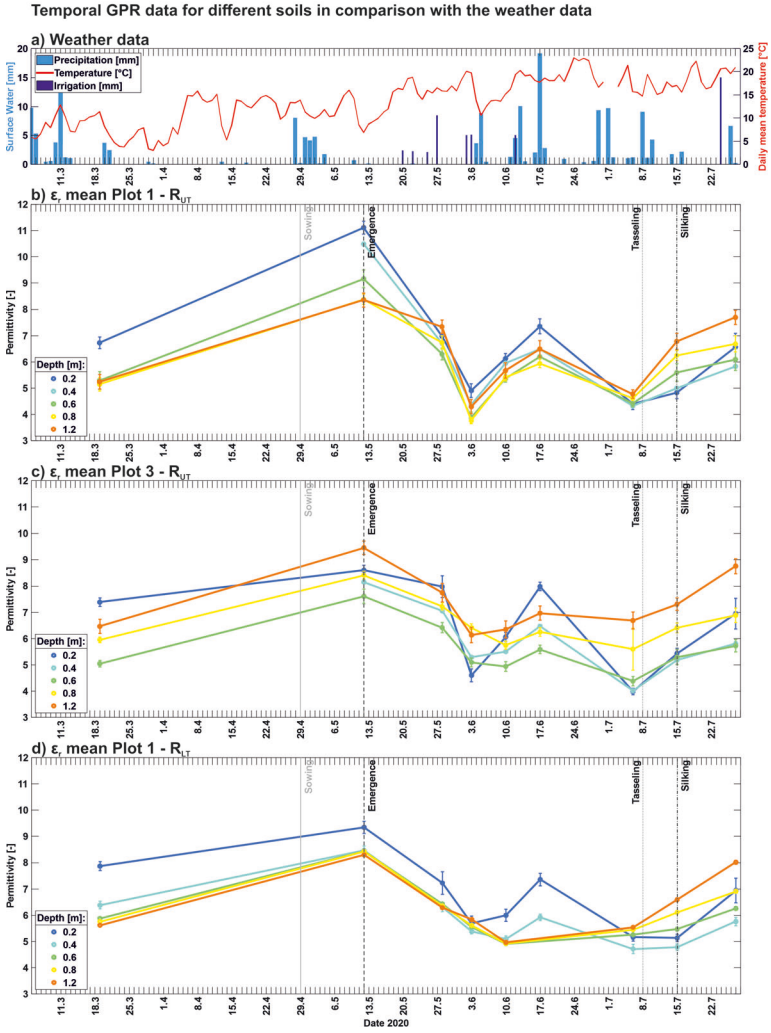

Figure A-3.6: Comparison of the weather data and permittivity for R_{UT} during the 2020 crop growing season. a) weather data: the solid red line represents the daily temperature values and the light blue bars represent the daily precipitation values. The dark blue irrigation values are only valid for Plot 3. b)-d) show mean permittivity per depth for Plot 1 2 & 3. The colored circles with the error bars indicate the permittivity mean along the rhizotube with its standard deviation as error bars. The colored solid lines connect the individual measurement days. The horizontal lines represent the dates for the vegetation stages and sowing and harvest dates. For convenience the approx. SWC values were added on the right-hand axis for b)-d) using the three-phase complex refractive index model (CRIM).

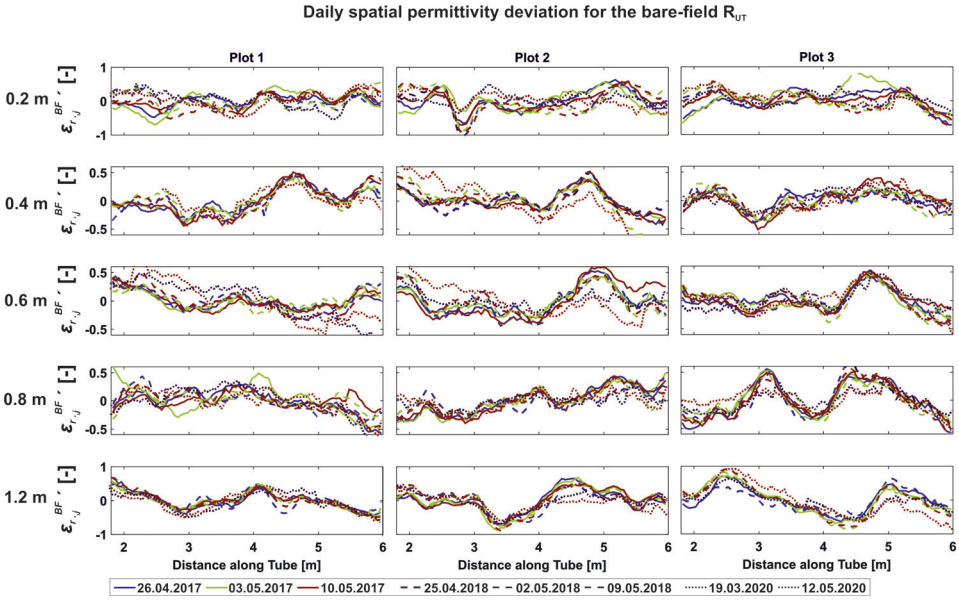

Figure A-3.7: Daily spatial permittivity deviation for the bare-field ${\varepsilon_r^{BF}}_{i,j}{}'$ along the rhizotubes under bare-field conditions for R_{UT} for the crop growing seasons 2017, 2018 & 2020. The colored solid lines indicate the daily spatial permittivity deviation for the bare-field ${\varepsilon_r^{BF}}_{i,j}{}'$ values of 2017 and the colored dashed lines the daily spatial permittivity deviation for the bare-field ${\varepsilon_r^{BF}}_{i,j}{}'$ of 2018 and the colored dotted lines for 2020.

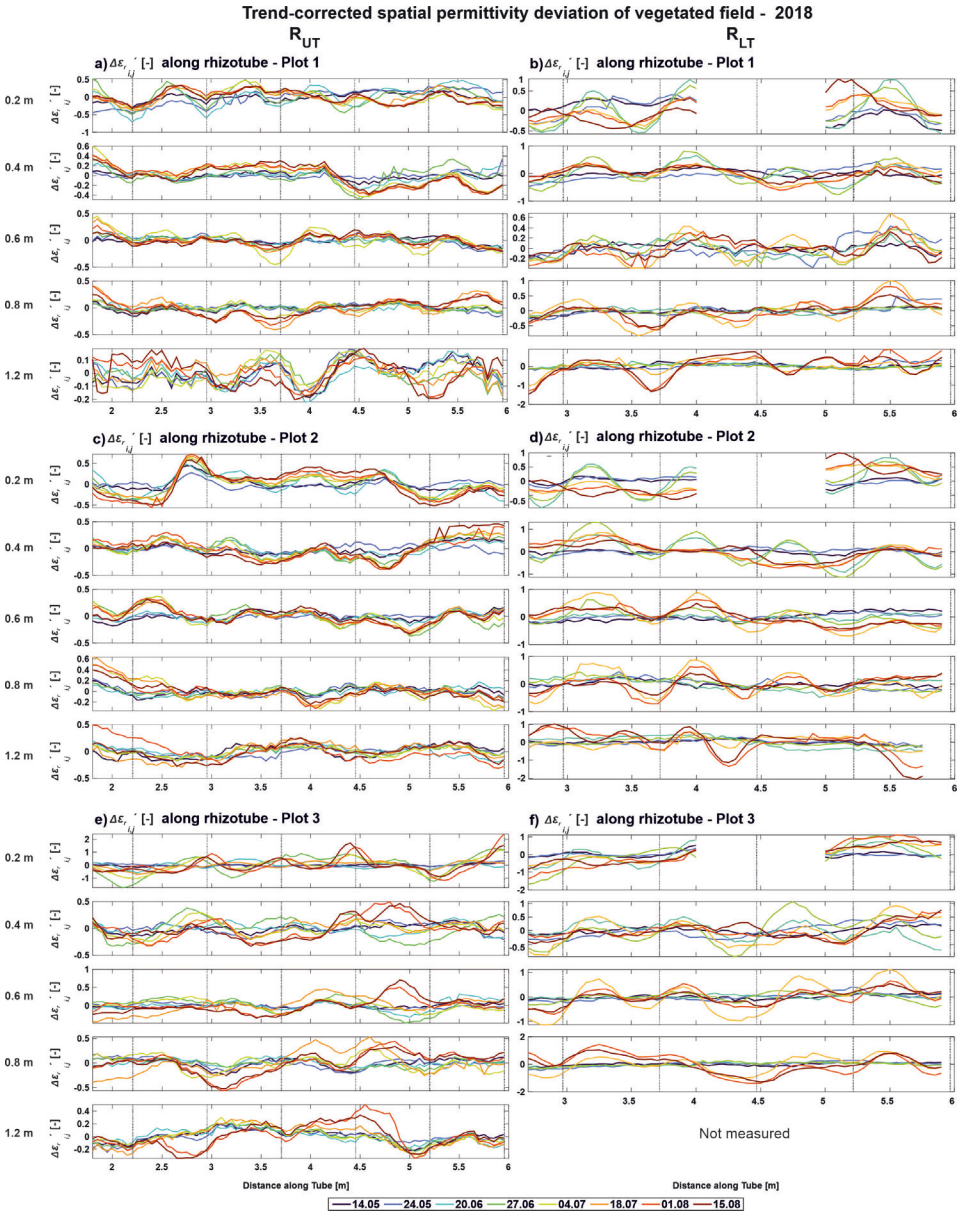

Figure A-3.8: Trend-corrected spatial permittivity deviation $\Delta\varepsilon_{ri,j}{}'$ of the vegetated field, along the rhizotubes over the different plots & depths, for R_{UT} and R_{LT} in 2018. The colored solid lines represent different dates during the crop growing season. The data gap of R_{LT} at 0.2 m depth is caused by the presence of the sEIT line.

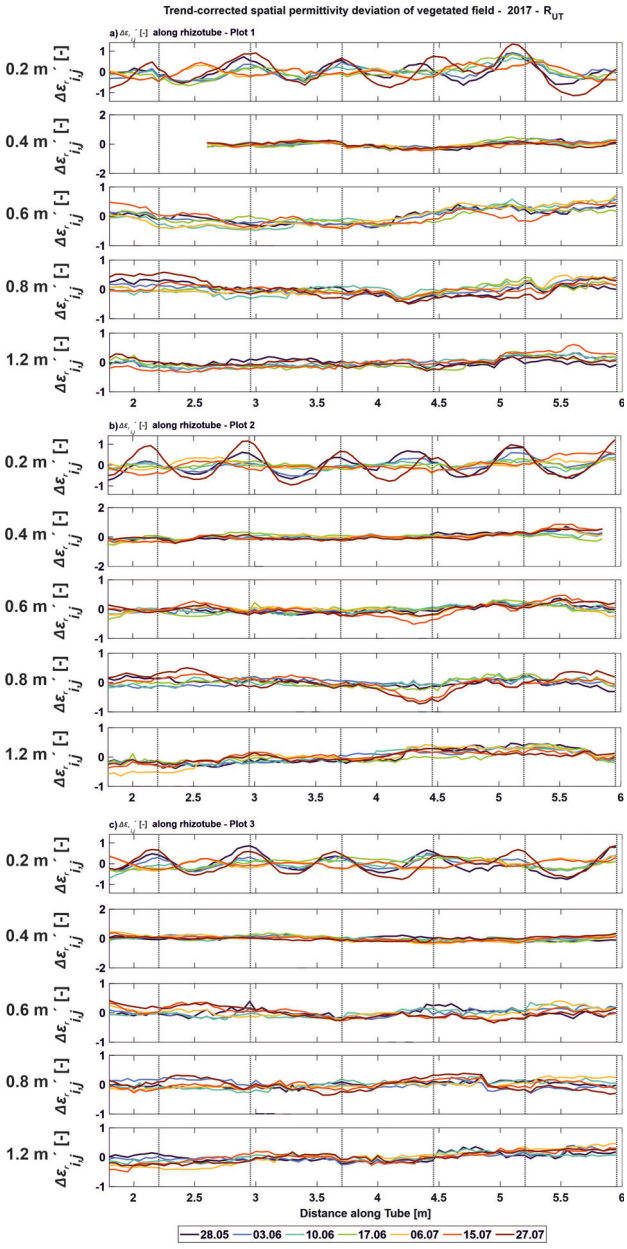

Figure A-3.9: Trend-corrected spatial permittivity deviation $\Delta\varepsilon_{ri,j}{}'$ of the vegetated field, along the rhizotubes over the different plots & depths, for R_{UT} in 2020. The colored solid lines represent different dates during the crop growing season.

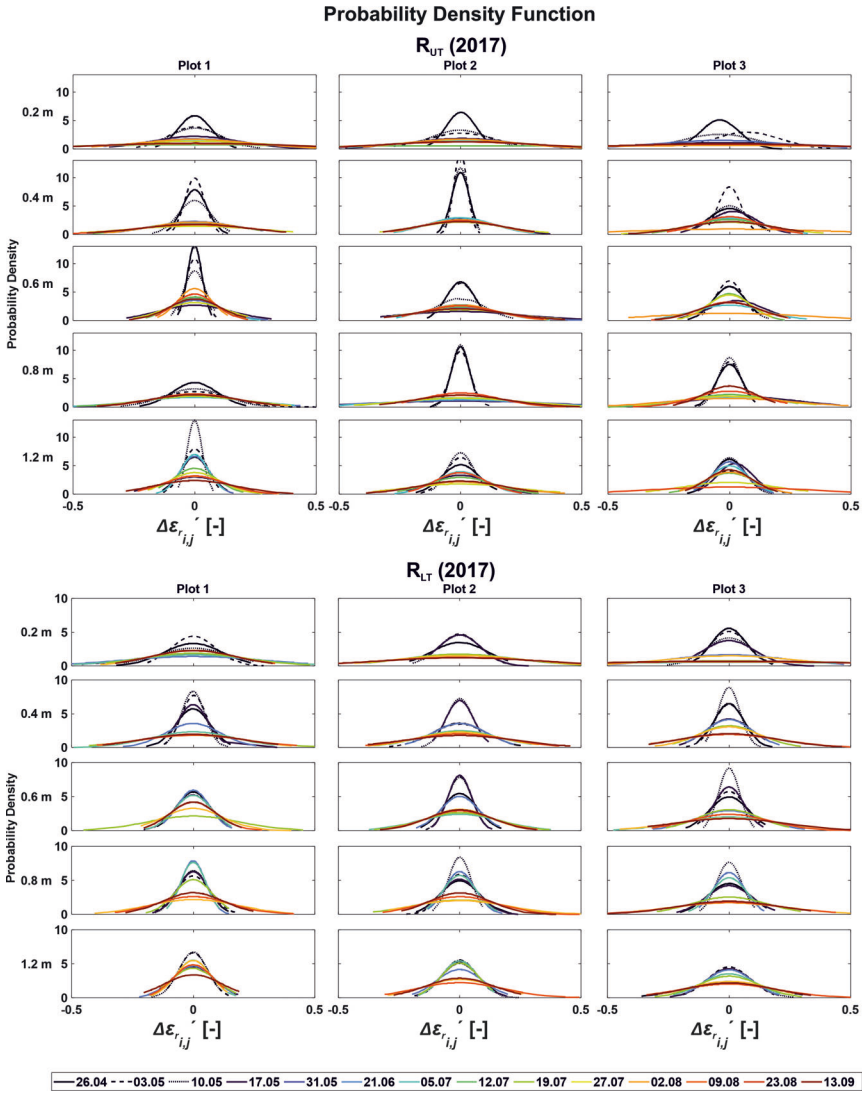

Figure A-3.10: Probability density function (PDF) of the trend-corrected spatial permittivity deviation $\Delta\varepsilon_{ri,j}{}'$ for all plots and depths of 2017, for both MR- facilities, respectively. The black solid, dashed and dotted lines represent the dates for the bare-field measurements and the colored lines represent the probability density functions of trend-corrected spatial permittivity deviation $\Delta\varepsilon_{ri,j}{}'$ for the crop growing season measurements.

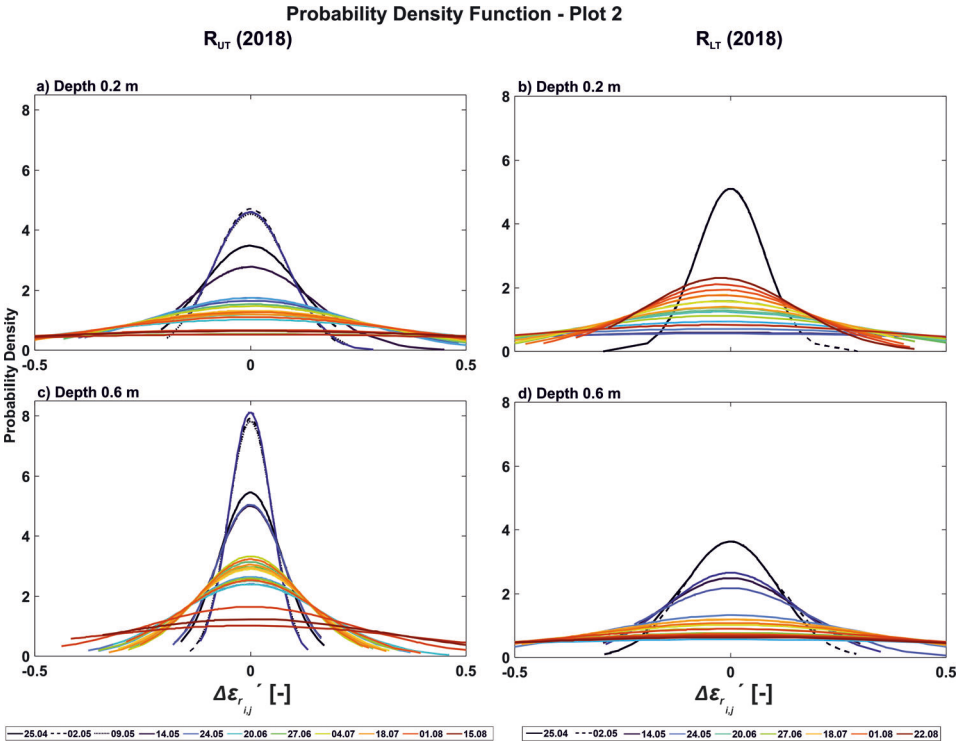

Figure A-3.11: Probability density function (PDF) of the trend-corrected spatial permittivity deviation $\Delta\varepsilon_{ri,j}{}'$ for depths 0.2 m and 0.6 m for Plot 2, for both MR- facilities of 2018, respectively. The black solid, dashed and dotted lines represent the dates for the bare-field measurements and the colored lines represent the probability density functions of the trend-corrected spatial permittivity deviation $\Delta\varepsilon_{ri,j}{}'$ for the crop growing season measurements.

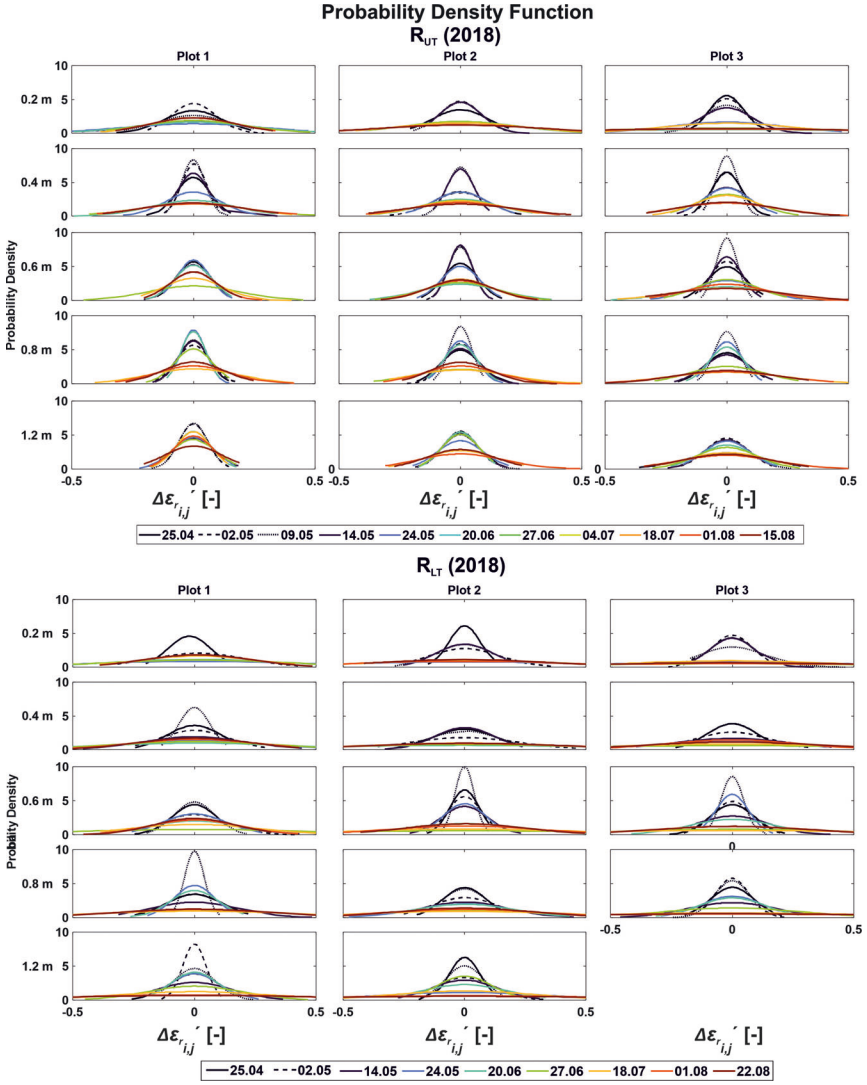

Figure A-3.12: Probability density function (PDF) of the trend-corrected spatial permittivity deviation $\Delta\varepsilon_{ri,j}{}'$ for all plots and depths of 2018, for both MR- facilities, respectively. The black solid, dashed and dotted lines represent the dates for the bare-field measurements and the colored lines represent the probability density functions of the trend-corrected spatial permittivity deviation $\Delta\varepsilon_{ri,j}{}'$ for the crop growing season measurements.

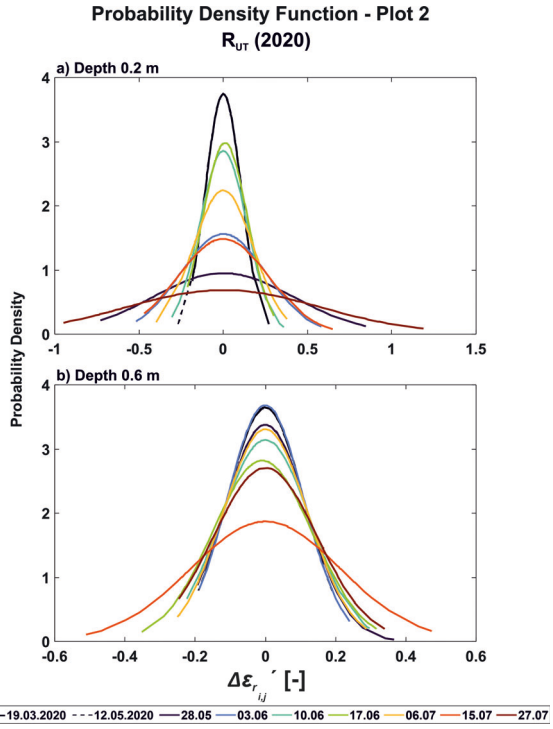

Figure A-3.13: Probability density function of the trend-corrected spatial permittivity deviation $\Delta\varepsilon_{ri,j}{}'$ for all depths and plots, for R_{UT} in 2020. The black, solid, dashed and dotted lines represent the date for the bare field days and the colored lines represent the probability density functions over the crop growing season

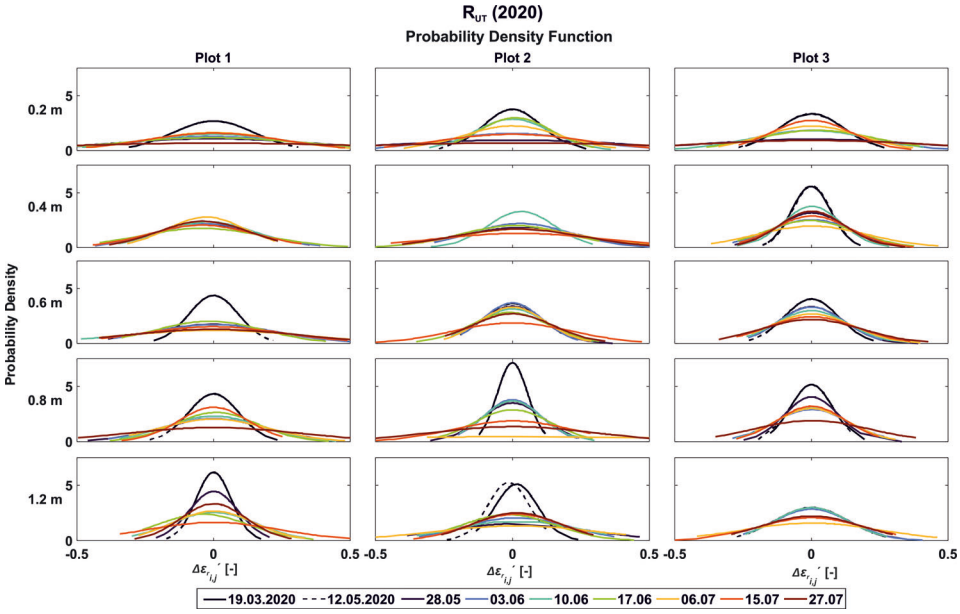

Figure A-3.14: Probability density function of the trend-corrected spatial permittivity deviation $\Delta\varepsilon_{ri,j}{}'$ for all depths and plots, for R_{UT} in 2020. The black, solid, dashed and dotted lines represent the date for the bare field days and the colored lines represent the probability density functions over the crop growing season

Chapter B

Appendix B: Spatial variability of hydraulic parameters of a cropped soil using horizontal crosshole ground penetrating radar

B-1 One dimensional field study – Cost function during optimization

The propagation of the cost function during optimization for soil hydraulic parameters indicates convergence across different parameters (Figure B-1.1). For specific parameters (θ_s, $\alpha 2$ subsoil layer) the convergence clearly headed towards a global minimum. For others, the funnel shape is more widespread out or skewed towards either side of the feasibility space boundary. Overall, all parameters exhibit a clear trend, minimizing the cost function.

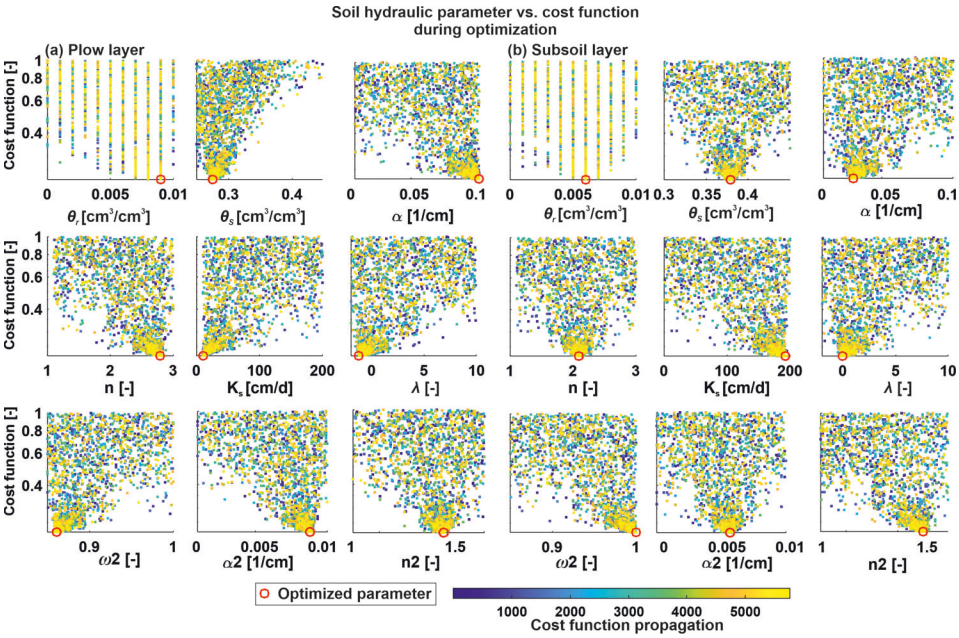

Figure B-1.1: Cost function values vs. soil hydraulic parameters during the optimization process. Note, that only cost function values between 0 and 1 are shown here.

B-2 Synthetic GPR modeling using gprMax

To verify the possibility of computing the SWCs by utilizing first arrival times obtained from time-lapse GPR measurements taken from horizontal rhizotubes, and subsequently estimating the SHP using sequential hydrogeophysical inversion, we conducted a synthetic experiment employing the three-dimensional finite-difference time-domain gprMax software (Warren et al., 2016). The SWC profiles were used for the second layer by optimizing the SHP in the two-layered unimodal model, as shown in Table 5-2 and Figure B-2.1. We derived the relative dielectric permittivity values for every 0.02 m from these profiles. For each of the 5 depths, a pair of rhizotubes with a spacing of 0.75 m between the receiver and transmitter antennae were used to compute the EM field components at the depth locations. The soil's electrical conductivity σ remained constant at 10 mS/m, while the source pulse was set to a Ricker wavelet centered at 200 MHz.

The EM waves generated from the calculations follow a processing similar to the one used for field measurements. The first break/first arrival time (FB) must be determined (see Figure B-2.1a), and from this the EM travel time, EM wave velocity, relative dielectric permittivity, and finally the SWC are calculated. This entire process is repeated for each depth at each timestep. The SWC profiles resulting from this processing can be compared to both the GPR-derived SWC measurements and the SWC profiles generated through optimized SWC employing HYDRUS 1D. Figure B-2.1b shows a comparison of the SWC

profiles for five dates during the measurement season. For depths ranging from 0.6 m to 1.2 m, the SWC derived from gprMax correlates with the optimized SWC profile, indicating the sufficiency of the first arrival time approach for estimating SWC. At depths of 0.2 m and 0.4 m, there is an observable offset between the SWC optimized and gprMax-derived SWC. This may be attributed to the difference in SHP between the plow layer and subsoil layer, resulting in significant differences in SWC values over short distances.

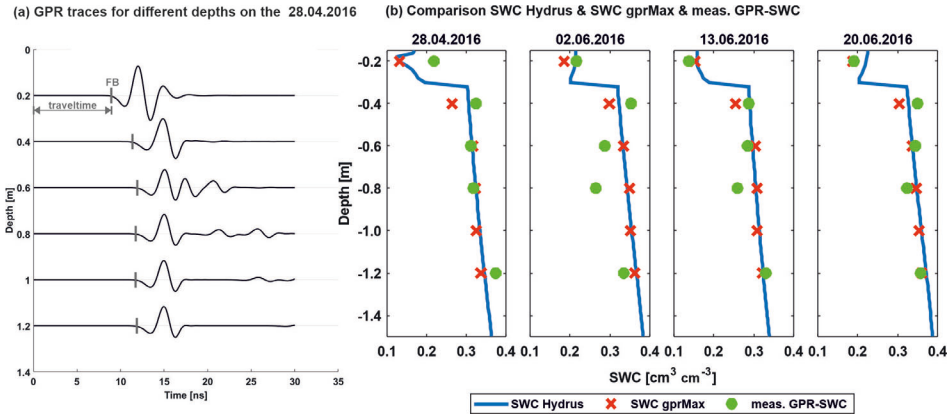

Figure B-2.1: Synthetic GPR traces modeled using gprMax (Warren et al, 2016) for the different depths on the 28.04.2016, where the black lines indicate the EM waves per depths and the grey marks represent the first break (FB) of the EM waves. SWC profile comparison for five exemplary GPR days (28.04.2016, 02.06.2016, 13.06.2016, 20.06.2016). The blues line presents the SWC profile resulting from the hydraulic SHP from the one-dimension inversion results, the red dashed line represents the results by using the SWC profile from the forward models as input for the synthetic gprMax modeling, and, the green line represents the GPR-SWC profile measured in the field.

B-3 Synthetic one-dimensional field study – Different measurement intervals and added noise

To assess the adequacy of recorded GPR information for retrieving hydraulic parameters using a sequential inversion approach, we conducted a synthetic study. We compiled synthetic GPR-SWC data using SHP results from a one-dimensional field study of a model with two layers and a single porosity retention curve. To reduce computing time, we adjusted the optimization search range (feasible space), as shown in Appendix B-2 Table B-3.1. Two distinct synthetic GPR-SWC datasets were compiled: (i) for the 20 GPR-days on which measurements were taken, and (ii) for the daily SWC values obtained over the entire modelling period, which spanned 323 days.

The optimization was conducted using the SCE-UA algorithm and Equation 11 as the cost function, as previously described. Table Appendix B-3 Table B-3.1 presents the results

of two models, where we compare their R^2 values. It is evident that the model utilizing solely GPR days exhibits the most suitable correspondence between synthetic GPR-SWC data and optimized SWC values (R^2=1.0), followed only by the model employing daily SWC values (R^2=0.999). The model with fewer measurement times outperforms the model with daily measurements. Therefore, the measurements taken throughout the crop growing season provide sufficient information for executing the sequential hydrogeophysical inversion.

The SCE-UA algorithm tests random values within the search range and calculates the cost function between the GPR-SWC and the optimized SWC using Equation 5-10. Figure B-3.1 shows the cost function values and corresponding SHP over the optimization course, indicating convergence towards the global minimum of the cost function and final set of SHP (only shown for i) the GPR days. The SHP converge towards the global minimum for the relatively small search range.

Table B-3.1: Results of the synthetic study. Comparison of the SHP of the forward model and the synthetic sequential inversion runs. R^2 is the variation between the synthetic GPR-SWC values and the optimized/ modeled SWC values.

			Lower boundary	Lower boundary	SHP		
					forward	GPR days	Daily
Plow layer	θ_s	[cm^3 cm^{-3}]	0	0.01	0.002	0.006	0.005
	θ_r	[cm^3 cm^{-3}]	0.2	0.3	0.25	0.25	0.251
	α	[1 cm^{-1}]	0.01	0.1	0.0795	0.0749	0.0763
	n	[-]	1.1	1.3	1.118	1.122	1.122
	K_s	[cm d^{-1}]	180	200	199.57	190.54	192.06
	λ	[-]	4	6	4.59	5.026	5.091
Subsoil layer	θ_s	[cm^3 cm^{-3}]	0	0.01	0.009	0.004	0.005
	θ_r	[cm^3 cm^{-3}]	0.35	0.4	0.387	0.388	0.384
	α	[1 cm^{-1}]	0.007	0.1	0.0086	0.0087	0.0085
	n	[-]	1.1	1.4	1.358	1.351	1.352
	K_s	[cm d^{-1}]	140	180	159.52	159.73	162.52
	λ	[-]	-1	0	-0.6	-0.625	-0.498
			R^2			**1.0**	**0.999**

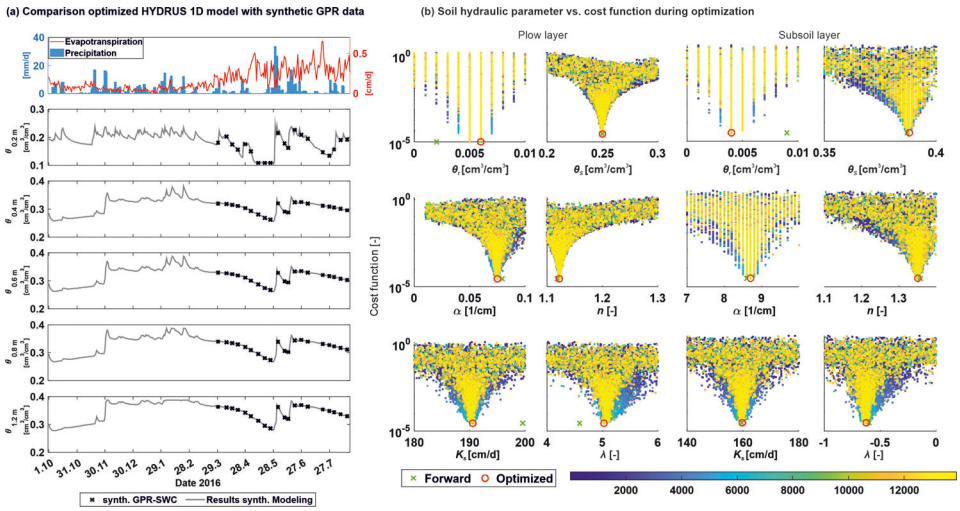

Figure B-3.1: Results of the synthetic modeling. The black crosses indicate the synthetic GPR-SWC values and the blue line represents the SWC optimized by the SCE-UA. Error Propagation for a.) topsoil and b.) subsoil, for the optimized parameters individually. The objective function value/ error is represented by the y-axis, the according value of the optimized parameter is indicated on the y-axis. The error propagation is shown as a color gradient, where blue colors represent early runs and yellow colors represents the runs before the termination of the SCE-UA. The green cross indicates the input hydraulic parameter value (parameter which originates the synthetic SWC values), the red circle indicates the optimized hydraulic parameter.

B-4 Correlation between λ and K_s for the upscaling results

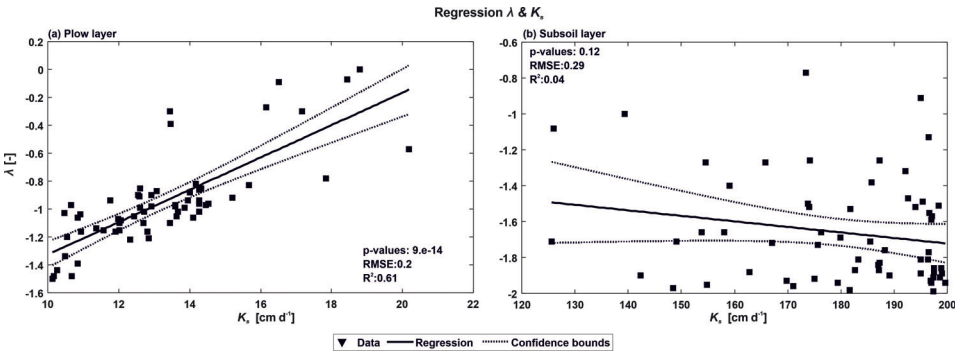

Figure B-4.1: Correlation between λ and K_s for the upscaling results.

Chapter C

Appendix C: High resolution soil-root modeling for crosshole GPR data

C-1 Feasibility study - petrophysical relationships considering roots

When a different porosity ($\phi = 0.25$) is present in the soil, the effect that with a certain RVF, the water remaining in the soil is 0, is enhanced for especially dry soil conditions. For a permittivity of $\varepsilon_r = 4$, a RVF values above 2.7% will lead to a four-phase SWC of 0, while the three-phase SWC is 0.03. For a soil with $\varepsilon_r = 8$, the threshold for the RVF, where there no water left in the soil is $RVF = 11.06\%$.

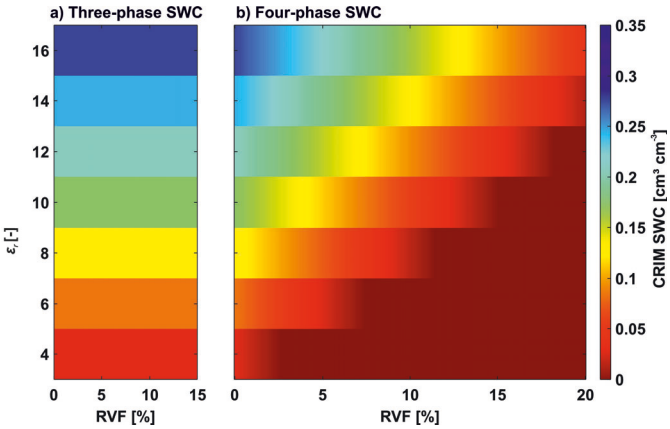

Figure C-1.1: Results of the feasibility study for a) three-phase and b) four-phase CRIM equation for varying bulk permittivity and root volume fraction (RVF) of the soil-plant continuum. Porosity was defined as $\phi = 0.25$.

C-2 Effects of roots on the GPR signal- depth 0.6 m

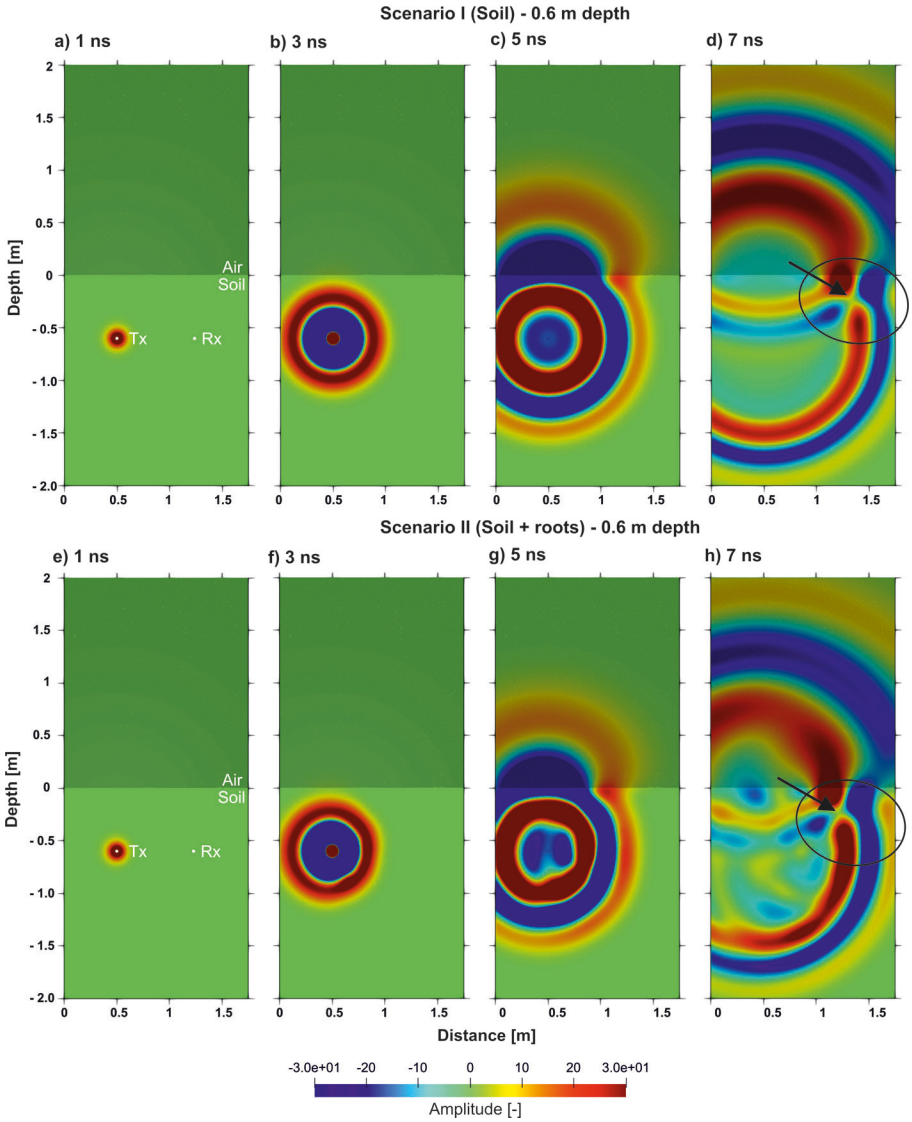

Figure C-2.1: Image plots a)-d) for Scenario I and e)-h) for Scenario II of the forward modelled electrical field distributions through the model domain for four time steps when the Tx and Rx are located at 0.6 m depth in the R_{LT} with a SWC of 0.1 [cm^3 cm^{-3}].

C-3 Effects of the measurement frequency on the GPR signal

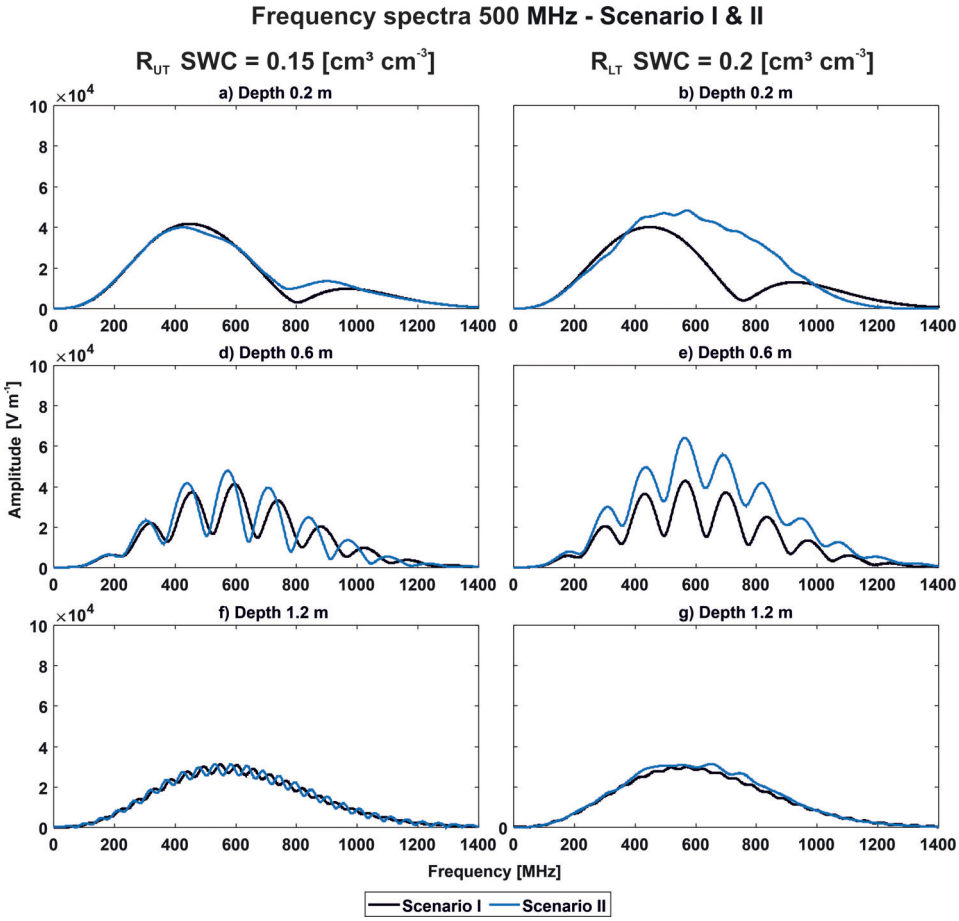

Figure C-3.1: Frequency spectra for 500 MHz data for a SWC of 0.15 cm^3 cm^{-3}] and 0.2 cm^3 cm^{-3} for a), c) and e) R_{UT} and b), d) and f) R_{LT}, respectively. The black and blue solid line indicates Scenario I and II, respectively, for the depths 0.2, 0.6, and 1.2 m.

C-4 Effects of the above-ground shoot on the GPR signal

Table C-4.1: Three-phase SWC for Scenario I and three-phase and four-phase SWC results for Scenario II for R_{UT} & R_{LT} and different SWC conditions between 0.05 – 0.35. The [%] misfit between the three- & four-phase SWC is provided in brackets.

Depth [m]	R_{UT} Scenario III	R_{UT} Scenario IV		R_{UT} + Scenario III	R_{UT} + Scenario IV	
SWC in HHS		**0.15**			**0.20**	
	three-phase SWC	three-phase SWC	four-phase SWC	three-phase SWC	three-phase SWC	four-phase four-phase SWC
Single above-ground shoot						
0.1	0.07	0.07	0.04 (-50.68%)	0.08	0.07	0.07 (-10.0)
0.2	0.16	0.16	0.13 (-19.14%)	0.17	0.18	0.18 (-1.68%)
0.4	0.18	0.19	0.16 (-16.40%)	0.20	0.24	0.23 (-1.69%)
0.6	0.18	0.19	0.16 (-15.96%)	0.20	0.25	0.25 (-1.18%)
0.8	0.18	0.18	0.15 (-16.85%)	0.20	0.24	0.24 (-1.65%)
1.2	0.18	0.18	0.15 (-16.67%)	0.20	0.20	0.20 (-1.45%)
Multiple above-ground shoots						
0.1	0.8	0.08	0.05 (-43.21%)	0.09	0.09	0.08 (-7.87%)
0.2	0.16	0.17	0.14 (-18.56%)	0.18	0.19	0.18 (-1.62%)
0.4	0.18	0.19	0.16 (-16.40%)	0.20	0.24	0.23 (-1.69%)
0.6	0.18	0.19	0.16 (-15.96%)	0.20	0.25	0.25 (-1.18%)
0.8	0.18	0.18	0.15 (-16.85%)	0.20	0.24	0.24 (-1.65%)
1.2	0.18	0.18	0.15 (-16.67%)	0.20	0.020	0.20 (-1.45%)

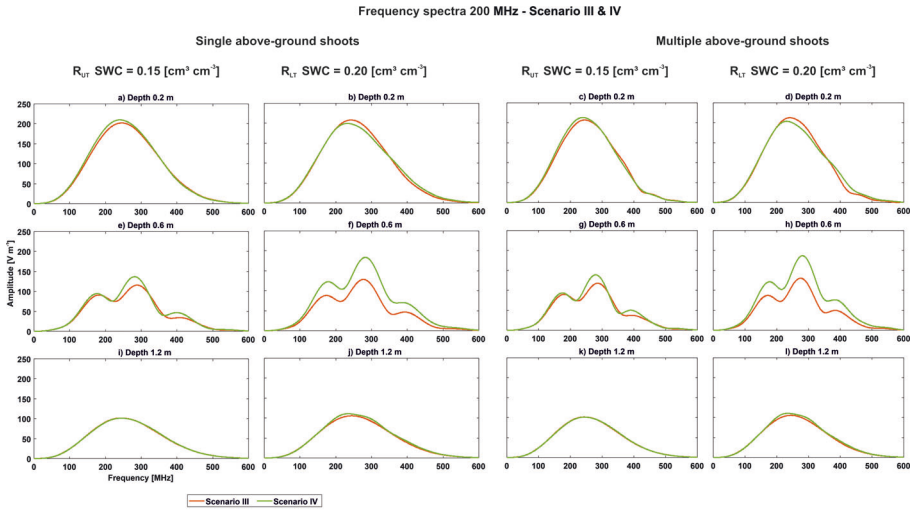

Figure C-4.1: Frequency spectra using 200 MH data for a SWC of 0.15 [cm³ cm^{-3}] and 0.2 [cm³ cm^{-3}] for a), c) and e) R_{UT}, and b), d) and f) R_{LT}, respectively. The black and blue solid line indicates Scenario I and II, respectively, for depths 0.2, 0.6, and 1.2 m.

Chapter D

Appendix D: Monitoring Soil Water Content Using Time-Lapse Horizontal Borehole GPR Data at the Field-Plot Scale

Abstract

Ground penetrating radar (GPR) has shown a high potential to derive soil water content (SWC) at different scales. Here, we combine horizontal GPR measurements with a novel experimental setup. Multiple horizontal minirhizotubes at different depths are used to investigate the spatial, and temporal variability of the SWC under cropped plots. Thereby, SWC data are analyzed for four growing seasons between 2014–2017, two soil types (gravelly and clayey/silty), two crops (wheat and maize), and three different water treatments: rainfed, irrigated, and sheltered. We acquired more than 150 time-lapse GPR datasets along 6 m long horizontal crossholes at six depths. To obtain accurate SWCs from GPR data, we optimized the calibration and processing steps of the GPR data and developed a processing tool to obtain SWC for each measurement location. The GPR SWC distributions show distinct horizontal and vertical heterogeneity and different SWC variabilities for both soil types. A clear change in porosity and SWC can be observed at both sites between the surface layer (> 0.3 m) and subsoil. Alternating patches of higher and lower SWC, probably caused by the soil heterogeneity, were observed along the horizontal SWC profiles, especially at the site with coarse soil material. To investigate the changes of SWC over time, GPR and TDR data are averaged for each depth and compared to changes in temperature and precipitation, treatment and soil type. The high temporal resolution TDR and the large sampling volume GPR show similar trends in SWC for both sites, but because of the different sensing volumes different responses are obtained due to the spatial heterogeneity. Difference in spatial variation of the crosshole GPR SWC data was detected between maize and wheat. The results for this four-year period

indicate the potential of this novel experimental setup to monitor spatial and temporal SWC changes. Such high spatial resolution data can be used to study the soil-plant-atmosphere interactions of agricultural crops at the field plot-scale.
Adapted from: Anja Klotzsche, Lena Lärm, Jan Vanderborght, Gaochai Cai, Shehan Morandage, Mirjam Zörner, Harry Vereecken, Jan van der Kruk (2019): Monitoring Soil Water Content Using Time-Lapse Horizontal Borehole GPR Data at the Field-Plot Scale, Vadose Zone Journal, 18(1), 190044. 2019, `https://doi.org/10.2136/vzj2019.05.0044`

D-1 Introduction

Soil water content (SWC) is an important state variable that is linked to several important soil functions and strongly depends on the internal organization of the soil-plant system. Soil water is important for crop growth and food and feed production, can percolate to deeper layers and replenish aquifers, can carry solutes towards the groundwater, and is required by micro-organisms that regulate biogeochemical cycles. Soil water and related soil processes vary considerably in space and time due to spatially variable soil properties and highly dynamic boundary conditions (e.g., precipitation, evapotranspiration). Understanding and subsequently predicting soil processes require information of SWC and how it varies in time and space. SWC can be monitored using in-situ sensors (that can be connected to the internet and provide seamless data streams of local SWC) and using remote sensing from satellites (e.g., Simmer et al. (2015a); Vereecken et al. (2016)). In-situ sensors have a small spatial support so that a large number of sensors would be required to obtain an accurate and precise estimate over large scales. Another challenge is to infer connected patterns of SWC that represent preferential flow paths in the soil or landscape with in-situ sensors since they do not provide a dense spatial coverage. The limitation of satellite SWC products is that they have a low spatial resolution and most sensors are only sensitive to the SWC in the upper few centimeters of the soil profile (Garré et al., 2013, 2011). To fill the gap between in-situ sensors and satellite products, high resolution nondestructive geophysical imaging methods show an increasing potential to further improve the detection, monitoring, and imaging of in-situ soil properties at the field-scale. Near surface geophysical methods, such as electrical resistivity tomography (ERT), electromagnetic induction (EMI), and ground penetrating radar (GPR) provide maps of SWC at the field plot scale up to the field and catchment scale with dense spatial coverage, and can be used to enhance agricultural, environmental and land surface models (Binley et al., 2015). Several geophysical studies have been performed to investigate the soil-plant system using time-lapse monitoring data at the laboratory or field-scale applying mainly ERT, time domain reflectometry (TDR), or EMI tools. For example, root water uptake was investigated with time-lapse ERT within lysimeters and for different cropping systems in the field (Garré et al., 2013, 2011). Several other field studies were performed using a fixed installed ERT monitoring transect to study the soil-plant interaction of orange trees (Vanella et al., 2022) and crops like wheat (Shanahan et al., 2015) and maize (Beff et al., 2012, Michot et al., 2003). Even though all these studies successfully demonstrated the potential to derive soil water and plant interaction, each of the methods has limitations. For example, TDR provides point information; ERT and EMI are sensitive to several other factors beyond water content, and EMI provides a good coverage in space but with limited spatial resolution.

The advantage of GPR in comparison to ERT and EMI is that GPR provides information about the relative dielectric permittivity ε_r of the soil, which is more directly related to SWC than the electrical conductivity σ (Huisman et al., 2003, Klotzsche et al., 2018). Since the emergence of the field of hydrogeophysics Binley et al. (2015), GPR has shown a high potential to map, detect and monitor SWC changes to improve the hydrological characterization of the vadose zone with the highest possible resolution compared to other geophysical methods because of the use of high frequencies between 25 MHz to 1.6 GHz (Binley et al., 2002b, Dafflon et al., 2011, Linde et al., 2006, Paz et al., 2017, Steelman et al., 2017). Because

of the large difference between the relative dielectric permittivity of air $\varepsilon_r = 1$ and water $\varepsilon_r = 80$, it can be used to obtain the SWC in the vadose zone. To investigate flow and transport processes, time-lapse GPR measurements with a high spatial and temporal resolution can be linked to soil hydrological parameters such as hydraulic conductivity. For example, Looms et al. (2008b) investigated unsaturated flow and transport processes using crosshole GPR and ERT in alluvial sandy sediments and estimated hydraulic patterns (Looms et al., 2008a). Strobach et al. (2014) combined surface and borehole GPR measurements to monitor rainfall infiltration in the vadose zone and to investigate characteristic infiltration regimes.

Allroggen et al. (2015) measured and monitored flow processes in the near subsurface using 3D surface GPR measurements during rainfall experiments and associated patterns of travel time changes of GPR signals with SWC variations. To further extend our knowledge about the relations between GPR data and hydrological parameters, controlled environments are essential. At the laboratory scale GPR measurements can be performed at lysimeters (Schmalholz et al., 2004, Wijewardana et al., 2017). Klenk et al. (2015) and Jaumann and Roth (2018) used surface GPR data to study SWC changes during pumping and infiltration experiments in the ASSESS site of the University of Heidelberg: a 20 m long, 4 m wide and approximately 1.9 m deep tank in which a known heterogeneous structure of different sand layers was created. Due to the control of these layers on the spatio-temporal distribution of SWC, which could be observed with surface GPR, they could infer the hydraulic properties of the layers. Furthermore, several surface GPR studies have been performed to detect and characterize the soil-plant systems and the influence of the SWC on plant development. For example, Rodríguez-Robles et al. (2017) used GPR to map tree roots. Wijewardana and Galagedara (2010) investigated the spatial and temporal variability of the SWC for different crop types. Nevertheless, the characterization of the climate-plant-soil interaction at the plot-scale is very limited until now and long-term monitoring using GPR or other geophysical methods over serval growing seasons are very sparse in literature (e.g., Jayawickreme et al. (2010) for 2 year ERT study). The disadvantage of 'classical' GPR is that it cannot be used in an automated monitoring mode and that the interpretation of surface GPR measurements to derive depth profiles of SWC is not straightforward in the absence of clear reflections and/or gradients. Cross-borehole GPR can be used to investigate the deeper near subsurface between boreholes. Borehole GPR measurements can provide higher resolution insights into the subsurface and are well suited to characterize the vadose zone (Binley et al., 2002a, Klotzsche et al., 2013) and to monitor infiltration and recharge processes Looms et al. (2008a). Horizontal cross-borehole acquisitions provide a direct link of SWC variations between the tubes at certain depth slices and are well suited to investigate how SWC varies both in time and space at a certain depth due to infiltration, redistribution and plant water uptake at the plot-scale. Parkin et al. (2000) first applied crosshole GPR measurements in horizontal tubes below a wastewater trench at 1.2 m depth. Thereby, they applied zero-offset profiling (ZOP) that provided an average SWC along the tubes, and, multi-offset gathers (MOG) to estimate a two-dimensional SWC distribution in a horizontal plane. Redman et al. (2000) and Galagedara et al. (2002) used GPR in horizontal boreholes to study the temporal and spatial variation of SWC under wetting and drying conditions. These studies indicated the potential to detect and map zones of higher water content in between tubes that could be linked to preferential flow paths at the plot-scale that are difficult to obtain using other methods. All these studies mainly concentrated on water content changes without considering the effect of plants. Especially the impact of plants has not been investigated so far using horizontal

borehole GPR data. Thereby, the challenging aspect is that GPR is able to retrieve SWC for a certain domain, but without further information, it is very difficult to distinguish between the part of the water in the soil and water related to root zones. For tree roots Al Hagrey (2007) stated a variation of the permittivity between 4.5 for dry wood up to 22 for wet wood, which is in a similar range as for example dry and wet sand. Therefore, to differentiate between soil and finer root effects on the permittivity/SWC long term monitoring that captures different variations of both are necessary.

In this paper, we used long-term time-lapse horizontal borehole GPR data to monitor and characterize SWC variation caused by plants for different surface treatments in two different soil types. The main aim of this study was to investigate how SWC can be observed at high temporal and spatial resolution. Since boreholes were installed at different depths, we also tested whether the vertical variations in SWC could be detected with GPR. A special focus will be to improve the understanding of how small-scale soil changes affect plant growth at the plot scale (e.g., zones of preferential flow) and how the SWC is changing over several measurement seasons for different soil and plant types. As part of it, we will characterize the plot-field-scale soil heterogeneity by capturing the structural organization of soil (layering and texture) using GPR. Therefore, we compared GPR derived water contents with TDR measurements and we carried out full wave form simulations to evaluate the effect of the sharp contrast of dielectric permittivity at the soil surface and the effect of vertical variations in SWC on the GPR derived vertical water content profiles. By monitoring SWC and its variation in a field plot over four growing seasons, we investigated the persistency of the patterns and the magnitude of the spatial SWC variations and distinguished a temporally stable component from a variable component that is linked to either temporally varying soil properties or changing rooting patterns between different growing seasons or crops.

D-2 Experimental setup

D-2-1 Test site and instrumentation of the minirhizotrons

Two minirhizotron facilities were installed in 2012 and in 2014 at the Selhausen site, Germany, which is part of the TERENO-Rur hydrological observatory (Bogena et al., 2018, Weihermüller et al., 2007). The field is located at a transition zone between the Upper and Lower Terrace of the Rhine/Meuse river system (see Figure D.1), which corresponds with a transition between a soil with a high gravel content and low apparent electrical conductivity in the upper part of the field and a soil with a clayey and silty texture and a higher electrical conductivity at the lower part of the field (Rudolph et al., 2015). To cover this variation in soil properties, one minirhizotron facility was installed in the upper part R_{UT} and the other one in the Lower Terrace R_{LT}. The so-called minirhizotron is an installation that allows repeatable and non-invasive measuring of plant roots and studying, root growth in interaction with changing soil conditions (Cai et al., 2016). Over the past years several geophysical and hydrological studies have been performed at this test site (Busch et al., 2014, Huisman et al., 2003, Rudolph et al., 2015, von Hebel et al., 2014). A weather station is installed by the TERENO project providing, e.g., precipitation and temperature values (blue dot in Figure D.1). The groundwater table depth is located between 3 m and 5 m below the surface depending on seasonal fluctuations.

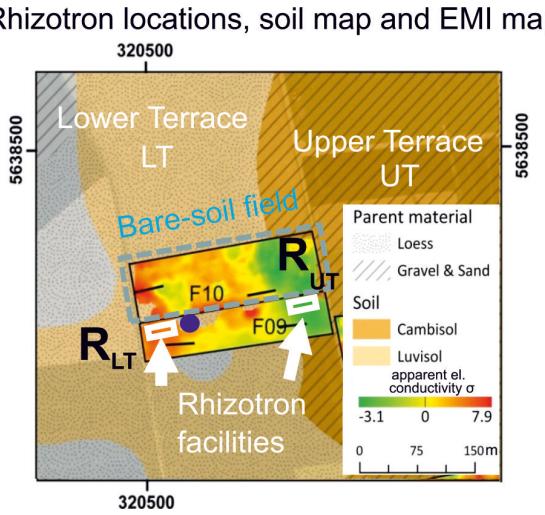

Figure D.1: Location of the minirhizotron facilities indicated on the (EMI) and soil map of the Selhausen test site. One rhizotron is located in the upper terrace (R_{UT}) and one in the lower terrace (R_{LT}) of the bare-soil field of the test site, and both are indicated with boxes. The R_{UT} and R_{LT} are positioned in lower and higher apparent conductivity areas, respectively, illustrating the different soil properties of the terraces. The blue dot indicates the location of the weather station. The map is modified from Rudolph et al. (2015).

Both facilities are equipped to obtain a full access to the near surface soil volume of 1.2 m depth by 9 m width by 6 m length. For the monitoring purposes, horizontal tubes with a total length of 7 m were installed at six different depths between 0.1 m and 1.2 m with 3 replicates for 3 treatments in both facilities (Figure D.2a, c). The boreholes were separated by 0.75 m. To avoid interferences between the different tubes, the boreholes are shifted horizontally (see Figure D.2c). In each facility, three 3 m by 7 m plots that received different water treatments: rainfed (natural conditions), irrigated, and sheltered. The facilities provide the opportunity to study at each site spatio-temporal variations of SWC under three different treatments: rainfed (natural conditions), irrigated, and sheltered (Figure D.2b). The R_{UT} site was excavated in layers, and after the boreholes where installed, refilled trying to keep the former layering and compaction of the soil. At R_{LT} a horizontal drilling device was used to install the boreholes, hence the soil is almost undisturbed. The tubes were drilled with a special tool designed by the Engineering und Technologie department (ZEA-1) of the Forschungszentrum Jülich GmbH. A sensor network with TDR sensors and one tensiometer was installed at each borehole depth and each treatment plot. For each treatment plot, four TDRs per depth were installed that measure hourly the SWC (see Cai et al. (2016) for more details). The TDR sensors are a three-rod system with a rod length of 200 mm and a rod separation of 26 mm. All TDRs are located 0.75 m away from the facility wall. Note that stones and gravel larger than 60 mm were removed around the places where the TDR sensors were installed (red dots in Figure D.2a). Due to compaction and erosion of the soil, the original planned depth of the tubes of 0.1 m - 1.2 m were slightly lowered by 4 cm (manually checked different times per year).

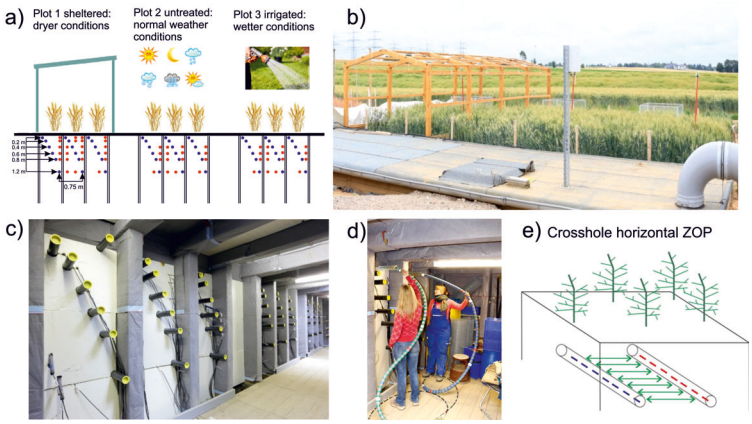

Figure D.2: (a) Schematic setup of the minirhizotron facility at the Selhausen test site, Germany, with the location of the horizontal boreholes and the time domain reflectometry (TDR) sensors indicated with blue and red dots; (b) picture of the facility from the top during the growing season; (c) picture of the facility inside; and (d) when measurements are performed; and (e) schematic setup of the zero-offset profile (ZOP) measurements along tubes at the same depth to obtain depth slices.

In this study, we will concentrate on the growing seasons of 2014, 2015, and 2016, when winter (Triticum aestivum cv. Ambello) and summer wheat (Triticum aestivum cv. Scirocco) was sown at both facilities. Subsequently, we present data of 2017, when maize (Zea mays cv. Zoey) was sown. The wheat was planted in narrow rows with a separation of 12 cm and the maximum crop height was approximately 0.95 m. The maximum observed rooting depth for the winter wheat was the same at all three plots at 0.8 m or 1.2 m for R_{UT} and R_{LT}, respectively (Cai et al., 2016). The maize was planted with a row separation of 0.75 m and at the end of the measurement period the plants reached a maximum height of approximately 2.1 m and a maximum rooting depth of around 0.8 m and 1.5 m for R_{UT} and R_{LT} was observed, respectively. The maize plants showed a gradation in height for the different plots (higher in the irrigated plot). Note that after 2016 no shelter was installed anymore because of the height of the plants. Instead, two rainfed plots were used. Table D.1 indicates the used plant type, sowing, emerging, flowering, and harvesting times. After harvest bare soil conditions were present at the three plots.

Table D.1: Measurement days for the upper terrace (R_{UT}) and lower terrace (R_{LT}) rhizotrons. Note that for each day, a minimum of one zero-offset profile was measured across the entire distance per depth.

Year	R_{UT}	R_{LT}	Plant	sowing	emerging	flowering	harvest
2012	23	-	-	-	-	-	-
2013	7†	-	Winter wheat	nk‡	nk	nk	nk
2014	19	15	Winter wheat	30-Oct-2013	nk	21-May-2014	17-Jul-2014
2015	17	16	Summer wheat	17-Mar-2015	21-Mar-2015	08-Jun-2015	30-Jul-2015
2016	22	21	Winter wheat	26-Oct-2015	01-Nov-2015	03-Jun-2016	26-Jul-2016
2017	22	22	Maize	05-May-2017	09-May-2017	14-Jul-2017	16-Sep-2017

† In October 2013, an infiltration experiment was additionally performed at R_{UT} at the sheltered plot, resulting in two extra undisturbed measurement days. Normally both facilities were measured on the same day.
‡ nk, not exactly known for this event.

D-2-2 GPR crosshole measurements and acquisition of time series

To map SWC at several depths and positions on a weekly basis, we used the ZOP technique. Thereby, the transmitter is positioned in one borehole, while the receiver is located in another borehole, and, both antennae are moved simultaneously to the next position with a constant spacing between the measurement points (Figure D.2e). ZOP measurements were performed using 200 MHz PulseEKKO borehole antennae (Sensors & Software (Figure D.2d, Table D.1) with a horizontal resolution of 5 cm. Because of the known distance between the transmitter and receiver, a velocity profile along the boreholes can be calculated assuming that the rays travel straight between the antennae (Binley et al., 2002b, Looms et al., 2008b). The ZOPs were measured in horizontal depth slices with a spatial separation of 5 cm with a borehole separation of 0.75 m at all depths and 3 lateral positions representing the different treatments of the plots. This results in a dataset for each measurement day covering a soil volume of about 1.2 m depth x 9 m width x 6 m length. In total, around 300 single traces per depth layer were recorded. Since 2016 additional geophysical measurements such as electrical impedance tomography (EIT) are performed at R_{LT}. To avoid interferences between the two techniques, 2 m of the GPR measurements were removed and not further analyzed.

D-3 GPR data analysis

To retrieve quantitative soil properties from the GPR ZOP data, several pre-processing steps are necessary. First, we applied a dewow filter to reduce low frequency noise in the measured GPR data. Second, a time-zero correction of the data is applied, which is necessary to account for time shifts of the data over the measuring period that can be caused by thermal drift, electronic instability, cable length differences and variations in antennae coupling. A common method for the time-zero estimation is to record repeated wide-angle-reflection-and-refractions (WARR) measurements in the air using the borehole antennae to determine an absolute time-zero and estimate individual time-zeros for each ZOP by time-interpolation. Thereby, the transmitter antenna is fixed at a certain location, while the receiver antenna is moved step wise along a profile with a fixed spacing of 0.1 m. Normally, at least three WARRs per

facility were measured per day. One example of this procedure is shown in Figure D.3, where four WARRs were measured during the measurement period. For each of these WARRs the first arrival air wave was picked and the actual time-zero was estimated using the known air velocity. In this case, the time-zero was around 17 ns and a variation of the time-zero of approximately 0.35 ns over the measurement period can be noticed. The time-zero estimates of the different WARRs were linearly interpolated, and the ZOP measurements in between were corrected using the corresponding time-zero as shown by the blue dots. For example, for dry ($\varepsilon_r = 9$) or wet ($\varepsilon_r = 24$) conditions in the rhizotrones the influence of a time shift of 0.35 ns can result in a difference of up to 1.8% or 2.2% in SWC, respectively. Therefore, to avoid these errors, detailed and accurate time-zero calibrations are essential.

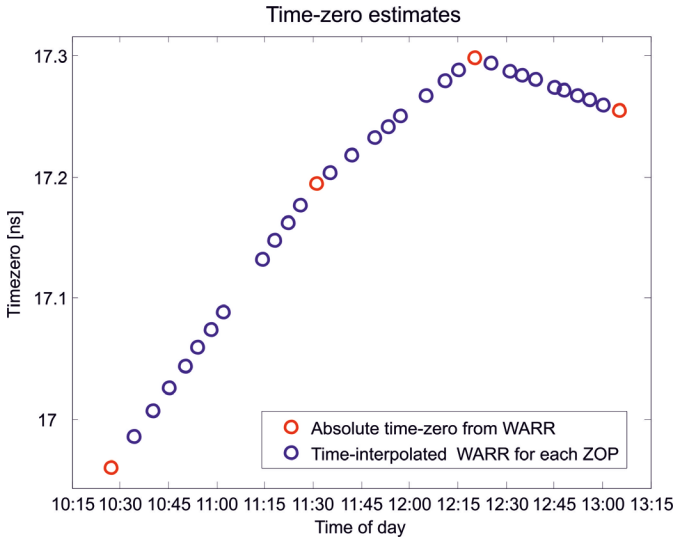

Figure D.3: Example for the time-zero (t_0) estimation obtained from the wide angle reflection and refraction (WARR) measurements (red) over the measurement period of one facility and interpolated t_0 for all the measured (ZOPs, blue).

After the GPR data are time-zero corrected, the first breaks of the ZOP data are picked using an automated user controlled picking routine. This routine was used due to the huge available amount of data and to avoid inconsistencies in the picking by different users to ensure constant and precise estimation of the first break. The automatic picking routine is able to find the maximum of the traces, but not the actual needed first break. Therefore, in the first step, we defined the time shift between the automatically found overall maximum of the traces and the actual first break point. This is done for the different measurements types WARR and ZOP data separately and by hand picking several noise-free traces of the entire data set per test site and day. These two types of time shifts between the first break and the first maximum are estimated for each measurement day and facility separately and it is assumed that these shifts are not changing over the measurement time of one facility. Note that for all the data analyses presented in this paper the same person defined these constants to avoid user influences. Second, the automatic picking routine determines the

overall maximum of all traces and subtracts the predefined constant time shift from the automatically picked maximum.

Using the known distance between the boreholes of 0.75 m and the first breaks of the ZOP, the electromagnetic (EM) wave velocity within the medium is calculated, which can be converted into relative permittivity ε_r of the soil using:

$$\varepsilon_r = \left(\frac{c}{v}\right)^2 \tag{D-1}$$

where v is the EM velocity, and c the speed of light. Both, WARR analysis for determining the absolute time-zero and ZOP analysis to obtain GPR travel times depend on an accurate and precise picking of the first arrival signals, otherwise errors can occur in the permittivity estimates. Normally for GPR applications, far field conditions are assumed, where no interferences with the antennae are expected, meaning that the antennae separations should be at least two times larger than the wave length. In the near-field regime (below one wavelength) the propagation of electromagnetic waves is interfered by the antennae. Depending on the soil properties, the far field conditions were not always reached for the borehole separation of 0.75 m and the frequencies of the 200 MHz antennae, which are the highest of commercially available borehole antennas. This is particularly important for R_{UT}, where a longer wavelength than in R_{LT} can be expected. This should be considered in the data analysis and picking of the first arrivals. For example, the first break picking in very dry soil is very difficult because no clear first break point is present in the data (long and slow raise of the trace). For such days, the time shift for the ZOP data was only defined using data where a clear point could be chosen (normally deeper depths that were wetter) and was then applied to all data of this day.

First tests indicated that the permittivities of the uppermost depth slice at 0.1 m depth are usually underestimated in comparison to GPR data of 0.2 m depth, and showed significantly lower and unrealistic values compared to the permittivities of the underlying depth slices. Because of the small distance between the air-soil interface and the shallow boreholes, an interference of the critically refracted air wave and direct wave is present (more details in Klotzsche et al. (2016)). Therefore, we investigated the influence of the air and direct wave interaction on the GPR traces and the retrieved permittivities and water contents using full-waveform simulations (see Section D-8-1). Summarizing the synthetic studies of Section D-8-1, using standard travel time picking procedures the travel time of the EM wave through the soil is underestimated for the shallow boreholes at 0.1 m depth and no reliable SWC can be obtained. Therefore, these data will not be shown in the following. Note, that for the depth of 0.2 m also a minor effect can be expected, especially under dry soil conditions.

Furthermore, we investigated the influence of the GPR picked permittivity if gradients or discontinuities in permittivity depth profiles at layer interfaces are present in the subsurface (see Section D-8-2). The standard first break picking approach of the travel times assumes that the waves travel directly and on a straight line between the transmitter and receiver antennae. Figure D.13 illustrates using a second synthetic study how strong and abrupt changes in water contents across layer interfaces or across infiltration or drying fronts, influence ray-based estimates of SWC. In particular special attention needs to be drawn towards the interpretation of the topsoil SWC for instance when a wetted soil is overlaying

drier subsoil. Such a condition could occur during an infiltration event.

D-4 Soil water content derived from GPR and TDR data

To convert the relative permittivity to SWC, appropriate empirical or petrophysical models are necessary (Huisman et al., 2003, Steelman and Endres, 2011). In general, these relationships can be divided into empirical models, volumetric mixing formulas and effective medium approximations. Empirical relationships like Topp's equation Topp et al. (1980) require very limited information about the soil type. In contrast, volumetric mixing formulae relate the measured bulk permittivity to the individual components within the system, weighted by their volume fractions. Effective medium approximations extend this mixing approach by considering structural and textural contributions to formulate microscale geometric models instead of a function of only porosity Φ and θ. For the right choice of the most appropriate model, information about the soil is needed. For this study. we used the complex refractive index model (CRIM) with a geometry factor of 0.5 considering a three-phase system using air, water, and soil components under consideration of the soil porosity Φ (Roth et al., 1990, Steelman and Endres, 2011):

$$SWC = \frac{\sqrt{\widetilde{\varepsilon}} - (1-\Phi)\sqrt{\varepsilon_s} - \Phi}{\sqrt{\varepsilon_w} - 1} \quad . \tag{D-2}$$

where $\widetilde{\varepsilon}$ is the relative bulk permittivity, Φ the soil porosity, and ε_w and ε_s the relative dielectric permittivity of water and soil particles, respectively. For both facilities R_{UT} and R_{LT}, higher porosities of 0.33 and 0.4 were considered for the top soil layer (0 m - 0.3 m), and 0.25 and 0.35 for the subsoil, respectively (Weihermüller et al., 2007). The permittivity of water at 10°C is $\varepsilon_w = 84$ and the permittivity of the soil ε_s was considered to be 4.7, and 4.0 for R_{UT} and R_{LT}, respectively (Robinson et al., 2005). For R_{LT}, the relations obtained by the CRIM were very similar to the empirical Topp equation Topp et al. (1980), which was used by Cai et al. (2016) to derive SWC from TDR measured $\widetilde{\varepsilon}$. For the stony soil in R_{UT}, CRIM deviated from Topp's equation and Cai et al. (2016) used the CRIM model to derive SWC from TDR measured permittivity.

D-5 Comparison of GPR and TDR soil water contents

The TDR sensors have a high temporal resolution, but a limited spatial coverage compared to the GPR measurements. Several other studies indicate a good correlation between SWC derived by TDR and surface GPR using the direct groundwave velocity for different soil state conditions (Huisman et al., 2002). To better quantify the sensing volume of the horizontal crosshole GPR, we performed a detailed analysis similar to Galagedara et al. (2003) by investigating the sampling volume for the different soils and states. The sampling zone for borehole GPR is often defined by the Fresnel zone as a 3D volume (Fresnel volume) and is depending on the distance between the antennae, center frequency, and permittivity of the medium. The Fresnel volume is described by an ellipsoid with its foci points at the location of the antennae positions. Thereby, the Fresnel zone is considered as an elliptical region

perpendicular to the ray paths in the center of the ellipsoid. We calculated the sampling volume SV and the radius of the Fresnel zone of both facilities for minimum, intermediate, and maximum observed permittivity/SWC (Table D.2). Because of the general lower permittivity values for R_{UT} the radius of the Fresnel zone R_{FR} and SV is larger compared to R_{LT}. The radius of the Fresnel zone for average permittivity is 0.39 m and 0.32 m for R_{UT} and R_{LT}, respectively. For very dry conditions, this radius can reach almost 0.5 m for R_{UT}. Note that these calculations do not consider inhomogeneity caused by infiltration events, rapid drainage or medium properties changes. The SV for R_{UT} and R_{LT} ranges between 0.26 – 0.53 and 0.17 – 0.3 m^3, respectively. In contrast, the SV of a TDR sensor is approximately 0.005 m^3 and much smaller (at least 30 times) than for GPR (Ferré et al., 1998, Hinnell et al., 2006). To compare GPR SWC with the TDR SWC values between 2014 and 2016, we averaged the horizontal GPR SWC values at each depth for each treatment and measurement day. A comparison of the mean TDR derived SWC plotted every hour and the GPR SWC values weekly measured at different depths at the R_{UT} and R_{LT} site are shown in Figure D.4 for the measurement period of 2014 (time series of 2015 and 2016 in Supplemental Figure S1 and S2 (`https://acsess.onlinelibrary.wiley.com/action/downloadSupplement?doi=10.2136%2Fvzj2019.05.0044&file=vzj2vzj2019050044-sup-0001.pdf`.) and D.14). The first row in Figure D.4 shows the precipitation and mean daily temperature data acquired at the weather station close by, whereas the panels below show the mean R_{UT} and R_{LT} SWC results for the sheltered, rainfed, and irrigated plots.

Table D.2: Estimated Fresnel zone radius (R_{FR}) and sampling volume (SV) for the upper terrace (R_{UT}) and lower terrace (R_{LT}) rhizotrons for a range of relative permittivity (ε_r) values. For all calculations, a center frequency of the measured data (f_c) of 170 MHz was used, and the associated wavelength (λ) was obtained.

	R_{UT}				R_{LT}			
conditions	ε_r [-]	λ [m]	R_{FR} [m]	SV [m^3]	ε_r [-]	λ [m]	R_{FR} [m]	SV [m^3]
Dry	4	0.88	0.46	0.53	7	0.67	0.39	0.35
Wet	10	0.56	0.35	0.26	20	0.39	0.29	0.17
Intermediate	7	0.67	0.39	0.35	14	0.47	0.32	0.21

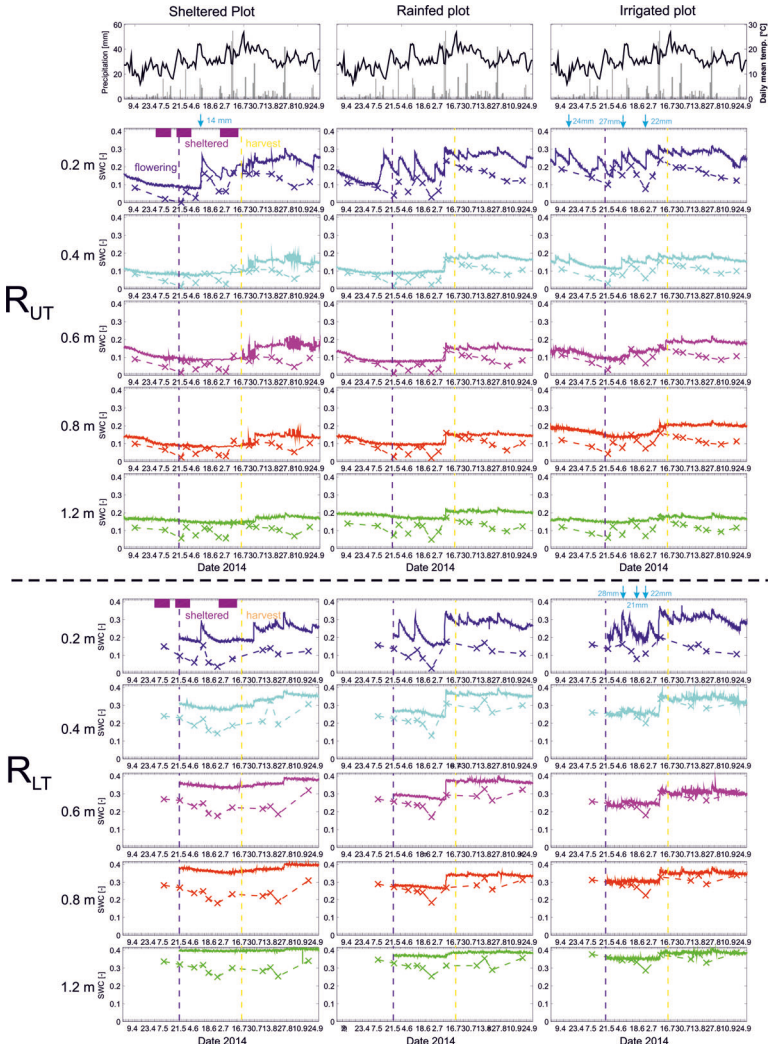

Figure D.4: Comparison of the temporal and spatial mean soil water content (SWC) of the upper terrace (R_{UT}) and the lower terrace (R_{LT}) rhizotrons derived by ground-penetrating radar (crosses) and time-domain reflectometry (TDR) sensors (solid lines) for 0.2- and 1.2-m depths using the 2014 data. Averaged horizontal SWC profiles were derived with the three-phase CRIM model. The top row shows the precipitation data obtained by pluviometer (gray bars) and the mean daily temperature (black solid line). Sheltered, flowering, and harvest times are marked as violet boxes, purple dashed lines, and orange dashed lines, respectively. Irrigation events are indicated with blue arrows with the corresponding amount. Note that the date of the year (x-axis label) is given with the first and second numbers as day and month, respectively.

D-5-1 Soil water content time series of 2014 for the upper terrace rhizotron

The averaged horizontal SWC profiles of R_{UT} are clearly showing an increase of SWC for all depths after major precipitation events such as in June and July 2014. After the rain events, the change in SWC values for the rainfed and irrigated plot is similar (5 Vol %), but larger for the rainfed plot (up to 10 Vol %). Note for example the large increase by 18 and 10 Vol. % at 0.2 and 0.4 m depth, respectively, in GPR SWC after the large rain event in the beginning of July in the rainfed plot. The irrigated plot had already a higher SWC compared to the other two plots before the rain event because of two previous irrigations. For the sheltered plot only a small increase of SWC for the July event can be observed, because of the applied shelter on top of the plot. Note that one irrigation in the sheltered plot was necessary in the beginning of June to prevent wilting of the plants. After harvesting of the winter wheat in mid-July, no shelter and irrigation was applied and the three different plots show a similar trend and behavior. Analyzing these graphs no immediate relation or dependency between SWC dynamic and crop stage can be noticed. The impact of the precipitation and drying events decreased with increasing depth. The changes in weather conditions can be recognized close to the surface, with increasing depth, the variations are less intense. Special care needs to be taken by interpreting the variability and the quantification of the GPR SWC at 0.2 m depth (also compare with the synthetic studies Section D-8-1). Especially for dry conditions, a possible critically refracted air-direct wave interaction could be present. But generally the 0.2 m depth data follow similar trends as the other depths. Similar observations were made for 2015 and 2016.

D-5-2 Soil water content time series of 2014 for the lower terrace rhizotron

SWCs in R_{LT} are generally higher than in R_{UT}, which can be related to a shallower water table at the lower part of the Selhausen test site and the finer soil texture and lower stone content at R_{LT}. For example, the maximum SWC of about 0.4 is obtained for the R_{LT} irrigated plot, whereas the maximum for the R_{UT} for the depth between 0.4 -1.2 m was around 0.24. Similar to the R_{UT} an increase and decrease of the GPR SWC can be observed in R_{LT} after rain and dry periods, respectively. An increase of the SWC with increasing depth can be noticed. For the depth below 0.3 m, the smallest SWC is about 0.17 indicating that the soil hardly dries out. For the large rain event in July an increase of the SWC for all the depths and plots and an SWC increase of up to 0.15 can be observed.

D-5-3 Direct comparison between GPR and TDR soil water content results

Figure D.5 shows a cross plot between the mean SWC derived from the horizontal GPR measurements and the mean of the SWC measured by the TDR. Note that the mean of the TDR is calculated from the 4 sensors of each depth (see Figure D.2a) that are closest in time with the GPR measurements for both sites from 2014 to 2016. Based on these data correlation coefficients r for R_{UT} and R_{LT} were estimated for each year separately and for all three years together and listed in Table D.3, whereas corresponding regression lines are plotted in Figure D.5. The regression lines for both facilities show that there is a bias between the TDR and GPR SWCs, with TDR showing larger SWC than GPR, and this bias is larger for smaller water contents. This bias could have several reasons.

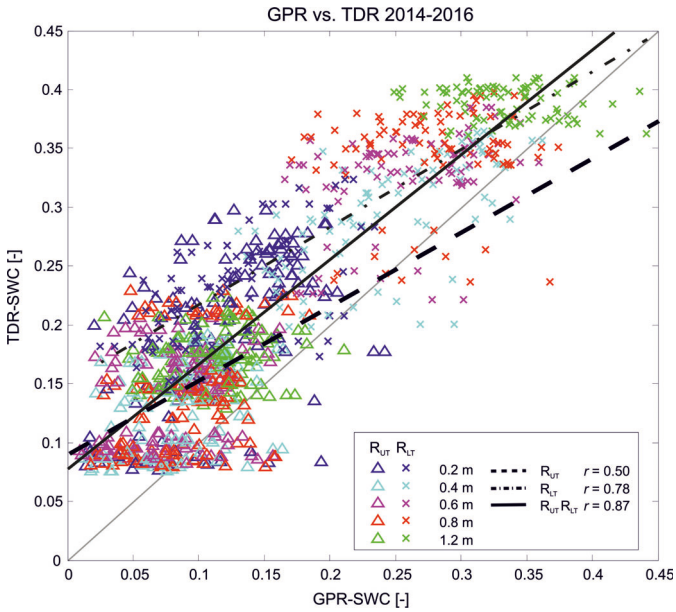

Figure D.5: Comparison of soil water content (SWC) estimated for both the upper terrace R_{UT} and lower terrace R_{LT} rhizotrons using time-domain reflectometry (TDR) and ground-penetrating radar (GPR) measurements for 2014 to 2016. Each color represents a different depth of investigation. Corresponding regression lines for only R_{UT}, R_{LT}, and combined R_{UT} and R_{LT} are indicated with a dashed, dotted, and solid black lines, respectively.

A first explanation could be the different SV of the GPR and TDR measurements. Since the TDR sensors are always at the same location, the deviation between the GPR and TDR SWC should reflect a difference due to variations in local soil properties and local root water uptake which do not lead to complete random deviations over time. While similar trends over time can be seen (Figure D.4, Supplemental Figure S1 and S2 `https://acsess.onlinelibrary.wiley.com/action/downloadSupplement?doi=10.2136%2Fvzj2019.05.0044&file=vzj2vzj2019050044-sup-0001.pdf`), the GPR SWCs show more variability at deeper depths than the TDR SWCs. For example for the R_{UT} site, except for the large precipitation event in the middle of July, only minor changes in TDR SWC are observed in the subsoil below 0.3 m depth, whereas the GPR SWCs react also to smaller rain events. These reactions could be caused by preferential flow events that are by coincidence not observed in the small sampling volume of the TDR sensors, but are detected in the larger GPR sampling volume. In this way, the GPR captures SWC changes that are controlled by heterogeneous structures at a larger scale, which could also include preferential flow patterns (indications seen during infiltration experiments) and different local SWC variability (see Figure D.6). Due to the larger SV, the GPR data can also be affected by shallower SWC changes that react faster on precipitation events. The difference in SV could also cause a bias when TDR probes are installed in zones that are consistently wetter or consistently drier than the soil volume that is sensed by GPR. But, it would be expected that such a bias would be

random between the different treatment or different soil depths. This hypothesis will be evaluated later when the spatial variation of the observed SWCs are discussed. Another reason for the noise could be the impact of the processing steps of the GPR signals that were adapted for each measurement day and soil plot. Looking at Figure 4, it seems that the deviations between GPR and TDR measurements are correlated for a certain observation day and facility for all depths and treatments. To what extent this is related to the signal processing requires further investigation.

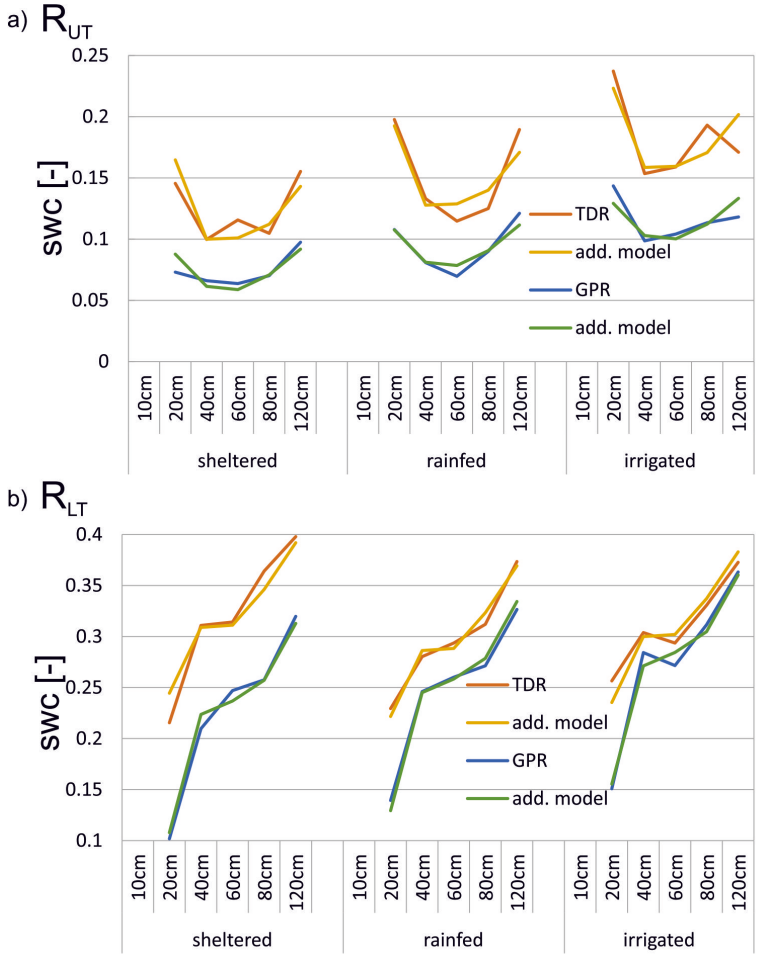

Figure D.6: Time-averaged water contents during the winter and summer wheat growing seasons (1 April–harvest) in 2014, 2015, and 2016 in (a) the upper terrace rhizotron R_{UT} and (b) the lower terrace rhizotron b) R_{LT} for different water treatments and depths derived from time-domain reflectometry (TDR) and ground-penetrating radar (GPR) measurements and calculated using the additive model.

Table D.3: Correlation coefficient r between time-domain reflectometry and ground-penetrating radar derived soil water contents for the upper terrace (R_{UT}) and lower terrace (R_{LT}) rhizotrons in 2014 to 2016.

Treatment	R_{UT}				R_{LT}				R_{UT} & R_{LT}
	2014	2015	2016	2014-2016	2014	2015	2016	2014-2016	2014-2016
Sheltered	0.65	0.66	0.19	0.57	0.89	0.82	0.86	0.86	0.91
Rainfed	0.78	0.71	0.59	0.66	0.89	0.80	0.87	0.81	0.88
Irrigated	0.73	0.54	0.30	0.19	0.76	0.72	0.89	0.77	0.85
All plots	0.76	0.68	0.58	0.50	0.77	0.75	0.82	0.78	0.87

Finally, it needs to be mentioned for the installation of the TDR probes in R_{UT}, the larger stones (with diameter larger than 30 mm) were excluded from the material that was packed around the soil sensors whereas the gravimetric fraction of coarse fragments (with diameter larger than 2 mm) was kept similar to guarantee a good coupling. This could have resulted in an higher water retention and hence higher SWCs that were measured with TDR than with GPR (Cai et al., 2016). However, this does not explain the bias that was observed in R_{LT} where the probes were inserted in the soil.

In order to evaluate the SWC measurements in the different facilities, at the different depths, and for the different water treatments, we calculated time averages of the measurements over the three wheat growing periods (from April 1 until harvest). A simple additive model of the water treatment and depth effects was set up:

$$SWC_{i,j} = SWC_{.,.} + \Delta SWC_{wateri,.} + \Delta SWC_{.,depthj} + E_{wateri,depthj} \tag{D-3}$$

where $SWC_{.,.}$ is the overall averaged SWC for all depths and water treatments in a given facility, $\Delta SWC_{wateri,.}$ is the effect of water treatment i (i = sheltered, rain fed or irrigated), which is calculated from the difference between the average SWC at all depths for treatment i and the overall average, $\Delta SWC_{.,depthj}$ is the effect of the depth, which is calculated from the difference between the average SWC in all treatments at depth j and the overall average, and $E_{wateri,depthj}$ is an error term that represents the interaction effect between water treatment i and depth j, effects of soil heterogeneity, and measurement errors. In the Supplemental Table S1 (`https://acsess.onlinelibrary.wiley.com/action/downloadSupplement?doi=10.2136%2Fvzj2019.05.0044&file=vzj2vzj2019050044-sup-0001.pdf`.), the mean SWC and the effects are given. In Figure D.6, time averaged SWCs for the different water treatments and depths in the two facilities that were measured with GPR and TDR and that were calculated using the additive model are shown. The additive model with error term presumes that the effect of the water treatment is the same for all depths and that the effect of the depth is independent of the water treatment. This implies that the SWC profiles with depth that are predicted by this model shift with a constant value between the different treatments (see Figure D.6).

The time, depth, and water treatment averaged water contents $SWC_{.,.}$ indicate that the TDR measured values are about 6 volume % higher than the GPR measurements in both facilities. The SWC in the stony soil of the upper facility are on average by 16 volume % lower than in the silty soil of the lower facility. Looking at the water treatment effects, the GPR measurements show that in both the upper and lower facility, the sheltered plots are

drier than the rain fed plots and irrigated plots, as expected. For the upper facility, the TDR measurements show similar water treatment effects as the GPR measurements. But for the lower facility, the TDR measurements indicated a wetter soil in the sheltered treatment than in the other treatments. This indicates a systematic difference in soil properties of the TDR measurement sites in the sheltered, rain fed, and irrigated plots of the lower facility. The top soil in the upper facility has a lower stone content than the subsoil, which is reflected in a higher SWC in the top soil layer (this is further confirmed by the SWCs measured by TDR probes at 0.1 m depth which are not shown here). For R_{LT}, the soil profile is on average the driest at 0.2 m and the SWC increases with depth. The difference between the additive model and the time averaged SWC for a certain water treatment and depth correspond with the interaction-error term E. For R_{UT}, both TDR and GPR measurements show a negative interaction at 0.2 m depth and a positive one at 1.2 m depth for the sheltered plot and opposite interactions in the irrigated plot. This demonstrates that root water uptake, which dries out the soil, and irrigation and rainfall, which wet up the soil, have a stronger impact in the upper soil layer and a smaller impact in the subsoil. Of note is that both GPR and TDR show lower SWCs at 1.2 m depth in the irrigated than in the rain fed plots which indicates the effect of soil heterogeneity on the SWC measurements in these plots. For the lower facility in the silty soil, the TDR measured SWCs show similar interactions as in the upper facility, but the GPR measurements show smaller or opposite interaction effects. The reason for the interactions in the TDR measurements could be the underestimation of the SWC in the deeper soil layer of the rain fed and irrigated plots by TDR sensors that were installed in an apparently drier region of the plot (see figure with the SWC along the GPR transect).

Based on these analyses, we can conclude that GPR and TDR measured and time averaged SWC in different soils, at different depths, and for different water treatments were generally consistent with each other. But, there was a clear bias between both measurements with TDR giving higher SWCs than GPR. Also inconsistencies could be observed and some of them could be related to the spatial variability of the soil properties within and between the plots. Therefore, in the next part we will investigate the behavior of the GPR SWC along the tubes to analyze the spatial variability in more detail.

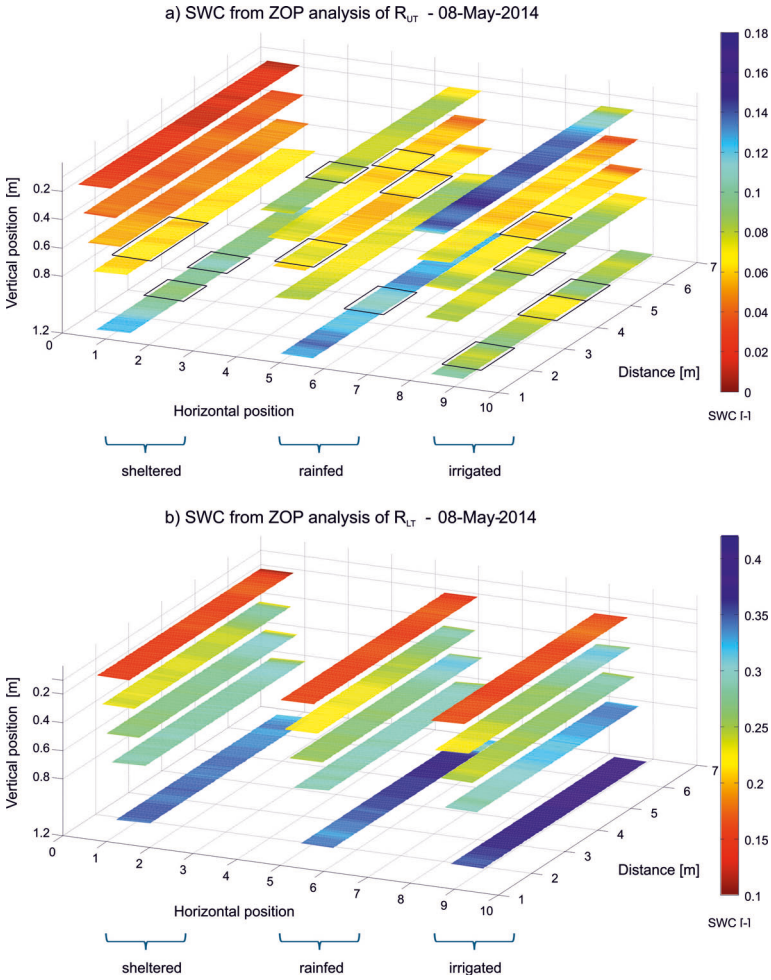

Figure D.7: Horizontal and lateral soil water content (SWC) variability as determined by zero-offset profile (ZOP) analysis for (a) the upper terrace rhizotron R_{UT} and (b) the lower terrace rhizotron R_{LT}. Horizontal SWC profiles after CRIM using the 8 May 2014 data for all three treatments: sheltered, rainfed (natural condition), and irrigated. Each measurement point (5-cm spacing) is color coded with the corresponding SWC. Note the different color bars of the SWC. The black outlined boxes indicate patches of higher or lower SWC that were consistent with the time during the 3 yr.

D-6 GPR soil water content variability

D-6-1 Semi-three-dimensional soil water content images of the rhizotrons

For each measurement day, the SWC values of the GPR measurements are estimated for all positions (every 5 cm) along the horizontal boreholes for five depths and three treatments. The obtained SWC values are then plotted as slices in between the horizontal boreholes for each depth level at five depths for the three treatments such that a semi-3D image is obtained of the volume 1.2 m depth x 9 m width x 6 m length for the R_{UT} and R_{LT}. Figure D.7a and b show the obtained SWC on 08-May-2014 for the R_{UT} and R_{LT}, respectively, where the SWC values located in the first meter close to the trench were excluded because of the presence of sensors. For this date, an increasing SWC with depth is visible for both facilities except the irrigated plot at R_{UT}. It can be noticed that the vertical variability of SWC is significantly larger than the horizontal although the horizontal SWC variability is still significant at all depths. Particularly remarkable is the large contrast between the topsoil (uppermost layer) and the subsoil. As expected, the sheltered plot shows lower SWC values compared to the rainfed and the irrigated plot, while the irrigated plots show slightly higher SWC than the rainfed ones.

The mean and corresponding STD of each depth and treatment for the data from 2014 to 2016 can be seen in Figure D.8. Every point represents the mean and STD of one ZOP crosshole measurement along a pair of 6 m boreholes during a measurement day. The R_{UT} STD reaches maximum values of 0.02 and the mean SWC is mostly below 0.2 (except for 0.2 m depth). Except for the lowest depth in the R_{UT}, the sheltered plots show a smaller STD in comparison to the rainfed and the irrigated plots. The R_{LT} STD reaches at a maximum value of 0.03 and for 1.2 m depth even 0.04. The mean R_{LT} SWC shows for depths between $0.4 - 1.2$ m minimum values of about 0.1 and maximum values of about 0.4, whereas for the shallow depth of 0.2 m a minimum values close to zero and maximum values up to 0.25 are obtained. Overall, more variability and scatter of the relation between the mean and STD of the SWC for all plots and depths can be observed for all plots and depths for R_{LT} compared to R_{UT}. This could be partly due to deviating boreholes present in R_{LT}.

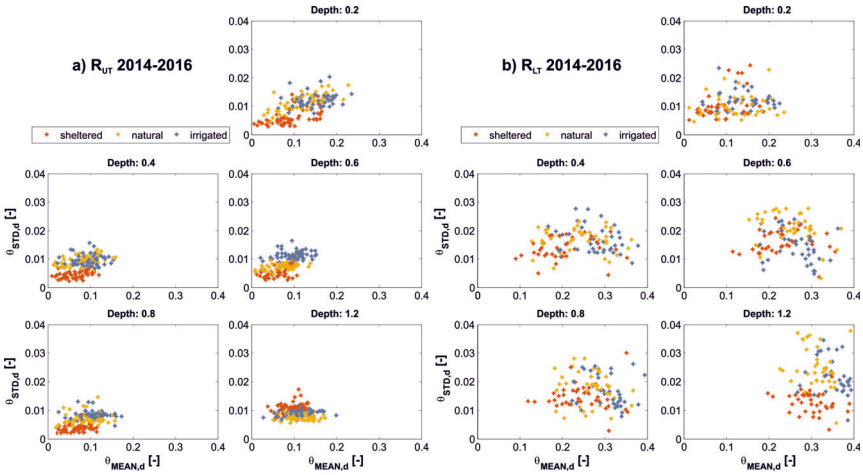

Figure D.8: Mean soil water content (SWC) for each depth and the corresponding standard deviation (SD) for (a) the upper terrace rhizotron (R_{UT}) and (b) the lower terrace rhizotron R_{LT} for the time series 2014 to 2016. The different treatments are indicated with different colors.

D-6-2 Spatial and temporal variability of GPR soil water content after rain events

For a more detailed illustration and characterization of the spatial and temporal variability of SWC for the large rain event in July 2014 the rainfed plot is analyzed in more detail in Figure D.9. The times series between 26-Jun-2014 and the 24-Jul-2014 show the highest variability of the SWC between dry and wet conditions as a response to the major rain events that took place between 08 to 10-Jul-2014 (Figure D.9). We observed an increase of 0.1 in SWC for the subsoil below 0.3 m depth, while for a depth of 0.2 m the increase in SWC is approximately 0.16, probably due to the higher porosity. For comparison, the mean of four TDR measurements at the same time as the GPR measurements are plotted. Although, the absolute values are higher, the general trends of increasing and decreasing SWC are present for both. Figure D.9b shows for the same dates the vertical SWC profiles over time, where it clearly can be seen that the rain events cause an increase in SWC for all depths over time, while in between the rain events the SWC is decreasing (indicated by the arrows on top). In Figure D.9a, a general increase of the SWC and also an increasing vertical SWC variability can be observed within the red ellipses for the first three days, which can also clearly be observed in Figure D.9c, where the lateral variability for these three days at five depths is shown. Here, also the consistent patches which remain either wetter or drier during and after the infiltration event can be identified.

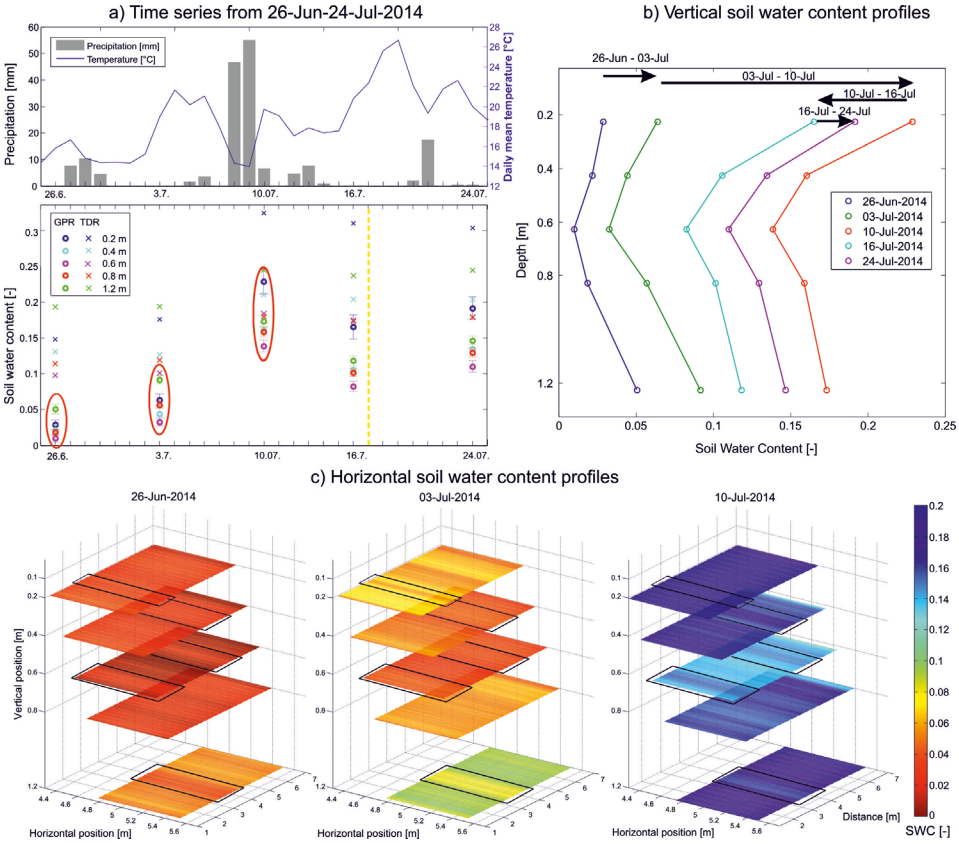

Figure D.9: Detailed analysis of the soil water content (SWC) distribution for 26 June to 24 July 2014 for the rainfed plot of the upper terrace rhizotron R_{UT}: (a) daily precipitation, mean temperature, and time series of the SWC for depths of 0.2, 0.4, 0.6, 0.8, and 1.2 m derived by time-domain reflectometry (TDR) and ground-penetrating radar (GPR) as crosses and circles, respectively, with the harvest date indicated by the yellow line (note that the date of the year [x-axis label] is given with the first and second number as day and month, respectively); (b) vertical GPR SWC for 26 June to 24 July 2014; (c) horizontal depth slices of the SWC for the 3 d marked in (a) by the red ellipses showing dry, intermediate, and wet conditions. The black outlined boxes indicate the SWC patches that were consistent with time (see Figure D.9).

D-6-3 Spatial variability along the rhizotubes

To investigate the consistency of the lateral SWC variability, we plotted the SWC variability of the different measurement days in 2014 with gray lines in Figure D.10. After subtracting the mean SWC at each depth from the individual SWC along the tubes for all measurement days separately for the three years of investigation, the solid black lines show the mean of all these gray lines providing a mean horizontal SWC variability for 2014. Similarly, the mean horizontal SWC variability for 2015 and 2016 are indicated by the red and green lines, respectively. In particular for R_{UT}, the site with the higher gravel content and coarse material, very clear and consistent patches over the three years can be seen (Figure D.10a, black circles). Furthermore, these consistent structures over time also indicate the repeatability and reproducibility of the GPR data analysis. This observation suggests that the SWC variability of R_{UT} is probably controlled by the soil properties rather than root growth of the wheat and indicates heterogeneity of the soil properties along the tubes. For the R_{LT}, the site in the more silty soil, the SWC variability of R_{LT} for the grey 2014 profiles is showing similar trends but a much larger spread. Contrary to R_{UT}, the mean R_{LT} SWC curves for 2014, 2015, and 2016 show also larger differences. This could be the result of varying root water uptake along the tubes during the different years. Note that some results show a clear increasing trend from low to higher SWC (e.g., 1.2 m of the irrigated and rainfed plot). This might reflect horizontal variations in SWC and suggests that the TDR sensors in 1.2 m and 0.8 m depth in the irrigated and rainfed plots are located in a drier part of the plot and might explain why the TDR sensors in the rainfed and irrigated plots show smaller SWC than in the sheltered plot of R_{LT}. But, the persistent increase in SWC along the tubes might also be caused by the horizontal boreholes having some deviation from the planned 0.75 m distance due to the horizontal drilling. Since for R_{UT} the tubes were buried and not drilled such deviations are not expected in R_{UT}. The boreholes are straight along the 7 m length (checked after drilling), but an unknown error in the angle of the tubes can be present. If we consider for example a maximum deviation away from the 75 cm offset from $\pm$ 5 cm ($\pm$ 10 cm) at the end of the tube for averaged soil condition of R_{LT} ($\varepsilon_r = 14$), the SWC would vary by $\pm$ 3 ($\pm$ 6) Vol. % SWC. This makes clear that a very detailed deviation logging needs to be carried out to investigate this effect on the SWC in more detail especially for R_{LT}. The reason why the R_{UT} shows a small spread and similar trends over the years, whereas R_{LT} shows a larger spread and different trends of the years is not clear and might be due to the different textures of the soil material.

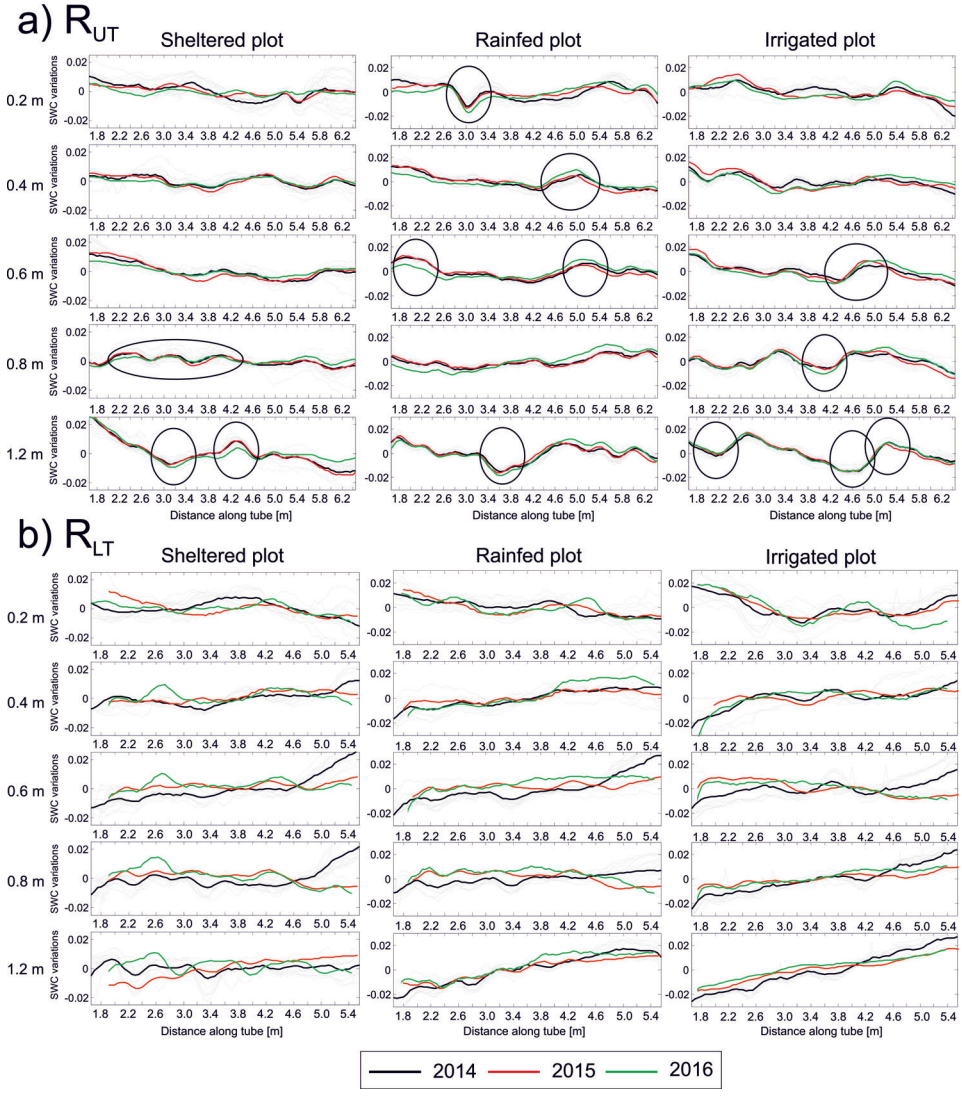

Figure D.10: Detailed analysis for (a) the upper terrace rhizotron (R_{UT}) nd (b) the lower terrace rhizotron (R_{LT}) of the soil water content (SWC) depth slices. The mean SWC of each depth slice was subtracted from the individual SWC values along the depth slices. The gray lines represent the individual SWC profiles for all the measurement days of 2014. The solid black, red, and green lines represent the means of all the measurement days of the years 2014, 2015, and 2016, respectively. The black circles indicate the higher and lower SWC patches that were consistent with time (see Figure D.9) along the horizontal slices.

D-7 Water content spatial distribution for different crop types

In 2017 maize, instead of wheat, was sown. The same analysis for the 2017 GPR data was applied as for the other years of both facilities. While the wheat showed no clear impact on the GPR recordings, the maize plants showed an impact, especially during dry conditions at R_{UT} (boxes in Figure D.11). In particular during the growing phase of the plants between July and August clear patches of where the plants are located can be observed. For example, for very dry conditions during the growing phase such as at the 27-Jul-2017 a higher SWC can be seen at the locations of the maize rows (very dry soil) and this contrast decreases with increasing depth. The measured SWC shows peaks with a separation of about 75 cm, which equals the distance between the crop rows (Figure D.11 right side). Ten rows are planted along the rhizotube profiles, of which seven can be detected with the GPR data. After some rain events at the end of July, the GPR SWC data of 02-Aug-2017 also show patches, but this time not that clearly. Furthermore, the SWC is lower at the maize plant rows (greatest for the irrigated plot). Therefore, the ZOP recordings and the interfered SWC variations are not only influenced by the weather conditions and the soil, but also by the presence of the crop. This becomes also clear by analyzing the SWC variation along the 7 m long tubes for the time period from July to August (Figure D.11 left side). For the dry day (cyan line) a very strong variation is visible with maximum peaks at the plant locations. By comparing these variations with Figure D.7c, where constant patches over the time for wheat were visible, for maize these constant patches are overlapped and controlled by the plant presence during the growing phase and more temporal changes are observed. One explanation could be that for very dry soil conditions, the SWC below the plant rows was higher than between the rows and this could be caused by the amount of water in the plant roots in combination with the higher root density below the plant row. These variations along the depth slices are already visible in the unprocessed data (not shown). As Figure D.11 indicates the SWC patterns caused by root zone are only visible in the shallow depths. The roots are very concentrated near the surface and are more distributed with increasing depths (Figure D.12). This is particularly true for R_{UT} with a high root count density is present near to the surface. For R_{LT} high root count density values are distributed over the entire depths (patches much harder to identify in the GPR data, not shown). Note, that the effects of the surface and above ground plant biomass (see Table D.2 for sensing volume) is currently not clear and needs to be investigated in future research.

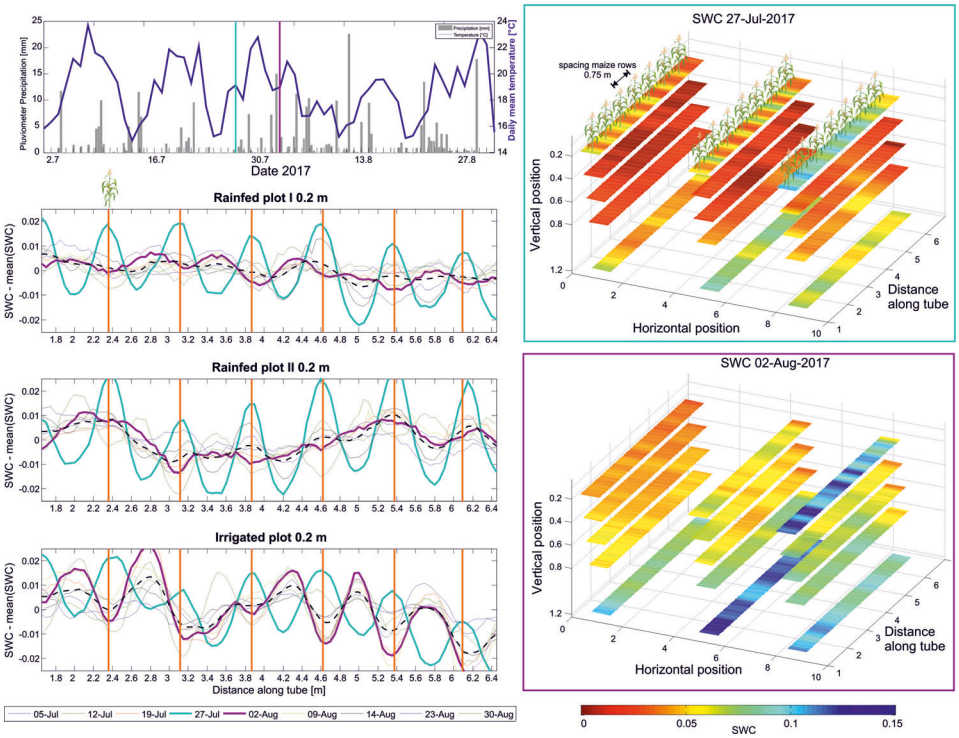

Figure D.11: etailed analysis for (a) the upper terrace rhizotron R_{UT} for the soil water content (SWC) in the presence of maize in 2017: weather conditions and the SWC variations (similar to Figure D.6) at the shallow depths for all three plots for the main growing period between July to August, with orange lines indicating the position of the maize plant along the tubes (left) and horizontal SWC profiles after CRIM for R_{UT} for two example dates during the growing phase for all three treatments: rainfed I (previously sheltered), rainfed II, and irrigated (right).

Summarizing, for plants like maize clearly the strength of the GPR SWC estimation is visible due to its power to sense lateral SWC changes and distribution. We have seen that a clear link between the SWC of the GPR and the plant location can be made. Such variations could maybe also have been shown for the upper few centimeters with TDR sensors, but to gain the same spatial resolution a large number of sensors would need to be installed, which would disturb the soil conditions. More research is necessary to link the measured SWC from the GPR to the SWC of the roots itself. Generally, the currently estimated SWC is an averaged value for a certain domain including all components, e.g., soil, roots, air. Interestingly, other studies that mainly conducted ERT measurements suggested an opposite row-interrow effect of the SWC in a maize crop stand with a smaller SWC under the rows (Garré et al., 2013, Michot et al., 2003). It must be noted that ERT does not measure the permittivity and the impact of root water content on bulk soil electrical conductivity is not unequivocal.

D-8 Conclusion and outlook

We used a novel experimental setup to map and monitor soil water content (SWC) variability and dynamics using horizontal crosshole GPR data in two minirhizotron facilities, R_{UT}, and R_{LT} in the upper and lower terrace, respectively. The setup allowed monitoring spatial and temporal variations in SWC variability caused by precipitation, different treatments (sheltered, rainfed, and irrigated), crops (wheat and maize), and soil types (gravelly soil and clayey/silty soil) during four growing seasons and bare field conditions. More than 150 time-lapse GPR days of measurements were performed. We generally found higher SWC at R_{LT} values than at R_{UT} due to the presence of a water table and the finer textured soil material. At both locations, vertical variability of SWC is significantly larger than the horizontal one. We observed a clear effect of the treatments on SWC. The sheltered plot shows lower SWC values compared to the rainfed and the irrigated plot, while the irrigated plots show slightly higher SWC than the rainfed ones. For R_{UT} with the higher gravel and sand content much more horizontal variability in SWC can be noticed compared to R_{LT}. Mapping the spatial variability of the SWC along the depth slices along the boreholes indicated especially for R_{UT} time alternating patches with lower and higher SWC ($\pm$ 0.02). The cause of these patches needs to be investigated in more detail and might be due to heterogeneous structures that could be related to preferential flow paths. To better quantify and illustrate the behavior of the spatial variability and to improve the investigation of wetting and drying of the identified patches along the depth slices, higher temporal sampled data of climate dependent GPR measurements are required than the weekly measured data presented here, especially during major precipitation events.

Comparison of the GPR SWC with TDR SWC values showed similar trends over time but consistently lower GPR SWC values. These differences between the TDR and GPR measurements can most likely be explained by different measurement volumes and spatial heterogeneity. Due to interfering critically-refracted air wave and direct subsurface waves, it was not possible to map the shallow SWC values at 0.1 m depth with GPR using first break picking. Here, more sophisticated methods such as full-waveform inversion approaches are needed that are able to model the entire GPR trace including these interferences (Klotzsche et al., 2016). Further, two uncertainties of the SWC estimates are discussed that could influence the SWC: 1) a possible deviation of the tubes away from the assumed offset of 0.75 m that is currently not considered (mainly for R_{LT}) and 2) the assumptions of the CRIM parameters to calculate the SWC. Further work, needs to involve accurate and detailed deviation measurements of the boreholes and laboratory studies to better define the CRIM parameters.

In contrast to TDR, crosshole GPR was able to detect differences in spatial variation of SWC in horizontal direction between maize and wheat. A major advantage of GPR based measurements compared to TDR is the fact that it may provide detailed information on the spatial and temporal variation of SWC in the subsurface. Our crosshole GPR setup in combination with rhizotron facilities allows studying the effect of crop and treatment differences on the spatial and temporal variation of SWC and may therefore be extremely useful for investigating root water uptake processes in function of soil and crop type. In addition, the long-term time-lapse GPR data can be used to derive relevant hydraulic properties such as

the Mualem-van-Genuchten parameters for both facilities and hence different soil types Busch et al. (2013), Rossi et al. (2015), where also the influence of the growing plants including roots can be incorporated. In this way, high spatial resolution investigations can be performed to study the soil-plant-atmosphere interactions of agricultural crops at the field plot-scale. To disentangle the SWC estimates from the root-system and the soil properties from the GPR SWC more research is needed, e.g., bare-soil field conditions can help to investigate the soil structures before sowing and after harvest. Furthermore, special care needs to be taken by the data analysis for very dry soil conditions.

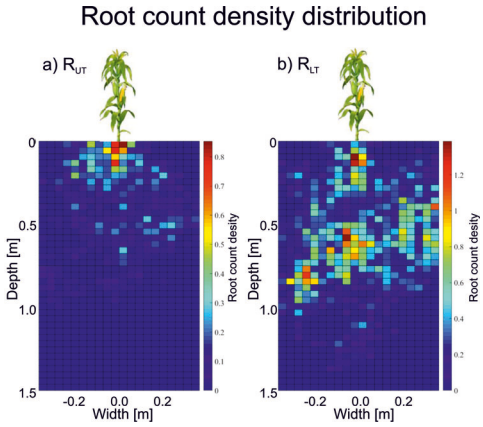

Figure D.12: Root count density distribution for maize after the growing phase measured in a grid of 0.0375 by 0.0375 m for (a) the upper terrace rhizotron R_{UT} nd (b) the lower terrace rhizotron R_{LT}. The data were acquired by excavating a trench close to the maize plants and counting the number of roots per grid cell (two replicates per site).

D-8-1 Synthetic study: GPR wave interference close to surface

We defined a 2-layer 3D model and computed the EM wave using the 3D finite difference time domain solver gprMax (Warren et al., 2016), where the air layer with permittivity $\varepsilon_r = 1$ was overlying a soil layer of $\varepsilon_r = 5$ (dry sand). We calculated the EM field components for the same depth positions and spacing of the transmitter and receivers that are present at the rhizotron facility. For comparison, we also modeled the electrical field in a homogenous medium with a permittivity of $\varepsilon_r = 5$ (Figure D.13a). For all the synthetic models the conductivity σ was chosen to be constant with $\sigma = 10$ mS/m for the soil and as source pulse we used a Ricker wavelet using a center frequency of 200 MHz. The results indicate that the influence of the interferences of air and direct wave on the first breaks is largest at 0.1 m and 0.2 m depth (Figure D.13a and b). With increasing depth the air wave interaction features decrease and arrives later as the first breaks of the direct wave of the traces and no interference on the first break is present (Figure D.13a). To investigate the influence of wet and dry soil conditions for the shallowest borehole pair at 0.1 m depth, the same 2-layered model was used with varying soil permittivity between 5 (dry sand) up to 20 (wet sand) and shown in Figure D.13b. In

all the models a phase shift and an influence of the amplitude on the trace can be observed (Figure D.13b), indicating that first-break picking and ray-based approaches would return erroneous results. To obtain reliable permittivity and SWC results for the shallow boreholes, we need to take this refracted airwave and direct wave interference into account and a more sophisticated analysis approach like full-waveform inversion (Klotzsche et al, 2016) needs to be used.

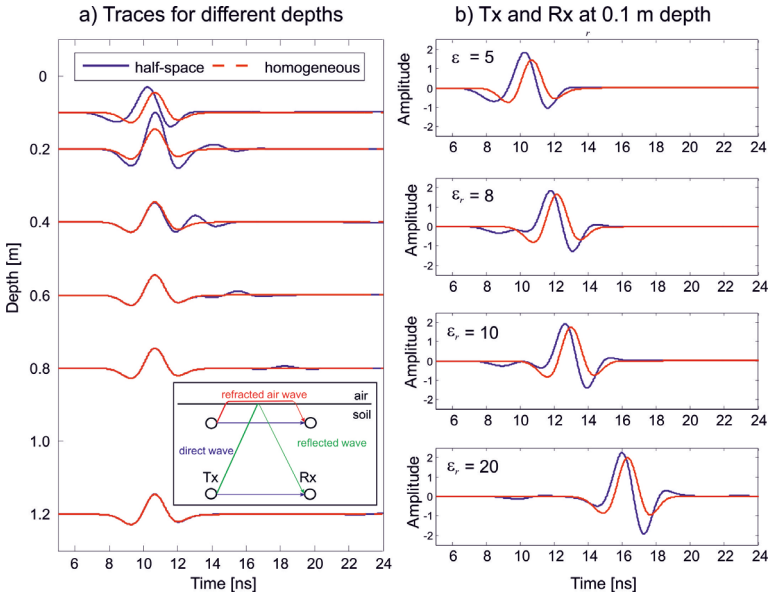

Figure D.13: Comparison of synthetic horizontal borehole traces with a borehole separation of 0.75 m. Traces for a three-dimensional homogenous space with a relative dielectric permittivity (ε_r) of 5 in red and traces for the presence of an air layer on top of the ε_r = 5 of the two-layered medium in blue: (a) traces for transmitter (Tx) and receiver (Rx) depths of 0.1, 0.2, 0.4, 0.6, 0.8, and 1.2 m, with the possible ray paths for a simple two-layered model in the embedded box; and (b) comparison of synthetic traces at the 0.1-m depth for ε_r values of 5, 8, 10, and 20 for the homogeneous and two-layered media.

D-8-2 Synthetic study: First break picking close to interfaces and soil water content gradients

To estimate the error of the travel time picking in the presence of interfaces and gradients additional synthetic models were investigated. Figure D.14 shows the different models and the picked permittivities and a detailed comparison between the picked and true values are shown in Table D-A.1. For model I and II, the first break picking at 0.4 m, and 0.2 m depth shows the largest deviation with a lower permittivity caused by a refracted wave traveling through the fastest layer with the lowest permittivity. For the increasing and decreasing gradients in permittivity (Model III and IV), relatively good agreement between the model and the

picked values were obtained, except for the Model IV topsoil pick at 0.2 m depth. Model V compromises a high permittivity zone embedded in a lower permittivity medium. Such a layer can cause a low-velocity waveguide for EM waves showing distinct wave propagating effects. In previous vertical crosshole studies (Klotzsche et al., 2013) such zones could be related to zones of higher porosity and zones of preferential flow. The first break picking of the traces for such a layer indicates the presence of a high permittivity zone but it underestimates the permittivity and hence SWC (see Table D-A.1).

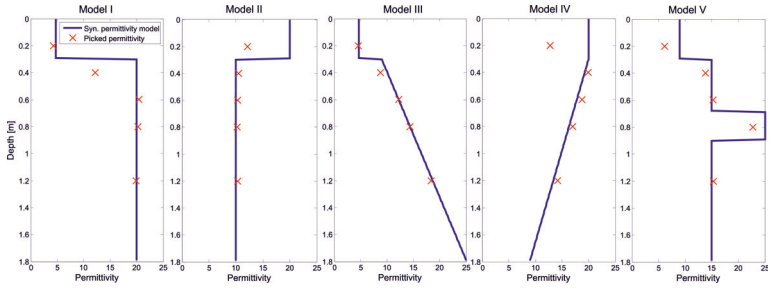

Figure D.14: Different synthetic models with varying permittivity for top and sub-soil (solid blue lines). Synthetic GPR traces were generated with gprMax 3D. The boundary of top and sub-soil is located at 0.3 m depth. Model II and III are modeled with a linear gradient of the permittivity in the subsoil. Conductivity is constant for all models with 10 mS/m. For the same depths of the rhizotrones the first arrival travel times were picked and converted into permittivity (red crosses). Exact values and corresponding differences are illustrated in Table D-A.1.

Table D-A.1: Results of the different synthetic models using gprMax. For Models I to V for each depth between 0.2 and 1.2 m, the relative dielectric permittivity (ε_r) used in the model and the handpicked transformed ε_r are shown. The difference between the modeled and handpicked permittivity values is indicated as $\Delta\varepsilon_r$. The resulting differences in SWC were calculated using Topp's equation (Eq. [2]) and are indicated as $\Delta\theta_{Topp}$.

	Depth [m]	ε_r model	ε_r picked	$\Delta\varepsilon_r$	$\Delta\theta_{Topp}$ [%]
	0.2	4.70	4.49	0.21	0.52
	0.4	20.00	12.23	7.77	11.56
Model I	0.6	20.00	20.40	-0.40	-0.49
	0.8	20.00	20.29	-0.29	-0.36
	1.2	20.00	19.86	0.14	0.17
	0.2	20.00	12.12	7.88	11.761
	0.4	10.00	10.48	-0.48	-0.932
Model II	0.6	10.00	10.30	-0.30	-0.586
	0.8	10.00	10.23	-0.23	-0.438
	1.2	10.00	10.30	-0.30	-0.586
	0.2	4.70	4.61	0.09	0.23
	0.4	9.97	8.77	1.19	2.39
Model III	0.6	12.11	12.23	-0.12	-0.21
	0.8	14.26	14.36	-0.10	-0.16
	1.2	18.56	18.40	0.16	0.21
	0.2	20.00	15.60	4.40	6.05
	0.4	19.34	19.90	-0.56	-0.71
Model IV	0.6	17.86	18.60	-0.74	-0.99
	0.8	16.38	16.98	-0.60	-0.87
	1.2	13.43	13.73	-0.30	-0.50
	0.2	9.00	6.69	2.31	4.94
	0.4	15.00	14.18	0.82	1.31
Model V	0.6	15.00	15.25	-0.25	-0.39
	0.8	25.00	22.78	2.22	2.29
	1.2	15.00	15.31	-0.31	-0.49

Chapter E

Appendix E: Development and validation of a deep learning based automated minirhizotron image analysis pipeline

Abstract

Root systems of crops play a significant role in agro-ecosystems. The root system is essential for water and nutrient uptake, plant stability, symbiosis with microbes and a good soil structure. Minirhizotrons have shown to be effective to non-invasively investigate the root system. Root traits, like root length, can therefore be obtained throughout the crop growing season. Analyzing datasets from minirhizotrons using common manual annotation methods, with conventional software tools, are time consuming and labor intensive. Therefore, an objective method for high-throughput image analysis that provides data for field root-phenotyping is necessary. In this study we developed a pipeline combining state-of-the-art software tools, using deep neural networks and automated feature extraction. This pipeline consists of two major components and was applied to large root image datasets from minirhizotrons. First, a segmentation by a neural network model, trained with a small image sample is performed. Training and segmentation are done using "RootPainter". Then, an automated feature extraction from the segments is carried out by "RhizoVision Explorer". To validate the results of our automated analysis pipeline, a comparison of root length between manually annotated and automatically processed data was realized with more than 36,500 images. Mainly the results show a high correlation (r=0.9) between manually and automatically determined root lengths. With respect to the processing time, our new pipeline outperforms manual annotation by 98.1 - 99.6 %. Our pipeline, combining state-of-the-art software tools, significantly reduces the processing time for minirhizotron images. Thus, image analysis is no longer the bottle-neck in high-throughput phenotyping approaches.

Adapted from: Felix Bauer, Lena Lärm, Shehan Morandage, Guillaume Lobet, Jan Vanderborght, Harry Vereecken, Andrea Schnepf (2022): Development and validation of a deep learning based automated minirhizotron image analysis pipeline. Plant Phenomics, 2022, https://doi.org/10.34133/2022/9758532.

E-1 Introduction

Roots are an essential component of the global biosphere. They are mainly responsible for the acquisition of the resources water and nutrients for the entire plant. In most ecosystems, these resources are the limiting factors for growth of plant organs and yield Atkinson (2000). Water and nutrient uptake are directly linked to the parameters defining the root system, like length, diameter or branching. Therefore, collecting information about the root system becomes increasingly significant. In order, to improve water and nutrient uptake of plants for specific soil and climatic conditions, it is essential to obtain information about the root system architecture of plant species that have been shown to be beneficial for the given conditions Lynch (2007). For plant breeding, this will help to develop new genotypes which are able to cope better with e.g. drought-stress and are more efficient in nutrient uptake Lynch (2013). This will not only help to increase the cultivated area for certain species, it might also lead to higher yields. Especially this applies to locations with less suitable environments for a highly productive agriculture. The negative impact on the soil should be minimized at the same time Bianco and Kepinski (2018).

The direct observation of roots is difficult, because the root system is surrounded by soil, making it challenging to visually measure the roots. To avoid that measurements heavily disturb the plant and its environment, permanent installed equipment, like rhizotubes, or the construction of a minirhizotron, are crucial Atkinson et al. (2019). Minirhizotrons are useful tools to collect data about the root system without disturbing the environment of the roots or the plant itself. Moreover, they allow root observations over the whole vegetation period at a high temporal resolution and the comparison of different vegetation periods and crop types. Transparent rhizotubes, installed below ground, function as a window in the soil. Guided scanners and camera-systems provide high resolution images of the roots and the surrounding soil. Consequently, the non-invasive root measurements can be repeated multiple times during the growing period under *in situ* conditions. However, large minirhizotron facilities include tubes in different depth-levels. Measurements in several depths and time lapse observations result in big datasets that often consist out of 10,000 images and more Cai et al. (2016). Images provided by minirhizotrons strongly differ from e.g. root scans gained from excavated and washed roots Zeng et al. (2010). Various soil conditions around the tubes in different depths lead to a wide range of heterogeneous images with different characteristics. Beside the actual roots, soil structures and disturbing fragments, including small animals, are depicted. Different soil conditions in various depths and at varying locations lead to varying color and light conditions and therefore make the automated processing of minirhizotron-images a challenging task Vamerali et al. (2011).

To analyze roots mainly two steps are needed, the segmentation of root objects and the object quantification Leitner et al. (2013). Due to the heterogeneity within minirhizotron images, the segmentation is very complicated. Different analysis approaches emerged, represented by a numerous collection of software tools, designed to extract the information about the root system Lobet et al. (2013). These tools work manually, or in a (semi-)automated way. Manual annotation tools for minirhizotron images, like "WinRhizoTRON" (Regent Instruments Incl.), or RhizoTrak Möller et al. (2019) rely on the human interaction with each individual image taken, to track each root by hand. It requires the

user to follow every root depicted in the image by hand and mark start, branch and endpoints.

Semi-automated and automated approaches with software-tools exist to facilitate and speed-up the post-processing of the images Vamerali et al. (2011). Filter algorithms used to increase the contrast between root and background and to find root structures by typical geometrical shapes, were proposed by several authors Dowdy et al. (1998), Murphy and Smucker (1995), Zeng et al. (2010). Semi-automated software like "RootSnap!" (CID Bioscience) and "Rootfly" Zeng et al. (2008) require a manual annotation, but also provide root suggestions by a filter created on an initial dataset. Consequently, most of these programs are strictly limited to certain type of images, like high-contrast root scans Yasrab et al. (2019). Eventually, this has the consequence that the annotation of the roots in most minirhizotron images needs to be done almost exclusively manually. Depending on the number of images taken and the number and length of roots, the manual and semi-automated analysis can take weeks to years. Previous studies found that the estimated amount of minirhizotron images, annotated with an annotation software, was between 17 and 38 images h^{-1} Ingram and Leers (2001). Adapted to the working routine with "Rootfly", it takes 1-1.5 h annotation time for an image area of 100 cm^2 depicted soil Smith et al. (2020b). Further, the results underlie the subjectivity of the annotator, because annotations are done according to personal experiences and knowledge of the annotator.

Deep learning has developed to the Gold Standard of machine learning methods within the recent years. Deep neural networks are able to learn from big datasets and provide outstanding results on complex cognitive challenges, even beating human performance in some application fields Alzubaidi et al. (2021). Convolutional Neural Networks (CNN), a subclass of deep learning models, have been created to deal with data in the shape of multiple arrays and are therefore suitable for high-dimensional data like images LeCun et al. (2015). They have the potential to perform a decent automated detection of regions of interests within a heterogeneous and noisy dataset Janiesch et al. (2021). Transferred to the analysis of minirhizotron images, CNNs should have the capability to precisely identify and segment roots in images, where the roots cannot be segmented sufficiently by e.g. explicitly programmed thresholds or filter algorithms. CNNs were already used successfully to localize plant organs, including roots Kamilaris and Prenafeta-Boldú (2018), Keller et al. (2018), Pound et al. (2017), Santos et al. (2020). However, the use of CNNs has mainly been proven on data originating from controlled environment, like lab experiments Yasrab et al. (2019). Furthermore, they are often limited to the use of one or a few fixed pre-trained neural network models Narisetti et al. (2021), or they are not easily usable for non IT-professionals Shen et al. (2020). The main reason for this is the required knowledge and competences in machine learning and programming needed to create a CNN-based system. Especially the data partition between training and validation, the process of annotation and the setup of network architecture make the use of CNNs complicated Smith (2018). Although the use of CNNs is promising for root segmentation and first approaches to use CNNs to segment roots have been successfully accomplished with e.g. the "SegRoot" networks, it is not subject of many published studies and not yet widely used as phenotyping tool for root traits Wang et al. (2019). To make the advantages of CNNs widely utilizable, a software, combining the annotation, training and segmentation process with CNN together in an interface easy to handle, is the key for general use of neural networks for automated root segmentation. The recently published software tool "RootPainter" is one of the most promising approaches for

this task Smith et al. (2020a).

However, fast and reliable segmentation is only the first step of root analysis. For the root quantification another tool is required to obtain morphological and topological features from segmented images. For this task conventional automated root analysis tools, like "WinRhizo" (Regent Instruments Incl.) and "IJ_Rhizo" Pierret et al. (2013) can be used. Recent progress in the development of root-system feature extraction from high-contrast images or scans have resulted in new software tool with the ability of extracting multiple features with a high precision. On the front line of current developments is the new software "RhizoVision Explorer", providing the functions to accurately skeletonize a high-contrast segmented image, to correct the skeleton and deriving several features from it Seethepalli and York (2020).

The aim of our study is to develop a generally applicable, automated analysis pipeline, based on state-of-the-art technologies and software to extract root traits from minirhizotron images. This includes data annotation for neural network training, segmentation and feature extraction. The automated analysis pipeline has to meet the requirements in *i)* availability and feasibility, *ii)* accuracy and comparability, *iii)* speed and efficiency. It was an important requirement to us that this workflow should be feasible for root scientists, who only have basic knowledge in programming or computer science. This workflow should make fast root phenotyping easily accessible for newcomers in root science and lower the time and effort needed to get into the topic. Therefore, it relies on already published software. This workflow further should underline the practicability of deep learning phenotyping tools for the scientific root analysis routine. All software required to use this automated root image analysis pipeline are freely available and easy to operate. Another key advantage of our study is the scope of data used for validation and comparison and the concomitant claim to a general validity of this pipeline. To test and validate the automated analysis pipeline, datasets obtained from several years and two minirhizotron facilities were processed and compared to previously manual annotated data Cai et al. (2018a, 2016, 2018b), Morandage et al. (2021). Previous studies evaluating the results of a CNN-automated image analysis for root images originating from (mini)rhizotrons used between 40 - 857 images Narisetti et al. (2021), Smith et al. (2020b), Wang et al. (2019). In our test we evaluated the results of more than 107,000 images of which we used more than 36,500 for a direct one-to-one comparison of manual human annotation to our automated analysis pipeline. The images represent different *in situ* conditions. In this paper we will present the detailed procedure on operating the automated analysis pipeline and compare its performance to a previously done manual annotation for a decent evaluation.

E-2 Materials and Methods

E-2-1 Experimental test site

The data used for the automated analysis pipeline were collected at the two minirhizotron facilities at the Selhausen test site of the Forschungszentrum Jülich GmbH (50°52'07.8"N, 6°26'59.7"E), Germany Bogena et al. (2018), Weihermüller et al. (2007). The field, in which the minirhizotron facilities are located, has a slight incline with a slope of under 4°. The two minirhizotron-facilities are approximately 150 m apart. The minihizotron facility located

at the top of the field is hereafter referred to as R_{UT} (rhizotron upper terrace) and the minirhizotron at the lower part of the field as R_{LT} (rhizotron lower terrace). The thickness of the soil layer with silty loam texture varies strongly along the field-slope. While it is not present at the top, its thickness at the bottom is up to 3 m. At R_{UT} the gravel content is 60 % while at R_{LT} it is only 4 %. Both facility contain 54 horizontally installed, transparent tubes with each a length of 7 m and an outer diameter of 6.4 cm. The tubes are separated into three plots with each three vertical, slightly shifted (10 cm) rows of six tubes, where three different treatments can be studied. The tubes in each row are installed in -10 cm, -20 cm, -40 cm, -60 cm, -80 cm and -120 cm depth. Past treatments include different irrigation patterns (sheltered, rainfed, irrigated), different sowing densities and dates (later sowing in sheltered plot), or cultivar mixtures (two single cultivar treatments and one mixture). The two minirhizotron facilities were installed in 2012 (R_{UT}) and 2014 (R_{LT}), respectively. Further construction details are explained in Cai et al. (2016).

E-2-2 Data acquisition

Two different camera systems manufactured by Bartz (Bartz Technology Corporation) and VSI (Vienna Scientific Instruments GmbH) were used to capture the root images in the minirhizotrons. Both camera-systems are designed to be used manually. A regular measurement produces 40 images per tube. 20 images are taken 80° clockwise and 20 images 80° counterclockwise from the tubes top point, see Cai et al. (2016, 2018b), Morandage (2020) and Appendix D. In this study, the collected images of three crop growing seasons from 2015/16 and 2017 were taken into account. Depending on the year and measurement date either the Bartz- or the VSI-system was used. The crops cultivated at the test site and used for this study were *Triticum aestivum* cv. Ambello in 2015/16 (winter wheat) and in 2017 *Zea mays* cv. Zoey. Table E.1 gives an overview on camera system used, the resolution of the images, measurement years, measured time period and cultivars observed. Depending on crop growing season, the total amount of measurement dates varied between 21 and 38. The amount of images, taken at one measurement date, varied according to the amount of tubes measured at this measurement date (Table E.4). This was depending on the state of vegetation evaluated in field. Over the past years, the root images collected in the minirhizotron facilities in

Table E.1: Overview of the camera-systems and experiment timeline of minirhizotron images acquisition

camera system	**Bartz**	**VSI**
original resolution [px]	754 x 510	3280 x 2464
converted resolution [px]	1508 x 1020	2060 x 2060
real size [mm]	16.5 x 23.5	20 x 20
growing season	2015/16 & 2017	2017
culture	2015/16: *Triticum aestivum* cv. Ambello 2017: *Zea mays* cv. Zoey	*Zea mays* cv. Zoey
time period (dd/mm/yy)	16/11/15 - 23/06/16 23/06/17 - 12/09/17	08/06/17 - 22/06/17

Selhausen were analyzed manually, using "Rootfly" as a semi-automated tracking tool for the

root length and root counts Cai et al. (2018a, 2016, 2018b), Morandage (2020), Zeng et al. (2008). In this study the images of the years 2015/16 and 2017 were analyzed. The manual annotation of 2015/16 and 2017 has been already published in Cai et al. (2018b), Morandage et al. (2021). Further a sub-sample of the root images was manually annotated by two persons separately in "Rootfly". 1,760 images were used for the comparison between both annotators, and the annotators and the results of the automated analysis pipeline, to test if there are differences in terms of human subjectivity.

E-2-3 Software tools

Our proposed automated minirhizotron image analysis pipeline is based on two software tools for the segmentation Smith et al. (2020a) and the automated feature extraction Seethepalli and York (2020). Furthermore, scripts to convert the segmented images and analyze the outcome are available. For an easy accessibility all scripts are available together within the GUI of the executable "RootAnalysisAssistance" (Supplementary Material). The conversion of the segmented images is also possible within "RootPainter".

Segmentation

"RootPainter", a software tool for the deep learning segmentation of biological images with an included annotation function provides an interactive training method within a GUI, using a U-net based CNN. U-net was developed to train with less images for a more precise segmentation and is therefore suitable when it comes to images where the manual annotation is especially time and labor consuming Ronneberger et al. (2015), Smith et al. (2020b). "RootPainter" was developed to make training-data creation, annotation and network-training accessible for ordinary users. It provides a dataset creation function, which allows an easy selection of training images and cropping them in multiple tiles and to a suitable size for the interactive training. The training mode provides an interactive graphical platform to manually annotate a small part of the dataset and create a neural network model. Further, a mode to segment whole image directories at once is provided. For training and segmentation a Graphics Processing Unit (GPU) is required Smith et al. (2020a). However, a full minirhizotron image analysis is based on two main components, the segmentation and the root trait extraction. Although "RootPainter" provides an inbuilt function for basic root trait extraction based on the previous segmented images, it does not provide e.g. a skeleton correction function and a comprehensive feature extraction including multiple root traits. For our pipeline the feature extraction part should provide multiple morphological and architectural root features with a high accuracy. Furthermore, the possibility of a systematic correction function should be implied. Therefore a platform fulfilling these requirements was used for feature extraction.

Feature extraction

"RhizoVision Explorer" represents the current state-of-the-art technology with a sophisticated automated root traits extraction from segmented root images, by combining the abilities of several existing root image analysis platforms. This includes skeletonization of the segments, filter, filling, smoothing and pruning functions Seethepalli et al. (2021), Seethepalli and York

(2020). However, like most programs for automated root system analysis it is built for the use with binary images or high contrast scans and therefore not suitable for minirhizotron images. The capability of "RhizoVision Explorer" are nevertheless useful when applied to already segmented minirhizotron images.

E-2-4 Analysis pipeline

The starting point for the automated analysis pipeline is a directory containing the raw images captured at the minirhizotron facility. The pipeline was run on a GPU-server with 4 Nvidia GeForce RTX 2080 Ti (NVIDIA Corporation). As client, a computer with an Intel i5-8265U processor and 24GB RAM, operated on Windows 10, was used. However, it is also possible to run the pipeline on one machine, if there is a GPU with CUDA available, or to use the "Google Colaboratory" (Google Colab). An overview of all following steps is explained in Figure E.1.

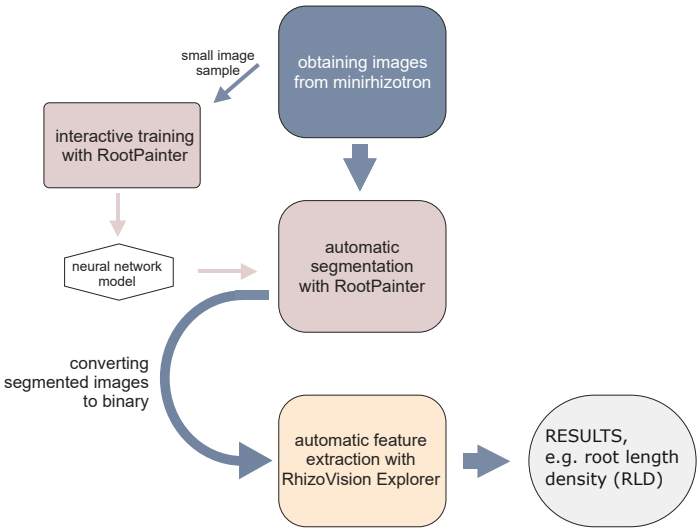

Figure E.1: Schematic overview of the workflow of the automated analysis pipeline starting with image acquisition in the minirhizotron facility.

Pre-processing

The first step of the pipeline is the pre-processing of the images. Depending on the image acquisition system either an up- or down-scaling and a distortion correction is performed (supplementary data). In the same step a labeling, sorting and registration of the images is done automatically. If the images are already ready to use, this step can be omitted.

Training

This step is only needed if no suitable neural network model exists for the targeted dataset. The process, to train a model for root segmentation starts with the creation of a training dataset and subsequently a new project in "RootPainter". We highly recommend to balance the training data according to the factors influencing image visually, in order to maximise the heterogeneity in the training data. Images with different quantities of roots and various root types at different locations should be included. In our case the training dataset for one model contains a balanced amount of images from two different minirhizotron facilities, respectively soil types, depths, tubes and dates. We used only a small amount of images from all available images. For each camera system a separate model was trained, because the images of the two cameras differ significantly. The annotation can be done in the GUI. The roots are annotated as "foreground", soil and other not root-belonging fragments as "background". After the training is started, "RootPainter" automatically creates neural network models, depending on the annotation done previously. The progress can be seen in real time, because "RootPainter" provides previews of the segmentation done by the actual model. These proposals can be corrected and supplemented by the user. The training procedure used in this study is the "corrective training". It is intended for large datasets and therefore suitable for the minirhizotron image data. Essentially this training approach starts with annotating a few images in detail and then continue with correcting only the false-positive and false-negative suggestions of the current model. After finishing the interactive annotation the training is completed automatically. Further details and instructions are explained in Smith et al. (2020a).

Segmentation

The fully-automated segmentation is done with the best model previously trained with a small selection of images from the corresponding measurements. To perform the fully-automatic segmentation, all images have to be located in one directory. The segmentation process itself is started from the "RootPainter" main menu. For each minirhizotron image stored in the directory, one segmented image will be created (Figure E.2a, Figure E.2b).

Converting

To import the segmented images into "RhizoVision Explorer" in the next step, it is essential to convert the images to binary, otherwise the images are not loaded properly (Figure E.2c). This step is performed by a conversion-script, which converts the mono-colored segmented images to black and white images and reduces the images information to binary by only giving information for either black or white pixels. The conversion-script is available as python script or within the *RootAnalysisAssistance*-GUI. It is possible to either browse the image-folders to convert manually, or to process the conversion of a certain image directory in a batch mode. This option is suitable for fast processing a large amount of segmented images. The conversion option is also available within the "RootPainter"-GUI.

Feature extraction

The final step is the feature extraction, performed by "RhizoVision Explorer". This is also done in batch mode. The threshold of the non-root filter, hole filling, edge smoothing and pruning was chosen in a standardized way and uniform for each parameter, depending on the resolution of the image. For the images resulting from the Bartz-system the threshold is 13 px and for the VSI-system 20 px. This results in filtering parts smaller then 0.2 mm^2 and filling holes bigger than 0.2 mm^2. To minimize the influence of segmentation mistakes at the border between root and soil and thus reduce the false detection of non-existent laterals, the minimum size for a lateral root to be detected as a branching root is the parent roots radius multiplied with 0.2 mm. The architectural and morphological information are exported as CSV and the processed segmented images with the calculated skeleton is saved as PNG (Figure E.2.d). The feature extraction is started from the "RhizoVision Explorer" GUI. Further details and background information are explained in Seethepalli et al. (2021).

Root analysis

As last step in addition to the feature extraction, the two-dimensional root length density (RLD) is calculated from the total root length and the window size of the image in the unit of cm cm^{-2}. Furthermore, the number of root tips and branch points, the total root length, the branching frequency, the network and surface area, the diameter (average, median and maximal), the perimeter and the volume can be extracted from the "RhizoVision Explorer" output CSV and applied to spatio-temporal analysis of the root system (Figure E.6 and supplementary data).

E-2-5 Statistics, data processing and visualization

Python 3.8 with *Pandas 1.0.5, Numpy 1.18.5, Matplotlib 3.2.2, Pillow 8.2.0* and *SciPy 1.5.0* have been used for statistics, data processing and visualization.

The F_1-score (Equation E-1) is a measure commonly used to evaluate neural network models Smith et al. (2020a). The F_1 combines precision and recall and has been designed to work on imbalanced data. Precision evaluates the percentage of all correct positive predictions and recall indicates how many positive of all positives the model found. F_1 values are bounded between 0 and 1, the highest value is indicating perfect precision and recall.

$$F_1 = 2 * \frac{precision * recall}{precision + recall} \tag{E-1}$$

$$precision = \frac{T_P}{T_P + F_P} \tag{E-2}$$

$$recall = \frac{T_P}{T_P + F_N} \tag{E-3}$$

where T_P are the *true positive*, F_P the *false positive* and F_N are the *false negative* pixels. The F_1-score was calculated during the interactive training. True positive pixels are correct recognized pixels, where roots are correctly classified as roots. False positive pixels are pixels

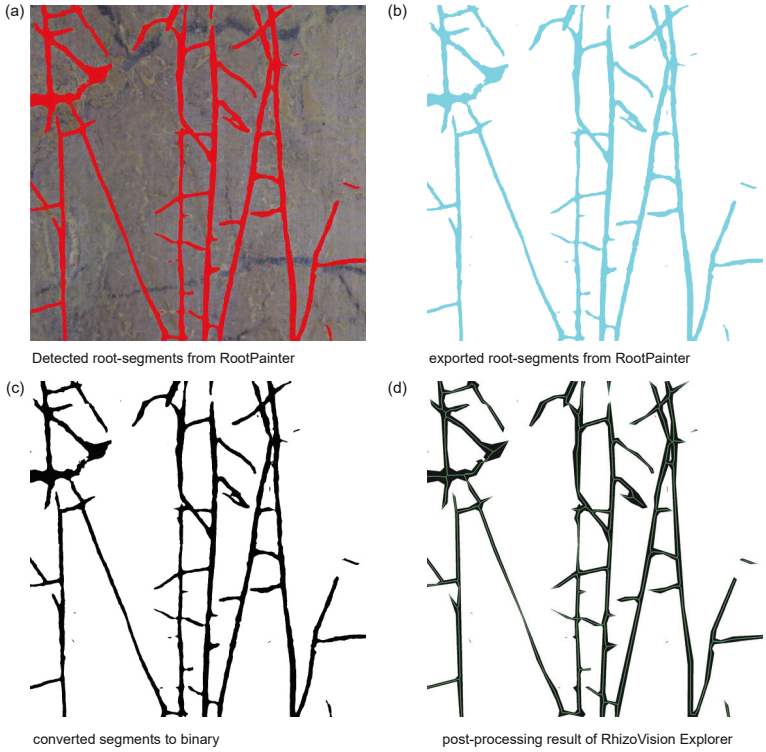

Figure E.2: Example for one image processed by the automated root analysis pipeline. (a) The roots are "detected" by RootPainter according to the previous trained model. (b) The segmented image is exported and (c) converted to binary. (d) The last step is the skeletonization and feature extraction with RhizoVision Explorer.

classified as root, not including a part of a root and false negative pixels are pixels including parts of a root, but are classified as background.

The outcome of the automated root annotation was compared to the manual annotation by means of the pearson correlation coefficient, both on the data set as a whole as well as on individual measurement dates for the seasons 2017. For the same season we calculated the mean of the total root length per image for each measurement date and used a Welch two-sample t-test to assess whether the differences between automated analysis and manual annotation of the total root length (ΔRL) were statistically significant.

Furthermore the normalized root mean squared error (NRMSE) was calculated according to Equation E-4.

$$NRMSE = \frac{\sqrt{\frac{\sum_{i=1}^{n}(y_i - \hat{y})^2}{n}}}{y_{max} - y_{min}} \tag{E-4}$$

where $n = sample\ size$, y_i is the $i^{th}\ observation\ of\ y$ and $\hat{y}$ is the $predicted\ y\ value$. Additionally a linear Model II regression (ordinary least products) was performed to test for fixed and proportional bias with the total root length of 2017 data. We choose this type of regression because the x-values might also be subject to errors Delory et al. (2017), Ludbrook (1997). For each measurement date and facility, a model was fitted and the 95% confidence interval (95% CI) of slope and intercept was calculated. We considered a fixed bias if the 95% CI of the intercept did not include 0 and there was a proportional bias if the 95% CI of the slope did not include 1.0.

The manual per-image annotation with "Rootfly" of 2015/16 data is no longer available. However, the images and mean RLD values per tube are available and therefore were used for comparison. Based on this the RLD resulting from automated and manual analysis methods was calculated for every minirhizotron tube and measurement date (Figure 5-1) and compared as a proxy for a common root measurement parameter Zuo et al. (2004). In this analysis, all growing periods 2015/16, and 2017 were included.

E-3 Results

E-3-1 Neural Network model validation

The F_1 for both neural network models trained for each camera-system is high. The F_1 for the Bartz-system is 0.78 and 0.81 for VSI-system model. After 60 epochs without any improvement the neural network training was stopped automatically.

E-3-2 Comparison of automated and manual annotation

Considering all images used for comparison, the overall correlation of total root length between manual annotation and automated analysis pipeline is very high with $r = 0.9$.

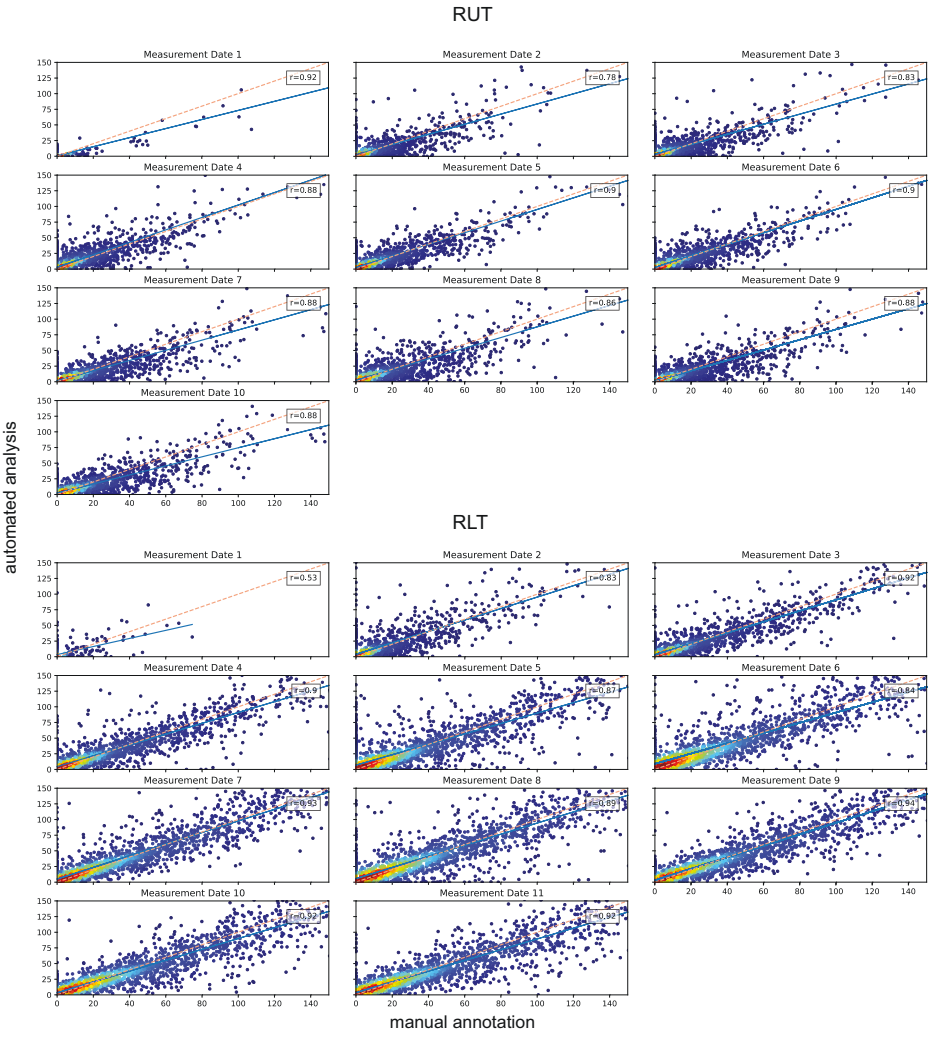

Figure E.3: Correlation of automated and manual analyzed root length, obtained from 2017. Each measurement date is considered separately for R_{UT} and R_{LT}. The color represents the density.

The correlation was performed with 16,599 images taken at R_{UT} and 21,082 images taken at R_{LT}. For the data obtained in the growing period 2017, the correlation is high to very high (r = 0.77 - 0.94) for every measurement date except the first measurement date at R_{LT} (r = 0.57) (Figure E.3). Generally, the correlation shows an increasing trend towards later measurement dates (Table E.2). ΔRL and NRMSE indicate low values for most measurements dates at both facilities. Regarding especially the ΔRL it can be seen, that the

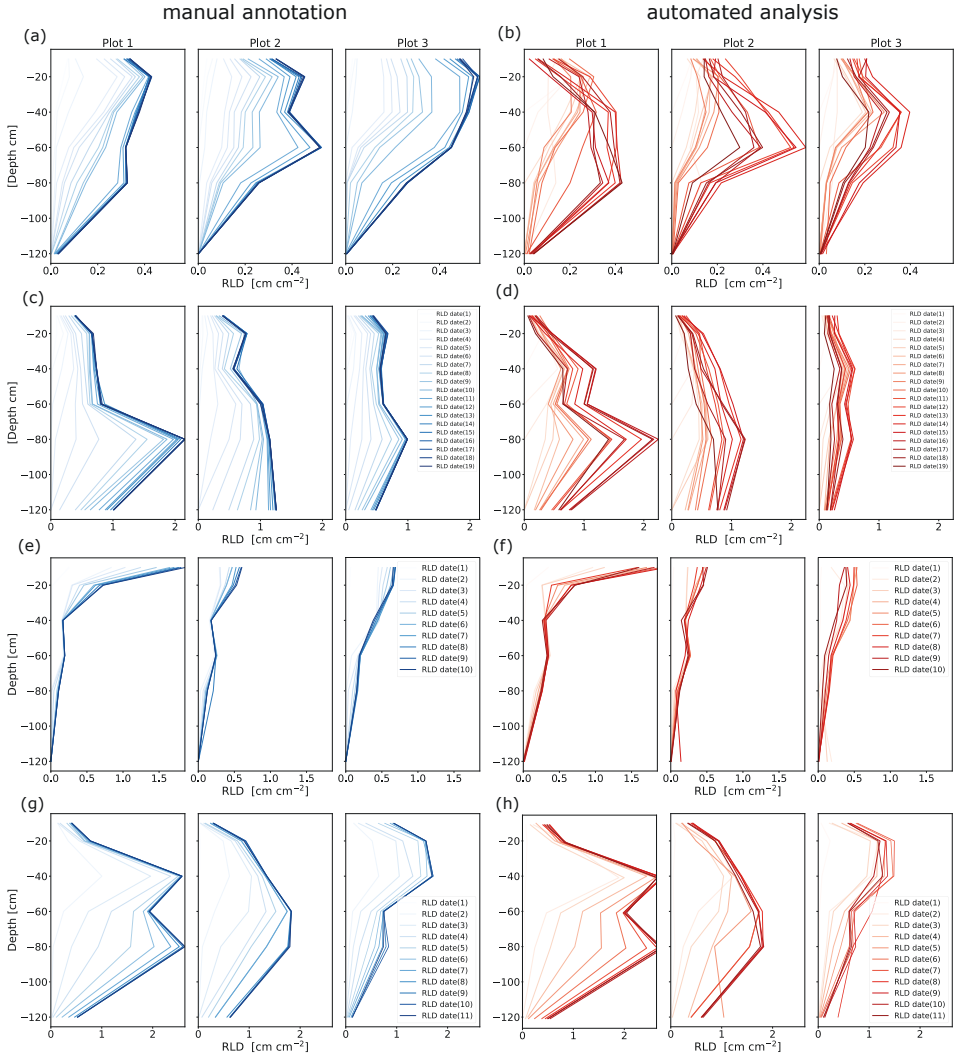

Figure E.4: Comparison RLD of the data obtained from images originating from two minirhizotrons in the growing season 2015/16 and 2017, separated by plots grown with different treatments. The images were analyzed by hand (blue: manual) and by the automated analysis pipeline (red: automated). 2015/16: (a) R_{UT} manual, (b) R_{UT} automated, (c) R_{LT} manual,(d) R_{LT} automated; 2017: (e) R_{UT} manual, (f) R_{UT} automated, (g) R_{LT} manual,(h) R_{LT} automated;

differences in mean between manual annotation and automated analysis pipeline in 2017 are very low -0.5 mm (R_{UT}), -0.77 mm (R_{LT}). However, the t-test indicates that there are no significant differences between the mean of total root length except for measurement date 4 at R_{UT}. The slope of the linear regression models is slightly under one in most cases and the intercept marginally higher than 0 for all measurement dates. Both fixed and proportional bias were detected within almost every measurement date (Table E.2).

Regarding the RLD values from 2015/16, one specific difference between manual and automated analysis is visible. Until the 14^{th} measurement date the RLD is continuously increasing and then stagnating in the 2015/16 data resulting from manual annotation. The RLD from the automated analysis follows the same trend but decreases from 14^{th} measurement date continuously. Beyond this, the RLD curves of both methods are very consistent (Figure E.4). In 2017 datasets, only negligible differences between manual and automated analysis method are recognizable, except for the first measurement date at R_{LT} (Figure E.4f, Figure E.7b) and first two dates and a small peak at the fourth measurement at R_{UT} (Figure E.4h).

The comparison between two human annotators and each annotator and the automated analysis pipeline separately shows that the correlation between the person 1 and the pipeline is $r = 0.92$ and the correlation between person 2 and the pipeline is $r = 0.79$. The correlation between both persons is the lowest ($r = 0.73$).

Table E.2: Overview of the statistical comparison of automated and manual annotation. ΔRL is the difference between the mean total root length (mm) obtained from automated and manual analysis methods, and a Welsch two sample t-test shows whether differences are significant (* = p<0.01).

		2017	
measurement date		$\mathbf{R_{UT}}$	$\mathbf{R_{LT}}$
1	ΔRL	0.45	0.42
	NRMSE	0.071	0.077
	r	0.92	0.53
2	ΔRL	0.89	1.17
	NRMSE	0.071	0.053
	r	0.78	0.83
3	ΔRL	0.95	0.54
	NRMSE	0.057	0.052
	r	0.83	0.92
4	ΔRL	2.94*	0.65
	NRMSE	0.051	0.055
	r	0.88	0.9
5	ΔRL	1.36	0.92
	NRMSE	0.041	0.072
	r	0.9	0.87
6	ΔRL	1.35	1.7
	NRMSE	0.044	0.065
	r	0.9	0.84
7	ΔRL	-1.46	1.8
	NRMSE	0.046	0.058
	r	0.88	0.93
8	ΔRL	0.11	0.55
	NRMSE	0.045	0.073
	r	0.86	0.89
9	ΔRL	-1.41	-0.97
	NRMSE	0.039	0.057
	r	0.88	0.94
10	ΔRL	-2.44	-2.89
	NRMSE	0.039	0.047
	r	0.88	0.92
11	ΔRL		0.65
	NRMSE		0.065
	r		0.92

E-3-3 Time evaluation

The time required to train the neural network model mostly depends on the amount of images included in the training dataset. Approximately 65 % of the time needed is used for training of the deep neural network. The annotation takes 40 % of the time, based on a mean of 200 annotated images h^{-1}. The range it took to annotate one image was between 1 and 180 s per image, depending on the accuracy of the proposed segmentation. The time required for annotation decreases significantly with increasing training time. The mean time needed by the network for the training of a dataset of 1,500 images, was approximately 5h, excluding the real-time training during the annotation. This is approximately 25 % of the entire processing time. Segmentation took around 27 % of the total time. With 4 Nvidia GeForce RTX 2080 Ti GPUs and a batch size of 12 the segmentation took around 0.7 s per image. Converting the segmented to binary images and the final feature extraction took around 8 % of the time (Figure E.5).

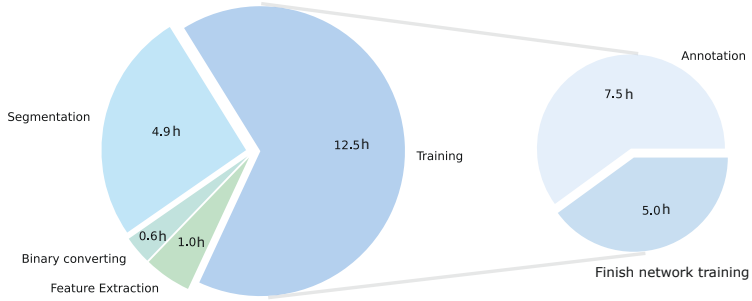

Figure E.5: Time requirements to run the automated analysis pipeline for a sample of 25,000 images. Left: All sub-processes together. Right: share of the neural network training, which is only required when no suitable model is available.

E-4 Discussion

E-4-1 Availability and feasibility

The availability is the parameter for how easily accessible all components of the automated pipeline are for everyone. The feasibility defines how easy the proposed pipeline and with that the required software can be operated.

The equipment needed to apply the new workflow requires a computer with a powerful GPU, or alternatively a basic computer, an additional server with powerful GPUs and a network-connection between both. Furthermore, the software packages of "RootPainter" and "RhizoVision Explorer" are needed and the conversion and analysis script are required. All this is open-source available Seethepalli and York (2020), Smith et al. (2020b). All software

can be found in the section "data availability".

The training of the model requires interaction with "RootPainter", if the user wants to start the training of a new model or corrects a segmentation within the training process. This step is therefore not fully automated. All other components of the automated analysis pipeline are automated. The interactive mode of the training represents a major time saving compared to the conventional separation of the training step and the application step. Adaptations to the model can be done “on the fly” with little time investment, facilitating e.g. the adaptation to new types of images. Once the model is trained, the human interaction needed to apply the pipeline is reduced to a few "clicks". With a suitable model available, the user has to interact actively three times with the automated pipeline, *(1.)* to start the segmentation, *(2.)* to convert the segments to binary and *(3.)* to start the feature extraction. No deeper knowledge in computer science is needed, because all intermediate steps are available within a GUI. However, the first implementation of the "RootPainter" environment at the server part of the setup requires basic knowledge in server administration or support.

In contrast to manual or semi-automated operated root analysis programs, like different tools based on "ImageJ", "DART", "GiA Roots", "SmartRoot", "EZ-Rhizo" or "Rootfly", the expenses in time, knowledge and experiences required to apply the automated workflow, are much lower. This is granted due to the very small interactions needed for the automated analysis pipeline Armengaud et al. (2009), Bot et al. (2009), Galkovskyi et al. (2012), Lobet et al. (2011), Pierret et al. (2013), Zeng et al. (2008).

E-4-2 Accuracy and comparability

The accuracy evaluates the automated analysis pipeline in terms of reliability and exactness of the generated data. Comparability is given, if the results of the automated analysis pipeline can be compared to the outcome of previously evaluated data of the same kind, like the manual annotation performed with "Rootfly". The most important characteristic of the automation of plant data analysis is the reliability of the generated datasets. Therefore, the accuracy of the observed root traits has to be as close to the ground truth as possible Atkinson et al. (2019). In our study we used the manual annotation of the roots as comparison. The manual annotation was performed by different persons and over a long time period. Consequently, a certain subjectivity was included in this process.

Generally, the results for 2017 data analyzed automatically and manually are very close to each other, indicating a general great fit of the models used for images originating from 2017. However, there is a fixed and proportional bias between automated analysis and manual annotation, showing a minor but systematic underestimation of total root length from the automated analysis (Table 11.2) that increases slightly to the later measurement dates, see also the negative ΔRL values in Table 11.2. This originates from the fact that the neural network model is only able to segment roots, if they are also visible by the human eye. Rarely, small parts of roots are covered by soil and this can only be compensated to a certain extend by training the neural network and filling holes with "RhizoVision Explorer" (Figure E.8). The more roots there are in the images, the more likely this segmentation mistake occur. Although this is a disadvantage of the automated analysis pipeline, its main purpose

is to provide reliable and consistent data for a qualitative biological analysis. The known systematic bias in the method is well predictable in contrast to the bias originating from different annotators. Consequently, the data obtained from the automated analysis pipeline are more robust and reliable, which is in advantage for further biological conclusions drawn from the data.

The consistency of the automated analysis results becomes especially visible regarding the RLD plots plotted from 2015/16 and 2017 data (Figure E.4). The decrease in 2015/16 RLD profiles that is not monitored in the manual annotation data, originated from the root senescence (Figure E.9). The senescence could be better evaluated by the neural network than by the human annotator. In manual annotation the slight, gradual discoloration of the roots visually revealing the senescence is easy to miss. Furthermore, it is a complicated work step in "Rootfly" to eliminate already annotated roots at the right point in the timeline. Taking this into consideration, the results of the method comparison for 2015/16 and 2017 data shows impressive results, regarding accuracy and comparability of the automated analysis pipeline.

Regarding the biological conclusions that could be derived from the data, the differences between the methods are negligible, as we are working with minirhizotron data that cover a huge spatial and temporal resolution and are measured in heterogeneous conditions. Especially the consistent low ΔRL and NRMSE (Table 11.2), as well as the high conformity of the RLD profiles (Figure E.4) indicate that the qualitative conclusions derived from data provided by the automated analysis pipeline are at least the same as from manual annotation. Considering the influence of the human subjectivity on manual annotation, the automated pipeline additionally provides objectivity that most likely cannot be reached, if more than one annotator does the manual annotation.

The manual annotation itself requires a certain level of expertise in root phenotyping. This expertise is gained with a lot of personal experiences Vamerali et al. (2011), Zeng et al. (2008). Therefore, it can be hypothesized that there is also a significant influence of subjectivity in human annotation. Over the years, different persons annotated the root datasets. Hence, the impact of differences resulting from varying manual annotation strategies might influence the results more than the differences between manual and automated analysis. The direct comparison between two annotators showed a lower correlation between the persons annotating, than between the automated analysis pipeline and each human annotator. Consequently, we concluded that the human effect on manual annotation is higher than the impact of a mistake done by the automated workflow.

The automated analysis pipeline provides a level of objectivity, a human annotator cannot achieve. Therefore, it is highly probable that with the application of the automated pipeline associated minimization of the human influence will significantly improve objectivity and also accuracy of the minirhizotron image analysis.

E-4-3 Speed and efficiency

The speed is the pure amount of time the pipeline requires to analyze a certain amount of images. Efficiency is defined through the amount of time and labor needed to analyze a

dataset in contrast to manual annotation. The time required to analyze root images by hand is enormous. The estimated time to analyze 100 cm^2 of depicted soil is 1 - 1.5 h Smith et al. (2020b). This is consistent with the results of other studies, needing approximately 1 h for annotating 17-38 images manually Ingram and Leers (2001). Intern evaluation reproduced the same results. To annotate 25,000 images, which is approximately the amount of images for a shorter growing season, the annotation time needed is 1,000 - 1,500 h. The time needed to process the same amount of images with the automated pipeline is approximately 19 h, including the training of the neural network. Without the training, the segmentation and feature extraction would only take around 6.5 h for all images. The resulting benefits in time saving are massive (Figure E.5).

Generally, only around 1.2 % - 1.9 % of the time needed for manual annotation is needed by the automated workflow to process the data, including the training. Excluding the entire training process, the automated workflow requires only 0.4 % - 0.65 % of the time needed to annotate the same amount of images manually with e.g. "Rootfly". Regarding the advantages of time saving, it further has to be taken into account that the time of interaction with the computer is decimated to almost zero, once the training is completed.

E-4-4 Limitations and further improvement

Although the current automated analysis pipeline does include time series in form of either root length density depth profiles at different time points or in form of root arrival curves, i.e., root length as a function of time at different depths, individual roots and their phenology are not followed from their birth to their death. This could be of high interest, for example, to root ecologists. To fully exploit minirhizotron data it would be a significant progress to add a single root tracking possibility, including root order and status. The implementation of these functions would improve the pipeline and enhance the use-cases for root ecologists.

E-5 Conclusion

We propose a new approach to analyze large amounts of 2D root image data. This became necessary with the big amount of data created in experimental field sites such as the minirhizotron facilities in Selhausen (Germany) as well as others Svane et al. (2019), Ytting et al. (2014). The automated analysis pipeline illustrated in this study, is a suitable solution to easily and accurately analyze minirhizotron images in significantly less time.

To the best of our knowledge, we are the first study testing a deep learning and automated feature extraction combining high-throughput minirhizotron image analysis pipeline to this extent. The biggest advantage of the automated workflow is the massive saving in time. Precisely expressed, the required time is reduced by more than 98 % in contrast to manual annotation, while providing several root traits, including number of root tips, number of branch points, root length, branching frequency, network area, perimeter, volume, surface area and diameter on a spatio-temporal scale. The required root traits can be made available quickly which may speed up further analysis and applications of this type of data. In conclusion, the automated pipeline outperforms the manual annotation in time requirements

and information density, while providing reliable data and feasibility for everyone. Tested with more than 107,000 minirhizotron images, including more than 36,500 images for detailed comparison, obtained from two growing seasons and different soil types, depths and cultures our results indicate a high general validity for the presented pipeline. Irregularities in the match of manual annotation and analysis pipeline can be essentially explained with rarely occurring missed segmentations of root fragments by the automated analysis pipeline, due to soil covered roots and mainly by the influence of human subjectivity in manual annotation. Balanced training datasets and consequent annotation of the training data are the key to good results. If these facts are considered, the here presented and evaluated pipeline has the potential to be the new standard method for reliable high-throughput root phenotyping of minirhizotron images.

Data Availability

- The supplementary data that support the findings of this study and help to operate the in this work introduced root image analysis pipeline, including an example, are open available. Furthermore, data and scripts to reproduce the RLD-profiles (Figure E.4) and RAC-curves (Figure E.7) are open to access with the same identifier: https://doi.org/10.34731/pbn7-8g89.
- RootPainter Smith et al. (2020a) is available at: https://github.com/Abe404/root_painter
- RhizoVision Explorer Seethepalli et al. (2021), Seethepalli and York (2020) is available at: https://zenodo.org/record/4095629
  and https://github.com/rootphenomicslab/RhizoVisionExplorer

Supplementary Materials

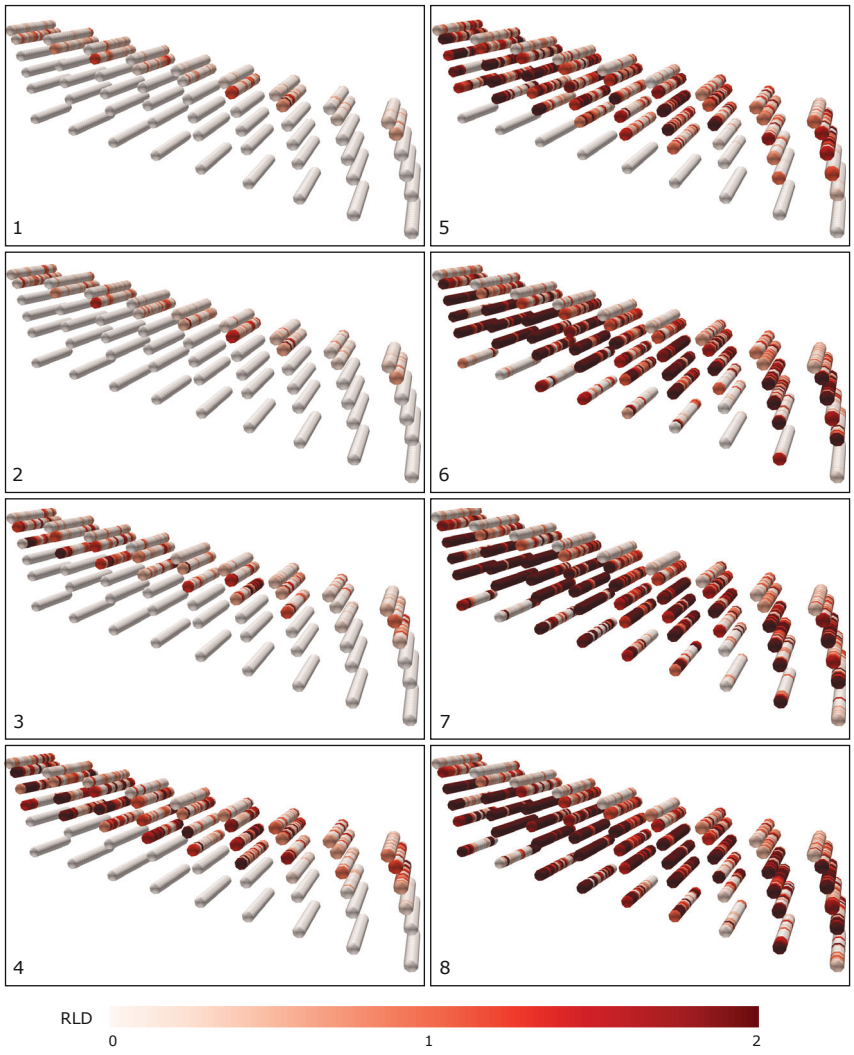

Figure E.6: 3D spatio-temporal distribution of RLD measured in all tubes at one minirhizotron. Distances between tubes are not to scale. 1-8 represents the time steps.

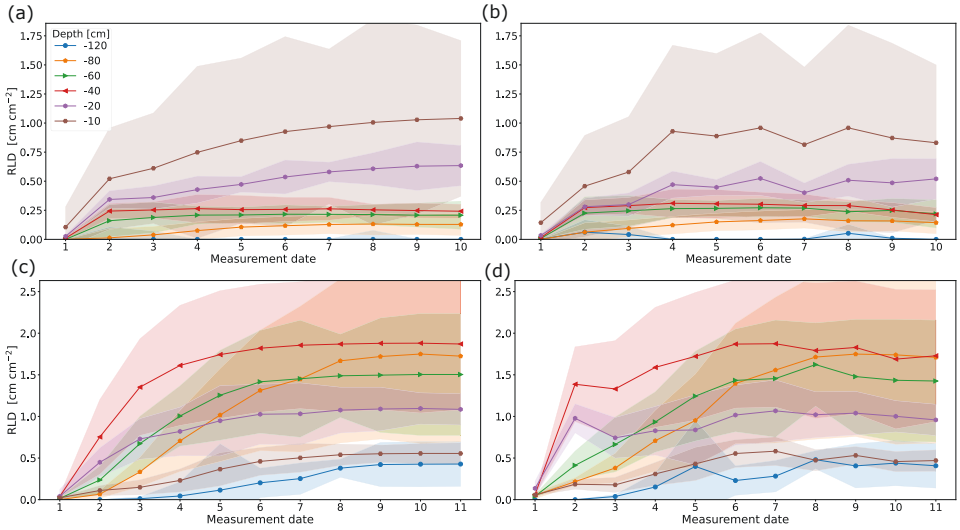

Figure E.7: Comparison of root arrival curves of the data obtained from images originating from two minirhizotrons in the growing season 2017. The images were analyzed by hand (left: manual) and by the automated analysis pipeline (right: automated). 2017: a) R_{UT} manual, b) R_{UT} automated, c) R_{LT} manual,d) R_{LT} automated.

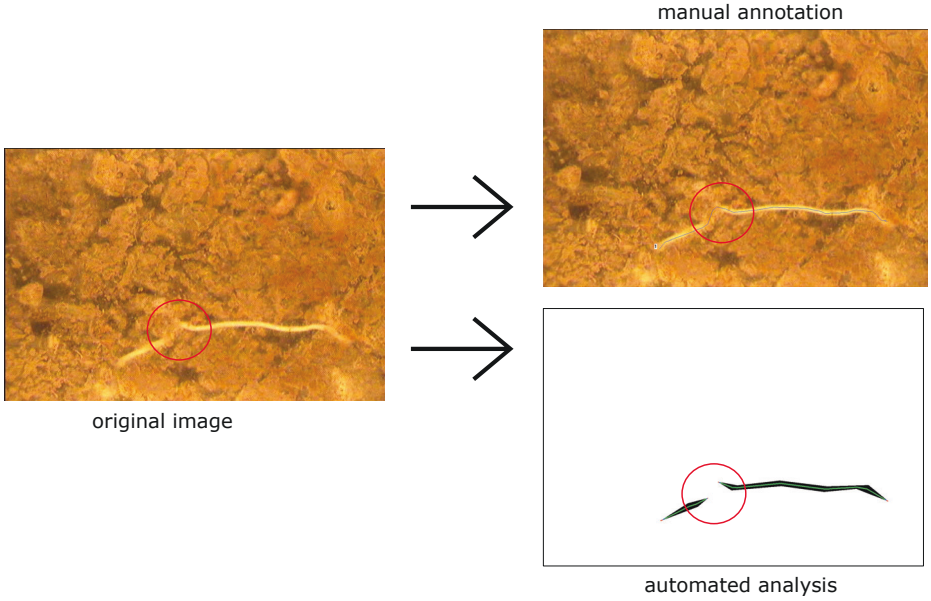

Figure E.8: Manual vs. automated analysis. The automated analysis misses a small part of the root and underestimates the total root length slightly.

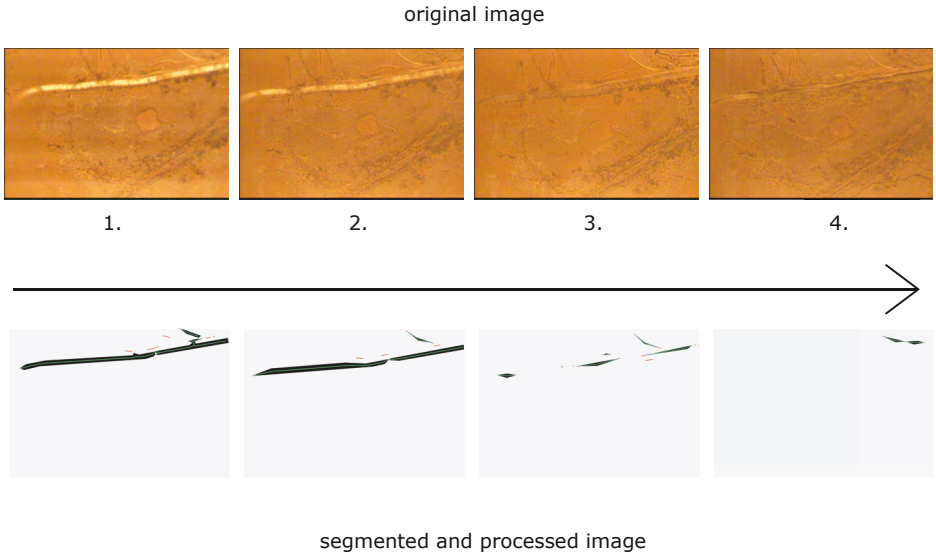

Figure E.9: Root senescence visible from early to late measurement dates in the growing season 2015/16 and the corresponding segmentation and skeletonization.

Table E.3: Detailed overview of the images taken at the growing season 2015/16 and 2017

	2015/16			2017	
measurement no.	facility	date	images	date	images
1	R_{UT}	16/11/15	720	08/06/17	480
	R_{LT}	16/11/15	720	08/06/17	584
2	R_{UT}	26/11/15	1,080	29/06/17	1,800
	R_{LT}	26/11/15	1,079	22/06/17	1,800
3	R_{UT}	17/12/15	1,800	06/07/17	1,800
	R_{LT}	17/12/15	1,439	29/06/17	2,160
4	R_{UT}	02/02/16	1,520	13/07/17	1,800
	R_{LT}	21/01/16	1,800	06/07/17	2,160
5	R_{UT}	12/02/16	1,800	20/07/17	1,800
	R_{LT}	12/02/16	1,800	13/07/17	2,160
6	R_{UT}	26/02/16	1,800	27/07/17	1,200
	R_{LT}	26/02/16	2,160	20/07/13	2,160
7	R_{UT}	14/03/16	1,800	02/08/17	1,840
	R_{LT}	14/03/16	2,160	27/07/17	1,430
8	R_{UT}	26/03/16	1,840	10/08/17	1,959
	R_{LT}	24/03/16	2,160	02/08/17	2,159
9	R_{UT}	07/04/16	2,160	23/08/17	2,120
	R_{LT}	07/04/16	2,160	10/08/17	2,160
10	R_{UT}	13/04/16	2,160	12/09/17	1,800
	R_{LT}	13/04/16	2,160	24/08/17	2,159
11	R_{UT}	29/04/16	2,160	-	-
	R_{LT}	29/04/16	2,160	12/09/17	2,150
12	R_{UT}	06/05/16	2,160	-	-
	R_{LT}	06/05/16	2,160	-	-
13	R_{UT}	13/05/16	2,160	-	-
	R_{LT}	13/05/16	2,160	-	-
14	R_{UT}	20/05/16	2,160	-	-
	R_{LT}	20/05/16	2,160	-	-
15	R_{UT}	27/05/16	2,160	-	-
	R_{LT}	27/05/16	2,159	-	-
16	R_{UT}	03/06/16	2,160	-	-
	R_{LT}	03/06/16	2,159	-	-
17	R_{UT}	09/06/16	2,160	-	-
	R_{LT}	09/06/16	2,160	-	-
18	R_{UT}	16/06/16	2,155	-	-
	R_{LT}	16/06/16	2,160	-	-
19	R_{UT}	23/06/16	2,149	-	-
	R_{LT}	23/06/16	2,156	-	-

Table E.4: Comparison of the automated analysis pipeline and the manual annotation of the total root length obtained in the growing season 2017 with a linear regression. The confidence interval (95%) of the regression coefficient (ordinary least products) are listed in parenthesis. The bias is fixed if the 95% CI of the intercept do not include 0 and the bias is proportional if the 95% CI of the slope do not include 1.

measurement no.	MR facility	Intercept (95% CI)	Slope (95% CI)	Bias	
				Fixed	Proportional
1	R_{UT}	0.26 (0.08, 0.45)	0.73 (0.71, 0.74)	yes	yes
	R_{LT}	1.09 (0.83, 1.36)	0.7 (0.65, 0.75)	yes	yes
2	R_{UT}	2.8 (2.16, 3.44)	0.81 (0.78, 0.84)	yes	yes
	R_{LT}	3.5 (2.78, 4.23)	0.92 (0.89, 0.94)	yes	yes
3	R_{UT}	3.07 (2.46, 3.69)	0.8 (0.78, 0.83)	yes	yes
	R_{LT}	3.12 (2.45, 3.79)	0.88 (0.86, 0.89)	yes	yes
4	R_{UT}	2.99 (2.28, 3.7)	0.99 (0.97, 1.02)	yes	no
	R_{LT}	4.53 (3.63, 5.43)	0.86 (0.85, 0.88)	yes	yes
5	R_{UT}	2.35 (1.72, 2.97)	0.93 (0.91, 0.95)	yes	yes
	R_{LT}	6.68 (5.65, 8.07)	0.83 (0.81, 0.85)	yes	yes
6	R_{UT}	2.43 (1.75, 3.11)	0.93 (0.91, 0.95)	yes	yes
	R_{LT}	8.99 (7.51, 10.48)	0.82 (0.8, 0.84)	yes	yes
7	R_{UT}	1.55 (0.86, 2.24)	0.81 (0.79, 0.83)	yes	yes
	R_{LT}	4.99 (3.95, 6.03)	0.93 (0.91, 0.94)	yes	yes
8	R_{UT}	2.37 (1.61, 3.12)	0.85 (0.83, 0.88)	yes	yes
	R_{LT}	5.71 (4.38, 7.05)	0.89 (0.87, 0.91)	yes	yes
9	R_{UT}	1.18 (0.57, 1.79)	0.82 (0.81, 0.84)	yes	yes
	R_{LT}	3.0 (1.95, 4.05)	0.92 (0.9, 0.93)	yes	yes
10	R_{UT}	2.31 (1.65, 2.98)	0.72 (0.7, 0.74)	yes	yes
	R_{LT}	3.35 (2.2, 4.5)	0.87 (0.85, 0.88)	yes	yes
11	R_{UT}	-	-	-	-
	R_{LT}	3.61 (2.47, 4.75)	0.86 (0.84, 0.87)	yes	yes

Chapter F

Appendix F: Sequential and coupled inversion of horizontal borehole ground penetrating radar data to estimate soil hydraulic properties at the field scale

Abstract

Horizontal borehole ground penetrating radar (GPR) measurements can provide valuable information on soil water content (SWC) dynamics in the vadose zone, and hence show potential to estimate soil hydraulic properties. In this study, the performance of both sequential and coupled inversion workflows to obtain soil hydraulic properties from time-lapse horizontal borehole GPR data obtained for an infiltration experiment were compared using a synthetic modelling study and the analysis of field data. The sequential inversion using the vadose zone flow model HYDRUS-1D directly relied on SWC profiles determined from the travel time of GPR direct waves using the straight-wave approximation. Synthetic modelling showed that sequential inversion did not provide accurate estimates of soil hydraulic parameters due to interpretation errors near the infiltration front and the ground surface. In contrast, the coupled inversion approach, which combined HYDRUS-1D with a forward model of GPR wave propagation (gprMax3D) and GPR travel time information, provided accurate estimates of the hydraulic properties in synthetic modelling. The application of the coupled inversion approach to measured borehole GPR data also resulted in plausible estimates of the soil hydraulic parameters. Concluding, that coupled inversion should be preferred over sequential inversion of time-lapse horizontal borehole GPR data in the presence of strong SWC gradients occuring during infiltration.

Adapted from: Yi Yu, Lutz Weihermüller, Anja Klotzsche, Lena Lärm, Harry Vereecken, Johan Alexander Huisman (2021): Sequential and coupled inversion of horizontal borehole ground penetrating radar data to estimate soil hydraulic properties at the field scale. Journal of Hydrology 296, https://doi.org/10.1016/j.jhydrol.2021.126010

F-1 Introduction

Obtaining accurate hydraulic parameters of the vadose zone is important in a wide range of applications, including modelling of water flow and contaminant transport (e.g., Wagner (1992);Vereecken et al. (2007)), managing water and soil resources (e.g., Blanco-Canqui and Lal (2007), Hartmann et al. (2014)), and evaluating climate change effects on forests (e.g., Martinez-Vilalta et al. (2002); McDowell and Allen (2015)). Hydraulic parameters can be determined by different laboratory methods (e.g., McDowell and Allen (2015), Neuzil et al. (1981)), but this typically leads to hydraulic property estimates that are not representative of field conditions (Kool et al. (1987)). Therefore, estimation of hydraulic properties at the field scale is preferred if characterization at this scale is intended (Klute and Dirksen (1986)).

Field-scale estimation of hydraulic properties is commonly based on measurements made with point-scale sensors, such as the neutron probe (Chanasyk and Naeth (1996)) and time domain reflectometry (TDR) Robinson et al. (2008). Such methods allow the accurate determination of soil water content (SWC) dynamics, and therefore have been widely used for parameterizing hydrological models (e.g., Abbaspour et al. (2000), Katul et al. (1993), Kumar et al. (2010), Malicki et al. (1992), Nandagiri and Prasad (1996), Steenpass et al. (2010), Wollschläger et al. (2009)). In some studies, SWC measurements were combined with matric potential measurements obtained by tensiometers (e.g., Zhang et al. (2003)) in order to better constrain the hydraulic parameter estimation (Vereecken et al., 2008). A major disadvantage of using point sensor information to estimate soil hydraulic properties is the relatively small sensing volume and the resulting limited representativeness for the field-scale soil states.

In the last decades, many studies reported the potential of using geophysical techniques, such as electromagnetic induction (EMI) (e.g., Bagnall et al. (2020), Brosten et al. (2011), Manoli et al. (2015), Moghadas et al. (2017)), electrical resistivity tomography (ERT) (e.g.,Brunet et al. (2010), Huisman et al. (2010), Manoli et al. (2015), Mboh et al. (2012), Pollock and Cirpka (2010)) and ground penetrating radar (GPR) (e.g., Hubbard and Rubin (2000), Looms et al. (2008a), Rossi et al. (2015)), to obtain accurate field-scale estimates of SWC and soil hydraulic properties. GPR uses the travel time and attenuation of high-frequency electromagnetic waves travelling through the ground to obtain the dielectric permittivity (ε) and electric conductivity (σ) of the subsurface (e.g., Holliger et al. (2001), Slob et al. (2010)). Due to the direct relationship between ε and SWC (Topp et al., 1980), GPR is the one of the most promising geophysical methods for SWC estimation (e.g., Huisman et al. (2003), Klotzsche et al. (2018)); . GPR can rapidly provide surveys for larger scales of interest (1 $\sim$ 1000 m profiles) (e.g., Ardekani (2013)), which implies that GPR is capable of characterizing the spatio-temporal SWC distribution at the field scale (e.g., Steelman et al. (2012)).
In general, GPR measurements can be performed off the ground surface (off-ground GPR) (e.g.,Lambot et al. (2004), on the soil surface (surface GPR) (e.g., Huisman et al. (2002), van Overmeeren et al. (1997)) or in vertical or horizontal boreholes (borehole GPR) (e.g., Redman et al. (2000)). Off-ground GPR relies on the use of an ultra-wide frequency band for subsurface investigations, and hence can potentially provide high-resolution information about the soil states. However, offground GPR measurements are influenced by surface roughness and only have a limited penetration depth (Lambot et al. (2006)). For surface

GPR measurements, SWC can be estimated based on the analysis of the direct ground wave (Grote et al. (2003), Weihermüller et al. (2007)) or reflected waves (Lunt et al. (2005)). Both GPR acquisition strategies have been successfully used to monitor water flow dynamics in unsaturated soil (Allroggen et al., 2015, Mangel et al., 2012, Moysey, 2010). The penetration depth of surface GPR is limited by the soil characteristics, especially by the bulk electric conductivity. Furthermore, there is no control on the vertical resolution when using reflected waves for SWC determination (Huisman et al., 2003). Borehole GPR can overcome these limitations but requires the availability and accessibility of appropriate boreholes or wells, and is therefore restricted to specialized test sites and experimental set-ups. Borehole GPR measurements have also been used to monitor SWC dynamics Looms et al. (2008a). In addition, Zero-Offset-Profiling (ZOP) measurements between horizontal boreholes have been used to monitor SWC dynamics, see Cai et al. (2016), Galagedara et al. (2002) and Appendix D. Due to the good control on the vertical resolution and the improved spatial representativeness for the field plot scale, this kind of set-up provides detailed information on the spatial and temporal variation of SWC.

In order to derive soil hydraulic parameters from time-lapse GPR data, two types of inversion strategy can be used. The first type is commonly called sequential inversion and consists of three steps (Hinnell et al., 2010, Huisman et al., 2010). First, the dielectric permittivity ε is determined from the first arrival time of a GPR measurement using a straight-ray approximation (e.g., Galagedara et al. (2002)) or a full-waveform inversion (e.g.,Appendix D). Second, a petrophysical relationship is used to convert ε to SWC using the empirical Topp's equation(Topp et al., 1980) or a more advanced dielectric mixing model Roth et al. (1990). Third, the obtained timelapse SWC data are used in combination with a hydrological model to estimate soil hydraulic parameters using inverse modelling. However, the use of a sequential inversion strategy may cause errors in the estimated soil hydraulic parameters when errors due to simplified geophysical data interpretations propagate into the estimated soil hydraulic parameters. An example of a potential source for such errors is the use of the straight-wave approximation for the travel path of the electromagnetic waves (Rucker and Ferré, 2004). To overcome this problem, a coupled inversion strategy can be used (Hinnell et al., 2010, Lambot et al., 2006). In contrast to sequential inversion, a coupled inversion links a hydrological model directly with a forward model of the geophysical data, and the mismatch between measured and modelled geophysical response is minimized (i.e. first arrival time or even the full waveform in the case of GPR). In doing so, the soil hydraulic parameters used in the hydrological model can be optimized, while error propagation is avoided. The coupled inversion approach relies heavily on an accurate forward hydrological model. A wrong conceptualization of the subsurface in terms of layering or processes not adequately captured by the hydrological model (e.g., dual porosity or macropore flow) will introduce errors that propagate into the estimated parameters.

A range of studies have employed off-ground GPR, surface GPR, and vertical borehole GPR measurements for estimating soil hydraulic properties from time-lapse SWC information by using either a sequential or a coupled inversion approach (e.g., Busch et al. (2013), Chen et al. (2001, 2004), Jadoon et al. (2012), Jaumann and Roth (2018), Jonard et al. (2015), Kowalsky et al. (2005), Lambot et al. (2009), Rucker and Ferré (2004)). Compared to these GPR acquisition strategies, horizontal borehole GPR measurements have several advantages to reveal the temporal and spatial SWC variations at the field plot scale. Firstly, horizontal

borehole GPR measurements can provide SWC information at specific depths and thus have larger penetration depth and better control on vertical resolution compared to off-ground and surface GPR. Secondly, horizontal borehole GPR measurements provide a higher lateral spatial representativeness of the field plot compared to vertical borehole GPR measurements. However, no studies have been conducted yet that use horizontal borehole GPR measurements to parameterize a hydrological model. In this study, the performance of both sequential and coupled inversion workflows to obtain soil hydraulic properties from time-lapse horizontal borehole GPR data obtained during an infiltration event will be compared. To systematically study the differences between the two inversion approaches, a synthetic modelling experiment will be presented first. In a second step, actual horizontal borehole GPR measurements will be inverted using a coupled inversion approach. The resulting estimates of the hydraulic parameters will be compared to available independent hydraulic property estimates obtained from TDR measurements.

F-2 Material and methods

F-2-1 Test site and GPR data acquisition

An infiltration experiment was carried out on a bare soil plot at a rhizotron facility in Selhausen, Germany. In this facility, three plots (7 × 3 m) were established with different treatments (natural rain, rainsheltered, and irrigated). GPR access tubes of 7 m length were horizontally installed at 0.1, 0.2, 0.4, 0.6, 0.8, and 1.2 m depth across the entire length of the plot. The soil in the facility originates from fluvial gravel deposits from the Rur river system and is characterized as an Orthic Luvisol with high stone content (>50%) and a loamy texture (Table F.1). Due to tillage activity, soil porosity ϕ changes from 0.33 cm^3 cm^{-3} near the surface to approximately 0.25 cm^3 cm^{-3} below 0.3 m depth. In order to install the GPR access tubes, the entire plot was dug out and refilled layer-wise. Therefore, no pedogenetic horizons are detectable anymore below the plough horizon. No clear pedogenetic layers are detectable in the gravely layers of the natural soil either. For more information about the rhizotron facility, the reader is referred to Cai et al. (2016) and Appendix D. The infiltration

Table F.1: Soil texture of fine soil, mass fraction of stones and porosity of the field according to Cai et al. (2016).

Depth cm	Sand Mass %	Silt	Clay	Stones	Porosity cm^3 cm^{-3}
Topsoil (0–30)	35	52	13	50	0.33
Subsoil (30 – 120)	37	47	16	69	0.25

experiment consisted of five infiltration events that were carried out at the rain-sheltered plot during a 4-day period Kelter et al. (2018). The experimental set-up, GPR data acquisition, and GPR data analysis were reported in (Yu et al., 2020) in detail. Therefore, only a short summary is provided here. Water was infiltrated using a drip irrigation system that was supplied by water from an underground tank at a constant rate (0.03 cm min^{-1}. Approximately 2.7 cm of water was applied for each infiltration event of 90 min (Figure F.1a). ZOP surveys were made using a GPR system (PulseEKKO, Sensors & Software, Canada) with 200 MHz borehole antenna. GPR measurements were made at six depths (0.1, 0.2, 0.4, 0.6, 0.8 and

1.2 m) before and after infiltration events. During the infiltration events, GPR measurements were restricted to the boreholes at 0.1, 0.2 and 0.4 m depth as the SWC was expected to increase mainly at shallow depths at the beginning of each infiltration event. For each ZOP survey, the transmitter and receiver were first pushed to the end of the borehole (7 m) and then pulled simultaneously throughout the boreholes in 0.05 m steps. The survey ended at 1.5 m distance from the access trench to avoid that reflections from the trench wall and installed sensors interfered with the direct waves.

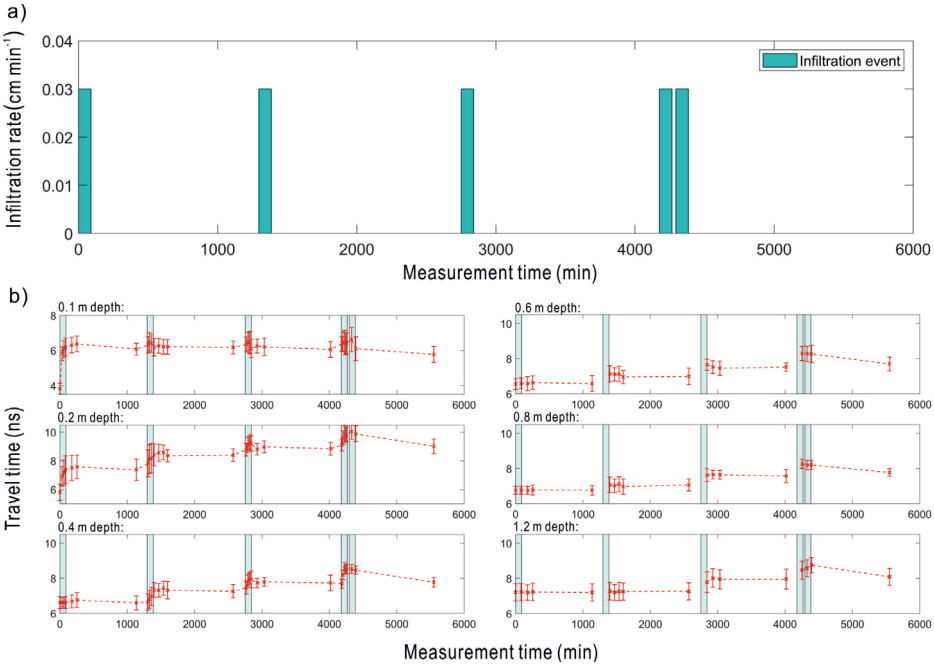

Figure F.1: (a) Schedule and amount of irrigated water for the five infiltration events and (b) GPR travel time data measured at 6 different depths during the infiltration experiment. The timing of the infiltration events was indicated by light green background. The spatial variation of the travel times along the 5.5 m borehole tube is indicated by the error bars. Note that different y-axis scales are used for the results of different depths. (For interpretation of the references to colour in this figure legend, the reader is referred to the web version of this article.)

The development of the mean GPR travel time at different depths is shown in Figure F.1b. To determine the GPR travel time from the ZOP data, the time-zero offset (T0) and first arrival time (t_{obs}) of the direct wave were determined using the strategy proposed in Appendix D. In this strategy, T0 was determined from wide angle reflection and refraction (WARR) measurements with the borehole antennae in air and t_{obs} was manually picked for each trace. GPR travel times measured at 0.1 and 0.2 m depth increased after the first infiltration event. In response to the second infiltration event, travel times up to a depth of 0.8 m responded to the infiltration. After the third infiltration event, the travel times increased at

all depths. The standard deviation of the travel times is also shown in in Figure F.1b, which illustrates the spatial variability along the 5.5 m borehole tubes that were generated by the expected differences in the irrigation rate of the used dripping system and smallscale lateral water content variations caused by the heterogeneity of the soil. Based on the straight-ray approximation and independent of SWC, the observed ± 0.5 ns for the standard deviation of the travel time would lead to an uncertainty of ± 0.025 $cm^3 cm^{-3}$ for SWC.

Based on the known distance between the horizontal boreholes (d = 0.75 m), a 1D dielectric permittivity profile (ε^{obs}) can be calculated from the measured GPR travel times using:

$$\varepsilon^{obs} = \left(\frac{c * (t^{obs}) - T_0}{d} \right)^2 \tag{F-1}$$

where c is the speed of light in vacuum (0.3 m ns^{-1}). SWC (θ_{obs}) was calculated from ε^{obs} using the complex refractive index model (CRIM) (Roth et al., 1990):

$$\theta^{obs} = \frac{\sqrt{\varepsilon^{obs}} - (1 - \Phi)\sqrt{\varepsilon_s} - \Phi}{\sqrt{\varepsilon_w} - 1} \tag{F-2}$$

where ε_w is the permittivity of water (84 at 10°C), Φ is the porosity of the respective layer, and ε_s is the permittivity of the solid soil fraction, which was assumed to be 4.7 for this facility, as considered in Appendix D. This value was also suggested by Robinson et al. (2005) for soil with high quartz content, as is the case for this facility.

F-2-2 Hydrological modelling

Vertical SWC dynamics during the infiltration experiment were simulated using HYDRUS 1D Šimůnek et al. (2008), which calculates one-dimensional variably-saturated water flow by solving the Richards equation:

$$\frac{\partial \theta}{\partial t} = \frac{\partial}{\partial z} \left[K(h) \left(\frac{\partial h}{\partial z} + 1 \right) \right] \tag{F-3}$$

where h is the pressure head (cm), θ is the volumetric water content (cm3 cm^{-3}), t is time (min), z refers to the positive upward spatial coordinate (cm), and K is the hydraulic conductivity (cm min^{-1}) as a function of h. $\theta(h)$ is the water retention function described by the van Genuchten model Van Genuchten (1980):

$$\theta(h) = \begin{cases} \theta_r + \frac{\theta_s - \theta_r}{(1 + |\alpha h|^n)^m} & , \ h < 0 \\ \theta_s & , \ h \geq 0 \end{cases}$$

where θ_r is the residual water content (cm3 cm^{-3}), θ_s is the saturated water content (cm3 cm-3), α (cm^{-1}) is the inverse of the air-entry value, n is the pore-size distribution index (-)

and m is related to n by m=1-1/n . The unsaturated hydraulic conductivity $K_r(h)$ is given by:

$$K_r\ (h) = K_s\ S_e^l \left[1 - \left(1 - S_e^{\left(\frac{1}{m}\right)}\right)^m\right]^2 \tag{F-5}$$

$$S_e = \frac{\theta - \theta_r}{\theta_s - \theta_r} \tag{F-6}$$

where K_s (cm min^{-1}) is the saturated hydraulic conductivity, S_e (-) is the effective saturation governed by Eq. 6 and l (-) is the tortuosity, which is generally set to 0.5 but can also be estimated for individual soils (e.g., Schaap and Leij, 2000). Using this Mualem – van Genuchten parameterization (Mualem, 1976, Van Genuchten, 1980), the soil hydraulic properties are described by five parameters (i.e. K_s, θ_s, θ_r, α, and n).

For the simulation of vertical SWC dynamics, the model domain was set to be 150 cm deep and was discretized with 151 nodes with an equal spacing of 1 cm. Simulations were initialized using linearly interpolated SWC estimates from measured permittivity obtained from borehole GPR data acquired prior to the first infiltration event. Evaporation and root water uptake were both neglected in the simulation, as evaporation was low with respect to the amount of infiltrated water and the soil was bare. An atmospheric boundary condition with surface run-off was used to represent the irrigation events at the upper boundary of the domain. At the lower boundary of the domain, a seepage face ($h = 0$) was used. The use of a seepage face was required to match SWC observations and avoid excessive drainage out of the profile, which occurred when a free drainage boundary condition was used. A physical explanation for the need to use a seepage face may be the presence of a compacted soil layer directly below the rhizotron facility caused by the construction of the facility. As an alternative to the use of a seepage face, a longer soil profile with a dense layer with low K_s could have been used. However, this would have made the hydrological simulations computationally more demanding, especially in the case of the coupled inversion.

F-2-3 GPR modeling

The gprMax3D model was used to simulate GPR wave propagation with a Finite-Difference Time-Domain (FDTD) numerical method Giannopoulos (2005), Warren et al. (2016). The size of the simulation domain for the gprMax3D simulation was set to 2 x 1.1 x 2.2 m, including a soil of 1.5 m thickness below an air layer of 0.7 m. The 3D domain was discretized with nodes with 0.02 m spacing and perfectly matched layers (PML) were used at the boundaries of the model domain (Berenger, 1994). The center frequency of the antenna was set to 200 MHz (i.e. the center frequency of the antenna) and the first derivative of a Gaussian waveform was selected as the excitation function for the current source. As we only considered the velocity information for the GPR data interpretation, the electric conductivity of the soil was assumed to be zero.

F-2-4 Set-up for sequential and coupled inversion

To estimate hydraulic parameters from horizontal borehole GPR measurements, both sequential and coupled inversion strategies were used. The general set-ups of the two inversion

strategies are illustrated in Figure F.2a and Figure F.2b. A key difference between the two approaches is that the sequential inversion approach directly optimizes the misfit between the SWC obtained from the GPR measurements (θ^{obs}) and the simulated SWC (θ^{mod}) provided by HYDRUS-1D, whereas the coupled inversion optimizes the misfit between the travel time of the measured GPR data (t^{obs}) and the simulated travel time (t^{mod}) obtained with gprMax3D using SWC information (θ^{mod}) provided by HYDRUS-1D. The misfits for the sequential and coupled inversions were described using cost functions based on the root-mean-square error (RMSE) between observed and simulated data:

$$C_{MVG}(\theta) = \sqrt{\frac{\sum_{i=1}^{n} \left(\theta_i^{mod} - \theta_i^{obs}\right)^2}{n}} \tag{F-7}$$

$$C_{MVG}(t) = \sqrt{\frac{\sum_{i=1}^{n} \left(t_i^{mod} - t_i^{obs}\right)^2}{n}} \tag{F-8}$$

where n is the number of GPR measurements.

In order to minimize these cost functions, the Shuffled Complex Evolution (SCE-UA) algorithm introduced by Duan et al. (1993) was used. SCE-UA is a global optimization algorithm that not only has been widely used in hydrological research (e.g., Chu et al. (2010), Thyer et al. (1999)) but also in geophysical applications (e.g., Liu et al. (2018), Mangel et al. (2017)). The SCE-UA algorithm requires the specification of parameter bounds for each parameter considered in the optimization. The optimization includes several steps. First, different sets of hydraulic parameters are randomly created in the feasible parameter space and the cost function value for each of these parameter sets is calculated. Second, the parameter sets are sorted in order of their cost function value and distributed into several complexes that are subsequently evolved using the competitive complex evolution (CCE) algorithm (Duan et al., 1994). After this first loop of evolution, the complexes are merged again into a single population, which again is sorted in order of increasing cost function value and divided into complexes for the next optimization loop. The algorithm is considered to be converged if the cost function valued reaches a specified value (i.e. the known error of the data) or if the improvement in the best model is below 0.01% in the last 10 evolution loops.

Since no GPR measurements were made in dry soil conditions, the inversion is not expected to be sensitive to θ_r. In order to build an independent hydrological model based on GPR measurement, θ_r was fixed it to 0 for the inversion and only K_s, θ_s, α, and n were estimated. K_s was inverted by using its log-transform ($\log(K_s)$). The algorithms for both sequential and coupled inversion were coded in GNU Octave (Eaton, 2012).

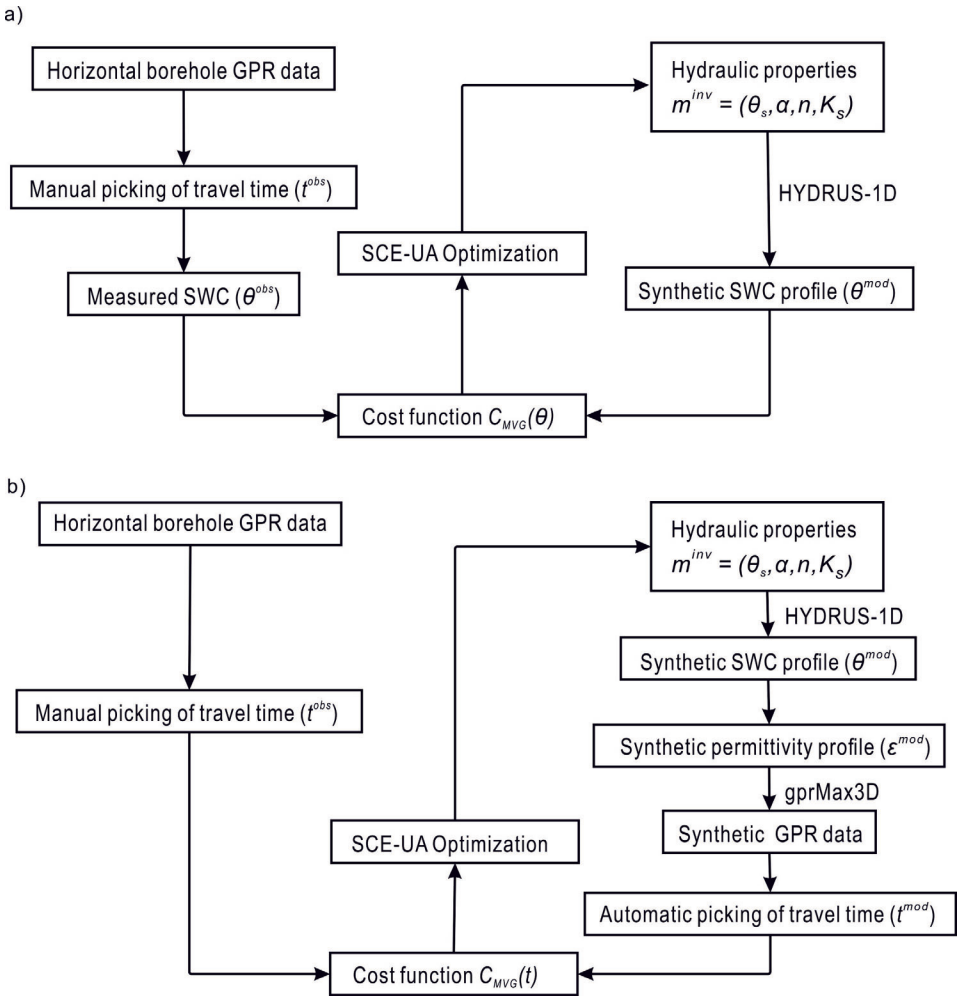

Figure F.2: Flow charts of (a) sequential inversion and (b) coupled inversion.

F-2-5 Set-up for synthetic infiltration experiments

Set-up for a 1-layer soil profile

Synthetic model experiments were performed to gain further insight into the feasibility of obtaining plausible parameter estimates from sequential and coupled inversion of time-lapse borehole GPR data. In a first model experiment, a 1-layer soil profile was considered. We used the soil hydraulic parameters for the top soil (0 - 30 cm) determined by Cai et al. (2018b), which were estimated from TDR measurements at the same depths as the GPR access tubes (Table F.2). In order to generate synthetic data for the model experiments, five infiltration events were simulated with an infiltration rate of 0.03 cm min^{-1}, which corresponds with the infiltration rate used in the actual field experiment. Since the 1-layer soil profile was constructed using the hydraulic parameters of the topsoil (higher θ_s), the amount of applied water was increased in the synthetic modelling experiment. In particular, the first three irrigation events now lasted 400 min whereas the last two infiltration events still lasted 90 min. After obtaining the SWC profile (θ_{mod}) from HYDRUS-1D, a dielectric permittivity profile (ε^{mod}) was calculated using the rearranged form of the CRIM model given in Eq. 2:

$$\varepsilon^{mod} = \left[(\sqrt{\varepsilon_w} - 1) \cdot \theta^{mod} + (1 - \phi) \cdot \sqrt{\varepsilon_s} + \phi\right]^2 \tag{F-9}$$

This dielectric permittivity profile was then used to simulate GPR measurements for the six depths using gprMax3D.

Table F.2: Soil hydraulic parameters according to Cai et al. (2018) for the rhizotron facility.

Depth	θ_r	θ_s	α	n	K_s	l
cm	cm^{3}cm^{-3}	cm^{3}cm^{-3}	cm^{-1}	-	cm min^{-1}	-
0–30	0.043	0.326	0.036	1.386	0.057	1.47
30 - 120	0.053	0.229	0.050	1.534	0.0004†; 0.04††	-2.78

† The K_s value of subsoil estimated by Cai et al. (2018).

†† The K_s value used for synthetic study of 2-layer soil profile.

Set-up for a 2-layer soil profile

A synthetic modelling experiment with a 2-layer soil profile was also performed. Sequential and coupled inversions for the 2-layer soil profile were conducted based on the infiltration schedule of the actual experiment (Figure F.1a). The hydraulic parameters in this second experiment were also based on Cai et al. (2018b) However, the saturated hydraulic conductivity of the subsoil (K_{s2}) was changed from 0.0004 cm min^{-1} reported by Cai et al. (2018b) to 0.04 cm min^{-1}, because it had to be larger than the infiltration rate of 0.03 cm min^{-1} to avoid ponding of water at the layer interface. For a more realistic synthetic modelling study, Gaussian noise with zero mean and a standard deviation of 0.1 ns and 0.01 cm3 cm-3 was added to the synthetic travel times and SWC data, respectively, for both the 1-layer and the 2-layer model.

Automatic picking of the first arrival time

The implementation of the coupled inversion approach requires an automatic picking of the first arrival time. For the simulated GPR data, the first arrival time can be automatically determined using an amplitude threshold. To obtain this threshold, the excitation moment (T_s) of the simulated data was determined from the onset of the source wavelet. The source wavelet is defined as the first derivative of the Gaussian waveform:

$$I = -2\zeta\sqrt{e^{\frac{1}{2\zeta}}}e^{-\zeta(t-\chi)^2}(t-\chi) \tag{F-10}$$

where $\zeta = 2\pi^2 f^2$ and $\chi = 1/f$, I is the electric current density (A m^{-2}), e is the natural logarithm, and f is the center frequency of the antenna (200 MHz). From this source wavelet, a T_s of 1.62 ns was manually determined (Figure F.3a). Subsequently, an air wave was simulated using antennas positioned at 0.1 m above the ground surface (Figure 3b). With the known propagation velocity in air (0.3 m ns^{-1}) and the antenna separation (0.75 m), the true travel time of the air wave is 2.5 ns. The appropriate amplitude threshold (0.0158 V m^{-1}) was then determined from the amplitude of the simulated air wave at the travel time of 4.12 ns, which is the sum of T_s (1.62 ns) and true travel time of the air wave (2.5 ns).

To verify the robustness of the automatic first arrival time determination, a synthetic infiltration-induced SWC profile was generated by HYDRUS-1D (Figure F.3c) and ZOP measurements were simulated using gprMax3D at different depths. The amplitude threshold of 0.0158 V m^{-1} was used to determine the first arrival time (Figure F.3d). It was found that the amplitude of the traces rapidly increased after the determined first arrival time, which confirms the robustness of automatic procedure for the determination of the first arrival time.

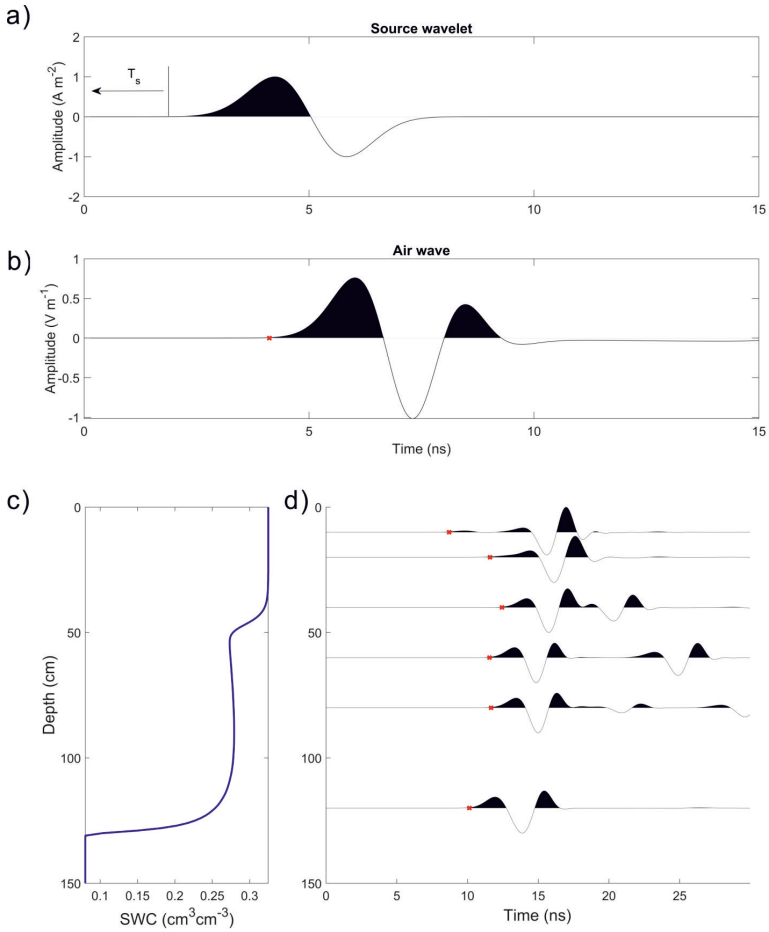

Figure F.3: (a) The source wavelet. (b) A synthetic trace of air wave generated by gprMax3D. (c) A synthetic vertical SWC profile generated by HYDRUS-1D. (d) Six synthetic GPR traces obtained using the synthetic vertical SWC distribution shown in (c). The red crosses indicate the first arrival time of the GPR traces. (For interpretation of the references to colour in this figure legend, the reader is referred to the web version of this article.)

F-2-6 Uncertainty Analysis

Proper quantification of uncertainty in the estimated soil hydraulic parameters is of great importance given that the information content of soil water content measurements for the estimation of soil hydraulic properties depends on the initial and boundary conditions during the experiment (Mboh et al., 2011). In this study, we used both response surface analysis Toorman et al. (1992) and a simple first-order approximationKool and Parker (1988), Kuczera and Mroczkowski (1998), Vrugt and Dane (2005) to investigate the uncertainty of the inverted hydraulic parameters.

Response surfaces provide a 2D view of the cost function distribution obtained with a grid search. In order to obtain such surfaces, two hydraulic parameters (e.g., α and n) are varied between defined bounds, whereas the other hydraulic parameters (e.g., $\log(K_s)$ and θ_s) are fixed at their true (or optimized) value. Response surfaces are a robust method to visualize parameter uncertainty and the minimum of the cost function. However, they commonly require a high computational effort, especially in the case of many model parameters (i.e. the 2-layer model). Therefore, this method was only used for the synthetic model study with a 1-layer soil profile.

A classic first-order approximation of parameter uncertainty was also used (Vrugt and Dane, 2006). It is based on the covariance matrix (C) of the optimized hydraulic parameters, which is calculated by:

$$C = s^2(J^T J)^{-1} \tag{F-11}$$

where s^2 is the error variance between simulated and observed data and J is the Jacobian matrix. The Jacobian matrix is the first-order partial derivative of the cost function for each inverted hydraulic parameter and was obtained using a finite difference approach. The marginal posterior distribution of the estimated hydraulic parameters (m_{est}) is assumed to be a multivariate normal distribution ($N(m_{est}, C)$). The uncertainty of the estimated hydraulic parameters can be approximated by the confidence interval for a given level (i.e. 99%) of significance calculated from the diagonal elements of C. A matrix (A) that provides the correlation between the estimated hydraulic parameters can be obtained by dividing the elements of C with the square root of the diagonal elements of C:

$$A_{ij} = \frac{C_{ij}}{C_{ii}^{1/2} C_{jj}^{1/2}} \tag{F-12}$$

This first-order approximation is an efficient way for estimating the uncertainty of the estimated hydraulic parameters for linear or nearly linear hydrologic models and the correlation matrix is a useful indicator of parameter correlation (Zhu and Mohanty, 2003). If the hydrological model is highly non-linear, the first-order approximation may be unreliable. Therefore, we only focus on A_{ij} values larger than 0.6 in our analysis.

F-3 Results and Discussion

F-3-1 Synthetic infiltration experiments

The simulated vertical SWC profiles at times where GPR measurements were obtained are shown in Figure F.4 for the synthetic modelling study with a 1-layer soil. It can be seen that the infiltration front moved down to 0.6 and 1.2 m depth after the first and second infiltration event, respectively. After the third infiltration event, the entire soil profile was saturated. Because of the high saturation after the third infiltration event, the infiltration front moved rapidly downward through the entire soil profile during infiltration events 4 and 5. The SWC estimates obtained from the first-arrival time of simulated horizontal borehole GPR measurements using a straight-wave approximation are also shown in Figure F.4b. It was found that SWC estimates obtained from GPR measurements at shallow depth ($0 - 0.2$ m) and near the infiltration front underestimated the actual SWC (Figure F.4b and F.4c). This is attributed to the interference of the direct wave with critical refractions generated at the air – soil interface and the infiltration front where the dielectric permittivity changes sharply (Rucker and Ferré, 2004a). For this reason, horizontal borehole GPR measurements at 0.1 m depth were previously not considered for SWC estimation (Appendix D). In the synthetic study, these data were also not used in the sequential inversion to reduce this interpretation error. Unfortunately, errors in SWC estimates near the infiltration front cannot be simply identified and eliminated and thus are expected to affect the estimated hydraulic parameters obtained with the sequential inversion approach. For the coupled inversion, the effect of the air-soil interface is considered in the simulation of GPR wave propagation and therefore there is no need to remove the measurement at 0.1 m depth. However, the information content with respect to the soil hydraulic properties is expected to be limited for these measurements because of the limited travel path length in the topsoil.

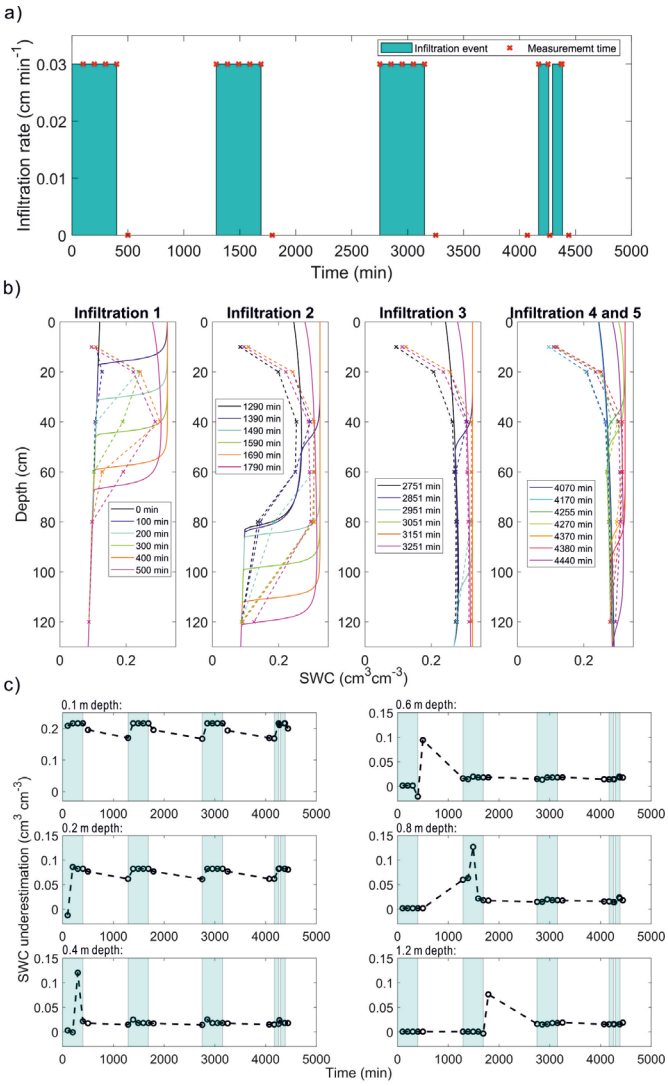

Figure F.4: (a) Schedule of the synthetic infiltration events and synthetic GPR measurements. (b) Synthetic vertical SWC profiles from HYDRUS-1D (solid lines) and synthetic vertical SWC profiles estimated by GPR data (dashed lines) based on the vertical water content distribution used as inputs in gprMax3D. The colors indicate different measurement times. The GPR estimated SWCs at 0.2 – 1.2 m depth were inverted using a sequential inversion approach to estimate the hydraulic parameters for the 1-layer soil. (c) Differences between GPR-estimated and simulated HYDRUS-1D SWCs. The timing of the infiltration events is indicated by the light green background. Note that different y-axis scales are used for the results of different depths.

Response surfaces for the 1-layer soil profile

Figure F.5a presents the response surface based on true SWC data that would be obtained using point measurements (i.e. TDR) at the same depth as the borehole GPR measurements. The corresponding response surfaces for the noise-free coupled inversion of the synthetic GPR data are shown in Figure F.1b. It can be seen that the cost functions for point and GPR measurements have a very similar misfit distribution. This is not unexpected given that point and GPR measurements provide a similar type of information, albeit with a different sampling volume (Appendix D). The response surfaces can be used to gain insight in the expected parameter uncertainty. In the case of the α parameter, the response surfaces for n- α, θ_r-α, and θ_s-α indicate that changes in the cost function are parallel to the α axis. This suggests that the α parameter is independent from the other parameters. Although a clear minimum in the cost function value can be observed in these three surfaces, it is also elongated in the direction of the α axis suggesting that the α parameter is expected to be less constrained in the inversion results compared to the other model parameters. According to the response surfaces for θ_s-n and θ_s- $\log(K_s)$, estimates of θ_s are expected to be correlated with the estimates of n and $\log(K_s)$. In the vicinity of the global minimum, the response surface is almost perpendicular to the θ_s axis and steep, which suggests that θ_s estimates are well-constrained during inversion. The global minimum in the response surface between $\log(K_s)$ and n is positioned in an elongated valley. A strong negative correlation between the parameter estimates for $\log(K_s)$ and n is thus expected, which implies that the GPR measurements may not contain sufficient information to simultaneously constrain both $\log(K_s)$ and n.

Inversion results for the 1-layer soil profile

Sequential and coupled inversions were performed using noisy simulated GPR measurements for the 1-layer soil profile. In the case of the sequential inversion, the fitted SWC data showed a large misfit with the expected SWC (Figure F.6a), particularly for the shallow depths (0.2 m). This is also reflected in the large cost function value (0.05 cm3 cm^{-3}) for the optimized parameters, which is much higher than the added uncertainty in the SWC data (0.01 cm3 cm^{-3}). Additionally, the SWC profiles simulated by using the estimated parameters from the sequential inversion showed large deviation with the SWC profiles from the true forward model (Figure F.7a). Due to the poor fit to the data, the hydraulic parameters were not accurately estimated by the sequential inversion (Table F.2). In particular, θ_s was strongly underestimated and this resulted in a large mismatch between the inverted and true water retention curves (Figure F.8a). Moreover, the estimated value for K_s was at the lower boundary of the feasible parameter space (0.035 cm min^{-1}), which is almost equal to the infiltration rate. The n and α parameters were also overestimated, which resulted in a large difference between the inverted and true relative hydraulic conductivity function (Figure F.8b). As detailed above, sequential inversion of ZOP data may lead to erroneous estimates of hydraulic parameters if strong vertical gradients in SWC are present (e.g. infiltration-induced gradients).

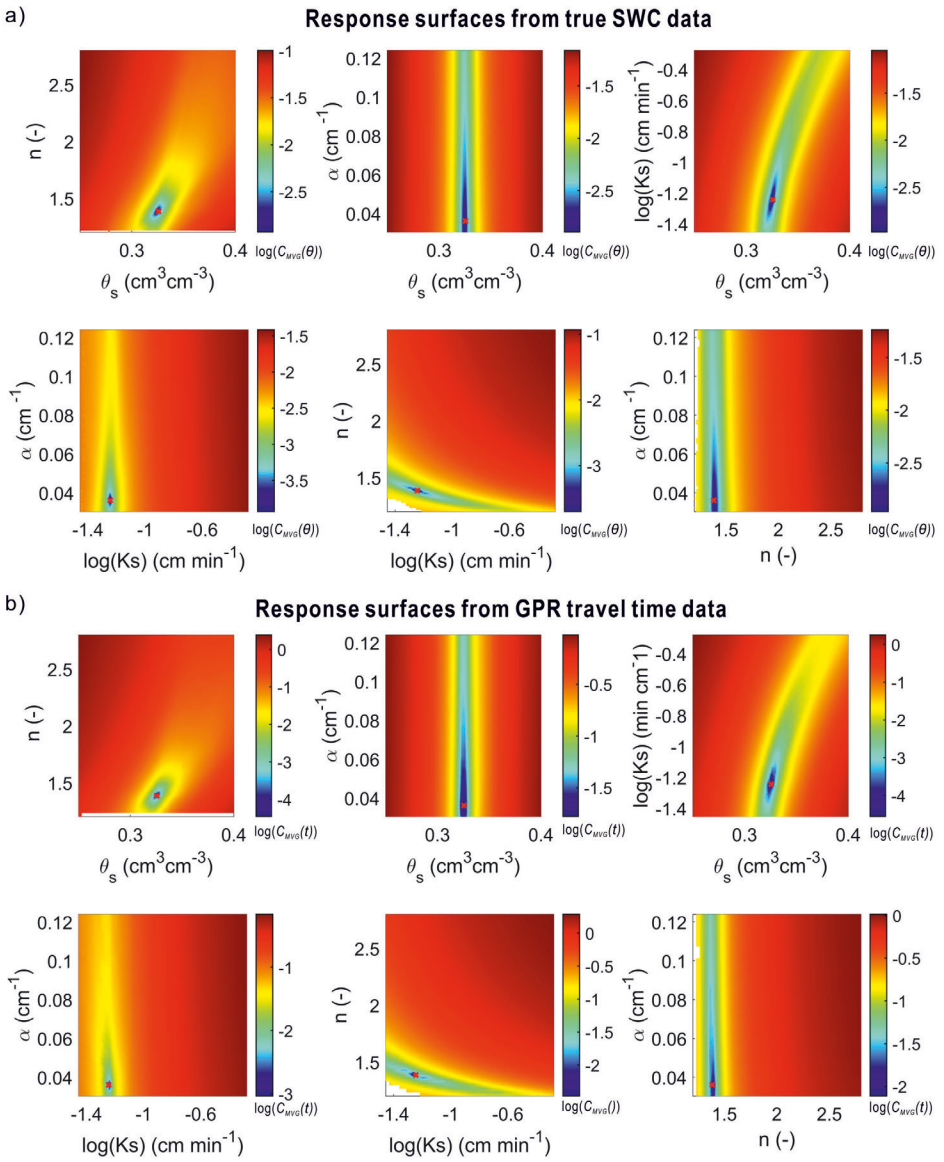

Figure F.5: Response surfaces for different pairs of hydraulic parameters obtained using (a) true SWC data simulated by HYDRUS-1D and (b) noise-free synthetic GPR travel times. The cost function values are shown in logarithmic scale. Blank spaces indicate that the hydrological model did not converge for the selected parameters. The global minimum of the cost function is shown by the red cross. Also note that the cost functions of sequential and coupled inversion ($C_{MVG}(\theta)$ and $C_{MVG}(t)$) have different units (cm3cm^{-3} and ns, respectively).

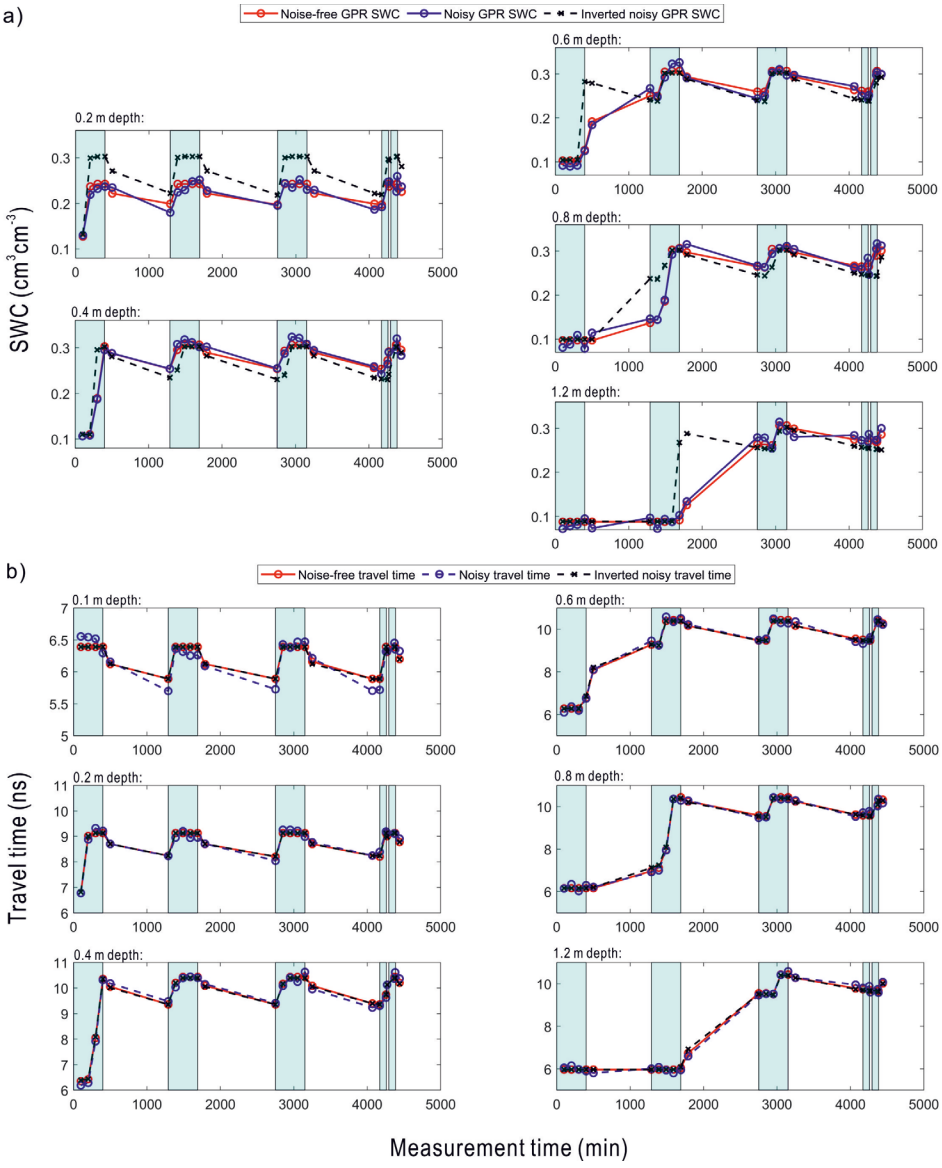

Figure F.6: (a) Sequential inversion results of noisy GPR SWC estimations. (b) Coupled inversion results of noisy GPR travel time data. SWC data at 0.1 m depth was not used for sequential inversion. The timing of the infiltration events is indicated by the light green background. Note that different y-axis scales are used to show the results for different depths.

In the case of the parameters estimated from coupled inversion, the simulated travel time fitted the known travel time from the true model well (Figure F.8b) as expressed by the low RMSE of 0.1 ns. Also, the simulated SWC profiles matched well the SWC profiles from the true model (Figure F.7a). It should be noted that the coupled inversion was ended when the cost function value decreased to the standard deviation of the Gaussian noise (0.1 ns) (Table F.3) to avoid overfitting. Therefore, the data simulated with the inverted model parameters have the same RMSE as the noise-free data and the simulated travel times based on the inverted parameters also match well with the noise-free data.

Table F.3: Inverted results of noisy synthetic data.

	True value	Bounds	Inverted results	
			Sequential inversion	Coupled inversion
homogenous soil profile				
$\theta_s (cm^3 cm^{-3})$	0.326	0.25-0.40	0.290	0.326 ± 0.001†
$\alpha (cm^{-1})$	0.036	0.030-0.125	0.106	0.036 ± 0.003
n (-)	1.386	1.1–2.8	1.431	1.358 ± 0.016
$\log(K_s)$ (cm min^{-1})	-1.244	-1.456– -0.276	-1.456	-1.168 ± 0.038
Cost-function	-	-	0.05	0.1
2-layer soil profile				
$\theta_{s1} (cm^3 cm^{-3})$	0.326	0.30-0.40	0.345	0.324 ± 0.007
$\alpha_1 (cm^{-1})$	0.036	0.030-0.125	0.036	0.036 ± 0.004
$n_1 (-)$	1.386	1.1-2.8	1.506	1.312 ± 0.024
$\log(K_{s1})$ (cm min^{-1})	-1.244	-1.456– -0.276	-0.276	-0.996 ± 0.048
$\theta_{s2} (cm^3 cm^{-3})$	0.229	0.15-0.30	0.300	0.240 ± 0.007
$\alpha_2 (cm^{-1})$	0.050	0.030-0.125	0.038	0.045 ± 0.004
$n_2 (-)$	1.534	1.1-2.8	1.696	1.431 ± 0.020
$\log(K_{s2})$ (cm min^{-1})	-1.398	-1.456- -0.276	-1.456	-1.108 ± 0.048
Cost-function	-	-	0.01	0.1

The values indicated the 99% confidence interval based on the first-order approximation.

The values for θ_s and α were accurately estimated by coupled inversion (Table F.3). However, the estimated values for n and $\log(K_s)$ showed a slight deviation from the true model, likely because of the strong correlation between these two parameters. The accurate estimation of the hydraulic parameters is also reflected in the good match between the estimated and known water retention and relative hydraulic conductivity function (Figure F.8a, F.8b). The first-order uncertainty estimates for the coupled inversion are presented in Table F.3 and the associated correlation matrix of the estimated hydraulic parameters is given in Table F.4. The results indicate a strong negative correlation for $\log(K_s)$ - n and weak correlations between other pairs of hydraulic parameters. This is consistent with the results of the response surface analysis and confirms that the first-order approximation provides a meaningful assessment of parameter uncertainty.

Table F.4: Correlation matrix of the estimated hydraulic parameters for the homogeneous profile.

	α cm^{-1}	n -	logK_s cm min^{-1}	θ_s cm^{3}cm^{-3}
n	-0.335	1		
logK_s	0.233	-0.694†	1	
θ_s	-0.086	0.256	0.186	1

The values indicated the pairs of parameters showing strong correlation.

Inversion results for the 2-layer soil profile

In a next step, the synthetic modelling study for the two-layer soil profile was analyzed. As expected from the results of the 1-layer soil profile, the parameters estimated using sequential inversion deviated considerably from the true hydraulic parameters (Table F.3) and the estimated and true water retention (Figure F.8c, F.8e) and relative hydraulic conductivity functions did not match well (Figure F.8d, F.8f). Hence, sequential inversion will not be considered for the analysis of the actual field measurements.

The results of the coupled inversion for the 2-layer soil profile generally were consistent with the results of the 1-layer profile, despite the dimensional expansion of the search space from four to eight parameters. Again, the estimated travel times from coupled inversion results nicely fitted the noisy synthetic travel time series (Figure F.9) and the vertical SWC profiles from the true model (Figure F.7b). In addition, accurate hydraulic parameter estimates were obtained (Table F.3), as also confirmed by the minor differences in estimated and true water retention (Figure F.8c, F.8e) and relative hydraulic conductivity functions (Figure F.8d, F.8f).

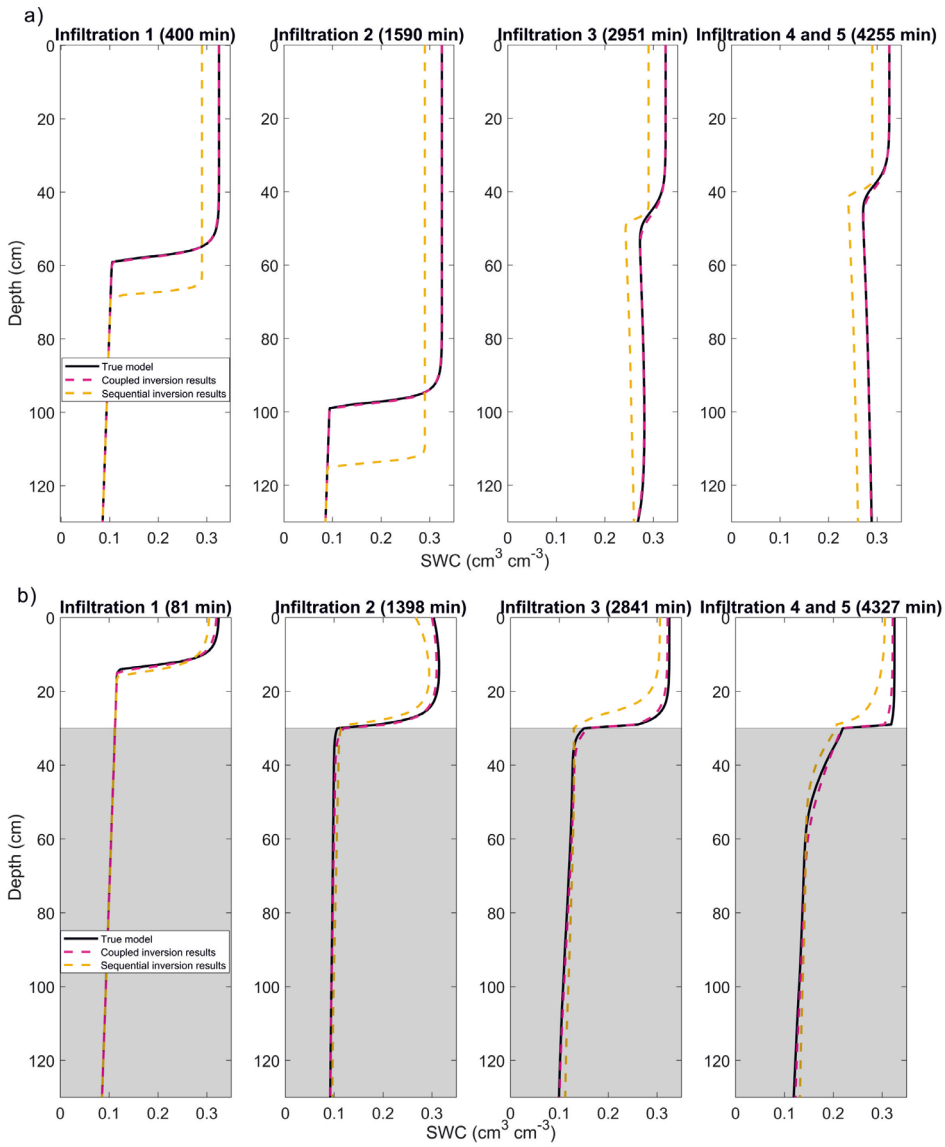

Figure F.7: Vertical SWC profiles of the (a) 1-layer and (b) 2-layer soil profile, which were simulated by using the true model (black solid line), parameters estimated from the coupled inversion (purple dashed line) and sequential inversion (yellow dashed line) at four different measurement times. Note that the different background indicates the different layers.

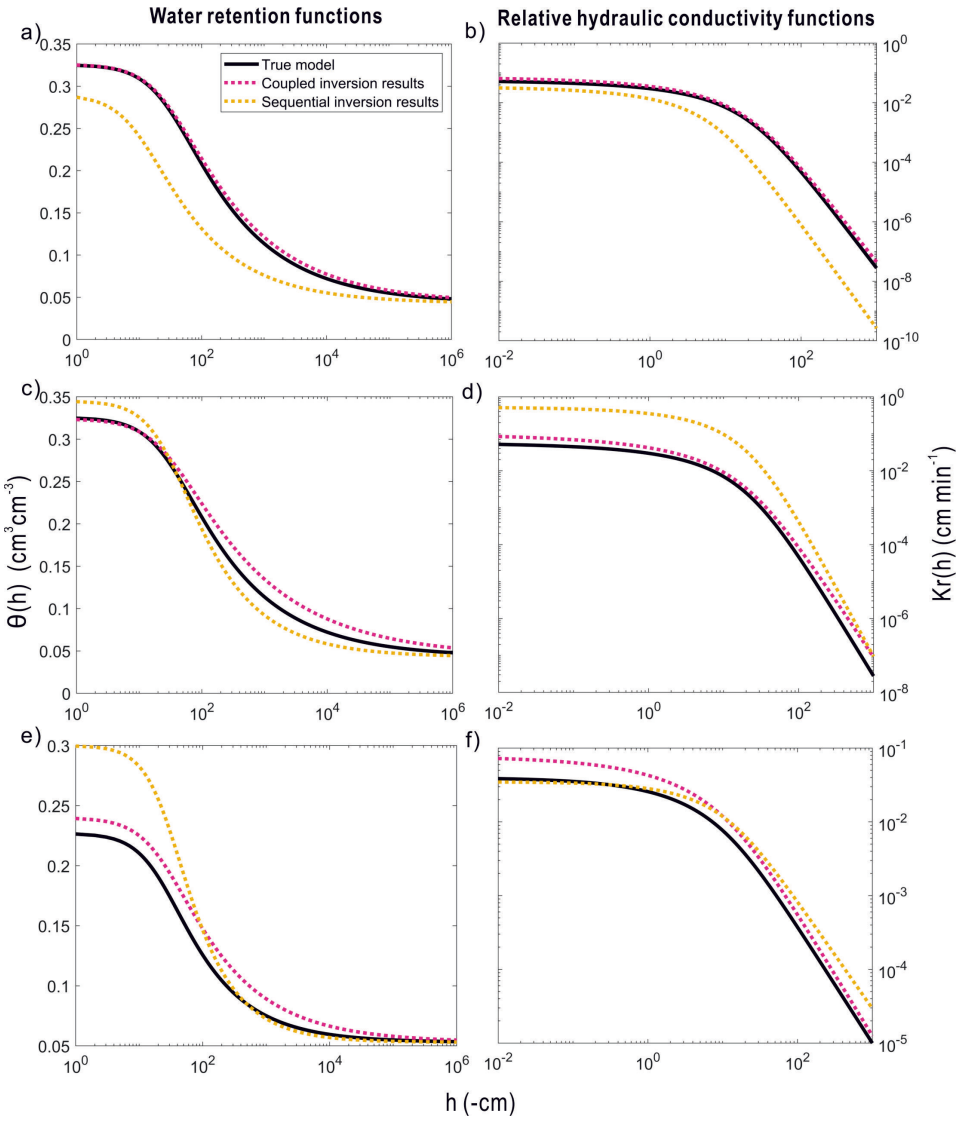

Figure F.8: Figure F.8. Water retention $\theta(D)$ and relative hydraulic conductivity $K_r(h)$ function for the (a,b) synthetic homogeneous soil profile, and the (c,d) topsoil and (e,f) subsoil of the 2-layer profile..

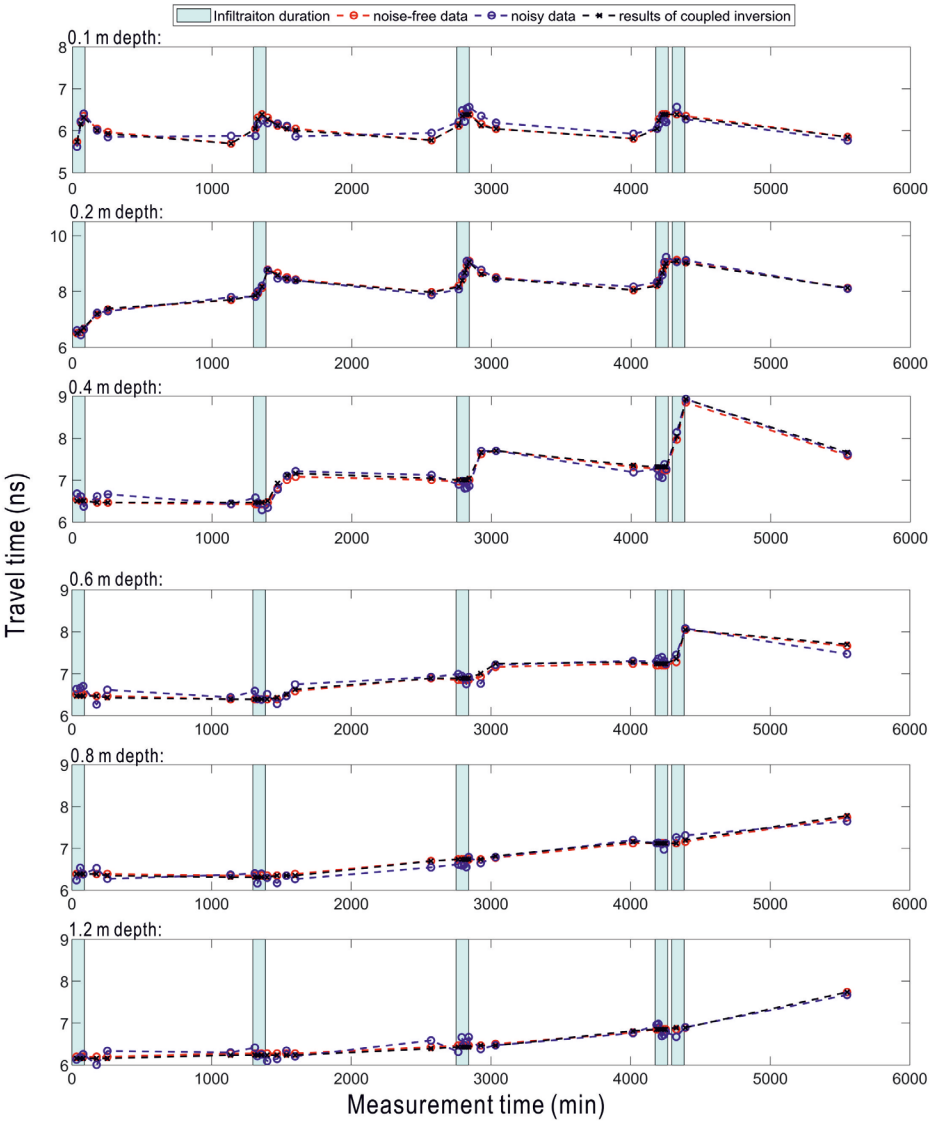

Figure F.9: Coupled inversion results of noisy GPR travel time data for 2-layer profile. The timing of the infiltration events is indicated by the light green background. Please note that results for different depths are shown with difference range of y-axis scale.

F-3-2 Inversion of experimental GPR data

Coupled inversion was used to estimate the hydraulic parameters from the measured horizontal borehole GPR data shown in Figure F.10. The resulting fit to the measured data is also shown in Figure F.10 and the estimated soil hydraulic parameters are provided in Table F.5. For comparison, the simulated data using the hydraulic parameters of Cai et al. (2018b) are also provided, which are based on long-term TDR measurements also made during vegetation periods. The comparison between measured and simulated travel times showed a good correspondence at 0.1 m depth both for the inverted hydraulic parameters and the parameters from Cai et al. (2018b) (Figure F.10). For 0.2 m depth, the measured GPR travel times steadily increased during the entire infiltration experiment, whereas the simulated travel times using both sets of hydraulic parameters remained constant after the second infiltration event because the soil reached saturation. This can be explained by the heterogeneous nature of the topsoil, which is supported by the large spatial variation of the GPR travel time data. For the subsoil, the key features of the measured time-lapse GPR data were well captured by the coupled inversion, also considering the spatial variability in the measured GPR data. The simulated travel time data based on the hydraulic parameters of Cai et al. (2018b) did not match the observed GPR data well in the subsoil (i.e. at 0.6, 0.8, and 1.2 m depth). This is attributed to the small K_{s2} used in Cai et al. (2018b), which results in a slow movement of the infiltration front in the subsoil (Figure F.11), and therefore, a reduced variation in simulated water content at large depths.

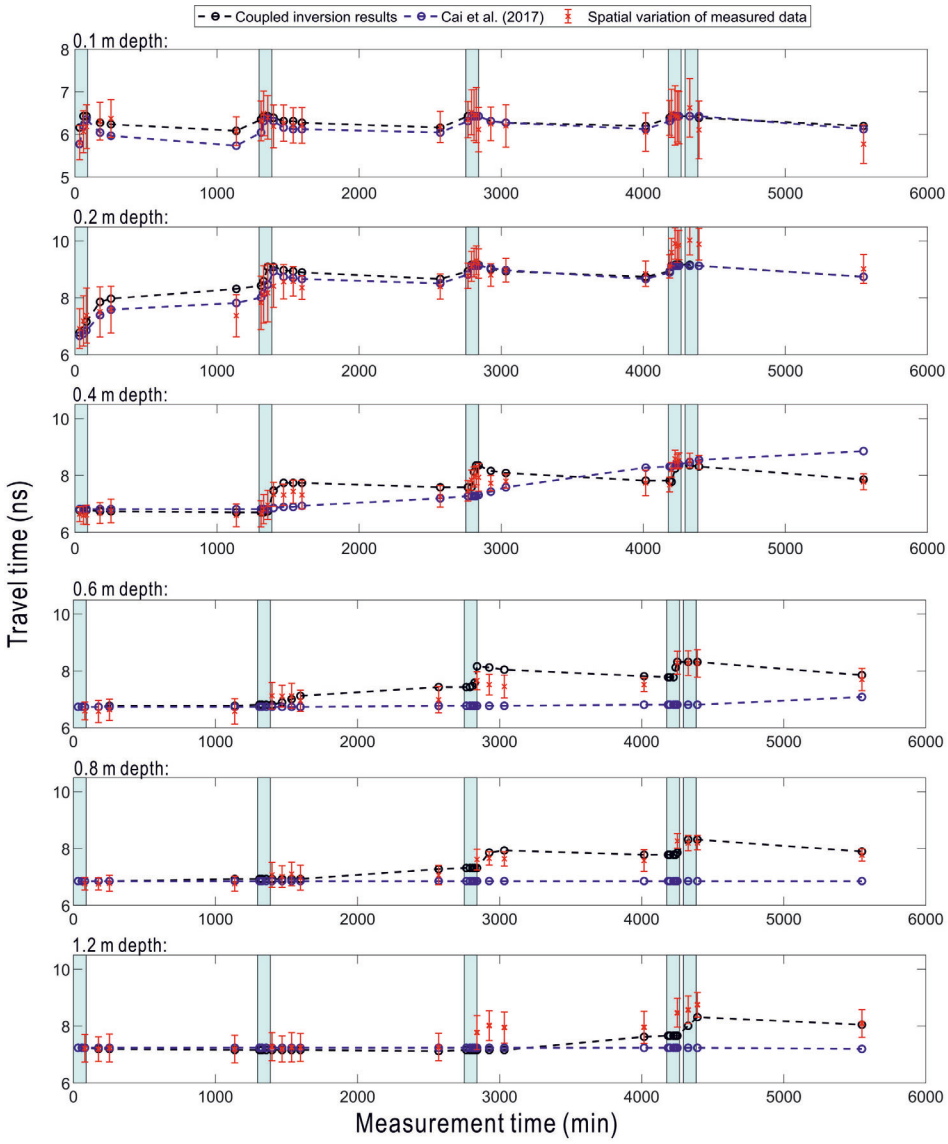

Figure F.10: Figure 10. Coupled inversion results of measured GPR travel time data at different depths. Simulated travel time using the hydraulic parameters of Cai et al. (2017) and inverted model are shown in blue and black dashed lines, respectively. The timing of infiltration events is indicated by the light green background. Please note that different y-axis scales are used for the results at different depths.

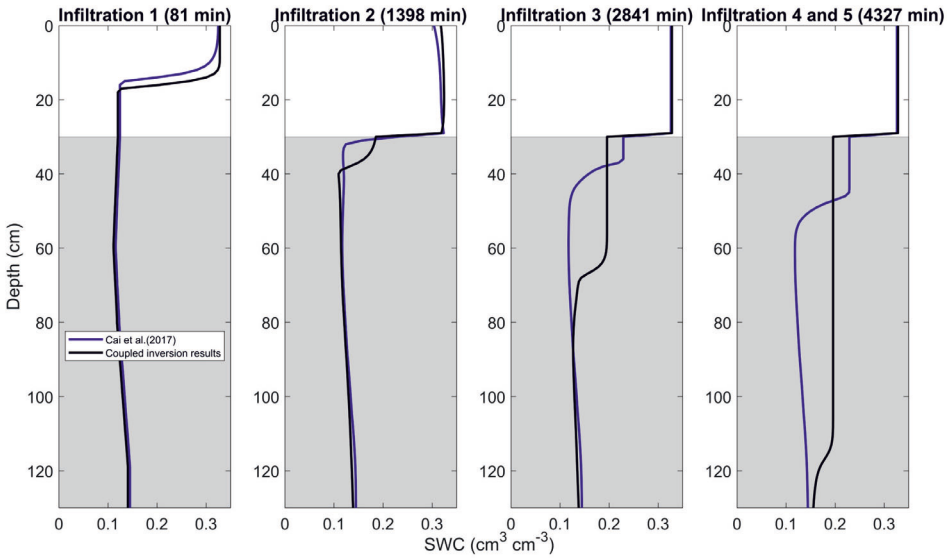

Figure F.11: Vertical SWC profiles simulated by using hydraulic parameters from the inversion of measured data (black lines) and Cai et al. (2018b) (blue lines). Note that the different backgrounds indicate the different soil types.

Table F.5: Inverted Soil hydraulic parameters for the rhizotron facility from measured GPR data.

Depth	θ_r	θ_s	α	n	$\log K_s$	l
cm	$cm^3 cm^{-3}$	$cm^3 cm^{-3}$	cm^{-1}	-	$cm\ min^{-1}$	-
[cost-function = 0.32 (ns)]						
0–30	0	0.328 ± 0.011†	0.032 ± 0.011	1.125 ± 0.028	-0.983 ± 0.266	0.5
30 – 120	0	0.196 ± 0.009	0.038 ± 0.015	1.202 ± 0.054	-1.022 ± 0.349	0.5

† The values indicated the 99% confidence interval based on the first-order approximation.

Measured and inverted GPR travel time data are directly compared in Figure F.12. The use of the hydraulic parameters from Cai et al. (2018b) clearly resulted in a systematic underestimation of the measured data and a relatively high RMSE of 0.43 ns. The hydraulic parameters obtained using coupled inversion better matched the measured travel time data, as indicated by the lower RMSE (0.32 ns) and a higher R2 value (0.90). Nevertheless, the RMSE between inverted and measured GPR data is still relatively large. This is partly attributed to the heterogeneity of the topsoil, as the measurements at 0.2 m depth make up a considerable part of the observed misfit. Furthermore, there is uncertainty in the initial SWC profile, which is solely based on GPR measurements at six different depths. Here, extrapolation from the shallowest borehole to the soil surface is problematic, and may have introduced some degree of uncertainty. Finally, there is intrinsic uncertainty in the field GPR measurements and data processing, such as the uncertainty in the position of the horizontal boreholes and the uncertainty in the determination of the time-zero or first arrival time of measured GPR data. These issues obviously did not affect the coupled inversion in the synthetic case study but they are highly relevant for the inversion of actual field measurements.

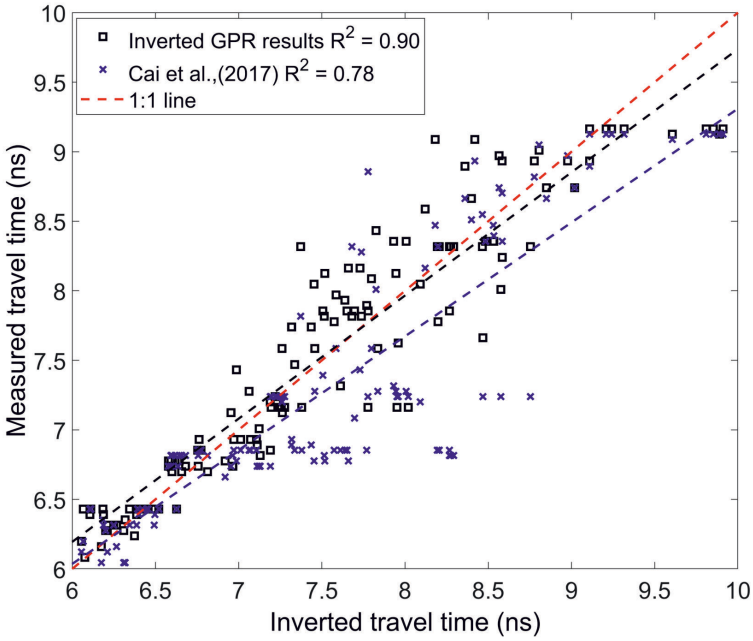

Figure F.12: Linear regression between measured and GPR travel time data obtained using the inverted hydraulic parameters (black squares) and the hydraulic parameters of Cai et al. (2017) (blue crosses). The 1:1 line is indicated by the dashed red line.

Table F.6: Correlation matrix of the inverted hydraulic parameters for the 2-layer model.

	α_1 cm^{-1}	n_1 -	logK_{s1} cm min^{-1}	α_2 cm^{-1}	n_2 -	logK_{s2} cm min^{-1}	θ_{s1} cm^{3}cm^{-3}	θ_{s2} cm^{3}cm^{-3}
n_1	-0.388	1						
logK_{s1}	0.324	0.045	1					
α_1	-0.077	0.129	0.138	1				
n_2	-0.119	-0.139	-0.163	-0.069	1			
logK_{s2}	0.061	-0.059	-0.046	0.549	-0.615†	1		
α_2								
θ_{s1}	-0.032	-0.226	0.189	0.040	-0.087	0.049	1	
θ_{s2}	-0.058	-0.347	-0.192	-0.083	0.404	0.070	-0.192	1

The values indicated the pairs of parameters showing strong correlation.

The results of the first-order uncertainty estimation of the inverted hydraulic parameters are provided in Table F.5. The uncertainty of α and θ_s are comparable for the top- and subsoil, whereas n and log(K_s) showed a larger uncertainty for the subsoil. This can be explained by the strong negative correlation (A = -0.615) between n_2 and log(K_{s2}) (Table F.5). All other pairs of hydraulic parameters did not show strong correlations. Figure F.13 presents the water

retention and relative hydraulic conductivity functions obtained using coupled inversion. The associated uncertainty was obtained by randomly plotting 100 sets of hydraulic parameters drawn from the uncertainty bounds provided in Table F.5. As can be seen from the uncertainty bounds, θ_s is associated with a relatively low uncertainty, whereas the n value is associated with a larger uncertainty as indicated by the increasing spread of the functions at lower pressure heads. Furthermore, uncertainty in the water retention function is similar for the top- and subsoil (Figure F.13a, F.13c). For comparison, the functions based on the hydraulic parameters of Cai et al. (2018b) were also provided. The water retention function obtained using coupled inversion clearly deviated from that of Cai et al. (2018b), which showed a faster decrease of water content with matric potential due to the larger n value. Additionally, a lower θ_s was estimated by the coupled inversion.

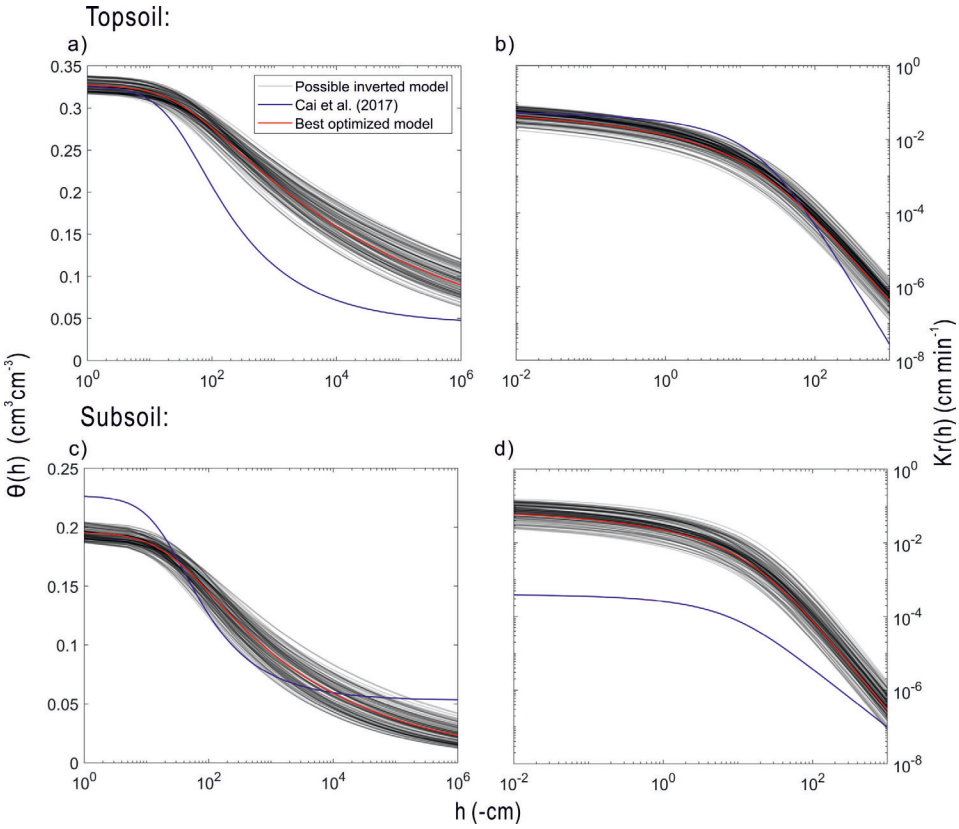

Figure F.13: Water retention $\theta(h)$ and relative hydraulic conductivity $K_r(h)$ function from 100 possible inverted hydraulic parameter sets (dark lines), the hydraulic parameters of Cai et al. (2018b) (blue line) and the hydraulic parameters with the best fit (red line) for the (a, c) top soil and (b, d) subsoil.

The hydraulic conductivity functions obtained using coupled inversion also showed a similar

uncertainty for the top- and subsoil (Figure F.13b, F.3d). For the topsoil, the hydraulic conductivity function obtained using coupled inversion corresponded well with the function obtained in Cai et al. (2018b). This is at least partly due to the similarity in the inverted K_s obtained in this study and in Cai et al. (2018b). However, there are obvious differences in the hydraulic conductivity functions for the subsoil due to differences in estimated K_s. There is a range of possible explanations for the observed differences. First, the estimation of K_s is known to be scale-dependent. For example, laboratory methods using small sample volumes often lead to lower K_s compared to estimates from in-situ measurement from a larger soil volume (Busch et al., 2013, Rovey and Cherkauer, 1995). The results of Cai et al. (2018b) were based on TDR measurement that only cover a small areal fraction of the rhizotron facility, whereas the GPR measurements represent a larger volume (Appendix D). Thus, a higher K_s is perhaps expected for the GPR measurements since the importance of preferential flow in macropores likely increased from the TDR to the GPR scale. The analysis presented here also indicated potential parameter correlations between K_s and n. Since larger n values were reported by Cai et al. (2018b), this may explain the small K_s values. It is also important to note that Cai et al. (2018b) estimated hydraulic parameters with a more complex model set-up that considered root water uptake. In particular, root water uptake parameters were estimated alongside the hydraulic parameters, which might have hampered the correct estimation of the soil hydraulic parameters and likely increased the uncertainty in the estimated hydraulic parameters obtained by Cai et al. (2018b). Finally, it is important to note that Cai et al. (2018b) assumed free drainage as a lower boundary condition whereas a seepage face was used in this study.

F-4 Summary and Conclusions

In this study, we used both sequential and coupled inversion strategies to estimate hydraulic parameters from horizontal borehole GPR measurements during an infiltration experiment. First, a synthetic modelling study was set-up to compare the two inversion approaches independent of measurement and model errors. In a noise-free synthetic study using a 1-layer soil profile, a response surface analysis was used to evaluate correlation between hydraulic parameters. The results showed that the hydraulic parameters n and $\log(K_s)$ were strongly correlated, which implies that the GPR measurements were not able to simultaneously constrain $\log(K_s)$ and n. In a next step, synthetic SWC and travel time data with added noise were used to estimate hydraulic parameters using sequential and coupled inversion approaches, respectively. It was observed that a sequential inversion approach relying on the conventional straight-ray approximation to estimate SWC did not provide accurate hydraulic parameter estimates if strong vertical gradients in SWC were present due to infiltration. The coupled inversion approach, which combined 3D modelling of GPR measurements with a 1D vadose zone flow model, was able to provide accurate estimates of the hydraulic parameters both for a 1-layer and a 2-layer soil profile because interpretation errors associated with the straight-ray approximation were avoided. In a final step, horizontal borehole GPR measurements made during an infiltration experiment were inverted using a coupled inversion approach. The estimated hydraulic parameters were reasonably consistent with water retention and relative hydraulic conductivity functions reported by Cai et al. (2018b) for the same site.

In conclusion, the coupled inversion of horizontal borehole GPR measurements provided accurate field-scale estimates of soil hydraulic parameters. Because of the larger sampling volume compared to point sensors, the estimated hydraulic parameters are expected to have an improved field representativeness. In future studies, coupled inversion of horizontal borehole GPR data may be used to estimate 2D and perhaps even 3D distributions of soil hydraulic parameters by considering all measured travel times over the profile, although this will obviously be associated with a higher computational effort. A disadvantage of the proposed approach is that GPR measurements are still taken manually and are thus time-consuming, whereas point sensors often allow automated data acquisition. As an alternative to GPR, other geophysical methods such as ERT can also be employed to estimate hydraulic parameters. ERT can investigate the subsurface with high resolution, and data acquisition can be automated. However, the electrical conductivity distribution obtained with ERT is not only sensitive to SWC but also depends on several other factors (e.g., clay content, pore water salinity) (Binley et al., 2015). This can complicate vadose zone model parameterization using ERT measurements considerably. It would be interesting to extend coupled inversion by considering the full GPR waveform instead of solely using travel time information, as was recently proposed for seismic data by Li et al. (2020). It is expected that this would increase the information content of the GPR measurements in the inversion, and therefore reduce uncertainty in the estimated hydraulic parameters and provide chances to estimate hydraulic properties of multi-layer soils.

Acknowledgements

My deepest gratitude goes to Prof. Dr. Anja Klotzsche and Prof. Dr. Andrea Schnepf, for making this doctoral project possible and for giving me the opportunity to complete it. I am very grateful for their guidance, support, motivation, persistent encouragement and professional and personal leadership. Over the past 3.5 years they put an enormous amount of time in the development of this dissertation. Every discussion, explanation and clarification of complex topics, advice on analysis, articles and presentations was very much appreciated.

Further, I would like to thank Prof. Dr. Harry Vereecken, Prof. Dr. Jan Vanderborght and Prof. Dr. Jan van der Kruk for their scientific guidance and insights throughout this project and their comments, suggestions and reviews of the different articles. I am very grateful to Dr. Lutz Weihermüller, for his patience and willingness to answer every question.

This work was been funded by the German Research Foundation under Germany's Excellence Strategy, EXC-2070 - 390732324 - PhenoRob. I am very grateful to have been part in this Cluster of Excellence and the contribution it made to my doctoral project by the financial support of workshops, seminar, travel opportunities and the building of a scientific community to exchange with peers and to make lasting connections.

I acknowledge the support by the SFB/TR32 "Pattern in Soil–Vegetation–Atmosphere Systems: Monitoring, Modelling, and Data Assimilation" funded by the Deutsche Forschungsgemeinschaft (DFG). Furthermore, I thank the Terrestrial Environmental Observatories (TERENO) for support at the test site and for the meteorological data.

The sequential hydrogeophysical inversion simulations in Chapter 5 were performed with computing resources granted by RWTH Aachen University under project rwth0620. The numerical study in Chapter 4, I gratefully acknowledge computing time on the supercomputer JURECA at Forschungszentrum Jülich under grant no. cjicg41.

I thank Normen Hermes, Moritz Harings, Tim Spieker, Dino Schmitz, Christopf Tempelmann and Anika Sommerfeld-Vreux for the cooperation, support, and maintenance of the

minirhizotron facilities and all the student assistants for their tremendous effort to acquire all the data. Additionally, I am grateful to Werner Küpper, Philipp Meulendick, Rainer Harms, Bernd Schilling and other technicians at IBG-3 for their support during field work campaigns. I thank Jan Rödder for his help in the data analysis and programming.

I am very grateful for the time at Forschungszentrum Jülich and the IBG-3 and having the opportunity the meet other doctoral students and scientist. I would like to thank the Multiscale Geophysics of soil-plant systems with Jessica Schmäck, Peleg Haruzi, Dominik Hoven and Sophia Schiebel. Further I would like to thank the ROSI group with Felix Bauer, Mona Giraud, Magdlena Landl, Tobias Selzner, Ullah Sibghat and Larissa Reineccius and the Phenorob PhDs Matthias Class, Jordan Bates, Rajina Bajracharya, Valentin Michels and Philipp Festhauer. Not only the scientific exchange but also the friendships made are very much appreciated.

Finally I would like thank my parents, sister and friends and especially my partner Pierre for their persistent support and encouragement.

Aachen Lena Lärm
July 22, 2024

Bibliography

Abbaspour, K., Kasteel, R., and Schulin, R. (2000). Inverse parameter estimation in a layered unsaturated field soil. *Soil Science*, 165(2):109–123.

Aggarwal, P. (1995). Uncertainties in crop, soil and weather inputs used in growth models: Implications for simulated outputs and their applications. *Agricultural Systems*, 48(3):361–384.

Akaike, H. (1974). A new look at the statistical model identification. *IEEE Transactions on Automatic Control*, 19(6):716–723.

Akinsunmade, A., Tomecka-Suchoń, S., and Pysz, P. (2019). Correlation between agrotechnical properties of selected soil types and corresponding GPR response. *Acta Geophysica*, 67(6):1913–1919.

Al Hagrey, A. (2007). Geophysical imaging of root-zone, trunk, and moisture heterogeneity. *J Exp Bot*, 58(4):839–54. Attia Al Hagrey, Said eng Research Support, Non-U.S. Gov't England J Exp Bot. 2007;58(4):839-54. doi: 10.1093/jxb/erl237. Epub 2007 Jan 17.

Alexandros, N., Bruinsma, J., Bodeker, G., Broca, S., and Ottaviani, M. (2012). World agriculture towards 2030/2050. *Food and Agriculture Organization of the United Nations: Rome, Italy*.

Algeo, J., Slater, L., Binley, A., Dam, R. L. V., and Watts, C. (2018). A comparison of ground-penetrating radar early-time signal approaches for mapping changes in shallow soil water content. *Vadose Zone Journal*, 17(1):1–11.

Allen, R. G., Pereira, L. S., Raes, D., and Smith, M. (1998). Fao irrigation and drainage paper no. 56. *Rome: Food and Agriculture Organization of the United Nations*, 56(97):e156.

Allroggen, N., van Schaik, N. L. M., and Tronicke, J. (2015). 4d ground-penetrating radar during a plot scale dye tracer experiment. *Journal of Applied Geophysics*, 118:139–144.

Altdorff, D., von Hebel, C., Borchard, N., van der Kruk, J., Bogena, H. R., Vereecken, H., and Huisman, J. A. (2017). Potential of catchment-wide soil water content prediction using electromagnetic induction in a forest ecosystem. *Environmental Earth Sciences*, 76(3).

Alzubaidi, L., Zhang, J., Humaidi, A. J., Al-Dujaili, A., Duan, Y., Al-Shamma, O., Santamaría, J., Fadhel, M. A., Al-Amidie, M., and Farhan, L. (2021). Review of deep learning: concepts, CNN architectures, challenges, applications, future directions. 8(1).

Anderson, E. (1987). Corn root growth and distribution as influenced by tillage and nitrogen fertilization1. *Agronomy Journal*, 79(3):544–549.

Angers, D. A. and Caron, J. (1998). Plant-induced changes in soil structure:processes and feedbacks. *Biogeochemistry*, 42(1/2):55–72.

Annan, A. P. (2005). *GPR Methods for Hydrogeological Studies*, pages 185–213. Springer Netherlands, Dordrecht.

Araus, J. L. and Cairns, J. E. (2014). Field high-throughput phenotyping: the new crop breeding frontier. *Trends in Plant Science*, 19(1):52–61.

Ardekani, M. R. M. (2013). Off- and on-ground GPR techniques for field-scale soil moisture mapping. *Geoderma*, 200-201:55–66.

Armengaud, P., Zambaux, K., Hills, A., Sulpice, R., Pattison, R. J., Blatt, M. R., and Amtmann, A. (2009). Ez-rhizo: integrated software for the fast and accurate measurement of root system architecture. *The Plant Journal*, 57(5):945–956.

Atkinson, D. (2000). *Root Characteristics: Why and What to Measure*. Springer Berlin Heidelberg, Berlin, Heidelberg.

Atkinson, J. A., Pound, M. P., Bennett, M. J., and Wells, D. M. (2019). Uncovering the hidden half of plants using new advances in root phenotyping. *Current Opinion in Biotechnology*, 55:1–8.

Bagnall, G. C., Koonjoo, N., Altobelli, S. A., Conradi, M. S., Fukushima, E., Kuethe, D. O., Mullet, J. E., Neely, H., Rooney, W. L., Stupic, K. F., Weers, B., Zhu, B., Rosen, M. S., and Morgan, C. L. (2020). Low-field magnetic resonance imaging of roots in intact clayey and silty soils. *Geoderma*, 370:114356.

Barej, J. A. M., Pätzold, S., Perkons, U., and Amelung, W. (2014). Phosphorus fractions in bulk subsoil and its biopore systems. *European Journal of Soil Science*, 65(4):553–561.

Baroni, G., Ortuani, B., Facchi, A., and Gandolfi, C. (2013). The role of vegetation and soil properties on the spatio-temporal variability of the surface soil moisture in a maize-cropped field. *Journal of Hydrology*, 489:148–159.

Bauer, F. M., Lärm, L., Morandage, S., Lobet, G., Vanderborght, J., Vereecken, H., and Schnepf, A. (2022). Development and validation of a deep learning based automated minirhizotron image analysis pipeline. *Plant Phenomics*, 2022:1–14.

Bauer, J., Weihermüller, L., Huisman, J. A., Herbst, M., Graf, A., Séquaris, J. M., and Vereecken, H. (2011). Inverse determination of heterotrophic soil respiration response to temperature and water content under field conditions. *Biogeochemistry*, 108(1-3):119–134.

Beaujean, J., Nguyen, F., Kemna, A., Antonsson, A., and Engesgaard, P. (2014). Calibration of seawater intrusion models: Inverse parameter estimation using surface electrical resistivity tomography and borehole data. *Water Resources Research*, 50(8):6828–6849.

Beff, L., Günther, T., Vandoorne, B., Couvreur, V., and Javaux, M. (2012). Three-dimensional monitoring of soil water content in a maize field using electrical resistivity tomography.

Berenger, J.-P. (1994). A perfectly matched layer for the absorption of electromagnetic waves. *Journal of Computational Physics*, 114(2):185–200.

Besma, Z., Christian, W., Didier, M., Pierre, M. J., and Mohamed, H. (2021). Soil salinization monitoring method evolution at various spatial and temporal scales in arid context: a review. *Arabian Journal of Geosciences*, 14(4).

Bianco, M. D. and Kepinski, S. (2018). Building a future with root architecture. *Journal of Experimental Botany*, 69(22):5319–5323.

Binley, A., Cassiani, G., Middleton, R., and Winship, P. (2002a). Vadose zone flow model parameterisation using cross-borehole radar and resistivity imaging. *Journal of Hydrology*, 267(3-4):147–159.

Binley, A., Hubbard, S. S., Huisman, J. A., Revil, A., Robinson, D. A., Singha, K., and Slater, L. D. (2015). The emergence of hydrogeophysics for improved understanding of subsurface processes over multiple scales. *Water Resources Research*, 51(6):3837–3866. Binley, Andrew Hubbard, Susan S Huisman, Johan A Revil, Andre Robinson, David A Singha, Kamini Slater, Lee D eng Review Water Resour Res. 2015 Jun;51(6):3837-3866. doi: 10.1002/2015WR017016. Epub 2015 Jun 15.

Binley, A., Winship, P., Middleton, R., Pokar, M., and West, J. (2001). High-resolution characterization of vadose zone dynamics using cross-borehole radar. *Water Resources Research*, 37(11):2639–2652.

Binley, A., Winship, P., West, L., Pokar, M., and Middleton, R. (2002b). Seasonal variation of moisture content in unsaturated sandstone inferred from borehole radar and resistivity profiles. *Journal of Hydrology*, 267(3-4):160–172.

Blanchy, G., Virlet, N., Sadeghi-Tehran, P., Watts, C. W., Hawkesford, M. J., Whalley, W. R., and Binley, A. (2020a). Time-intensive geoelectrical monitoring under winter wheat. *Near Surface Geophysics*, 18(4):413–425.

Blanchy, G., Watts, C. W., Ashton, R. W., Webster, C. P., Hawkesford, M. J., Whalley, W. R., and Binley, A. (2020b). Accounting for heterogeneity in the theta-sigma relationship: Application to wheat phenotyping using emi. *Vadose Zone Journal*, 19(1).

Blanchy, G., Watts, C. W., Richards, J., Bussell, J., Huntenburg, K., Sparkes, D. L., Stalham, M., Hawkesford, M. J., Whalley, W. R., and Binley, A. (2020c). Time-lapse geophysical assessment of agricultural practices on soil moisture dynamics. *Vadose Zone Journal*, 19(1).

Blanco-Canqui, H. and Lal, R. (2007). Impacts of long-term wheat straw management on soil hydraulic properties under no-tillage. *Soil Science Society of America Journal*, 71(4):1166–1173.

Bogena, H., Montzka, C., Huisman, J., Graf, A., Schmidt, M., Stockinger, M., von Hebel, C., Hendricks-Franssen, H., van der Kruk, J., Tappe, W., Lücke, A., Baatz, R., Bol, R., Groh,

J., Pütz, T., Jakobi, J., Kunkel, R., Sorg, J., and Vereecken, H. (2018). The TERENO-rur hydrological observatory: A multiscale multi-compartment research platform for the advancement of hydrological science. *Vadose Zone Journal*, 17(1):180055.

Bot, J. L., Serra, V., Fabre, J., Draye, X., Adamowicz, S., and Pagès, L. (2009). DART: a software to analyse root system architecture and development from captured images. *Plant and Soil*, 326(1-2):261–273.

Brogi, C., Huisman, J., Pätzold, S., von Hebel, C., Weihermüller, L., Kaufmann, M., van der Kruk, J., and Vereecken, H. (2019). Large-scale soil mapping using multi-configuration EMI and supervised image classification. *Geoderma*, 335:133–148.

Brogi, C., Huisman, J. A., Weihermüller, L., Herbst, M., and Vereecken, H. (2021). Added value of geophysics-based soil mapping in agro-ecosystem simulations. *SOIL*, 7(1):125–143.

Brosten, T. R., Day-Lewis, F. D., Schultz, G. M., Curtis, G. P., and Lane, J. W. (2011). Inversion of multi-frequency electromagnetic induction data for 3d characterization of hydraulic conductivity. *Journal of Applied Geophysics*, 73(4):323–335.

Brovelli, A. and Cassiani, G. (2011). Combined estimation of effective electrical conductivity and permittivity for soil monitoring. *Water Resources Research*, 47(8).

Brown, A. L. P., Day, F. P., and Stover, D. B. (2008). Fine root biomass estimates from minirhizotron imagery in a shrub ecosystem exposed to elevated CO2. *Plant and Soil*, 317(1-2):145–153.

Brunet, P., Clément, R., and Bouvier, C. (2010). Monitoring soil water content and deficit using electrical resistivity tomography (ERT) – a case study in the cevennes area, france. *Journal of Hydrology*, 380(1-2):146–153.

Buczko, U. and Kuchenbuch, R. O. (2013). Spatial distribution assessment of maize roots by 3d monolith sampling. *Communications in Soil Science and Plant Analysis*, 44(14):2127–2151.

Buczko, U., Kuchenbuch, R. O., and Gerke, H. H. (2008). Evaluation of a core sampling scheme to characterize root length density of maize. *Plant and Soil*, 316(1-2):205–215.

Bui, E. N. and Box, J. E. (1992). Stemflow, rain throughfall, and erosion under canopies of corn and sorghum. *Soil Science Society of America Journal*, 56(1):242–247.

Busch, S., van der Kruk, J., and Vereecken, H. (2014). Improved characterization of fine-texture soils using on-ground GPR full-waveform inversion. *IEEE Transactions on Geoscience and Remote Sensing*, 52(7):3947–3958.

Busch, S., Weihermüller, L., Huisman, J. A., Steelman, C. M., Endres, A. L., Vereecken, H., and van der Kruk, J. (2013). Coupled hydrogeophysical inversion of time-lapse surface GPR data to estimate hydraulic properties of a layered subsurface. *Water Resources Research*, 49(12):8480–8494.

Butnor, J., Roth, B., and Johnsen, K. (2005). Feasibility of using ground-penetrating radar to quantify root mass in florida's intensively managed pine plantations. *Forest Biology Research Cooperative Report# 38. Gainsesville, FL 13 p.*

Butnor, J. R., Barton, C., Day, F. P., Johnsen, K. H., Mucciardi, A. N., Schroeder, R., and Stover, D. B. (2012). Using ground-penetrating radar to detect tree roots and estimate biomass. *Measuring roots: an updated approach*, pages 213–245.

Butnor, J. R., Doolittle, J. A., Johnsen, K. H., Samuelson, L., Stokes, T., and Kress, L. (2003). Utility of ground-penetrating radar as a root biomass survey tool in forest systems. *Soil Science Society of America Journal*, 67(5):1607–1615. 721ec Times Cited:105 Cited References Count:17.

Butnor, J. R., Doolittle, J. A., Kress, L., Cohen, S., and Johnsen, K. H. (2001). Use of ground-penetrating radar to study tree roots in the southeastern united states. *Tree Physiol*, 21(17):1269–78. Butnor, J R Doolittle, J A Kress, L Cohen, S Johnsen, K H eng Canada Tree Physiol. 2001 Nov;21(17):1269-78. doi: 10.1093/treephys/21.17.1269.

Böhm, W. (1978). Untersuchungen zur wurzelentwicklung bei winterweizen.zeitschrift für acker- und pflanzenbau. *147:264–9*.

Cai, G., Morandage, S., Vanderborght, J., Schnepf, A., and Vereecken, H. (2018a). Erratum to "construction of minirhizotron facilities for investigating root zone processes" and "parameterization of root water uptake models considering dynamic root distributions and water uptake compensation". *Vadose Zone Journal*, 17(1):170201.

Cai, G., Vanderborght, J., Couvreur, V., Mboh, C. M., and Vereecken, H. (2017). Parameterization of root water uptake models considering dynamic root distributions and water uptake compensation. *Vadose Zone Journal*, 17(1):1–21.

Cai, G., Vanderborght, J., Klotzsche, A., van der Kruk, J., Neumann, J., Hermes, N., and Vereecken, H. (2016). Construction of minirhizotron facilities for investigating root zone processes. *Vadose Zone Journal*, 15(9):1–13.

Cai, G., Vanderborght, J., Langensiepen, M., Schnepf, A., Hüging, H., and Vereecken, H. (2018b). Root growth, water uptake, and sap flow of winter wheat in response to different soil water conditions. *Hydrology and Earth System Sciences*, 22(4):2449–2470.

Camporese, M., Cassiani, G., Deiana, R., Salandin, P., and Binley, A. (2015). Coupled and uncoupled hydrogeophysical inversions using ensemble kalman filter assimilation of ERT-monitored tracer test data. *Water Resources Research*, 51(5):3277–3291.

Carminati, A., Schneider, C. L., Moradi, A. B., Zarebanadkouki, M., Vetterlein, D., Vogel, H.-J., Hildebrandt, A., Weller, U., Schüler, L., and Oswald, S. E. (2011). How the rhizosphere may favor water availability to roots. *Vadose Zone Journal*, 10(3):988–998.

Cassiani, G., Binley, A., and Ferré, T. P. (2006). Unsaturated zone processes. In *Applied hydrogeophysics*, pages 75–116. Springer.

Cassiani, G., Boaga, J., Rossi, M., Putti, M., Fadda, G., Majone, B., and Bellin, A. (2016). Soil–plant interaction monitoring: Small scale example of an apple orchard in trentino, north-eastern italy. *Science of The Total Environment*, 543:851–861.

Cassiani, G., Ursino, N., Deiana, R., Vignoli, G., Boaga, J., Rossi, M., Perri, M. T., Blaschek, M., Duttmann, R., Meyer, S., Ludwig, R., Soddu, A., Dietrich, P., and Werban, U. (2012).

Noninvasive monitoring of soil static characteristics and dynamic states: A case study highlighting vegetation effects on agricultural land. *Vadose Zone Journal*, 11(3):vzj2011.0195.

Cassidy, N. J. (2009). Electrical and magnetic properties of rocks, soils and fluids. In *Ground Penetrating Radar Theory and Applications*, pages 41–72. Elsevier.

Chanasyk, D. S. and Naeth, M. A. (1996). Field measurement of soil moisture using neutron probes. *Canadian Journal of Soil Science*, 76(3):317–323.

Chen, J., Hubbard, S., and Rubin, Y. (2001). Estimating the hydraulic conductivity at the south oyster site from geophysical tomographic data using bayesian techniques based on the normal linear regression model. *Water Resources Research*, 37(6):1603–1613.

Chen, J., Hubbard, S., Rubin, Y., Murray, C., Roden, E., and Majer, E. (2004). Geochemical characterization using geophysical data and markov chain monte carlo methods: A case study at the south oyster bacterial transport site in virginia. *Water Resources Research*, 40(12).

Chu, W., Gao, X., and Sorooshian, S. (2010). Improving the shuffled complex evolution scheme for optimization of complex nonlinear hydrological systems: Application to the calibration of the sacramento soil-moisture accounting model. *Water Resources Research*, 46(9).

Cimpoiaşu, M. O., Kuras, O., Pridmore, T., and Mooney, S. J. (2020). Potential of geoelectrical methods to monitor root zone processes and structure: A review. *Geoderma*, 365:114232.

Cimpoiaşu, M. O., Kuras, O., Wilkinson, P. B., Pridmore, T., and Mooney, S. J. (2021). Hydrodynamic characterization of soil compaction using integrated electrical resistivity and x-ray computed tomography. *Vadose Zone Journal*, 20(4).

Claes, N., Paige, G. B., Grana, D., and Parsekian, A. D. (2020). Parameterization of a hydrologic model with geophysical data to simulate observed subsurface return flow paths. *Vadose Zone Journal*, 19(1).

Corwin, D. and Lesch, S. (2005). Apparent soil electrical conductivity measurements in agriculture. *Computers and Electronics in Agriculture*, 46(1-3):11–43.

Cox, K., Scherm, H., and Serman, N. (2005). Ground-penetrating radar to detect and quantify residual root fragments following peach orchard clearing. *HortTechnology*, 15(3):600–607.

Cui, X., Chen, J., Shen, J., Cao, X., Chen, X., and Zhu, X. (2010). Modeling tree root diameter and biomass by ground-penetrating radar. *Science China Earth Sciences*, 54(5):711–719.

Cui, X., Zhang, Z., Guo, L., Liu, X., Quan, Z., Cao, X., and Chen, X. (2021). The root-soil water relationship is spatially anisotropic in shrub-encroached grassland in north china: Evidence from GPR investigation. *Remote Sensing*, 13(6):1137.

Dafflon, B., Irving, J., and Barrash, W. (2011). Inversion of multiple intersecting high-resolution crosshole GPR profiles for hydrological characterization at the boise hydrogeophysical research site. *Journal of Applied Geophysics*, 73(4):305–314.

Das, A., Schneider, H., Burridge, J., Ascanio, A. K. M., Wojciechowski, T., Topp, C. N., Lynch, J. P., Weitz, J. S., and Bucksch, A. (2015). Digital imaging of root traits (DIRT): a high-throughput computing and collaboration platform for field-based root phenomics. *Plant Methods*, 11(1).

Davis, J. L. and Annan, A. P. (1989). GROUND-PENETRATING RADAR FOR HIGH-RESOLUTION MAPPING OF SOIL AND ROCK STRATIGRAPHY1. *Geophysical Prospecting*, 37(5):531–551.

Delgado, A., Hays, D. B., Bruton, R. K., Ceballos, H., Novo, A., Boi, E., and Selvaraj, M. G. (2017). Ground penetrating radar: a case study for estimating root bulking rate in cassava (manihot esculenta crantz). *Plant Methods*, 13(1).

Delory, B. M., Weidlich, E. W., Meder, L., Lütje, A., van Duijnen, R., Weidlich, R., and Temperton, V. M. (2017). Accuracy and bias of methods used for root length measurements in functional root research. *Methods in Ecology and Evolution*, 8(11):1594–1606.

do Rosário G. Oliveira, M., van Noordwijk, M., Gaze, S. R., Brouwer, G., Bona, S., Mosca, G., and Hairiah, K. (2000). Auger sampling, ingrowth cores and pinboard methods. In *Root Methods*, pages 175–210. Springer Berlin Heidelberg.

Doetsch, J., Linde, N., and Binley, A. (2010). Structural joint inversion of time-lapse crosshole ERT and GPR traveltime data. *Geophysical Research Letters*, 37(24):n/a–n/a.

Doetsch, J., Linde, N., Vogt, T., Binley, A., and Green, A. G. (2012). Imaging and quantifying salt-tracer transport in a riparian groundwater system by means of 3d ERT monitoring. *GEOPHYSICS*, 77(5):B207–B218.

Dowdy, R., Smucker, A., Dolan, M., and Ferguson, J. (1998). Automated image analysis for separating547 plant roots from soil debris elutriated from soil core. *Plant and Soil*, 200(1):91–94.

Duan, Q., Gupta, V. K., and Sorooshian, S. (1993). Shuffled complex evolution approach for effective and efficient global minimization. *Journal of optimization theory and applications*, 76(3):501–521.

Duan, Q., Sorooshian, S., and Gupta, V. K. (1994). Optimal use of the sce-ua global optimization method for calibrating watershed models. *Journal of hydrology*, 158(3-4):265–284.

Durner, W. (1994). Hydraulic conductivity estimation for soils with heterogeneous pore structure. *Water Resources Research*, 30(2):211–223.

Durner, W. and Lipsius, K. (2005). Determining soil hydraulic properties.

Ehosioke, S., Nguyen, F., Rao, S., Kremer, T., Placencia-Gomez, E., Huisman, J. A., Kemna, A., Javaux, M., and Garré, S. (2020). Sensing the electrical properties of roots: A review. *Vadose Zone Journal*, 19(1).

Entekhabi, D., Njoku, E. G., O'Neill, P. E., Kellogg, K. H., Crow, W. T., Edelstein, W. N., Entin, J. K., Goodman, S. D., Jackson, T. J., Johnson, J., et al. (2010). The soil moisture active passive (smap) mission. *Proceedings of the IEEE*, 98(5):704–716.

Farmani, M. B., Kitterød, N.-O., and Keers, H. (2008). Inverse modeling of unsaturated flow parameters using dynamic geological structure conditioned by GPR tomography. *Water Resources Research*, 44(8).

Feddes, R., Kabat, P., Van Bakel, P., Bronswijk, J., and Halbertsma, J. (1988). Modelling soil water dynamics in the unsaturated zone—state of the art. *Journal of hydrology*, 100(1-3):69–111.

Feddes, R. A., Bresler, E., and Neuman, S. P. (1974). Field test of a modified numerical model for water uptake by root systems. *Water Resources Research*, 10(6):1199–1206.

Ferré, P. A., Knight, J. H., Rudolph, D. L., and Kachanoski, R. G. (1998). The sample areas of conventional and alternative time domain reflectometry probes. *Water Resources Research*, 34(11):2971–2979.

Food and of the United Nations, A. O. (2022). *The future of food and agriculture – Drivers and triggers for transformation*. FAO.

Galagedara, L., Parkin, G., Redman, J., and Endres, A. (2003). Assessment of soil moisture content measured by borehole gpr and tdr under transient irrigation and drainage. *Journal of Environmental & Engineering Geophysics*, 8(2):77–86.

Galagedara, L. W., Parkin, G. W., Redman, J. D., and Endres, A. L. (2002). Temporal and spatial variation of soil water content measured by borehole GPR under irrigation and drainage/title. In Koppenjan, S. and Lee, H., editors, *Ninth International Conference on Ground Penetrating Radar*. SPIE.

Galkovskyi, T., Mileyko, Y., Bucksch, A., Moore, B., Symonova, O., Price, C. A., Topp, C. N., Iyer-Pascuzzi, A. S., Zurek, P. R., Fang, S., Harer, J., Benfey, P. N., and Weitz, J. S. (2012). GiA roots: software for the high throughput analysis of plant root system architecture. *BMC Plant Biology*, 12(1):116.

Garré, S., Coteur, I., Wongleecharoen, C., Kongkaew, T., Diels, J., and Vanderborght, J. (2013). Noninvasive monitoring of soil water dynamics in mixed cropping systems: A case study in ratchaburi province, thailand. *Vadose Zone Journal*, 12(2):vzj2012.0129.

Garré, S., Hyndman, D., Mary, B., and Werban, U. (2021). Geophysics conquering new territories: The rise of "agrogeophysics". *Vadose Zone Journal*, 20(4).

Garré, S., Javaux, M., Vanderborght, J., Pagès, L., and Vereecken, H. (2011). Three-dimensional electrical resistivity tomography to monitor root zone water dynamics. *Vadose Zone Journal*, 10(1):412–424.

Garré, S., Pagés, L., Laloy, E., Javaux, M., Vanderborght, J., and Vereecken, H. (2012). Parameterizing a dynamic architectural model of the root system of spring barley from minirhizotron data. *Vadose Zone Journal*, 11(4):vzj2011.0179.

Ge, X., Ding, J., Jin, X., Wang, J., Chen, X., Li, X., Liu, J., and Xie, B. (2021). Estimating agricultural soil moisture content through UAV-based hyperspectral images in the arid region. *Remote Sensing*, 13(8):1562.

Gerke, H. H. and Kuchenbuch, R. O. (2007). Root effects on soil water and hydraulic properties. *Biologia*, 62(5):557–561.

Ghanbarian-Alavijeh, B., Liaghat, A., Huang, G.-H., and Van Genuchten, M. T. (2010). Estimation of the van genuchten soil water retention properties from soil textural data. *Pedosphere*, 20(4):456–465.

Giannopoulos, A. (2005). Modelling ground penetrating radar by GprMax. *Construction and Building Materials*, 19(10):755–762.

González-Quirós, A. and Comte, J.-C. (2021). Hydrogeophysical model calibration and uncertainty analysis via full integration of PEST/PEST and COMSOL. *Environmental Modelling &amp Software*, 145:105183.

Graf, A., Klosterhalfen, A., Arriga, N., Bernhofer, C., Bogena, H., Bornet, F., Brüggemann, N., Brümmer, C., Buchmann, N., Chi, J., Chipeaux, C., Cremonese, E., Cuntz, M., Dušek, J., El-Madany, T. S., Fares, S., Fischer, M., Foltýnová, L., Gharun, M., Ghiasi, S., Gielen, B., Gottschalk, P., Grünwald, T., Heinemann, G., Heinesch, B., Heliasz, M., Holst, J., Hörtnagl, L., Ibrom, A., Ingwersen, J., Jurasinski, G., Klatt, J., Knohl, A., Koebsch, F., Konopka, J., Korkiakoski, M., Kowalska, N., Kremer, P., Kruijt, B., Lafont, S., Léonard, J., Ligne, A. D., Longdoz, B., Loustau, D., Magliulo, V., Mammarella, I., Manca, G., Mauder, M., Migliavacca, M., Mölder, M., Neirynck, J., Ney, P., Nilsson, M., Paul-Limoges, E., Peichl, M., Pitacco, A., Poyda, A., Rebmann, C., Roland, M., Sachs, T., Schmidt, M., Schrader, F., Siebicke, L., Šigut, L., Tuittila, E.-S., Varlagin, A., Vendrame, N., Vincke, C., Völksch, I., Weber, S., Wille, C., Wizemann, H.-D., Zeeman, M., and Vereecken, H. (2020). Altered energy partitioning across terrestrial ecosystems in the european drought year 2018. *Philosophical Transactions of the Royal Society B: Biological Sciences*, 375(1810):20190524.

Groh J., Luecke A., P. T. (2020). Tereno data from station(s) se y 040 with parameter(s) soilmatrixpotential, soilmatrixpotential, soilmatrixpotential, soilmatrixpotential for time period 2013-10-01 to 2016-08-18.

Grote, K., Hubbard, S., and Rubin, Y. (2003). Field-scale estimation of volumetric water content using ground-penetrating radar ground wave techniques. *Water Resources Research*, 39(11).

Guo, D., Li, H., Mitchell, R. J., Han, W., Hendricks, J. J., Fahey, T. J., and Hendrick, R. L. (2007). Fine root heterogeneity by branch order: exploring the discrepancy in root turnover estimates between minirhizotron and carbon isotopic methods. *New Phytologist*, 177(2):443–456.

Guo, L., Chen, J., Cui, X. H., Fan, B. H., and Lin, H. (2013). Application of ground penetrating radar for coarse root detection and quantification: a review. *Plant and Soil*, 362(1-2):1–23. 059tw Times Cited:63 Cited References Count:52.

Guo, L., Wu, Y., Chen, J., Hirano, Y., Tanikawa, T., Li, W., and Cui, X. (2015). Calibrating the impact of root orientation on root quantification using ground-penetrating radar. *Plant and Soil*, 395(1-2):289–305.

Hampel, F. R. (1974). The influence curve and its role in robust estimation. *Journal of the American Statistical Association*, 69(346):383–393.

Han, E., Smith, A. G., Kemper, R., White, R., Kirkegaard, J. A., Thorup-Kristensen, K., and Athmann, M. (2021). Digging roots is easier with AI. *Journal of Experimental Botany*, 72(13):4680–4690.

Hartmann, A., Goldscheider, N., Wagener, T., Lange, J., and Weiler, M. (2014). Karst water resources in a changing world: Review of hydrological modeling approaches. *Reviews of Geophysics*, 52(3):218–242.

Haruzi, P., Katsman, R., Halisch, M., Waldmann, N., and Spiro, B. (2021). Benchmark study using a multi-scale, multi-methodological approach for the petrophysical characterization of reservoir sandstones. *Solid Earth*, 12(3):665–689.

Hebel, C., Reynaert, S., Pauly, K., Janssens, P., Piccard, I., Vanderborght, J., Kruk, J., Vereecken, H., and Garré, S. (2021). Toward high-resolution agronomic soil information and management zones delineated by ground-based electromagnetic induction and aerial drone data. *Vadose Zone Journal*, 20(4).

Hinnell, A., Ferré, T., Vrugt, J., Huisman, J., Moysey, S., Rings, J., and Kowalsky, M. (2010). Improved extraction of hydrologic information from geophysical data through coupled hydrogeophysical inversion. *Water resources research*, 46(4).

Hinnell, A. C., Ferré, T. P. A., and Warrick, A. W. (2006). The influence of time domain reflectometry rod induced flow disruption on measured water content during steady state unit gradient flow. *Water Resources Research*, 42(8).

Hobley, E., Steffens, M., Bauke, S. L., and Kögel-Knabner, I. (2018). Hotspots of soil organic carbon storage revealed by laboratory hyperspectral imaging. *Scientific Reports*, 8(1):13900.

Holliger, K., Musil, M., and Maurer, H. (2001). Ray-based amplitude tomography for crosshole georadar data: a numerical assessment. *Journal of Applied Geophysics*, 47(3-4):285–298.

Hossne, A. J., Méndez N., J., Leonett P., F. A., Meneses L., J. E., and Gil M., J. A. (2016). Maize root growth under regular water content, subjected to compaction, irrigation frequencies, and shear stress. *Revista Facultad Nacional de Agronomía Medellín*, 69(1):7867–7881.

Hruska, J., Cermak, J., and Sustek, S. (1999). Mapping tree root systems with ground-penetrating radar. *Tree Physiology*, 19(2):125–130.

Hubbard, S., Chen, J., Williams, K., Peterson, J., and Rubin, Y. (2005). Environmental and agricultural applications of gpr.

Hubbard, S. S. and Rubin, Y. (2000). Hydrogeological parameter estimation using geophysical data: a review of selected techniques. *Journal of Contaminant Hydrology*, 45(1-2):3–34.

Huisman, J., Hubbard, S., Redman, J., and Annan, A. (2003). Measuring soil water content with ground penetrating radar. *Vadose zone journal*, 2(4):476–491.

Huisman, J., Rings, J., Vrugt, J., Sorg, J., and Vereecken, H. (2010). Hydraulic properties of a model dike from coupled bayesian and multi-criteria hydrogeophysical inversion. *Journal of Hydrology*, 380(1-2):62–73.

Huisman, J., Snepvangers, J., Bouten, W., and Heuvelink, G. (2002). Mapping spatial variation in surface soil water content: comparison of ground-penetrating radar and time domain reflectometry. *Journal of Hydrology*, 269(3-4):194–207.

Hupet, F., Lambot, S., Feddes, R. A., van Dam, J. C., and Vanclooster, M. (2003). Estimation of root water uptake parameters by inverse modeling with soil water content data. *Water Resources Research*, 39(11).

Hupet, F. and Vanclooster, M. (2002). Intraseasonal dynamics of soil moisture variability within a small agricultural maize cropped field. *Journal of Hydrology*, 261(1-4):86–101.

Hupet, F. and Vanclooster, M. (2005). Micro-variability of hydrological processes at the maize row scale: implications for soil water content measurements and evapotranspiration estimates. *Journal of Hydrology*, 303(1-4):247–270.

Ingram, K. T. and Leers, G. A. (2001). Software for measuring root characters from digital images. *Agronomy Journal*, 93(4):918–922.

Irving, J. and Singha, K. (2010). Stochastic inversion of tracer test and electrical geophysical data to estimate hydraulic conductivities. *Water Resources Research*, 46(11).

Jadoon, K. Z., Weihermüller, L., Scharnagl, B., Kowalsky, M. B., Bechtold, M., Hubbard, S. S., Vereecken, H., and Lambot, S. (2012). Estimation of soil hydraulic parameters in the field by integrated hydrogeophysical inversion of time-lapse ground-penetrating radar data. *Vadose Zone Journal*, 11(4).

Janiesch, C., Zschech, P., and Heinrich, K. (2021). Machine learning and deep learning. *Electronic Markets*.

Jaumann, S. and Roth, K. (2018). Soil hydraulic material properties and layered architecture from time-lapse GPR. *Hydrology and Earth System Sciences*, 22(4):2551–2573.

Jayawickreme, D. H., Dam, R. L. V., and Hyndman, D. W. (2010). Hydrological consequences of land-cover change: Quantifying the influence of plants on soil moisture with time-lapse electrical resistivity. *GEOPHYSICS*, 75(4):WA43–WA50.

Johnson, M., Tingey, D., Phillips, D., and Storm, M. (2001). Advancing fine root research with minirhizotrons. *Environmental and Experimental Botany*, 45(3):263–289.

Jol, H. M. (2009). *Ground Penetrating Radar Theory and Applications*. Elsevier Science.

Jonard, F., Mahmoudzadeh, M., Roisin, C., Weihermüller, L., André, F., Minet, J., Vereecken, H., and Lambot, S. (2013). Characterization of tillage effects on the spatial variation of soil properties using ground-penetrating radar and electromagnetic induction. *Geoderma*, 207-208:310–322.

Jonard, F., Weihermuller, L., Schwank, M., Jadoon, K. Z., Vereecken, H., and Lambot, S. (2015). Estimation of hydraulic properties of a sandy soil using ground-based active and passive microwave remote sensing. *IEEE Transactions on Geoscience and Remote Sensing*, 53(6):3095–3109.

Joslin, J. D., Gaudinski, J. B., Torn, M. S., Riley, W. J., and Hanson, P. J. (2006). Fine-root turnover patterns and their relationship to root diameter and soil depth in a 14c-labeled hardwood forest. *New Phytologist*, 172(3):523–535.

Kamilaris, A. and Prenafeta-Boldú, F. X. (2018). A review of the use of convolutional neural networks in agriculture. *The Journal of Agricultural Science*, 156(3):312–322.

Katul, G. G., Wendroth, O., Parlange, M. B., Puente, C. E., Folegatti, M. V., and Nielsen, D. R. (1993). Estimation of in situ hydraulic conductivity function from nonlinear filtering theory. *Water Resources Research*, 29(4):1063–1070.

Kaufmann, M. S., Hebel, C., Weihermüller, L., Baumecker, M., Döring, T., Schweitzer, K., Hobley, E., Bauke, S. L., Amelung, W., Vereecken, H., and Kruk, J. (2019). Effect of fertilizers and irrigation on multi-configuration electromagnetic induction measurements. *Soil Use and Management*, 36(1):104–116.

Kaufmann, M. S., Klotzsche, A., Vereecken, H., and der Kruk, J. (2020). Simultaneous multichannel multi-offset ground-penetrating radar measurements for soil characterization. *Vadose Zone Journal*, 19(1).

Kautz, T., Amelung, W., Ewert, F., Gaiser, T., Horn, R., Jahn, R., Javaux, M., Kemna, A., Kuzyakov, Y., Munch, J.-C., Pätzold, S., Peth, S., Scherer, H. W., Schloter, M., Schneider, H., Vanderborght, J., Vetterlein, D., Walter, A., Wiesenberg, G. L., and Köpke, U. (2013). Nutrient acquisition from arable subsoils in temperate climates: A review. *Soil Biology and Biochemistry*, 57:1003–1022.

Keller, K., Kirchgessner, N., Khanna, R., Siegwart, R., Walter, A., and Aasen, H. (2018). Soybean leaf coverage estimation with machine learning and thresholding algorithms for field phenotyping. In *Proceedings of the British Machine Vision Conference, Newcastle, UK*, pages 3–6.

Kelter, M., Huisman, J., Zimmermann, E., and Vereecken, H. (2018). Field evaluation of broadband spectral electrical imaging for soil and aquifer characterization. *Journal of Applied Geophysics*, 159:484–496.

Kemna, A., Binley, A., Cassiani, G., Niederleithinger, E., Revil, A., Slater, L., Williams, K. H., Orozco, A. F., Haegel, F.-H., Hördt, A., Kruschwitz, S., Leroux, V., Titov, K., and Zimmermann, E. (2012). An overview of the spectral induced polarization method for near-surface applications. *Near Surface Geophysics*, 10(6):453–468.

Kemna, A., Vanderborght, J., Kulessa, B., and Vereecken, H. (2002). Imaging and characterisation of subsurface solute transport using electrical resistivity tomography (ERT) and equivalent transport models. *Journal of Hydrology*, 267(3-4):125–146.

Klenk, P., Jaumann, S., and Roth, K. (2015). Quantitative high-resolution observations of soil water dynamics in a complicated architecture using time-lapse ground-penetrating radar. *Hydrology and Earth System Sciences*, 19(3):1125–1139.

Klotzsche, A., Jonard, F., Looms, M., van der Kruk, J., and Huisman, J. (2018). Measuring soil water content with ground penetrating radar: A decade of progress. *Vadose Zone Journal*, 17(1):180052.

Klotzsche, A., Lärm, L., Vanderborght, J., Cai, G., Morandage, S., Zörner, M., Vereecken, H., and Kruk, J. (2019). Monitoring soil water content using time-lapse horizontal borehole GPR data at the field-plot scale. *Vadose Zone Journal*, 18(1):190044.

Klotzsche, A., van der Kruk, J., He, G., and Vereecken, H. (2016). GPR full-waveform inversion of horizontal ZOP borehole data using GprMax. In *2016 16th International Conference on Ground Penetrating Radar (GPR)*. IEEE.

Klotzsche, A., van der Kruk, J., Linde, N., Doetsch, J., and Vereecken, H. (2013). 3-d characterization of high-permeability zones in a gravel aquifer using 2-d crosshole gpr full-waveform inversion and waveguide detection. *Geophysical Journal International*, 195(2):932–944.

Klotzsche, A., Vereecken, H., and van der Kruk, J. (2019b). Review of crosshole ground-penetrating radar full-waveform inversion of experimental data: Recent developments, challenges, and pitfalls. *GEOPHYSICS*, 84(6):H13–H28.

Klute, A. and Dirksen, C. (1986). Hydraulic conductivity and diffusivity: Laboratory methods. *Methods of soil analysis: Part 1 physical and mineralogical methods*, 5:687–734.

Kodešová, R., Kodeš, V., Žigová, A., and Šimůnek, J. (2006). Impact of plant roots and soil organisms on soil micromorphology and hydraulic properties. *Biologia*, 61(S19):S339–S343.

Koestel, J., Kemna, A., Javaux, M., Binley, A., and Vereecken, H. (2008). Quantitative imaging of solute transport in an unsaturated and undisturbed soil monolith with 3-d ERT and TDR. *Water Resources Research*, 44(12).

Koestel, J., Vanderborght, J., Javaux, M., Kemna, A., Binley, A., and Vereecken, H. (2009). Noninvasive 3-d transport characterization in a sandy soil using ERT: 1. investigating the validity of ERT-derived transport parameters. *Vadose Zone Journal*, 8(3):711–722.

Kool, J., Parker, J., and van Genuchten, M. (1987). Parameter estimation for unsaturated flow and transport models — a review. *Journal of Hydrology*, 91(3-4):255–293.

Kool, J. B. and Parker, J. C. (1988). Analysis of the inverse problem for transient unsaturated flow. *Water Resources Research*, 24(6):817–830.

Kowalsky, M. B., Finsterle, S., Peterson, J., Hubbard, S., Rubin, Y., Majer, E., Ward, A., and Gee, G. (2005). Estimation of field-scale soil hydraulic and dielectric parameters through joint inversion of gpr and hydrological data. *Water Resources Research*, 41(11).

Kravchenko, A. N., Toosi, E. R., Guber, A. K., Ostrom, N. E., Yu, J., Azeem, K., Rivers, M. L., and Robertson, G. P. (2017). Hotspots of soil n2o emission enhanced through water absorption by plant residue. *Nature Geoscience*, 10(7):496–500.

Krizhevsky, A., Sutskever, I., and Hinton, G. E. (2012). Imagenet classification with deep convolutional neural networks. *Advances in neural information processing systems*, 25:1097–1105.

Kuczera, G. and Mroczkowski, M. (1998). Assessment of hydrologic parameter uncertainty and the worth of multiresponse data. *Water Resources Research*, 34(6):1481–1489.

Kuhl, A. S., Kendall, A. D., Dam, R. L. V., and Hyndman, D. W. (2018). Quantifying soil water and root dynamics using a coupled hydrogeophysical inversion. *Vadose Zone Journal*, 17(1):170154.

Kumar, S., Sekhar, M., Reddy, D. V., and Kumar, M. S. M. (2010). Estimation of soil hydraulic properties and their uncertainty: comparison between laboratory and field experiment. *Hydrological Processes*, 24(23):3426–3435.

Lambot, S., Antoine, M., van den Bosch, I., Slob, E. C., and Vanclooster, M. (2004). Electromagnetic inversion of GPR signals and subsequent hydrodynamic inversion to estimate effective vadose zone hydraulic properties. *Vadose Zone Journal*, 3(4):1072–1081.

Lambot, S., Antoine, M., Vanclooster, M., and Slob, E. C. (2006). Effect of soil roughness on the inversion of off-ground monostatic GPR signal for noninvasive quantification of soil properties. *Water Resources Research*, 42(3).

Lambot, S., Slob, E., Rhebergen, J., Lopera, O., Jadoon, K. Z., and Vereecken, H. (2009). Remote estimation of the hydraulic properties of a sand using full-waveform integrated hydrogeophysical inversion of time-lapse, off-ground gpr data. *Vadose Zone Journal*, 8(3):743–754.

Landl, M., Phalempin, M., Schlüter, S., Vetterlein, D., Vanderborght, J., Kroener, E., and Schnepf, A. (2021). Modeling the impact of rhizosphere bulk density and mucilage gradients on root water uptake. *Frontiers in Agronomy*, 3.

Landl, M., Schnepf, A., Uteau, D., Peth, S., Athmann, M., Kautz, T., Perkons, U., Vereecken, H., and Vanderborght, J. (2019). Modeling the impact of biopores on root growth and root water uptake. *Vadose Zone Journal*, 18(1):1–20.

LeCun, Y., Bengio, Y., and Hinton, G. (2015). Deep learning. *Nature*, 521(7553):436–444.

Leitner, D., Felderer, B., Vontobel, P., and Schnepf, A. (2013). Recovering root system traits using image analysis exemplified by two-dimensional neutron radiography images of lupine . *Plant Physiology*, 164(1):24–35.

Li, D., Xu, K., Harris, J. M., and Darve, E. (2020). Coupled time-lapse full-waveform inversion for subsurface flow problems using intrusive automatic differentiation. *Water Resources Research*, 56(8).

Liang, H., Fan, G., Li, Y., and Zhao, Y. (2021). Theoretical development of plant root diameter estimation based on GprMax data and neural network modelling. *Forests*, 12(5):615.

Linde, N., Binley, A., Tryggvason, A., Pedersen, L. B., and Revil, A. (2006). Improved hydrogeophysical characterization using joint inversion of cross-hole electrical resistance and ground-penetrating radar traveltime data. *Water Resources Research*, 42(12).

Liu, T., Klotzsche, A., Pondkule, M., Vereecken, H., Su, Y., and van der Kruk, J. (2018). Radius estimation of subsurface cylindrical objects from ground-penetrating-radar data using full-waveform inversion. *Geophysics*, 83(6):H43–H54.

Liu, X., Chen, J., Butnor, J. R., Qin, G., Cui, X., Fan, B., Lin, H., and Guo, L. (2020). Noninvasive 2d and 3d mapping of root zone soil moisture through the detection of coarse roots with ground-penetrating radar. *Water Resources Research*, 56(5).

Liu, X., Cui, X., Guo, L., Chen, J., Li, W., Yang, D., Cao, X., Chen, X., Liu, Q., and Lin, H. (2019). Non-invasive estimation of root zone soil moisture from coarse root reflections in ground-penetrating radar images. *Plant and Soil*, 436(1-2):623–639.

Liu, X., Dong, X., and Leskovar, D. I. (2016). Ground penetrating radar for underground sensing in agriculture: a review. *International Agrophysics*, 30(4):533–543.

Liu, X., Dong, X., Xue, Q., Leskovar, D. I., Jifon, J., Butnor, J. R., and Marek, T. (2017). Ground penetrating radar (gpr) detects fine roots of agricultural crops in the field. *Plant and Soil*, 423(1-2):517–531.

Lobet, G., Couvreur, V., Meunier, F., Javaux, M., and Draye, X. (2014). Plant water uptake in drying soils. *Plant Physiology*, 164(4):1619–1627.

Lobet, G., Draye, X., and Périlleux, C. (2013). An online database for plant image analysis software tools. *Plant methods*, 9(1):1–8.

Lobet, G., Pagès, L., and Draye, X. (2011). A novel image-analysis toolbox enabling quantitative analysis of root system architecture . *Plant Physiology*, 157(1):29–39.

Looms, M. C., Binley, A., Jensen, K. H., Nielsen, L., and Hansen, T. M. (2008a). Identifying unsaturated hydraulic parameters using an integrated data fusion approach on cross-borehole geophysical data. *Vadose Zone Journal*, 7(1):238–248.

Looms, M. C., Jensen, K. H., Binley, A., and Nielsen, L. (2008b). Monitoring unsaturated flow and transport using cross-borehole geophysical methods. *Vadose Zone Journal*, 7(1):227–237.

Looy, K. V., Bouma, J., Herbst, M., Koestel, J., Minasny, B., Mishra, U., Montzka, C., Nemes, A., Pachepsky, Y. A., Padarian, J., Schaap, M. G., Tóth, B., Verhoef, A., Vanderborght, J., Ploeg, M. J., Weihermüller, L., Zacharias, S., Zhang, Y., and Vereecken, H. (2017). Pedotransfer functions in earth system science: Challenges and perspectives. *Reviews of Geophysics*, 55(4):1199–1256.

Ludbrook, J. (1997). Comparing methods of measurement. *Clinical and Experimental Pharmacology and Physiology*, 24(2):198–203.

Lunt, I., Hubbard, S., and Rubin, Y. (2005). Soil moisture content estimation using ground-penetrating radar reflection data. *Journal of Hydrology*, 307(1-4):254–269.

Lynch, J. P. (2007). Roots of the second green revolution. *Australian Journal of Botany*, 55(5):493.

Lynch, J. P. (2013). Steep, cheap and deep: an ideotype to optimize water and n acquisition by maize root systems. *Annals of Botany*, 112(2):347–357.

Lärm, L.; Bauer, F. M. . v. d. K. J. V. J. M. S. V. H. S. A. . K. A. (2023). Linking horizontal crosshole gpr variability with root image information for maize crops. *Vadose Zone Journal*, e20293.

Lärm, L., Bauer, F. M., Hermes, N., van der Kruk, J., Vereecken, H., Vanderborght, J., Nguyen, T. H., Lopez, G., Seidel, S. J., Ewert, F., Schnepf, A., and Klotzsche, A. (2023). Multi-year belowground data of minirhizotron facilities in selhausen. *Scientific Data*, 10(1).

Maeght, J.-L., Rewald, B., and Pierret, A. (2013). How to study deep roots—and why it matters. *Frontiers in Plant Science*, 4.

Malicki, M., Plagge, R., Renger, M., and Walczak, R. (1992). Application of time-domain reflectometry (TDR) soil moisture miniprobe for the determination of unsaturated soil water characteristics from undisturbed soil cores. *Irrigation Science*, 13(2).

Mangel, A. R., Moysey, S. M., and Kruk, J. (2017). Resolving infiltration-induced water content profiles by inversion of dispersive ground-penetrating radar data. *Vadose Zone Journal*, 16(10):1–11.

Mangel, A. R., Moysey, S. M. J., Ryan, J. C., and Tarbutton, J. A. (2012). Multi-offset ground-penetrating radar imaging of a lab-scale infiltration test. *Hydrology and Earth System Sciences*, 16(11):4009–4022.

Manoli, G., Rossi, M., Pasetto, D., Deiana, R., Ferraris, S., Cassiani, G., and Putti, M. (2015). An iterative particle filter approach for coupled hydro-geophysical inversion of a controlled infiltration experiment. *Journal of Computational Physics*, 283:37–51.

Mapoka, K. O. M., Birrell, S. J., Tekeste, M. Z., Steward, B., and Eisenmann, D. (2019). Using gprMax to model ground-penetrating radar (GPR) to locate corn seed as an attempt to measure planting depth. *Transactions of the ASABE*, 62(3):673–686.

Martinez-Vilalta, J., Pinol, J., and Beven, K. (2002). A hydraulic model to predict drought-induced mortality in woody plants: an application to climate change in the mediterranean. *Ecological Modelling*, 155(2-3):127–147.

Mboh, C., Huisman, J., Gaelen, N. V., Rings, J., and Vereecken, H. (2012). Coupled hydro-geophysical inversion of electrical resistances and inflow measurements for topsoil hydraulic properties under constant head infiltration. *Near Surface Geophysics*, 10(5):413–426.

Mboh, C., Huisman, J., and Vereecken, H. (2011). Feasibility of sequential and coupled inversion of time domain reflectometry data to infer soil hydraulic parameters under falling head infiltration. *Soil Science Society of America Journal*, 75(3):775–786.

McDowell, N. G. and Allen, C. D. (2015). Darcy's law predicts widespread forest mortality under climate warming. *Nature Climate Change*, 5(7):669–672.

Merrill, S. and Upchurch, D. (1994). Converting root numbers observed at minirhizotrons to equivalent root length density. *Soil Science Society of America Journal*, 58(4):1061–1067.

Michels, V., W. M. and Kemna, A. (2022). Sensing of winter wheat root systems at the field scale using spectral electricalimpedance tomography.

Michot, D., Benderitter, Y., Dorigny, A., Nicoullaud, B., King, D., and Tabbagh, A. (2003). Spatial and temporal monitoring of soil water content with an irrigated corn crop cover using surface electrical resistivity tomography. *Water Resources Research*, 39(5).

Minervini, M., Scharr, H., and Tsaftaris, S. A. (2015). Image analysis: the new bottleneck in plant phenotyping [applications corner]. *IEEE signal processing magazine*, 32(4):126–131.

Mitchell, A., Ellsworth, T., and Meek, B. D. (1995). Effect of root systems on preferential flow in swelling soil. *Communications in Soil Science and Plant Analysis*, 26(15-16):2655–2666.

Moghadas, D., André, F., Slob, E. C., Vereecken, H., and Lambot, S. (2010). Joint full-waveform analysis of off-ground zero-offset ground penetrating radar and electromagnetic induction synthetic data for estimating soil electrical properties. *Geophysical Journal International*, 182(3):1267–1278.

Moghadas, D. and Badorreck, A. (2019). Machine learning to estimate soil moisture from geophysical measurements of electrical conductivity. *Near Surface Geophysics*, 17(2):181–195.

Moghadas, D., Jadoon, K. Z., and McCabe, M. F. (2017). Spatiotemporal monitoring of soil water content profiles in an irrigated field using probabilistic inversion of time-lapse EMI data. *Advances in Water Resources*, 110:238–248.

Möller, B., Chen, H., Schmidt, T., Zieschank, A., Patzak, R., Türke, M., Weigelt, A., and Posch, S. (2019). rhizotrak: a flexible open source fiji plugin for user-friendly manual annotation of time-series images from minirhizotrons. *Plant and Soil*, 444:519–534.

Morandage, S. (2020). *Characterization of Root System Architectures from Field Root Sampling Methods*. PhD thesis, Rheinische Friedrich-Wilhelms-Universität Bonn.

Morandage, S., Schnepf, A., Leitner, D., Javaux, M., Vereecken, H., and Vanderborght, J. (2019). Parameter sensitivity analysis of a root system architecture model based on virtual field sampling. *Plant and Soil*, 438(1-2):101–126.

Morandage, S., Vanderborght, J., Zörner, M., Cai, G., Leitner, D., Vereecken, H., and Schnepf, A. (2021). Root architecture development in stony soils. *Vadose Zone Journal*, 20(4).

Moysey, S. M. (2010). Hydrologic trajectories in transient ground-penetrating-radar reflection data. *GEOPHYSICS*, 75(4):WA211–WA219.

Mualem, Y. (1976). A new model for predicting the hydraulic conductivity of unsaturated porous media. *Water resources research*, 12(3):513–522.

Murphy, S. L. and Smucker, A. J. M. (1995). Evaluation of video image analysis and line-intercept methods for measuring root systems of alfalfa and ryegrass. *Agronomy Journal*, 87(5):865–868.

Musil, M., Maurer, H., Hollinger, K., and Green, A. G. (2006). Internal structure of an alpine rock glacier based on crosshole georadar traveltimes and amplitudes. *Geophysical Prospecting*, 54(3):273–285.

Müller, H.-W., Dohrmann, R., Klosa, D., Rehder, S., and Eckelmann, W. (2009). Comparison of two procedures for particle-size analysis: Köhn pipette and x-ray granulometry. *Journal of Plant Nutrition and Soil Science*, 172(2):172–179.

Nandagiri, L. and Prasad, R. (1996). Field evaluation of unsaturated hydraulic conductivity models and parameter estimation from retention data. *Journal of Hydrology*, 179(1-4):197–205.

Narisetti, N., Henke, M., Seiler, C., Junker, A., Ostermann, J., Altmann, T., and Gladilin, E. (2021). Fully-automated root image analysis (faRIA). *Scientific Reports*, 11(1).

Neuzil, C., Cooley, C., Silliman, S., Bredehoeft, J., and Hsieh, P. (1981). A transient laboratory method for determining the hydraulic properties of 'tight' rocks—II. application. *International Journal of Rock Mechanics and Mining Sciences &amp Geomechanics Abstracts*, 18(3):253–258.

Nguyen, T. H., Langensiepen, M., Gaiser, T., Webber, H., Ahrends, H., Hueging, H., and Ewert, F. (2022a). Responses of winter wheat and maize to varying soil moisture: From leaf to canopy. *Agricultural and Forest Meteorology*, 314:108803.

Nguyen, T. H., Langensiepen, M., Hueging, H., Gaiser, T., Seidel, S. J., and Ewert, F. (2022b). Expansion and evaluation of two coupled root–shoot models in simulating co2 and h2o fluxes and growth of maize. *Vadose Zone Journal*, 21(3):e20181.

Nguyen, T. H., Langensiepen, M., Vanderborght, J., Hüging, H., Mboh, C. M., and Ewert, F. (2020). Comparison of root water uptake models in simulating co 2 and h 2 o fluxes and growth of wheat. *Hydrology and Earth System Sciences*, 24(10):4943–4969.

Olof Andrén, Kálmán Rajkai, T. K. (1991). A non-destructive technique for studies of root distribution in relation to soil moisture. *Agriculture, Ecosystems and Environment,34*.

Pan, X., Jaumann, S., Zhang, J., and Roth, K. (2019). Efficient estimation of effective hydraulic properties of stratal undulating surface layer using time-lapse multi-channel GPR. *Hydrology and Earth System Sciences*, 23(9):3653–3663.

Parkin, G., Redman, D., von Bertoldi, P., and Zhang, Z. (2000). Measurement of soil water content below a wastewater trench using ground-penetrating radar. *Water Resources Research*, 36(8):2147–2154.

Parsekian, A. D., Slater, L., and Schäfer, K. V. R. (2012). Small root biomass effect on the dielectric properties of soil. *Vadose Zone Journal*, 11(1).

Paz, C., Alcalá, F. J., Carvalho, J. M., and Ribeiro, L. (2017). Current uses of ground penetrating radar in groundwater-dependent ecosystems research. *Science of The Total Environment*, 595:868–885. Paz, Catarina Alcala, Francisco J Carvalho, Jorge M Ribeiro, Luis eng Review Netherlands Sci Total Environ. 2017 Oct 1;595:868-885. doi: 10.1016/j.scitotenv.2017.03.210. Epub 2017 Apr 18.

Peters, A., Durner, W., and Wessolek, G. (2011). Consistent parameter constraints for soil hydraulic functions. *Advances in Water Resources*, 34(10):1352–1365.

Pierret, A., Gonkhamdee, S., Jourdan, C., and Maeght, J.-L. (2013). IJ_rhizo: an open-source software to measure scanned images of root samples. *Plant and Soil*, 373(1-2):531–539.

Pleasants, M. S., dos A. Neves, F., Parsekian, A. D., Befus, K. M., and Kelleners, T. J. (2022). Hydrogeophysical inversion of time-lapse ERT data to determine hillslope subsurface hydraulic properties. *Water Resources Research*, 58(4).

Pokorny, J. (2019). Evapotranspiration. In *Encyclopedia of Ecology*, pages 292–303. Elsevier.

Pollock, D. and Cirpka, O. A. (2010). Fully coupled hydrogeophysical inversion of synthetic salt tracer experiments. *Water Resources Research*, 46(7).

Pound, M. P., Atkinson, J. A., Townsend, A. J., Wilson, M. H., Griffiths, M., Jackson, A. S., Bulat, A., Tzimiropoulos, G., Wells, D. M., Murchie, E. H., Pridmore, T. P., and French, A. P. (2017). Deep machine learning provides state-of-the-art performance in image-based plant phenotyping. *GigaScience*, 6(10).

Priesack, E. and Durner, W. (2006). Closed-form expression for the multi-modal unsaturated conductivity function. *Vadose Zone Journal*, 5(1):121–124.

Pritchard, S. G., S. A. E. M. M. L. D. M. A. . O. R. (2008). Mycorrhizal and rhizomorph dynamics in a loblolly pine forest during 5 years of free-air-co2-enrichment. *Global Change Biology*, 14(6):1252–1264.

Pütz, T., Kiese, R., Wollschläger, U., Groh, J., Rupp, H., Zacharias, S., Priesack, E., Gerke, H. H., Gasche, R., Bens, O., Borg, E., Baessler, C., Kaiser, K., Herbrich, M., Munch, J.-C., Sommer, M., Vogel, H.-J., Vanderborght, J., and Vereecken, H. (2016). TERENO-SOILCan: a lysimeter-network in germany observing soil processes and plant diversity influenced by climate change. *Environmental Earth Sciences*, 75(18).

Qin, R., Stamp, P., and Richner, W. (2005). Impact of tillage and banded starter fertilizer on maize root growth in the top 25 centimeters of the soil. *Agronomy Journal*, 97(3):674–683.

Rahmati, M., Groh, J., Graf, A., Pütz, T., Vanderborght, J., and Vereecken, H. (2020). On the impact of increasing drought on the relationship between soil water content and evapotranspiration of a grassland. *Vadose Zone Journal*, 19(1).

Rao, S., Lesparre, N., Flores-Orozco, A., Wagner, F., Kemna, A., and Javaux, M. (2020). Imaging plant responses to water deficit using electrical resistivity tomography. *Plant and Soil*, 454(1-2):261–281.

Rao, S., Meunier, F., Ehosioke, S., Lesparre, N., Kemna, A., Nguyen, F., Garré, S., and Javaux, M. (2019). Impact of maize roots on soil–root electrical conductivity: A simulation study. *Vadose Zone Journal*, 18(1):190037.

Rasmussen, C. R., Thorup-Kristensen, K., and Dresbøll, D. B. (2020). Uptake of subsoil water below 2 m fails to alleviate drought response in deep-rooted chicory (cichorium intybus l.). *Plant and Soil*, 446:275–290.

Rasse, D. P., Smucker, A. J. M., and Santos, D. (2000). Alfalfa root and shoot mulching effects on soil hydraulic properties and aggregation. *Soil Science Society of America Journal*, 64(2):725–731.

Raz-Yaseef, N., Koteen, L., and Baldocchi, D. D. (2013). Coarse root distribution of a semi-arid oak savanna estimated with ground penetrating radar. *Journal of Geophysical Research: Biogeosciences*, 118(1):135–147.

Redman, D., Parkin, G. W., and Annan, A. P. (2000). Borehole gpr measurement of soil water content during an infiltration experiment. In *Eighth International Conference on Ground Penetrating Radar*, volume 4084, pages 501–505. SPIE.

Revil, A., Jougnot, D., Halisch, M., and Deparis, J. (2022). Booklet of the 6th international workshop on induced polarization.

Rewald, B. and Ephrath, J. (2013). *Minirhizotron techniques*, pages 735–750. CRC Press. Publisher Copyright: © 2013 by Taylor Francis Group, LLC.

Richards, L. A. (1931). Capillary conduction of liquids through porous mediums. *physics*, 1(5):318–333.

Ritchie, Steven W, H. J. J. B. G. (1986). How a corn plant develops (special report no. 48). iowa state university of science and technology. *Cooperative Extension Service. Ames, IA, USA*.

Robinson, D. A., Abdu, H., Lebron, I., and Jones, S. B. (2012). Imaging of hill-slope soil moisture wetting patterns in a semi-arid oak savanna catchment using time-lapse electromagnetic induction. *Journal of Hydrology*, 416-417:39–49.

Robinson, D. A., Campbell, C. S., Hopmans, J. W., Hornbuckle, B. K., Jones, S. B., Knight, R., Ogden, F., Selker, J., and Wendroth, O. (2008). Soil moisture measurement for ecological and hydrological watershed-scale observatories: A review. *Vadose Zone Journal*, 7(1):358–389.

Robinson, D. A., Jones, S. B., Blonquist, J. M., and Friedman, S. P. (2005). A physically derived water content/permittivity calibration model for coarse-textured, layered soils. *Soil Science Society of America Journal*, 69(5):1372–1378.

Rodríguez-Robles, U., Arredondo, T., Huber-Sannwald, E., Ramos-Leal, J. A., and Yépez, E. A. (2017). Technical note: Application of geophysical tools for tree root studies in forest ecosystems in complex soils. *Biogeosciences*, 14(23):5343–5357.

Romero-Ruiz, A., Linde, N., Baron, L., Breitenstein, D., Keller, T., and Or, D. (2022). Lasting effects of soil compaction on soil water regime confirmed by geoelectrical monitoring. *Water Resources Research*, 58(2).

Ronneberger, O., Fischer, P., and Brox, T. (2015). U-net: Convolutional networks for biomedical image segmentation. In Navab, N., Hornegger, J., Wells, W. M., and Frangi, A. F., editors, *Medical Image Computing and Computer-Assisted Intervention – MICCAI 2015*, pages 234–241, Cham. Springer International Publishing.

Rossi, M., Manoli, G., Pasetto, D., Deiana, R., Ferraris, S., Strobbia, C., Putti, M., and Cassiani, G. (2015). Coupled inverse modeling of a controlled irrigation experiment using multiple hydro-geophysical data. *Advances in Water Resources*, 82:150–165.

Roth, K., Schulin, R., Flühler, H., and Attinger, W. (1990). Calibration of time domain reflectometry for water content measurement using a composite dielectric approach. *Water Resources Research*, 26(10):2267–2273.

Rovey, C. W. and Cherkauer, D. S. (1995). Scale dependency of hydraulic conductivity measurements. *Ground Water*, 33(5):769–780.

Rubin, Y. and Hubbard, S. S., editors (2005). *Hydrogeophysics*. Springer Netherlands.

Rucker, D. F. and Ferré, T. (2004). Parameter estimation for soil hydraulic properties using zero-offset borehole radar. *Soil Science Society of America Journal*, 68(5):1560–1567.

Rucker, D. F. and Ferré, T. P. A. (2004). Correcting water content measurement errors associated with critically refracted first arrivals on zero offset profiling borehole ground penetrating radar profiles. *Vadose Zone Journal*, 3(1):278–287.

Rudolph, S., van der Kruk, J., Von Hebel, C., Ali, M., Herbst, M., Montzka, C., Pätzold, S., Robinson, D., Vereecken, H., and Weihermüller, L. (2015). Linking satellite derived lai patterns with subsoil heterogeneity using large-scale ground-based electromagnetic induction measurements. *Geoderma*, 241:262–271.

Salman, S. and Liu, X. (2019). Overfitting mechanism and avoidance in deep neural networks. *CoRR*, abs/1901.06566.

Samouëlian, A., Cousin, I., Tabbagh, A., Bruand, A., and Richard, G. (2005). Electrical resistivity survey in soil science: a review. *Soil and Tillage Research*, 83(2):173–193.

Samuelson, L. J., Butnor, J., Maier, C., Stokes, T. A., Johnsen, K., and Kane, M. (2008). Growth and physiology of loblolly pine in response to long-term resource management: defining growth potential in the southern united states. *Canadian Journal of Forest Research*, 38(4):721–732.

Santos, L., Santos, F. N., Oliveira, P. M., and Shinde, P. (2020). Deep learning applications in agriculture: A short review. In Silva, M. F., Luís Lima, J., Reis, L. P., Sanfeliu, A., and Tardioli, D., editors, *Robot 2019: Fourth Iberian Robotics Conference*, pages 139–151, Cham. Springer International Publishing.

Scharnagl, B., Vrugt, J. A., Vereecken, H., and Herbst, M. (2011). Inverse modelling of in situ soil water dynamics: investigating the effect of different prior distributions of the soil hydraulic parameters. *Hydrology and Earth System Sciences*, 15(10):3043–3059.

Schenk, M. K. and Barber, S. A. (1980). Potassium and phosphorus uptake by corn genotypes grown in the field as influenced by root characteristics. *Plant and Soil*, 54(1):65–76.

Schindler, U., Durner, W., von Unold, G., and Müller, L. (2010). Evaporation method for measuring unsaturated hydraulic properties of soils: Extending the measurement range. *Soil Science Society of America Journal*, 74(4):1071–1083.

Schlüter, S., Vogel, H.-J., Ippisch, O., and Vanderborght, J. (2013). Combined impact of soil heterogeneity and vegetation type on the annual water balance at the field scale. *Vadose Zone Journal*, 12(4):vzj2013.03.0053.

Schmalholz, J., Stoffregen, H., Kemna, A., and Yaramanci, U. (2004). Imaging of water content distributions inside a lysimeter using GPR tomography. *Vadose Zone Journal*, 3(4):1106–1115.

Schmäck, J., Weihermüller, L., Klotzsche, A., Hebel, C., Pätzold, S., Welp, G., and Vereecken, H. (2021). Large-scale detection and quantification of harmful soil compaction in a post-mining landscape using multi-configuration electromagnetic induction. *Soil Use and Management*, 38(1):212–228.

Schnepf, A., Carminati, A., Ahmed, M. A., Ani, M., Benard, P., Bentz, J., Bonkowski, M., Knott, M., Diehl, D., Duddek, P., Kröner, E., Javaux, M., Landl, M., Lehndorff, E., Lippold, E., Lieu, A., Mueller, C. W., Oburger, E., Otten, W., Portell, X., Phalempin, M., Prechtel, A., Schulz, R., Vanderborght, J., and Vetterlein, D. (2022a). Linking rhizosphere processes across scales: Opinion. *Plant and Soil*, 478(1-2):5–42.

Schnepf, A., Leitner, D., Bodner, G., and Javaux, M. (2022b). Editorial: Benchmarking 3d-models of root growth, architecture and functioning. *Frontiers in Plant Science*, 13.

Seethepalli, A., Dhakal, K., Griffiths, M., Guo, H., Freschet, G. T., and York, L. M. (2021). Rhizovision explorer: open-source software for root image analysis and measurement standardization. *AoB Plants*, 13(6).

Seethepalli, A. and York, L. M. (2020). Rhizovision explorer - interactive software for generalized root image analysis designed for everyone.

Shanahan, P. W., Binley, A., Whalley, W. R., and Watts, C. W. (2015). The use of electromagnetic induction to monitor changes in soil moisture profiles beneath different wheat genotypes. *Soil Science Society of America Journal*, 79(2):459–466.

Shen, C., Liu, L., Zhu, L., Kang, J., Wang, N., and Shao, L. (2020). High-throughput in situ root image segmentation based on the improved DeepLabv3+ method. *Frontiers in Plant Science*, 11.

Shin, H.-C., Blanchy, G., Shield, I., Fruen, P., Barraclough, T., Watts, C. W., Binley, A., and Whalley, W. R. Geophysical methods to assess soil characteristics.

Shinoda, M. and Nandintsetseg, B. (2011). Soil moisture and vegetation memories in a cold, arid climate. *Global and Planetary Change*, 79(1-2):110–117.

Silva, D. D. and Beeson, R. C. (2011). A large-volume rhizotron for evaluating root growth under natural-like soil moisture conditions. *HortScience horts*, 46(12):1677 – 1682.

Simmer, C., Thiele-Eich, I., Masbou, M., Amelung, W., Bogena, H., Crewell, S., Diekkrüger, B., Ewert, F., Hendricks Franssen, H.-J., Huisman, J. A., et al. (2015a). Monitoring and modeling the terrestrial system from pores to catchments: The transregional collaborative research center on patterns in the soil–vegetation–atmosphere system. *Bulletin of the American Meteorological Society*, 96(10):1765–1787.

Simmer, C., Thiele-Eich, I., Masbou, M., Amelung, W., Bogena, H., Crewell, S., Diekkrüger, B., Ewert, F., Hendricks Franssen, H.-J., Huisman, J. A., et al. (2015b). Monitoring and

modeling the terrestrial system from pores to catchments: The transregional collaborative research center on patterns in the soil–vegetation–atmosphere system. *Bulletin of the American Meteorological Society*, 96(10):1765–1787.

Šimůnek, J., Genuchten, M. T., and Šejna, M. (2008). Development and applications of the HYDRUS and STANMOD software packages and related codes. *Vadose Zone Journal*, 7(2):587–600.

Simunek, J., Van Genuchten, M. T., and Sejna, M. (2013). The hydrus-1d software package for simulating the one-dimensional movement of water, heat, and multiple solutes in variably-saturated media. *University of California-Riverside Research Reports*, 4.17:1–308.

Singha, K., Day-Lewis, F. D., Johnson, T., and Slater, L. D. (2014). Advances in interpretation of subsurface processes with time-lapse electrical imaging. *Hydrological Processes*, 29(6):1549–1576.

Slater, L. and Binley, A. (2021). Advancing hydrological process understanding from long-term resistivity monitoring systems. *WIREs Water*, 8(3).

Sławiński, C. and Sobczuk, H. (2011). Soil–plant–atmosphere continuum. In *Encyclopedia of Agrophysics*, pages 805–810. Springer Netherlands.

Slob, E., Sato, M., and Olhoeft, G. (2010). Surface and borehole ground-penetrating-radar developments. *GEOPHYSICS*, 75(5):75A103–75A120.

Smith, A. G., Han, E., Petersen, J., Olsen, N. A. F., Giese, C., Athmann, M., Dresbøll, D. B., and Thorup-Kristensen, K. (2020a). RootPainter: Deep learning segmentation of biological images with corrective annotation.

Smith, A. G., Han, E., Petersen, J., Olsen, N. A. F., Giese, C., Athmann, M., Dresbøll, D. B., and Thorup-Kristensen, K. (2022). Rootpainter: Deep learning segmentation of biological images with corrective annotation. *New Phytologist*, 236(2):774–791.

Smith, A. G., Petersen, J., Selvan, R., and Rasmussen, C. R. (2020b). Segmentation of roots in soil with u-net. *Plant Methods*, 16(1).

Smith, L. N. (2018). A disciplined approach to neural network hyper-parameters: Part 1– learning rate, batch size, momentum, and weight decay. *arXiv preprint arXiv:1803.09820*.

Song, P., Wang, J., Guo, X., Yang, W., and Zhao, C. (2021). High-throughput phenotyping: Breaking through the bottleneck in future crop breeding. *The Crop Journal*, 9(3):633–645.

Srinivasan, A., editor (2006). *Handbook of Precision Agriculture*. CRC Press.

Steele, S. J., Gower, S. T., Vogel, J. G., and Norman, J. M. (1997). Root mass, net primary production and turnover in aspen, jack pine and black spruce forests in saskatchewan and manitoba, canada. *Tree physiology*, 17(8-9):577–587.

Steelman, C. M. and Endres, A. L. (2011). Comparison of petrophysical relationships for soil moisture estimation using gpr ground waves. *Vadose Zone Journal*, 10(1):270–285.

Steelman, C. M., Endres, A. L., and Jones, J. P. (2012). High-resolution ground-penetrating radar monitoring of soil moisture dynamics: Field results, interpretation, and comparison with unsaturated flow model. *Water Resources Research*, 48(9).

Steelman, C. M., Klazinga, D. R., Cahill, A. G., Endres, A. L., and Parker, B. L. (2017). Monitoring the evolution and migration of a methane gas plume in an unconfined sandy aquifer using time-lapse GPR and ERT. *Journal of Contaminant Hydrology*, 205:12–24.

Steenpass, C., Vanderborght, J., Herbst, M., Šimůnek, J., and Vereecken, H. (2010). Estimating soil hydraulic properties from infrared measurements of soil surface temperatures and TDR data. *Vadose Zone Journal*, 9(4):910–924.

Steinbeck, L., Mester, A., Zimmermann, E., Klotzsche, A., and van Waasen, S. (2022). In situ time-zero correction for a ground penetrating radar monitoring system with 3000 antennas. *Measurement Science and Technology*, 33(7):075904.

Stover, D. B., Day, F. P., Butnor, J. R., and Drake, B. G. (2007). Effect ofelevated co-2 on coarse-root biomass in florida scrubdetected by ground-penetrating radar. *Ecology*, 88(5):1328–1334.

Strobach, E., Harris, B. D., Dupuis, J. C., and Kepic, A. W. (2014). Time-lapse borehole radar for monitoring rainfall infiltration through podosol horizons in a sandy vadose zone. *Water Resources Research*, 50(3):2140–2163.

Svane, S. F., Jensen, C. S., and Thorup-Kristensen, K. (2019). Construction of a large-scale semi-field facility to study genotypic differences in deep root growth and resources acquisition. *Plant Methods*, 15(1).

Taylor, H., Upchurch, D., and McMichael, B. (1990). Applications and limitations of rhizotrons and minirhizotrons for root studies. *Plant and Soil*, 129:29–35.

Terry, N., Day-Lewis, F. D., Lane, J. W., Johnson, C. D., and Werkema, D. (2023). Field evaluation of semi-automated moisture estimation from geophysics using machine learning. *Vadose Zone Journal*, 22(2).

Teuling, A. J., Hupet, F., Uijlenhoet, R., and Troch, P. A. (2007). Climate variability effects on spatial soil moisture dynamics. *Geophysical Research Letters*, 34(6).

Thorup-Kristensen, K., Cortasa, M. S., and Loges, R. (2009). Winter wheat roots grow twice as deep as spring wheat roots, is this important for n uptake and n leaching losses? *Plant and Soil*, 322(1-2):101–114.

Thorup-Kristensen, K., Halberg, N., Nicolaisen, M. H., Olesen, J. E., and Dresbøll, D. B. (2020). Exposing deep roots: A rhizobox laboratory. *Trends in Plant Science*, 25(4):418–419.

Thyer, M., Kuczera, G., and Bates, B. C. (1999). Probabilistic optimization for conceptual rainfall-runoff models: A comparison of the shuffled complex evolution and simulated annealing algorithms. *Water Resources Research*, 35(3):767–773.

Toorman, A. F., Wierenga, P. J., and Hills, R. G. (1992). Parameter estimation of hydraulic properties from one-step outflow data. *Water Resources Research*, 28(11):3021–3028.

Topp, G. C., Davis, J. L., and Annan, A. P. (1980). Electromagnetic determination of soil water content: Measurements in coaxial transmission lines. *Water Resources Research*, 16(3):574–582.

Trachsel, S., Kaeppler, S. M., Brown, K. M., and Lynch, J. P. (2010). Shovelomics: high throughput phenotyping of maize (zea mays l.) root architecture in the field. *Plant and Soil*, 341(1-2):75–87.

Tran, A. P., Dafflon, B., Hubbard, S. S., Kowalsky, M. B., Long, P., Tokunaga, T. K., and Williams, K. H. (2016). Quantifying shallow subsurface water and heat dynamics using coupled hydrological-thermal-geophysical inversion. *Hydrology and Earth System Sciences*, 20(9):3477–3491.

Tronicke, J. and Hamann, G. (2014). Vertical radar profiling: Combined analysis of travel-times, amplitudes, and reflections. *Geophysics*, 79(4):H23–H35.

Tso, C.-H. M., Kuras, O., and Binley, A. (2019). On the field estimation of moisture content using electrical geophysics: The impact of petrophysical model uncertainty. *Water Resources Research*, 55(8):7196–7211.

Ubbens, J. R. and Stavness, I. (2017). Deep plant phenomics: a deep learning platform for complex plant phenotyping tasks. *Frontiers in plant science*, 8:1190.

Vamerali, T., Bandiera, M., and Mosca, G. (2011). Minirhizotrons in modern root studies. In *Measuring Roots*, pages 341–361. Springer Berlin Heidelberg.

Vamerali, T., Bandiera, M., and Mosca, G. (2012). Minirhizotrons in modern root studies. *Measuring roots: An updated approach*, pages 341–361.

Van de Geijn, S., Vos, J., Groenwold, J., Goudriaan, J., and Leffelaar, P. (1994). The wageningen rhizolab—a facility to study soil-root-shoot-atmosphere interactions in crops: I. description of main functions. *Plant and Soil*, 161:275–287.

Van de Geijn, S., V. J. G. J. G. J. . L. P. (1994). The wageningen rhizolab- a facility to study soil-root-shoot-atmosphere interactions in crops: Ii. methods of root observations. *Plant and Soil*, 161(2):289–298.

Van Genuchten, M. T. (1980). A closed-form equation for predicting the hydraulic conductivity of unsaturated soils 1. *Soil science society of America journal*, 44(5):892–898.

Van Keulen, H. ; Seligman, N. G. (1987). *Simulation of water use, nitrogen nutrition and growth of a spring wheat crop*. Number 2. Cambridge University Press.

van Noordwijk, M., Brouwer, G., Meijboom, F., do Rosário G. Oliveira, M., and Bengough, A. G. (2001). Trench profile techniques and core break methods. In *Root Methods*, pages 211–233. Springer Berlin Heidelberg.

van Overmeeren, R., Sariowan, S., and Gehrels, J. (1997). Ground penetrating radar for determining volumetric soil water content results of comparative measurements at two test sites. *Journal of Hydrology*, 197(1-4):316–338.

Vanderborght, J., Kemna, A., Hardelauf, H., and Vereecken, H. (2005). Potential of electrical resistivity tomography to infer aquifer transport characteristics from tracer studies: A synthetic case study. *Water Resources Research*, 41(6).

Vanella, D., Ramírez-Cuesta, J. M., Longo-Minnolo, G., Longo, D., D'Emilio, A., and Consoli, S. (2022). Identifying soil-plant interactions in a mixed-age orange orchard using electrical resistivity imaging. *Plant and Soil*, 483(1-2):181–197.

Vargas, J. A., Gil, P. M., Meza, F. J., Yáñez, G., Menanno, G., García-Gutiérrez, V., Luque, A. J., Poblete, F., Figueroa, R., Maringue, J., Pérez-Estay, N., and Sanhueza, J. (2020). Soil electrical resistivity monitoring as a practical tool for evaluating irrigation systems efficiency at the orchard scale: a case study in a vineyard in central chile. *Irrigation Science*, 39(1):123–143.

Vereecken, H., Amelung, W., Bauke, S. L., Bogena, H., Brüggemann, N., Montzka, C., Vanderborght, J., Bechtold, M., Blöschl, G., Carminati, A., Javaux, M., Konings, A. G., Kusche, J., Neuweiler, I., Or, D., Steele-Dunne, S., Verhoef, A., Young, M., and Zhang, Y. (2022). Soil hydrology in the earth system. *Nature Reviews Earth &amp Environment*, 3(9):573–587.

Vereecken, H., Huisman, J., Pachepsky, Y., Montzka, C., van der Kruk, J., Bogena, H., Weihermüller, L., Herbst, M., Martinez, G., and Vanderborght, J. (2014). On the spatio-temporal dynamics of soil moisture at the field scale. *Journal of Hydrology*, 516:76–96.

Vereecken, H., Huisman, J. A., Bogena, H., Vanderborght, J., Vrugt, J. A., and Hopmans, J. W. (2008). On the value of soil moisture measurements in vadose zone hydrology: A review. *Water Resources Research*, 44(4).

Vereecken, H., Kasteel, R., Vanderborght, J., and Harter, T. (2007). Upscaling hydraulic properties and soil water flow processes in heterogeneous soils: A review. *Vadose Zone Journal*, 6(1):1–28.

Vereecken, H., Schnepf, A., Hopmans, J., Javaux, M., Or, D., Roose, T., Vanderborght, J., Young, M., Amelung, W., Aitkenhead, M., Allison, S., Assouline, S., Baveye, P., Berli, M., Brüggemann, N., Finke, P., Flury, M., Gaiser, T., Govers, G., Ghezzehei, T., Hallett, P., Franssen, H. H., Heppell, J., Horn, R., Huisman, J., Jacques, D., Jonard, F., Kollet, S., Lafolie, F., Lamorski, K., Leitner, D., McBratney, A., Minasny, B., Montzka, C., Nowak, W., Pachepsky, Y., Padarian, J., Romano, N., Roth, K., Rothfuss, Y., Rowe, E., Schwen, A., Šimůnek, J., Tiktak, A., Dam, J. V., van der Zee, S., Vogel, H., Vrugt, J., Wöhling, T., and Young, I. (2016). Modeling soil processes: Review, key challenges, and new perspectives. *Vadose Zone Journal*, 15(5):vzj2015.09.0131.

Viliam Novák, H. H. (2018). *Applied Soil Hydrology*. Springer-Verlag GmbH.

Viscarra Rossel, R., McBratney, A., and Minasny, B. (2010). Proximal soil sensing.

von Hebel, C., Rudolph, S., Mester, A., Huisman, J. A., Kumbhar, P., Vereecken, H., and van der Kruk, J. (2014). Three-dimensional imaging of subsurface structural patterns using quantitative large-scale multiconfiguration electromagnetic induction data. *Water Resources Research*, 50(3):2732–2748.

Vrugt, J. A. and Dane, J. H. (2005). Inverse modeling of soil hydraulic properties.

Vrugt, J. A., Stauffer, P. H., Wöhling, T., Robinson, B. A., and Vesselinov, V. V. (2008). Inverse modeling of subsurface flow and transport properties: A review with new developments. *Vadose Zone Journal*, 7(2):843–864.

Wagner, B. J. (1992). Simultaneous parameter estimation and contaminant source characterization for coupled groundwater flow and contaminant transport modelling. *Journal of Hydrology*, 135(1-4):275–303.

Wang, T., Rostamza, M., Song, Z., Wang, L., McNickle, G., Iyer-Pascuzzi, A. S., Qiu, Z., and Jin, J. (2019). Segroot: A high throughput segmentation method for root image analysis. *Computers and Electronics in Agriculture*, 162:845–854.

Wang, Y.-H. and Su, W.-H. (2022). Convolutional neural networks in computer vision for grain crop phenotyping: A review. *Agronomy*, 12(11):2659.

Warren, C., Giannopoulos, A., and Giannakis, I. (2016). gprMax: Open source software to simulate electromagnetic wave propagation for ground penetrating radar. *Computer Physics Communications*, 209:163–170.

Wasson, A., Bischof, L., Zwart, A., and Watt, M. (2016). A portable fluorescence spectroscopy imaging system for automated root phenotyping in soil cores in the field. *Journal of Experimental Botany*, 67(4):1033–1043.

Wasson, A. P., Nagel, K. A., Tracy, S., and Watt, M. (2020). Beyond digging: Noninvasive root and rhizosphere phenotyping. *Trends in Plant Science*, 25(1):119–120.

Weaver, J. E. (1926). *Root development of field crops*. McGraw-Hill Book Company.

Weigand, M. and Kemna, A. (2017). Multi-frequency electrical impedance tomography as a non-invasive tool to characterize and monitor crop root systems. *Biogeosciences*, 14(4):921–939.

Weigand, M. and Kemna, A. (2018). Imaging and functional characterization of crop root systems using spectroscopic electrical impedance measurements. *Plant and Soil*, 435(1-2):201–224.

Weigand, M., Zimmermann, E., Michels, V., Huisman, J. A., and Kemna, A. (2022). Design and operation of a long-term monitoring system for spectral electrical impedance tomography (sEIT). *Geoscientific Instrumentation, Methods and Data Systems*, 11(2):413–433.

Weihermüller, L., Huisman, J., Lambot, S., Herbst, M., and Vereecken, H. (2007). Mapping the spatial variation of soil water content at the field scale with different ground penetrating radar techniques. *Journal of Hydrology*, 340(3-4):205–216.

Weihermüller, L., Huisman, J., Hermes, N., Pickel, S., and Vereecken, H. (2013). A new TDR multiplexing system for reliable electrical conductivity and soil water content measurements. *Vadose Zone Journal*, 12(2):vzj2012.0194.

Weihermüller, L., Huisman, J. A., Lambot, S., Herbst, M., and Vereecken, H. (2007). Mapping the spatial variation of soil water content at the field scale with different ground penetrating radar techniques. *Journal of Hydrology*, 340(3-4):205–216.

Whalley, W., Binley, A., Watts, C., Shanahan, P., Dodd, I., Ober, E., Ashton, R., Webster, C., White, R., and Hawkesford, M. J. (2017). Methods to estimate changes in soil water for phenotyping root activity in the field. *Plant and Soil*, 415(1-2):407–422.

Wijewardana, Y. G. N. S. and Galagedara, L. W. (2010). Estimation of spatio-temporal variability of soil water content in agricultural fields with ground penetrating radar. *Journal of Hydrology*, 391(1-2):26–35. 658kz Times Cited:17 Cited References Count:32.

Wijewardana, Y. N. S., Shilpadi, A. T., Mowjood, M. I. M., Kawamoto, K., and Galagedara, L. W. (2017). Ground-penetrating radar (GPR) responses for sub-surface salt contamination and solid waste: modeling and controlled lysimeter studies. *Environmental Monitoring and Assessment*, 189(2).

Wollschläger, U., Pfaff, T., and Roth, K. (2009). Field-scale apparent hydraulic parameterisation obtained from TDR time series and inverse modelling. *Hydrology and Earth System Sciences*, 13(10):1953–1966.

Yan, H., Dong, X., Feng, G., Zhang, S., and Mucciardi, A. (2013). Coarse root spatial distribution determined using a ground-penetrating radar technique in a subtropical evergreen broad-leaved forest, china. *Science China Life Sciences*, 56(11):1038–1046.

Yang, W., Feng, H., Zhang, X., Zhang, J., Doonan, J. H., Batchelor, W. D., Xiong, L., and Yan, J. (2020). Crop phenomics and high-throughput phenotyping: past decades, current challenges, and future perspectives. *Molecular Plant*, 13(2):187–214.

Yasrab, R., Atkinson, J. A., Wells, D. M., French, A. P., Pridmore, T. P., and Pound, M. P. (2019). RootNav 2.0: Deep learning for automatic navigation of complex plant root architectures. *GigaScience*, 8(11).

Yeh, T.-C. J. and Šimůnek, J. (2002). Stochastic fusion of information for characterizing and monitoring the vadose zone. *Vadose Zone Journal*, 1(2):207–221.

York, L. M. (2021). *Phenotyping Root System Architecture, Anatomy, and Physiology to Understand Soil Foraging*, pages 209–221. Springer International Publishing.

Ytting, N. K., Andersen, S. B., and Thorup-Kristensen, K. (2014). Using tube rhizotrons to measure variation in depth penetration rate among modern north-european winter wheat (triticum aestivum l.) cultivars. *Euphytica*, 199(1-2):233–245.

Yu, Y., Huisman, J. A., Klotzsche, A., Vereecken, H., and Weihermüller, L. (2022). Coupled full-waveform inversion of horizontal borehole ground penetrating radar data to estimate soil hydraulic parameters: A synthetic study. *Journal of Hydrology*, 610:127817.

Yu, Y., Klotzsche, A., Weihermüller, L., Huisman, J. A., Vanderborght, J., Vereecken, H., and der Kruk, J. (2020). Measuring vertical soil water content profiles by combining horizontal borehole and dispersive surface ground penetrating radar data. *Near Surface Geophysics*, 18(3):275–294.

Yu, Y., Weihermüller, L., Klotzsche, A., Lärm, L., Vereecken, H., and Huisman, J. A. (2021). Sequential and coupled inversion of horizontal borehole ground penetrating radar data to estimate soil hydraulic properties at the field scale. *Journal of Hydrology*, 596:126010.

Zeng, G., Birchfield, S. T., and Wells, C. E. (2008). Automatic discrimination of fine roots in minirhizotron images. *New Phytologist*, 177(2):549–557.

Zeng, G., Birchfield, S. T., and Wells, C. E. (2010). Rapid automated detection of roots in minirhizotron images. *Machine Vision and Applications*, 21(3):309–317.

Zhang, Y., Weihermüller, L., Toth, B., Noman, M., and Vereecken, H. (2022). Analyzing dual porosity in soil hydraulic properties using soil databases for pedotransfer function development. *Vadose Zone Journal*, 21(5).

Zhang, Z. F., Ward, A. L., and Gee, G. W. (2003). Estimating soil hydraulic parameters of a field drainage experiment using inverse techniques. *Vadose Zone Journal*, 2(2):201–211.

Zhu, J. and Mohanty, B. P. (2003). Effective hydraulic parameters for steady state vertical flow in heterogeneous soils. *Water Resources Research*, 39(8).

Zhuang, J., Nakayama, K., Yu, G.-R., and Urushisaki, T. (2001). Estimation of root water uptake of maize: an ecophysiological perspective. *Field Crops Research*, 69(3):201–213.

Zotarelli, L., Dukes, M. D., Romero, C. C., Migliaccio, K. W., and Morgan, K. T. (2010). Step by step calculation of the penman-monteith evapotranspiration (fao-56 method). *Institute of Food and Agricultural Sciences. University of Florida*.

Zuo, Q., Jie, F., Zhang, R., and Meng, L. (2004). A generalized function of wheat's root length density distributions. *Vadose Zone Journal*, 3(1):271–277.

Abbreviations

AIC	Akaike Information Criteria
BC	Boundary condition
CF	Cost function
CMP	Common midpoint profiling
CNN	convolutional neural network
COP	Common offset profiling
CRIM	Complex refractive index model
DC	Direct Current
E	Evoporation
EF	extra field
EIT	electrical impedance tomography
EM	Electromagnetic
EMI	Electromagnetic induction
ERT	Electrical resistivity tomography
ERT	Electrical resistivity tomography
ET	Evopatranspiration
FB	first break
FC	field capacity
FDEM	frequency domain electromagnetics

GHG	greenhouse gas
GPR	Ground penetrating radar
GS	growing season
HCC	hydraulic conductivity characteristics
HHS	homogeneous half space
INRES	Institute of Crop Science and Resource Conservation
IP	induced polarization
LAI	Leaf area index
LAI	leaf area index
MOG	Multi offset gathers
MR	Minirhizotron
MRI	magnetic resonance imaging
MVG	Mualem-van-Genuchten
NMR	Nuclear magnetic resonance
PAW	plant available water
PDR	probability density function
PWP	permanent wilting point
RLT	Lower Terrace rhizotron facility
RUT	Upper Terrace rhizotron facility
RCD	root count density
RL	root length
RLD	root length density
RMSE	root mean square error
RMSE	Root mean square error
RVF	volumetric root volume fraction
Rx	Receiver antennae
SCE-UA	Shuffled complex evolution developed by the University of Arizona
SD	Standard deviation
sEIT	spectral electrical impedance tomography

SHP	soil hydraulic properties
SIP	spectral induced polarization
SSR	sum of squared residuals
SV	sensing volume
SWC	Soil water content
SWP	soil water potential
SWR	soil water retention
T	Transpiration
TDR	Time domain reflectometry
TERENO	TERrestrial ENvironmental Observatories
Tx	Transmitter antennae
UAV	unmanned aerial vehicle
VRP	vertical radar profiling
WARR	Wide angle reflection refraction
ZOP	Zero offset profile

List of Figures

List of Tables

Band / Volume 629
Structure and properties of electrochemical interfaces from first principles simulations
R. Tesch (2024), xvi, 161 pp
ISBN: 978-3-95806-753-0

Band / Volume 630
Elucidation of Barocaloric Effect in Spin Crossover Compounds
H. Shahed (2024), x, 261 pp
ISBN: 978-3-95806-758-5

Band / Volume 631
Computational Investigation of Solvation Phenomena at Metal-Electrolyte Interfaces
O. Cheong (2024), xvii, 142 pp
ISBN: 978-3-95806-759-2

Band / Volume 632
Senkung zukünftiger Stickoxid- und Partikelemissionen in Nordrhein-Westfalen durch den Einsatz alternativer Energieträger und Antriebe
J. L. Breuer (2024), vii, 339 pp
ISBN: 978-3-95806-760-8

Band / Volume 633
Development of Model-Based Correction Methods for Temperature-Dependent Electromagnetic Induction (EMI) Measurement Errors in Soil Conductivity Estimations
T. M. Tchantcho Amin (2024), xx, 100 pp
ISBN: 978-3-95806-761-5

Band / Volume 634
Investigation and implementation of improved and degradation-tolerant fuel electrodes for solid oxide cells
A. Schwiers (2024), VI, 163, XIII pp
ISBN: 978-3-95806-762-2

Band / Volume 635
In Situ Time Calibration for Stationary Multichannel GPR Monitoring Systems
L. Steinbeck (2024), xvi, 98, xxxi pp
ISBN: 978-3-95806-767-7

Band / Volume 636
Erneuerbares Methanol als Ausgangsstoff für die Bereitstellung von flüssigen Kraftstoffen für den Transportsektor
F. Schorn (2024), VI, 275 pp
ISBN: 978-3-95806-769-1

Band / Volume 637
Investigation of Lower Boundary Conditions of Brominated Very Short-lived Species (VSLS)
S. Zheng (2024), 2, iii, 160 pp
ISBN: 978-3-95806-770-7

Band / Volume 638
Modellgestützte Analyse zukünftigen Mobilitätsverhaltens
J. P. Reul (2024), XVI, 291 pp
ISBN: 978-3-95806-771-4

Band / Volume 639
Insights into Mechanisms of Secondary Organic Aerosol Formation: Approaching Atmospherically Relevant Conditions in an Atmospheric Reaction Chamber
Y. Baker (2024), XVII, 122 pp
ISBN: 978-3-95806-776-9

Band / Volume 640
Advancing the representation of agricultural systems in Land Surface Models: systematic model evaluations and technical model developments
T. S. Boas (2024), xxi, 145 pp
ISBN: 978-3-95806-777-6

Band / Volume 641
Imaging spatial and temporal soil water content variations of the soil-plant continuum using ground penetrating radar
L. Lärm (2024), xii, 303 pp
ISBN: 978-3-95806-778-3

Weitere ***Schriften des Verlags im Forschungszentrum Jülich*** unter
http://wwwzb1.fz-juelich.de/verlagextern1/index.asp

Energie & Umwelt / Energy & Environment
Band / Volume 641
ISBN 978-3-95806-778-3

Mitglied der Helmholtz-Gemeinschaft

JÜLICH
Forschungszentrum